frontiers | Research Topics

Neutrino nuclear responses for astro-particle physics by nuclear reactions and nuclear decays

Edited by
Hiroyasu Ejiri, Francesco Cappuzzello
and Theocharis S. Kosmas

Published in
Frontiers in Astronomy and Space Sciences
Frontiers in Physics

ISSN 1664-8714
ISBN 978-2-8325-2740-5
DOI 10.3389/978-2-8325-2740-5

About Frontiers

Frontiers is more than just an open access publisher of scholarly articles: it is a pioneering approach to the world of academia, radically improving the way scholarly research is managed. The grand vision of Frontiers is a world where all people have an equal opportunity to seek, share and generate knowledge. Frontiers provides immediate and permanent online open access to all its publications, but this alone is not enough to realize our grand goals.

Frontiers journal series

The Frontiers journal series is a multi-tier and interdisciplinary set of open-access, online journals, promising a paradigm shift from the current review, selection and dissemination processes in academic publishing. All Frontiers journals are driven by researchers for researchers; therefore, they constitute a service to the scholarly community. At the same time, the *Frontiers journal series* operates on a revolutionary invention, the tiered publishing system, initially addressing specific communities of scholars, and gradually climbing up to broader public understanding, thus serving the interests of the lay society, too.

Dedication to quality

Each Frontiers article is a landmark of the highest quality, thanks to genuinely collaborative interactions between authors and review editors, who include some of the world's best academicians. Research must be certified by peers before entering a stream of knowledge that may eventually reach the public - and shape society; therefore, Frontiers only applies the most rigorous and unbiased reviews. Frontiers revolutionizes research publishing by freely delivering the most outstanding research, evaluated with no bias from both the academic and social point of view. By applying the most advanced information technologies, Frontiers is catapulting scholarly publishing into a new generation.

What are Frontiers Research Topics?

Frontiers Research Topics are very popular trademarks of the *Frontiers journals series*: they are collections of at least ten articles, all centered on a particular subject. With their unique mix of varied contributions from Original Research to Review Articles, Frontiers Research Topics unify the most influential researchers, the latest key findings and historical advances in a hot research area.

Find out more on how to host your own Frontiers Research Topic or contribute to one as an author by contacting the Frontiers editorial office: frontiersin.org/about/contact

Neutrino nuclear responses for astro-particle physics by nuclear reactions and nuclear decays

Topic editors

Hiroyasu Ejiri — Osaka University, Japan

Francesco Cappuzzello — University of Catania, Italy

Theocharis S. Kosmas — University of Ioannina, Greece

Citation

Ejiri, H., Cappuzzello, F., Kosmas, T. S., eds. (2023). *Neutrino nuclear responses for astro-particle physics by nuclear reactions and nuclear decays*. Lausanne: Frontiers Media SA. doi: 10.3389/978-2-8325-2740-5

Table of contents

frontiers | Frontiers in Astronomy and Space Sciences

EDITORIAL
published: 31 May 2022
doi: 10.3389/fspas.2022.836881

Editorial: Neutrino Nuclear Responses for Astro-Particle Physics by Nuclear Reactions and Nuclear Decays

Hiroyasu Ejiri[1]*, *Francesco Cappuzzello*[2,3] and *Theocharis Kosmas*[4]

[1]Research Center for Nuclear Physics, Osaka University, Osaka, Japan, [2]Department of Physics and Astronomy "Ettore Majorana", University of Catania, Catania, Italy, [3]Istituto Nazionale di Fisica Nucleare, Laboratori Nazionali del Sud, Catania, Italy, [4]Department of Physics, University of Ioannina, Ioannina, Greece

Keywords: neutrino nuclear responses, neutrino mass, nuclear reactions, nuclear decays, double beta decays

Editorial on the Research Topic

Neutrino Nuclear Responses for Astro-Particle Physics by Nuclear Reactions and Nuclear Decays

1 AIM OF THE RESEARCH TOPICS

The special issue of the research topics "Neutrino Nuclear Responses for Astro-Particle Physics by Nuclear Reactions and Nuclear Decays" includes 10 contributions by 88 authors. Here we briefly report about the aim of the special issue and summarize the contributions.

Fundamental properties of neutrinos, such as the Majorana nature and the neutrino masses, which are beyond the standard model, are searched for by measuring neutrinoless double beta decays (DBDs) in nuclei. Astro-neutrino nucleosyntheses and astro-neutrino productions are studied by investigating neutrino nuclear interactions. The neutrino nuclear response, given by the square of the nuclear matrix element (NME), is crucial for neutrino studies in nuclei.

The neutrino nuclear responses have been studied experimentally by means of charge-exchange nuclear reactions, nuclear scatterings, and ordinary muon capture reactions and theoretically by various nuclear models. The present special issue reports recent experimental and theoretical studies of the neutrino nuclear responses and discusses perspectives of these studies.

2 EXPERIMENTAL STUDIES OF NEUTRINO NUCLEAR RESPONSES

Current experimental approaches to neutrino nuclear responses for DBDs and astro-neutrinos and field perspectives are briefly reviewed by H. Ejiri. Recent experimental studies discuss nuclear weak decays, charge-exchange reactions, double charge-exchange reactions, muon-capture reactions, photon capture reactions, and neutrino reactions. It is emphasized that experimental studies of the neutrino responses and the quenching of the axial-vector coupling are useful for neutrino studies in nuclei.

Ordinary muon captures (OMCs), which are lepton charge-exchange reactions, are used for studying anti-neutrino nuclear responses for astro-neutrinos and the $\tau+$ (isospin raising operator) responses for DBDs. Recent experimental studies of OMCs at RCNP Osaka are briefly reviewed by

OPEN ACCESS

Edited and reviewed by:
J. W. F. Valle,
Spanish National Research Council (CSIC), Spain

***Correspondence:**
Hiroyasu Ejiri
ejiri@rcnp.osaka-u.ac.jp

Specialty section:
This article was submitted to High-Energy and Astroparticle Physics, a section of the journal Frontiers in Astronomy and Space Sciences

Received: *16 December 2021*
Accepted: *01 February 2022*
Published: *31 May 2022*

Citation:
Ejiri H, Cappuzzello F and Kosmas T (2022) Editorial: Neutrino Nuclear Responses for Astro-Particle Physics by Nuclear Reactions and Nuclear Decays. Front. Astron. Space Sci. 9:836881. doi: 10.3389/fspas.2022.836881

I. H. Hashim and H. Ejiri. OMCs give access to neutrino nuclear responses in wide excitation-energy and momentum-transfer regions, which are relevant to neutrinoless DBDs and supernova neutrinos.

Heavy ion charge-exchange reactions are useful tools to probe neutrino nuclear responses. A constrained analysis of the ^{40}Ca (^{18}O,^{18}F) ^{40}K reaction mechanism at 275 MeV is reported by M.Cavallaro et al. The elastic and inelastic scattering data at the same energy are used for the analyses. The direct single charge-exchange reaction mechanism describes the cross-section and the shape of the angular distribution.

Double charge-exchange (DCE) reactions with light heavy ions provide valuable information on neutrino nuclear responses for neutrinoless DBDs. F. Cappuzzello et al. reported the NUMEN project, which aims to access experimentally driven information of NMEs for neutrinoless DBDs by measuring DCE. Recent R&D activities for upgrading the superconducting cyclotron accelerator and the magnetic spectrometer for the DCE reactions are discussed.

In order to study the axial-vector weak coupling in nuclei, H. Matsubara and A. Tamii discussed the quenching of the isovector and isoscalar spin-M1 excitation strengths in $N = Z$ nuclei. They were studied by measuring the inelastic scattering of 295 MeV protons from the RCNP ring cyclotron. The isoscalar M1 strengths are consistent with the shell-model predictions, while the isovector ones are quenched in comparison with the predictions.

3 THEORETICAL STUDIES OF NEUTRINO NUCLEAR RESPONSES AND DOUBLE BETA DECAY MECHANISMS

DBD NMEs have been studied theoretically using proton-neutron quasiparticle random phase approximation (pnQRPA), interacting boson model (IBM), interacting shell model (ISM), and other models. A comparative analysis of the DBD NMEs and the OMC NMEs for ^{106}Cd is reported by L. Jokiniemi, J. Suhonen, and J. Kotila. The NMEs are derived using the pnQRPA with the large no-core single-particle basis. Good correspondence between the DBD NMEs and the OMC NMEs is found.

A comparison of the microscopic IBM (IBM-2) NMEs and the pnQRPA NMEs for DBD nuclei is made by J. Kotila. The IBM NMEs agree with the pnQRPA ones for most DBD nuclei, except for the nuclei with A=110 and 124, in the case of the light-neutrino exchange. However, the IBM NMEs disagree with the pnQRPA NMEs in the case of the heavy-neutrino exchange. Detailed discussions are made for the two models.

ISM calculations for the ^{82}Se DBD with the left-right weak-boson exchange are reported by Y. Iwata and S. Sarkar. The DBD NMEs for the λ-mechanism (the left-right weak-boson exchange) and the neutrino-mass mechanism (light neutrino exchange) are evaluated, and bounds on the neutrino mass and the lepton-number violation parameters are derived.

DBD phase space factors are required to extract the neutrino mass and other physics parameters beyond the standard model (BSM). Recent theoretical results of DBD NMEs and DBD phase space factors are briefly reviewed by A. Neacsu, V. A. Sevestreen, and S. Stoica. Constraints on the BSM parameters are derived using the DBD NMEs, the phase space factors, and the most stringent limit on the experimental DBD rate.

Weak interactions of leptons with nucleons and nuclei in stars are interesting subjects of neutrino nuclear responses. The role of the lepton interactions in the late stage of the stellar evolution and the astro-neutrino nuclear interactions relevant to terrestrial detection of astro-neutrinos are briefly reviewed by T. S. Kosmas, I. Tsoulos, O. T. Kosmas, and P. G. Giannaka.

In summary, the scientific benefits of the present special issue are evident from the wide range of the research subjects covered by the included papers. The selected topics fall at the forefront of multidisciplinary investigations within experimental, phenomenological, and theoretical nuclear physics, in major overlap with atomic physics, particle physics, astrophysics, and cosmology.

AUTHOR CONTRIBUTIONS

All authors listed have made a substantial, direct, and intellectual contribution to the work and approved it for publication.

Conflict of Interest: The authors declare that the research was conducted in the absence of any commercial or financial relationships that could be construed as a potential conflict of interest.

Publisher's Note: All claims expressed in this article are solely those of the authors and do not necessarily represent those of their affiliated organizations or those of the publisher, the editors, and the reviewers. Any product that may be evaluated in this article, or claim that may be made by its manufacturer, is not guaranteed or endorsed by the publisher.

frontiers in Physics

ORIGINAL RESEARCH
published: 01 April 2021
doi: 10.3389/fphy.2021.652536

Comparative Analysis of Nuclear Matrix Elements of $0\nu\beta^+\beta^+$ Decay and Muon Capture in ^{106}Cd

Lotta Jokiniemi[1*†], *Jouni Suhonen*[1] *and Jenni Kotila*[2,3]

[1] Department of Physics, University of Jyväskylä, Jyväskylä, Finland, [2] Finnish Institute for Educational Research, University of Jyväskylä, Jyväskylä, Finland, [3] Center for Theoretical Physics, Sloane Physics Laboratory Yale University, New Haven, CT, United States

Comparative analyses of the nuclear matrix elements (NMEs) related to the $0\nu\beta^+\beta^+$ decay of ^{106}Cd to the ground state of ^{106}Pd and the ordinary muon capture (OMC) in ^{106}Cd are performed. This is the first time the OMC NMEs are studied for a nucleus decaying via positron-emitting/electron-capture modes of double beta decay. All the present calculations are based on the proton-neutron quasiparticle random-phase approximation with large no-core single-particle bases and realistic two-nucleon interactions. The effect of the particle-particle interaction parameter $g_{\rm pp}$ of pnQRPA on the NMEs is discussed. In the case of the OMC, the effect of different bound-muon wave functions is studied.

Keywords: nuclear double beta decay, nuclear muon capture, nuclear matrix elements, quasiparticle random-phase approximation, bound-muon wave function, particle-particle interaction parameter

OPEN ACCESS

Edited by:
Theocharis S. Kosmas, University of Ioannina, Greece

Reviewed by:
Zhenbin Wu, University of Illinois at Chicago, United States
Janusz Gluza, University of Silesia in Katowice, Poland

****Correspondence:***
Lotta Jokiniemi
lotta.jokiniemi@gmail.com

†Present address:
Lotta Jokiniemi, Department of Quantum Physics and Astrophysics and Institute of Cosmos Sciences, University of Barcelona, Barcelona, Spain

Specialty section:
This article was submitted to High-Energy and Astroparticle Physics, a section of the journal Frontiers in Physics

Received: *12 January 2021*
Accepted: *05 March 2021*
Published: *01 April 2021*

Citation:
Jokiniemi L, Suhonen J and Kotila J (2021) Comparative Analysis of Nuclear Matrix Elements of $0\nu\beta^+\beta^+$ Decay and Muon Capture in ^{106}Cd. Front. Phys. 9:652536. doi: 10.3389/fphy.2021.652536

1. INTRODUCTION

Neutrinoless double beta ($0\nu\beta\beta$) decay is a process in which a nucleus (A, Z), with mass number A and proton number Z, decays to a daughter nucleus with two more or two less protons. In the $0\nu\beta^-\beta^-$ mode the final nucleus is $(A, Z+2)$, and two electrons are emitted. In the case of the $0\nu\beta^+\beta^+$ mode the final nucleus is $(A, Z-2)$, and two positrons are emitted. In the latter case also the electron capture (EC) is possible through the mode $0\nu\beta^+$EC. In this article we denote also this mode by the generic symbol $0\nu\beta^+\beta^+$. In the case of ^{106}Cd also the 0νECEC (neutrinoless double electron capture) [1] is possible, but it goes to an excited state, and thus is beyond the scope of the present work, as we analyze here only the ground-state-to-ground-state transition. In addition, it should be noted that the same nuclear matrix elements (NMEs) are involved in the $0\nu\beta^+\beta^+$ and $0\nu\beta^+$EC modes. In any case, the neutrinoless double beta decay would immediately provide striking new-physics vistas beyond the standard model, since it not only violates lepton-number conservation, but also requires the neutrino to be of Majorana character. After the discovery of neutrino oscillations [2–4], this process has become even the more of vital interest because its discovery could potentially provide us with information on the yet-unknown absolute mass scale of neutrinos.

While neutrinoless double beta decay remains hypothetical, the two-neutrino decay mode ($2\nu\beta\beta$), which is allowed by the standard model, has been observed in several isotopes. Most of the observed decays are of two-neutrino double-beta minus ($2\nu\beta^-\beta^-$) type, and there are only six isotopes capable of $2\nu\beta^+\beta^+$ decaying: ^{78}Kr, ^{96}Ru, ^{106}Cd, ^{124}Xe, ^{130}Ba, and ^{136}Ce. Naturally, these isotopes can also decay via the $2\nu\beta^+$EC and 2νECEC (two-neutrino double electron capture) modes. Of these isotopes, ^{106}Cd is a particularly promising candidate for the $2\nu\beta^+\beta^+$-decay searches since it has the biggest decay energy, $Q_{\beta\beta} = 2775.39(10)$ keV, as well as

other experimentally favorable features. At present, there are three running experiments searching for the $\beta^+\beta^+$ decay of ^{106}Cd, namely COBRA [5, 6], TGV-2 [7], and $^{106}CdWO_4$ crystal scintillator [8].

Ordinary muon capture (OMC) on nuclei is a weak-interaction nuclear process, in which a negative muon μ^- is captured by a nucleus (A, Z) resulting in an atomic-number reduction by one and emission of a muon neutrino. It can significantly extend the kinematic region of ordinary beta decay, owing to the high energy release and large momentum transfer associated with the process. The energy release in the nuclear capture process is about 100 MeV, of which the largest fraction is donated to the neutrino, being the lightest particle in the process. Large mass of the captured muon allows highly-forbidden transitions and high excitation energies of the final states. These features make the OMC a particularly promising probe for the $0\nu\beta\beta$ decay. In fact, there are several completed, ongoing and planned experiments aiming to study OMC in double-beta-decay triplets. In [9], partial OMC rates to numerous excited states of intermediate nuclei of $\beta\beta$-decay triplets, including the $A = 106$ triplet we are studying here, were extracted from γ-ray spectra. In [10], on the other hand, OMC strength function and the associated giant resonances in ^{100}Nb were studied for the first time. There is an ongoing joint program pursued at RCNP, J-PARC, and the Paul Scherrer Institute (PSI) aiming to extend these studies to a wide range of nuclei from *sd*-shell nuclei such as ^{24}Mg up to as heavy nuclei as ^{240}Pu [11].

In the work of Kortelainen et al. [12] the OMC rates were compared against the $2\nu\beta^-\beta^-$-decay NMEs for light nuclei using the nuclear shell model. It was found that there was a clear correlation between the energy-distributed OMC rates to 1^+ states and the energy-based decomposition of the NMEs for the $2\nu\beta^-\beta^-$ decays of the sd-shell nuclei ^{36}Ar, ^{46}Ca, and ^{48}Ca. In [13], we extended these studies to $0\nu\beta^-\beta^-$ decays of medium-heavy and heavy nuclei by computing the average matrix elements corresponding to the OMC transitions to the intermediate nuclei of $0\nu\beta^-\beta^-$ decays up to some 50 MeV using the pnQRPA formalism. We then compared these matrix elements with the energy-multipole decompositions of the NMEs of $0\nu\beta^-\beta^-$ decays computed using the same formalism and model spaces. We found that there are clear correspondencies between the $0\nu\beta^-\beta^-$-decay NMEs and the average OMC matrix elements, especially for the $J^\pi = 3^+, 3^-, 4^+$, and 4^- states.

In [14], double beta decays of ^{106}Cd were studied in the pnQRPA framework using ^{40}Ca as the inert core. Here we extend those studies, for the ground-state-to-ground-state transition, by making a comparative analysis of the $0\nu\beta^+\beta^+$-decay and OMC NMEs of ^{106}Cd in the pnQRPA formalism with large no-core single-particle bases, in a manner pursued in [13]. The OMC on ^{106}Cd leads to excited states of ^{106}Ag which, on the other hand, act as virtual intermediate states of the $\beta^+\beta^+$ decay of ^{106}Cd (see **Figure 1**). Hence, we hope the comparison between OMC and $0\nu\beta^+\beta^+$-decay matrix elements will help improve the accuracy of the $0\nu\beta^+\beta^+$-decay NMEs by using the data of future muon-capture experiments. Particularly, in the case of ^{106}Cd, a measured OMC-strength spectrum would help pin down the value of the particle-particle parameter $g_{\rm pp}$ of pnQRPA, which in this case cannot be adjusted to $2\nu\beta\beta$-decay data. We also study the effect of different bound-muon wave function on the OMC matrix elements. This is the first time when such calculations are being done on the positron-decay side of the nuclear chart.

2. TWO-NEUTRINO DOUBLE-BETA DECAY

The half-life of a ground-state-to-ground-state two-neutrino double-beta decay can be written in the form

$$\left[t_{1/2}^{(2\nu)}(0_i^+ \to 0_f^+)\right]^{-1} = (g_{\rm A}^{\rm eff})^4 G_{2\nu} \left|M^{(2\nu)}\right|^2 , \tag{1}$$

where $g_{\rm A}^{\rm eff}$ is the effective value of the weak axial-vector coupling strength. The factor $G_{2\nu}$ is a leptonic phase-space factor (in units of inverse years) defined in [15, 16]. The ground states of the initial and final nuclei are denoted by 0_i^+ and 0_f^+, correspondingly.

The Gamow-Teller NME involved in Equation (1) can be written as

$$M^{(2\nu)} = \sum_{m,n} \frac{(0_f^+ \| \sum_k t_k^- \boldsymbol{\sigma}_k \| 1_m^+)\langle 1_m^+ | 1_n^+ \rangle (1_n^+ \| \sum_k t_k^- \boldsymbol{\sigma}_k \| 0_i^+)}{D_m + 1} , \tag{2}$$

with the energy denominator

$$D_m = \left(\tfrac{1}{2}\Delta + \tfrac{1}{2}[E(1_m^+) + \tilde{E}(1_m^+)] - M_i\right)/m_e , \tag{3}$$

where Δ is the nuclear mass difference between the initial and final 0^+ ground states, M_i the mass of the initial nucleus, and m_e the electron rest mass. $\tilde{E}(1_m^+)$ and $E(1_m^+)$ are the (absolute) energies of the mth 1^+ state in a pnQRPA calculation based on the left- and right-side ground states.

In principle, the expression in Equation (2) could also contain a Fermi NME. However, the ground states of the mother and daughter nuclei belong to different isospin multiplets, and due to the isospin symmetry, the Fermi contribution to the $2\nu\beta\beta$-decay NME should vanish, leaving the Gamow-Teller NME in Equation (2) as the sole contributor to the $2\nu\beta\beta$-decay rate.

In [16], the phase-space factors for the $2\nu\beta^+\beta^+$ decay, as well as for the competing modes $2\nu\beta^+$EC and 2νECEC were computed. In [8], the experimentally extracted lower limits for half-lives of the different modes for ^{106}Cd were given. These values, together with the corresponding phase-space factors and resulting experimental matrix elements, are listed in **Table 1**.

3. NEUTRINOLESS DOUBLE-BETA DECAY

We assume that the $0\nu\beta\beta$ decay is dominated by the light-Majorana-neutrino-exchange mechanism, and exploit the formalism presented in [17]. Here we are only interested in the ground-state-to-ground-state transitions. The half-life for such a $0\nu\beta\beta$ transition can be written as

$$\left[t_{1/2}^{(0\nu)}(0_i^+ \to 0_f^+)\right]^{-1} = (g_{\rm A}^{\rm eff})^4 G_{0\nu} \left|M^{(0\nu)}\right|^2 \left|\frac{\langle m_\nu \rangle}{m_e}\right|^2 , \tag{4}$$

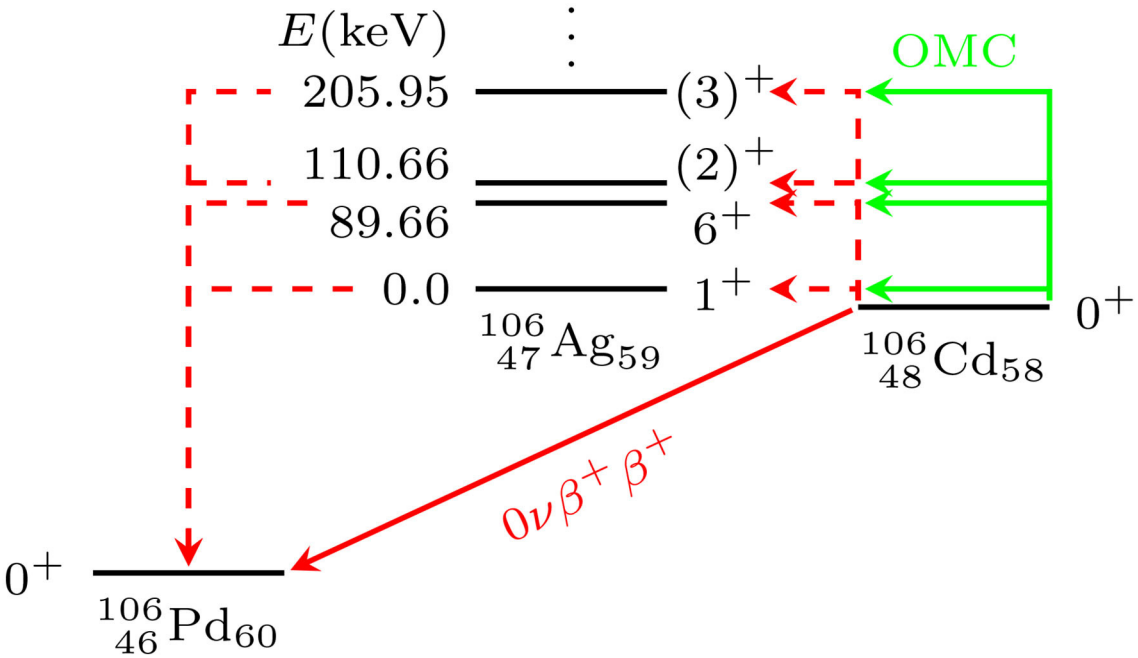

FIGURE 1 | Level scheme of the $A = 106$ system. The solid red line indicates the $0\nu\beta^+\beta^+$-decay transition from the ground state of ^{106}Cd to the ground state of ^{106}Pd, and the dashed red lines refer to virtual transitions related to the $0\nu\beta^+\beta^+$ decay. The green lines correspond to OMC on the ground state of ^{106}Cd leading to different excited states of ^{106}Ag. The excitation energies of ^{106}Ag are shown in units of keV.

where $G_{0\nu}$ is a phase-space factor for the final-state leptons in units of inverse years (see [15, 16]), defined here without including the axial-vector coupling g_A. The effective light-neutrino mass, $\langle m_\nu \rangle$, of Equation (4) is defined as

$$\langle m_\nu \rangle = \sum_j (U_{ej})^2 m_j \tag{5}$$

with m_j being the mass eigenstates of light neutrinos. The amplitudes U_{ej} are the components of the electron row of the light-neutrino-mass mixing matrix.

The $0\nu\beta\beta$-decay NME $M^{(0\nu)}$ in Equation (4) is defined as

$$M^{(0\nu)} = M^{(0\nu)}_{\rm GT} - \left(\frac{g_{\rm V}}{g^{\rm eff}_{\rm A}}\right)^2 M^{(0\nu)}_{\rm F} + M^{(0\nu)}_{\rm T}\,, \tag{6}$$

where we adopt the CVC value $g_{\rm V} = 1.0$ for the weak vector coupling strength. The definitions for the double Fermi, Gamow-Teller, and tensor NMEs $M^{(0\nu)}_{\rm F}$, $M^{(0\nu)}_{\rm GT}$, and $M^{(0\nu)}_{\rm T}$ can be found e.g., in [17].

For the nucleon-nucleon short-range correlations (SRC) [18, 19], included in the NMEs, we use the CD-Bonn form [20] with the parametrization,

$$f_{\rm CD}(r) = 1 - 0.46e^{-(1.52/{\rm fm}^2)r^2}[1 - (1.88/{\rm fm}^2)r^2]\,. \tag{7}$$

TABLE 1 | Phase-space factors [16], half-lives [8], and the resulting experimental NMEs of different decay modes of ^{106}Cd.

Decay mode	$G_{2\nu}$[1/y]	$t_{1/2}$[y]	$M^{(2\nu)}$
$2\nu\beta^+\beta^+$	2×10^{-26}	$\geq 1.7 \times 10^{21}$	≤ 171.5
2νECβ^+	7.02×10^{-22}	$\geq 2.1 \times 10^{21}$	≤ 0.824
2νECEC	5.41×10^{-21}	$\geq 4.7 \times 10^{20}$	≤ 0.627

The results correspond to the effective value $g_A^{\rm eff} = 1.0$ of the axial coupling.

4. MUON CAPTURE

Ordinary muon capture (OMC) is a semileptonic weak interaction process, quite like electron capture (EC). The OMC process we are interested in here can be written as

$$\mu^- + {}^A_Z{\rm X}(0^+) \rightarrow \nu_\mu + {}^A_{Z-1}{\rm Y}(J^\pi)\,, \tag{8}$$

where the negatively charged muon (μ^-) is captured by the 0^+ ground state of the even-even nucleus X of mass number A and atomic number Z. The process leads to the J^π multipole states of Y, the odd-odd isobar of the mother nucleus, of atomic number $Z - 1$; here J is the angular momentum and π the parity of the final state. At the same time a muon neutrino ν_μ is emitted.

4.1. Bound-Muon Wave Functions

The wave function of the muon bound on an atomic orbit of the initial nucleus can be written as an expansion in terms of the

normalized spherical spinors $\chi_{\kappa\mu}$

$$\psi_\mu(\kappa,\mu;\mathbf{r}) = \psi^{(\mu)}_{\kappa\mu} = \begin{bmatrix} -iF_\kappa\,\chi_{-\kappa\mu} \\ G_\kappa\,\chi_{\kappa\mu} \end{bmatrix}, \tag{9}$$

where G_κ and F_κ are the large and small radial components of the wave functions of the bound state [21]. Here κ denotes the atomic orbit in the following manner

$$\begin{cases} l = \kappa \text{ and } j = l - \frac{1}{2}, & \text{for } \kappa > 0 \\ l = -\kappa - 1 \text{ and } j = l + \frac{1}{2}, & \text{for } \kappa < 0. \end{cases} \tag{10}$$

After being stopped in the outermost shell of an atom, the negatively charged muon undergoes a cascade of transitions to lower atomic orbitals, leaving it finally on the lowest, K atomic orbit. Hence, the captured muon can be assumed to be initially bound in the lowest state, $1s_{1/2}$, corresponding to $\kappa = -1$ and $\mu = \pm\frac{1}{2}$. Making this assumption, we can estimate the bound-muon wave function by the Bethe-Salpeter point-like-nucleus approximation formulae [22]

$$\begin{aligned} G_{-1} &= (2Z/a_0)^{\frac{3}{2}} \sqrt{\frac{1+\gamma}{2\Gamma(2\gamma+1)}} \left(\frac{2Zr}{a_0}\right)^{\gamma-1} e^{-Zr/a_0}\,, \\ F_{-1} &= -\sqrt{\frac{1-\gamma}{1+\gamma}}\,G_{-1}\,, \end{aligned} \tag{11}$$

where γ is defined as

$$\gamma = \sqrt{1-(\alpha Z)^2}\,,$$

where α is the fine-structure constant and Z the atomic number of the nucleus. The Bohr radius of the μ-mesonic atom is

$$a_0 = \frac{\hbar}{m'_\mu c\alpha} = \frac{1}{m'_\mu}\,,$$

where we have adopted the values $\hbar = c = 1$. The

$$m'_\mu = \frac{m_\mu}{1 + \frac{m_\mu}{AM}} \tag{12}$$

is the reduced muon mass in the μ-mesonic atom. If we assume that αZ is very small, $\gamma \approx 1$, and therefore

$$\begin{aligned} G_{-1} &= 2(\alpha Z m'_\mu)^{\frac{3}{2}} e^{-\alpha Z m'_\mu r}\,, \\ F_{-1} &= 0\,. \end{aligned} \tag{13}$$

Alternatively, we can reconstruct a realistic bound-muon wave function by solving from the Dirac wave equations the large, G_{-1}, and small, F_{-1}, parts of the wave function (9) in the Coulomb field created by the nucleus. If we assume that the muon is in the lowest state $1s_{1/2}$ ($\kappa = -1$), the components satisfy the coupled differential equations (see, e.g., [23], but note that they use different notations for the large and small parts)

$$\begin{cases} \frac{\mathrm{d}}{\mathrm{d}r}G_{-1} + \frac{1}{r}G_{-1} = \frac{1}{\hbar c}(mc^2 - E + V(r))F_{-1}\,, \\ \frac{\mathrm{d}}{\mathrm{d}r}F_{-1} - \frac{1}{r}F_{-1} = \frac{1}{\hbar c}(mc^2 + E - V(r))G_{-1}\,. \end{cases} \tag{14}$$

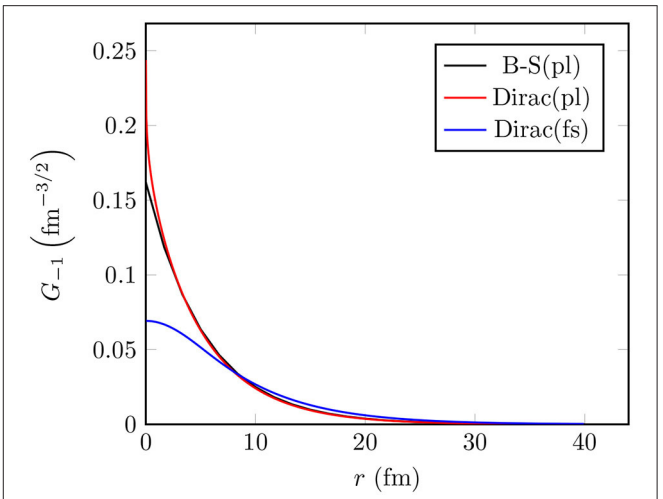

FIGURE 2 | The large component, G_{-1}, of the bound-muon wave function in ^{106}Cd. Here "B-S" refers to the Bethe-Salpeter approximation formula and "Dirac" to the wave function obtained by solving the Dirac equation. Furthermore, "pl" refers to a point-like nucleus and "fs" to a finite-size nucleus.

Assuming finite nuclear size and uniform distribution of the nuclear charge within a charge radius $R_c = r_0 A^{1/3}$ with $r_0 = 1.2$ fm, the potential energy $V(r)$ in Equation (14) can be written in the form

$$V(r) = \begin{cases} \frac{(Z-1)e^2}{2R_c}\left[3 - \left(\frac{r}{R_c}\right)^2\right], & \text{if } r \le R_c \\ \frac{(Z-1)e^2}{r}, & \text{if } r > R_c\,, \end{cases} \tag{15}$$

similarly as in [15, 16, 24] in the case of bound-electron wave functions in the context of double beta decay. Equation (14) can then be solved by means of the package RADIAL [25] by using a piecewise-exact power-series expansion of the radial functions, which then are summed up to a prescribed accuracy.

In **Figure 2**, we compare the large component, G_{-1}, of the bound-muon wave function, computed using this method (blue line), with the approximate wave function (black line) of Equation (13). For the sake of comparison, we have also plotted the exact solution of the Dirac equation corresponding to point-like nucleus (red line). The exact solution for the point-like nucleus is notably close to the Bethe-Salpeter approximation, whereas the finite-size-nucleus solution differs significantly from the point-like-nucleus solution, especially at $r \le 7$ fm.

4.2. Muon-Capture Matrix Elements

We compute the OMC matrix elements using the formalism that was originally developed by Morita and Fujii [21]. This formalism takes into account both the genuine and induced vector and axial-vector weak nucleon currents. The OMC rate from a J_i initial state to a J_f final state can be written as

$$W = 2\pi\,\langle|\text{M.E.}|^2\rangle_{av} q^2\,\frac{dq}{dE_f}\,, \tag{16}$$

where

$$\frac{dq}{dE_f} = \left[1 - \frac{q}{m_\mu + AM}\right] \tag{17}$$

and the Q-value of the OMC process can be computed from

$$q = (m_\mu - W_0)\left(1 - \frac{m_\mu - W_0}{2(M_f + m_\mu)}\right), \tag{18}$$

where $W_0 = M_f - M_i + m_e + E_X$ [21]. Here M_f (M_i) is the nuclear mass of the final (initial) nucleus, m_e the rest mass of an electron and E_X the excitation energy of the final J^π state. The expectation value in Equation (16) can be written as

$$\langle|\text{M.E.}|^2\rangle_{av} = \frac{2J_f + 1}{(2j' + 1)(2J_i + 1)} \times \sum_{ij}\sum_{\kappa u}\left[\sum_{\nu} C^{(i)}\mathcal{M}^{(i)}_{\nu u}\right]^*\left[\sum_{\nu'} C^{(j)}\mathcal{M}^{(j)}_{\nu' u}\right], \tag{19}$$

where j' is the angular momentum of the bound muon. The definitions of the matrix elements $\mathcal{M}^{(i)}_{\nu u}$ and the corresponding coefficients $C^{(i)}$ can be found in Table 5.1 of [26] (or in Table 1 of [21]). However, note that we use different notation for the coupling constants.

The factors $C^{(i)}$ contain the usual weak vector and axial-vector couplings $g_{\rm V} \equiv g_{\rm V}(q)$ and $g_{\rm A} \equiv g_{\rm A}(q)$ at finite momentum transfer $q > 0$. The conserved vector current (CVC) and partially conserved axial-vector current (PCAC) hypotheses give the values $g_{\rm V}(0) = 1.00$ and $g_{\rm A}(0) = 1.27$ for a free nucleon at zero momentum transfer, and for finite momentum transfer we can use the dipole approximation [27]. For the induced pseudoscalar coupling $g_{\rm P}$ the Goldberger-Treiman PCAC relation [28] gives $g_{\rm P}/g_{\rm A} = 7.0$. However, at zero momentum transfer deviations from the CVC and PCAC values have been obtained in several analyses [29–32].

The matrix elements $\mathcal{M}^{(i)}_{\nu u}$ in Equation (19) consist of radial integrals of different integrands containing spherical harmonics, geometric factors and components of neutrino and muon wave functions. The different terms are listed in Table 5.1 of [26]. We assume that the muon is bound on the $\kappa = -1$ orbit and that the small component of the bound muon wave function is negligible, which simplifies the expressions of the matrix elements notably [see Equation (5.26) and Table 5.2 of [26] for the Bethe-Salpeter approximation and Equation (5.37) and Table 5.3 for a general muon wave function].

Here we define an average OMC matrix element as

$$|M^{(\mu)}|_{av} = \sqrt{\langle|\text{M.E.}|^2\rangle_{av}} \tag{20}$$

and compare this quantity, instead of OMC rate, with the $0\nu\beta^+\beta^+$-decay NME in order to reduce the phase-space effects.

In this work we choose the slightly quenched values of $g_{\rm A}(0) = g_{\rm A}^{\rm eff} = 1.0$ and $g_{\rm P}(0) = 7.0$ and keep the CVC value $g_{\rm V}(0) = 1.0$ for all the studied cases. In general, OMC serves as a probe of the effective values of these parameters at the momentum-exchange region $g \approx 100$ MeV, which is particularly relevant for $0\nu\beta\beta$ decay. These parameter values could be constrained by the measured capture rates to individual excited nuclear states, especially in light nuclei which are well-described by shell-model and different *ab initio* methods. However, for the lack of the OMC data on the OMC in ^{106}Cd, this is not possible in the present study.

5. SPHERICAL PROTON-NEUTRON QRPA AND ITS HAMILTONIAN PARAMETERS

The results reported in the present study are based on a spherical proton-neutron quasiparticle random-phase approximation (pnQRPA), which describes nuclear excitations in odd-odd nuclei (such as ^{106}Ag) as proton-neutron quasiparticle pairs. In order to reach wide region of excitation-energies up to 50 MeV, we use large no-core single-particle bases consisting of proton and neutron states from the $0s-0p-1s-0d-1p-0f-2s-1d-0g-2p-1f-0h-1g-0i$ oscillator shells. As a starting point, the single-particle energies were generated by a spherical Coulomb-corrected Woods-Saxon (WS) potential with the parametrization of [33]. This basis is denoted as "WS" in this study. Furthermore, we modified the WS energies in the same way as in [34] in order to better reproduce the spectra of the neighboring odd-A nuclei. This basis, in turn, is denoted by "Adj.".

For the muon-capture calculations, we generate the pnQRPA excitations in ^{106}Ag starting from the even-even mother nucleus, ^{106}Cd. As for the $0\nu\beta^+\beta^+$ decay, we generate two sets of pnQRPA excitations for each J^π multipole—one based on the mother nucleus ^{106}Cd, and one based on the daughter nucleus ^{106}Pd. We call these sets the right- and left-hand pnQRPA sets, correspondingly. In the $0\nu\beta^+\beta^+$-decay calculations, we then use the average of the left- and right-hand-side excitation energies as the excitation energy of a given intermediate state. We also take into account the overlap of these two sets in the definition of the matrix element.

The quasiparticle spectra for protons and neutrons, needed in the pnQRPA diagonalization, are obtained by solving the BCS equations for protons and neutrons in the even-even reference nuclei. The calculated BCS pairing gaps are adjusted to the phenomenological proton and neutron pairing gaps in a way described in detail in [35].

The X and Y amplitudes in the pnQRPA equations are calculated by diagonalizing the pnQRPA matrix separately for each multipole J^π. We adopt as the two-body interaction the one derived from the Bonn-A one-boson-exchange potential, introduced in [36]. The particle-hole part was scaled by a common factor $g_{\rm ph}$ fixed by fitting the centroid of the Gamow-Teller giant resonance (GTGR) in the 1^+ channel of the calculations.

As for the particle-particle parameter $g_{\rm pp}$, we follow the partial isospin-restoration scheme introduced in [37], and multiply the isoscalar ($T = 0$) and isovector ($T = 1$) parts of the particle-particle G-matrix elements by factors $g_{\rm pp}^{(T=0)}$ and $g_{\rm pp}^{(T=1)}$, respectively. The isovector parameter $g_{\rm pp}^{(T=1)}$ is adjusted such that the Fermi part of the corresponding two-neutrino

TABLE 2 | Adopted values of the pairing parameters of the BCS and the particle-hole and particle-particle parameters of the pnQRPA.

Basis	^{106}Pd		^{106}Cd				
	$g_{\text{pair}}^{(n)}$	$g_{\text{pair}}^{(p)}$	$g_{\text{pair}}^{(n)}$	$g_{\text{pair}}^{(p)}$	g_{ph}	$g_{\text{pp}}^{(T=0)}$	$g_{\text{pp}}^{(T=1)}$
"WS"	0.872	0.932	0.867	0.934	1.405	0.6 – 0.80	0.90
"Adj."	0.798	0.794	0.785	0.881	1.290	0.6 – 0.80	0.84

The selection procedures of these values are explained in the text.

double beta ($2\nu\beta^+\beta^+$) NME vanishes, leading to partial isospin-symmetry restoration. Usually, for the $2\nu\beta^-\beta^-$ decays, the value of the isoscalar parameter $g_{\text{pp}}^{(T=0)}$ is determined by fitting the corresponding experimental half-life. Here we do not have a measured half-life and the corresponding experimental NME available (see **Table 1**) so that the value of $g_{\text{pp}}^{(T=0)}$ is a matter of choice. In this work we choose to adopt the rather wide range of values $g_{\text{pp}}^{(T=0)} = 0.6 - 0.8$ for this parameter, where the upper limit is at a safe distance from the collapse point of the pnQRPA for both single-particle bases.

All the parameter values resulting from the above-described procedures are listed in **Table 2**.

6. RESULTS

In order to investigate the possibility of using the OMC as a probe of $0\nu\beta\beta$ decay, we have studied the $0\nu\beta^+\beta^+$-decay matrix elements and the average OMC matrix elements of ^{106}Cd in the pnQRPA framework in detail. The results are presented in the following subsections. In order to make the comparison between the two processes meaningful, we need to adjust the excitation energies in ^{106}Ag (being the intermediate nucleus of $0\nu\beta^+\beta^+$ decay and the final nucleus of OMC) in a consistent manner. For muon capture, the excitation energy of the lowest pnQRPA excited state for each J^π multipole is adjusted to the measured excitation energy, when available. For the $0\nu\beta^+\beta^+$ decay we adjust the right-hand pnQRPA set of states in a similar manner. Hence, we can compare the two processes as a function of the excitation energy in ^{106}Ag in a consistent way.

6.1. Multipole Decompositions of the Total $0\nu\beta\beta$-Decay and OMC Matrix Elements

In contrast to the $2\nu\beta\beta$ decay which has only the $J^\pi = 1^+$ states active in the process, in the case of the $0\nu\beta\beta$ decay all the multipole states J^π of the intermediate nucleus are active. On the other hand, in the OMC the large mass of the captured muon allows highly forbidden transitions to all possible J^π final states up to highest excitation energy. Hence, by studying the OMC on relevant nuclei, one can access the intermediate states of $0\nu\beta\beta$ decay by complementary means. In this section we investigate the multipole decompositions of the $0\nu\beta^+\beta^+$-decay and OMC matrix elements.

In **Figures 3**, **4**, we show the multipole decompositions of the total $0\nu\beta^+\beta^+$-decay NME and the average OMC matrix element of ^{106}Cd, respectively. The compositions correspond to the parameter value $g_{\text{pp}}^{(T=0)} = 0.7$, which is at a safe distance from the pnQRPA breaking point. In the case of the $0\nu\beta^+\beta^+$ decay, the 1^+ multipole plays a dominant role both for the bare Woods-Saxon basis and for the adjusted basis. This ensues from the dominating role of the Gamow-Teller type of transitions. The 1^- contribution is the second largest, whereas the 0^+ and 0^- contributions are negligible. The contributions coming from the higher multipoles decrease rather smoothly as a function of J.

As for the muon capture (see **Figure 4**), the major part of the average matrix element consists of transitions to the states with $1 \leq J \leq 4$, the leading multipoles being those with $J^\pi = 2^-, 2^+, 1^-$, and 3^+. In contrast to $0\nu\beta^+\beta^+$ decay, the strength is more evenly distributed among the few leading multipoles. On the other hand, the multipoles with $J \geq 6$ play a minor role compared with the $0\nu\beta^+\beta^+$ decay.

6.2. Dependence of the Matrix Elements on the Single-Particle Bases and g_{pp}

As mentioned in section 5, the particle-particle strength parameter g_{pp} strongly affects the $\beta\beta$-decay rates. In the muon-capture studies of e.g., [38, 39] it was found that g_{pp} affects also the muon capture rates. Hence, in this section we study the effect of g_{pp} on both the $0\nu\beta^+\beta^+$-decay and OMC matrix elements of ^{106}Cd in detail. The exploration also paves the way for possible future adjustments of g_{pp} using, e.g., the shape of the OMC strength function.

The total $0\nu\beta^+\beta^+$-decay NME of ^{106}Cd is plotted as a function of the isoscalar part of the particle-particle parameter $g_{\text{pp}}^{(T=0)}$ in different single-particle bases in **Figure 5**. For the isovector part $g_{\text{pp}}^{(T=1)}$, we adopt the value that was adjusted so that the Fermi part of the $2\nu\beta^+\beta^+$-decay NME vanishes, as explained in section 5. It is evident from the plots that the value of $M^{(0\nu)}$ is sensitive to the value of $g_{\text{pp}}^{(T=0)}$: increasing $g_{\text{pp}}^{(T=0)}$ decreases the value of the matrix element. In both bases, varying g_{pp} from 0.6 to 0.8 reduces the value of $M^{(0\nu)}$ by some 25%. Hence, constraining the value of g_{pp} is of utmost importance in the $0\nu\beta^+\beta^+$-decay studies. In the absence of a measured $2\nu\beta^+\beta^+$-decay half-life, adjusting g_{pp} to OMC data, once measured, would help reduce the large uncertainty related to g_{pp}. It is seen that in the adjusted ("Adj.") basis, the matrix element is consistently about 20% larger than in the bare Woods-Saxon ("WS") basis. It is to be noted that soon after the $g_{\text{pp}}^{(T=0)}$ values shown in the x axis, between $g_{\text{pp}}^{(T=0)}0.82 - 0.84$, depending on the single-particle basis, the ground state of pnQRPA collapses and the value of $M^{(0\nu)}$ blows up: the value rapidly increases by some 10%. Since the values after the pnQRPA breaking point are not physically meaningful, they are not shown in the figure.

In **Figure 6**, we plot the average OMC matrix element $|M^{(\mu)}|_{\text{av}}$ as a function of $g_{\text{pp}}^{(T=0)}$. Contrary to the $0\nu\beta^+\beta^+$-decay NME, the OMC matrix element is not sensitive to the small adjustments of the single-particle bases or to the value of the $g_{\text{pp}}^{(T=0)}$ between $g_{\text{pp}}^{(T=0)} = 0.5 - 0.8$. Instead, after $g_{\text{pp}}^{(T=0)} = 0.8$, close to the pnQRPA breaking point, the average OMC matrix element becomes unstable. On the other hand, the value of the average OMC matrix element is much more dependent on

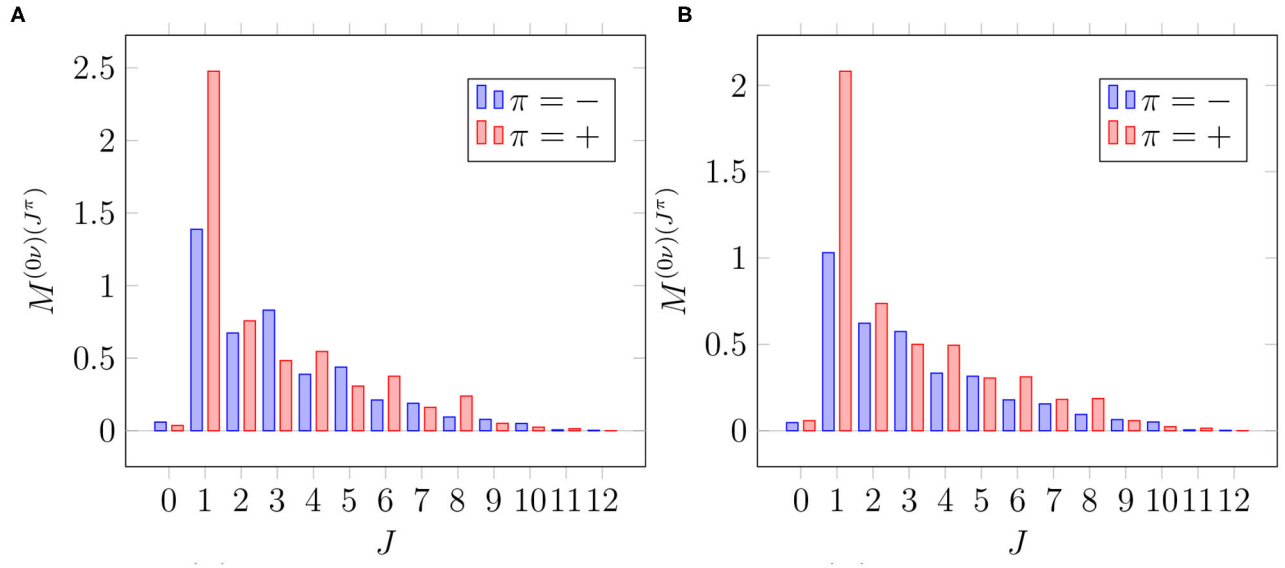

FIGURE 3 | Multipole decomposition of the total $0\nu\beta^+\beta^+$-decay matrix element in different single-particle bases. The decompositions correspond to the parameter value $g_{\rm pp}^{(T=0)} = 0.7$. **(A)** Basis: "Adj.". **(B)** Basis: "WS".

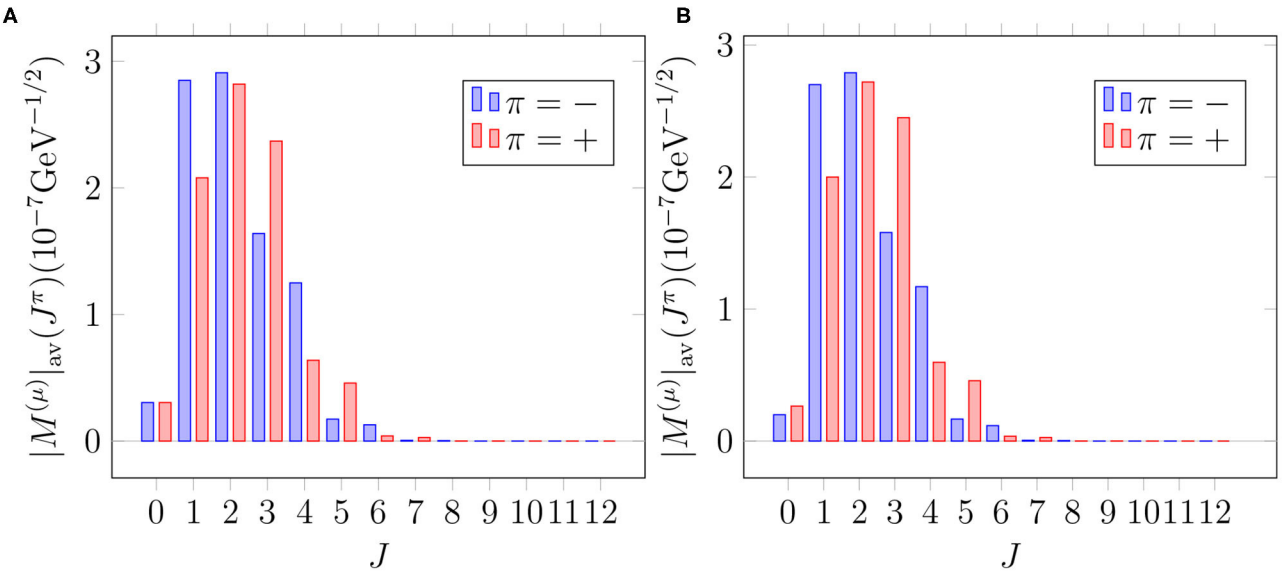

FIGURE 4 | Multipole decomposition of the total OMC matrix element in different single-particle bases. Here we have used the bound muon wave function solved from the Dirac equation. The decompositions correspond to the parameter value $g_{\rm pp}^{(T=0)} = 0.7$. Note that the unit and scale of the matrix element comes from our definition of the average OMC matrix element (20). For more information, see the text and [26]. **(A)** Basis: "Adj.". **(B)** Basis: "WS".

the bound-muon wave function: the use of the Bethe-Salpeter approximation results in about three times larger values than those obtained with the exact Dirac wave function.

The different parts of the $0\nu\beta^+\beta^+$-decay NMEs in different single-particle bases in the adopted ranges of the parameter $g_{\rm pp}^{(T=0)}$ (see **Table 2**) are listed in **Table 3**. In **Table 4**, we list the corresponding values obtained in [14] in a smaller single-particle basis, which corresponds to the "Adj." basis in the present study. In [14], the NMEs were computed by the use of Jastrow [18] and UCOM [19] short-range correlations.

The total $0\nu\beta^+\beta^+$-decay NMEs computed in the present study (**Table 3**) are consistently larger than those computed in the smaller, core-based single-particle bases, used in [14]. The values computed with the UCOM short-range correlations are closer to the values computed in the present study, which is natural since the presently adopted short-range correlations are

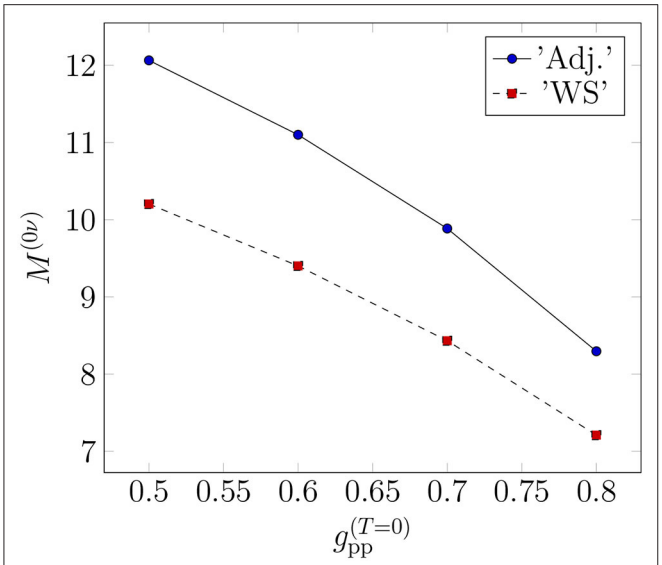

FIGURE 5 | Dependence of the $0\nu\beta^+\beta^+$-decay NME on the isoscalar part of the particle-particle parameter $g_{\rm pp}$ in the two different single-particle bases.

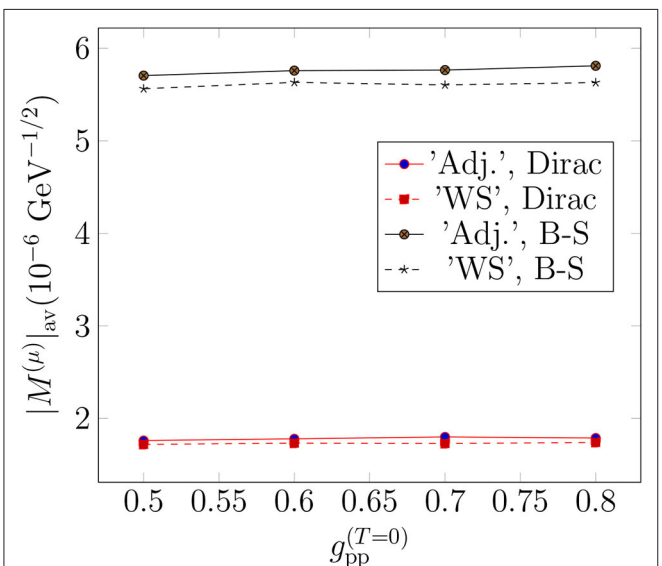

FIGURE 6 | Dependence of the average OMC matrix element on the isoscalar part of the particle-particle parameter $g_{\rm pp}$ in the two different single-particle bases, and for the exact Dirac finite-nucleus and approximate Bethe-Salpeter point-like-nucleus bound-muon wave functions.

a parametrization of the UCOM correlator. The dependence of the NMEs on the size of the single-particle bases is in accordance with the findings of our previous work [40], where we noticed that the size of the single-particle bases affects the $0\nu\beta^-\beta^-$-decay NMEs much more than the different adjustment procedures of the particle-hole parameter $g_{\rm ph}$ of the pnQRPA. This is most likely due to the fact that in the smaller bases we cannot reach the highly-excited intermediate states which play a non-negligible role in the $0\nu\beta\beta$-decay process.

According to **Figures 3**, **4** the multipoles $J^\pi = 1^+$ and 2^+ are among the leading ones for both the $0\nu\beta^+\beta^+$-decay and OMC

TABLE 3 | Nuclear matrix elements for $0\nu\beta^+\beta^+$ decay of ^{106}Cd corresponding to $g_{\rm A}(0) = g_{\rm A}^{\rm eff} = 1.0$.

Basis	$g_{\rm pp}^{(T=0)}$	$M_{\rm F}^{(0\nu)}$	$M_{\rm GT}^{(0\nu)}$	$M_{\rm T}^{(0\nu)}$	$M^{(0\nu)}$
"WS"	0.6	−1.90	7.91	−0.41	9.40
	0.7	−1.90	6.95	−0.42	8.43
	0.8	−1.89	5.75	−0.43	7.21
"Adj."	0.6	−2.34	9.24	−0.48	11.10
	0.7	−2.35	8.04	−0.50	9.89
	0.8	−2.35	6.47	−0.52	8.30

The matrix elements are computed in different single-particle bases with different values of g_{pp}.

TABLE 4 | Nuclear matrix elements for $0\nu\beta^+\beta^+$ decay of ^{106}Cd corresponding to $g_{\rm A}(0) = g_{\rm A}^{\rm eff} = 1.0$ in the single-particle bases used in [14], corresponding to the "Adj." basis of the present study.

Short-range correlation	$g_{\rm pp}$	$M_{\rm F}^{(0\nu)}$	$M_{\rm GT}^{(0\nu)}$	$M^{(0\nu)}$
Jastrow	0.8	−2.243	6.838	5.812
UCOM	0.8	−2.718	8.307	7.056

The results are adopted from [14].

matrix elements of ^{106}Cd. Hence, it is illuminating to study the effect of $g_{\rm pp}$ on these multipoles in more detail. In **Figures 7**, **8** we plot the total $0\nu\beta^+\beta^+$-decay NME on the positive y axis and the average OMC matrix element on the negative y axis in the cases of $J^\pi = 1^+$ and 2^+, respectively. We decompose the average OMC NME for the $J^\pi = 1^+, 2^+$ multipole states within MeV energy bins while for the $0\nu\beta^+\beta^+$ decay the energy-multipole decomposition entails division of the NMEs into multipoles $J^\pi = 1^+, 2^+$ and their energy distributions binned by MeV-energy intervals. We have chosen to plot only the absolute values of the matrix elements since they carry the essential information needed in the present comparison of the basic features of the OMC and $0\nu\beta^+\beta^+$ decay.

Figures 7, **8** show similar behavior for both the multipoles $J^\pi = 1^+$ and 2^+: decreasing the value of $g_{\rm pp}^{(T=0)}$ from 0.8 to 0.6 shifts the spectrum to lower energies for both the $0\nu\beta^+\beta^+$ decay and OMC. Note that the present comparison does not reflect the results of **Figure 5**, since here we are considering the absolute values of the $0\nu\beta^+\beta^+$-decay NME for each bin. However, these figures show that even though the average OMC matrix element is quite independent of the value of $g_{\rm pp}$, the shape of the OMC spectrum depends on $g_{\rm pp}$. This, in turn, raises interest of studying the possibility of adjusting $g_{\rm pp}$ to the locations of OMC giant resonances, once measured.

6.3. Dependence of the OMC Matrix Elements on the Bound-Muon Wave Function

As mentioned in section 4.1, the OMC matrix elements have usually been computed by approximating the bound-muon wave function by a point-like-nucleus approximation. In our previous works [13, 41, 42] we used the Bethe-Salpeter point-like-nucleus approximation formula for the muon wave function.

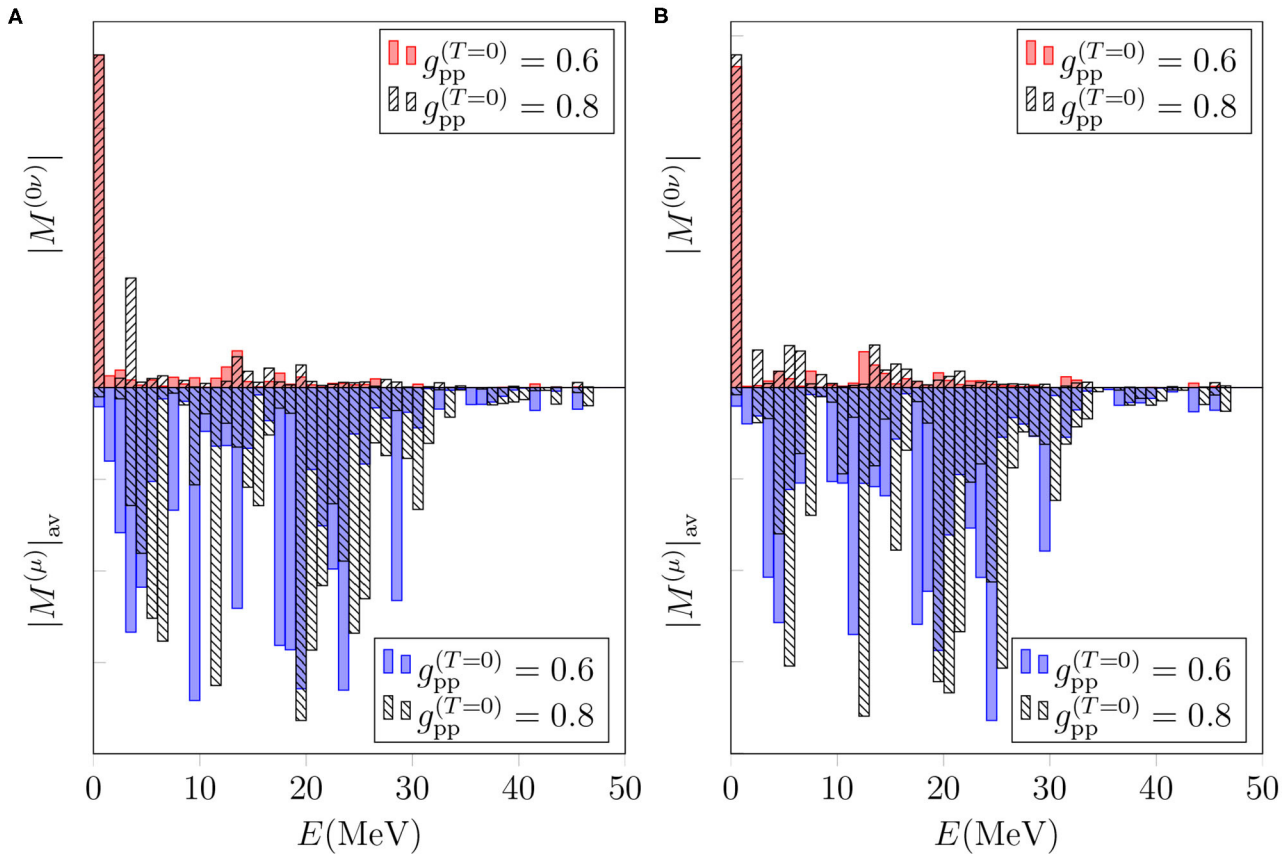

FIGURE 7 | Dependence of the energy distributions of the $0\nu\beta^+\beta^+$-decay and OMC matrix elements for the $J^\pi = 1^+$ multipole on the particle-particle parameter $g_{\rm pp}^{(T=0)}$ in different bases. The OMC matrix elements are computed assuming the exact Dirac wave functions for a finite nucleus with uniform charge distribution. **(A)** Basis: "Adj.". **(B)** Basis: "WS".

Here we study the effect of the exact muon wave function, solved from the Dirac equation by taking into account the finite size of the nucleus with uniform charge distribution, on the OMC matrix elements. The effects of the two muon wave functions (see **Figure 2**) on the OMC matrix element are clearly seen in **Figure 6**, where the $g_{\rm pp}$ dependence of the OMC matrix element is displayed in the two different single-particle bases and for the exact Dirac finite-nucleus and approximate Bethe-Salpeter point-like-nucleus bound-muon wave functions. The difference between the matrix elements is considerable. However, one has to keep in mind that in the OMC-rate calculations this difference is to a major part compensated by the use of a phenomenological effective charge $Z_{\rm eff}$ (the so-called Primakoff approximation [43]) in the calculations using the Bethe-Salpeter approximation.

Next we study the effect of the different bound-muon wave functions on the multipole decomposition of the average OMC matrix elements in the cases of the multipoles $J^\pi = 1^+, 2^+$, which are among the leading ones for both the $0\nu\beta^+\beta^+$ decay and the OMC. In **Figures 9**, **10** we plot the energy-decompositions of the average OMC matrix element for the transitions to $J^\pi = 1^+$ and 2^+ states, respectively. In both figures, the Bethe-Salpeter point-like-nucleus approximation (blue bars) results in notably larger values of the average OMC matrix element than the Dirac wave function (black and white bars). All in all, the use of the Dirac wave function results in about 50–60% reduction of the matrix elements in all the energy bins. This makes sense, since looking at **Figure 2**, especially at $r \leq 7$ fm, the behavior of the Dirac wave function, taking into account the finite size of the nucleus, differs significantly from the Bethe-Salpeter approximation. The finding is also in keeping with results for the total OMC matrix element, depicted in **Figure 6**.

6.4. Comparison of the $0\nu\beta^+\beta^+$ and OMC Matrix Elements

Here we finally compare the absolute values of the $0\nu\beta^+\beta^+$-decay and average OMC matrix elements in the same manner as in [13]. We analyze the summed absolute values of the matrix elements in the same way as we did in **Figures 7**, **8**. We plot the summed absolute values of the $0\nu\beta^+\beta^+$-decay NMEs and the average OMC matrix elements for $J^\pi = 0^+, 1^+, 2^+, 3^+, 4^+, 1^-, 2^-, 3^-$, and 4^- in **Figure 11**. The matrix elements are computed in the adjusted Woods-Saxon basis ("Adj.") with the parameter value $g_{\rm pp}^{(T=0)} = 0.7$. The OMC matrix elements are computed with the exact Dirac muon wave function.

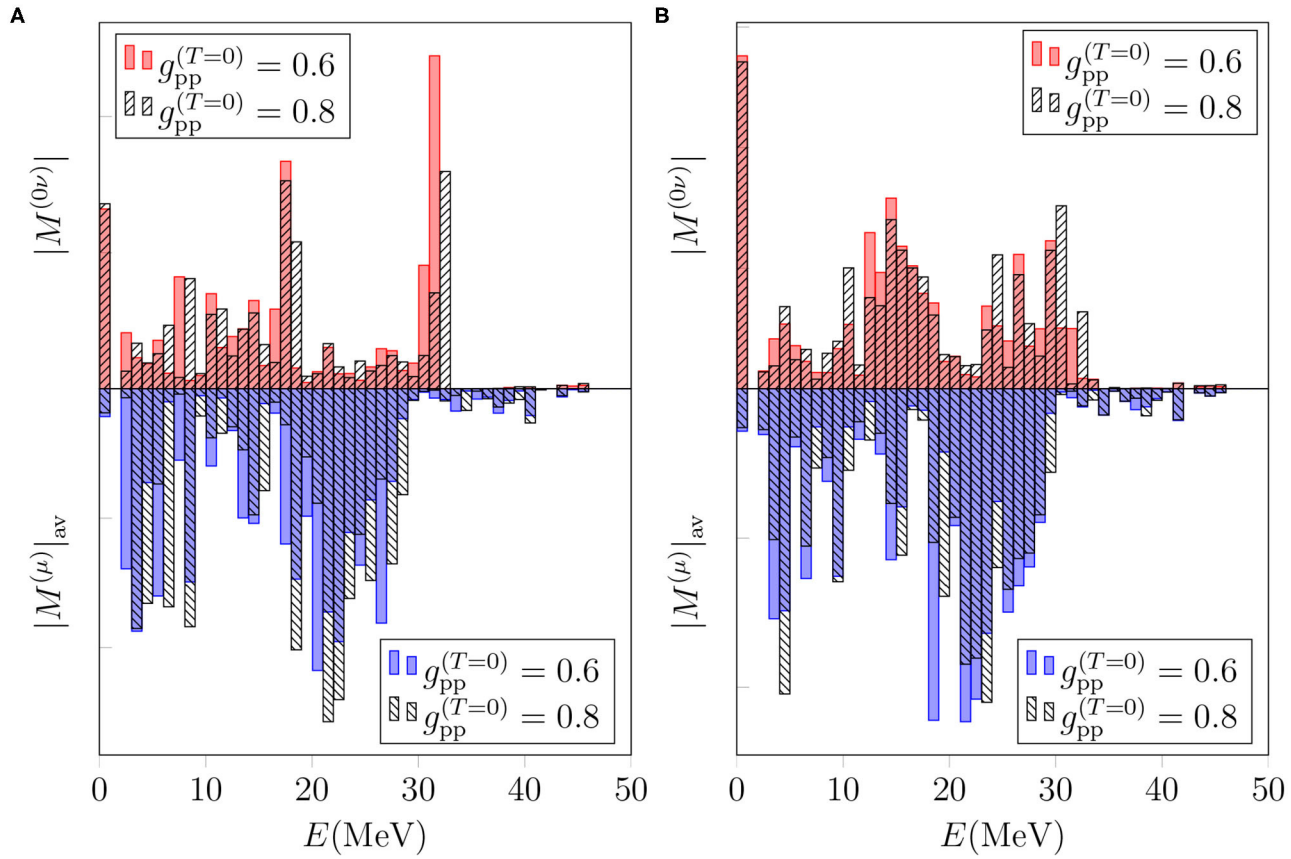

FIGURE 8 | Dependence of the energy distributions of the $0\nu\beta^+\beta^+$-decay and OMC matrix elements for the $J^\pi = 2^+$ multipole on the particle-particle parameter $g_{pp}^{(T=0)}$ in different bases. The OMC matrix elements are computed assuming the exact Dirac wave functions for a finite nucleus with uniform charge distribution. **(A)** Basis: "Adj.". **(B)** Basis: "WS".

Looking at **Figure 11**, one can see clear correspondences between the $0\nu\beta^+\beta^+$-decay and OMC matrix elements, especially in the cases of $J^\pi = 3^+$ (**Figure 11D**), $J^\pi = 4^+$ (**Figure 11E**) and $J^\pi = 4^-$ (**Figure 11I**). This observation is in accordance with our earlier study in the $0\nu\beta^-\beta^-$ side of double beta decays [13]. There are also notable similarities in the distributions corresponding to multipoles $J^\pi = 2^-$ (**Figure 11G**) and $J^\pi = 3^-$ (**Figure 11H**). For the rest of the multipoles, the correspondencies are not so well visible. Especially, in the case of $J^\pi = 1^+$ (**Figure 11B**), the major part of the $0\nu\beta^+\beta^+$-decay NME is coming from the first energy bin $E \leq 1$ MeV, while the OMC distribution is clearly more spread to higher energies. This is also the most notable difference between the present results and those of our earlier study [13], where the 1^+ contributions to the $0\nu\beta^-\beta^-$-decay matrix elements were more evenly distributed to higher excitation energies.

7. DISCUSSION

Double beta decay is one of the most intensively studied topics in neutrino, nuclear and particle physics. While the ordinary two-neutrino double beta decay mode has been observed in several isotopes, the neutrinoless decay mode remains hypothetical. Most of the observed decays are of $\beta^-\beta^-$ type, and there are only six isotopes known to be capable of $\beta^+\beta^+$ decaying. Here we have studied a particularly promising candidate: ^{106}Cd, for which currently only the lower limit of the $2\nu\beta^+\beta^+$-decay half-life has been extracted experimentally.

In the present work, we have made a comparative analysis of the $0\nu\beta^+\beta^+$-decay and average OMC matrix elements of ^{106}Cd in the pnQRPA framework using large no-core single-particle bases. This comparison is the first ever done on the positron-emission side of the nuclear chart, and could potentially help improve the accuracy of the $0\nu\beta^+\beta^+$-decay matrix elements once access to the data of future muon-capture experiments is gained. In particular, adjusting the g_{pp} parameter to future data on OMC giant resonances could help reducing the sizeable uncertainty related to the unknown value of g_{pp}.

Analysis of the multipole decompositions of the total $0\nu\beta^+\beta^+$-decay matrix element and the average OMC matrix element shows that the $J^\pi = 1^+$ multipole has a dominating role in the $0\nu\beta^+\beta^+$-decay process, while the total OMC matrix

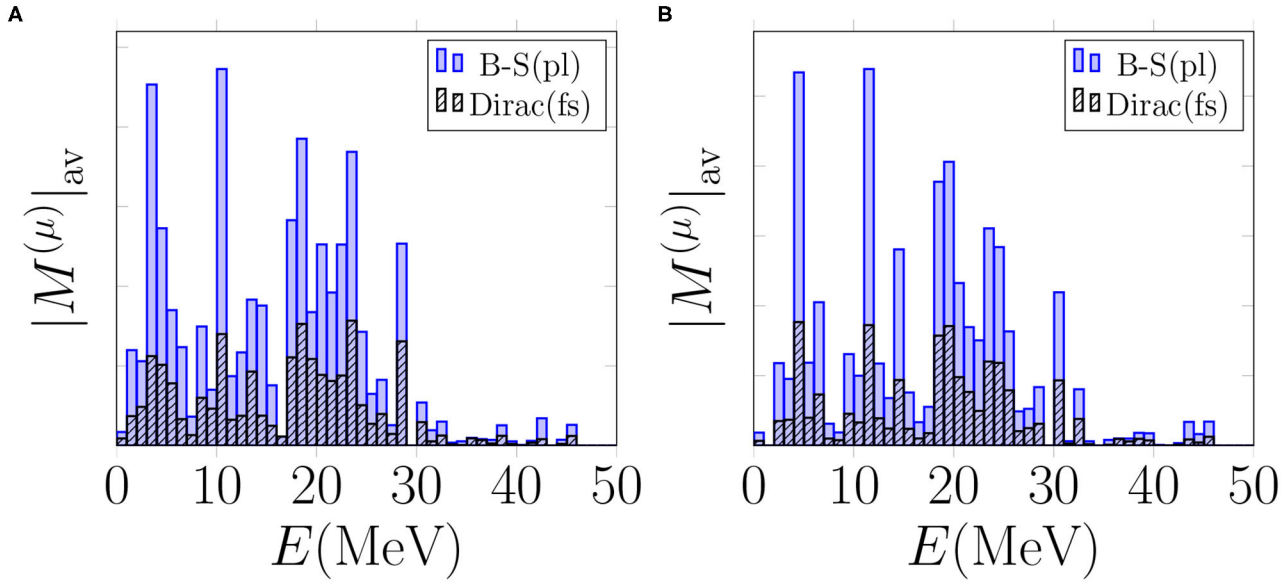

FIGURE 9 | Average OMC matrix elements for the captures to $J^\pi = 1^+$ states computed with different bound-muon wave functions. "B-S(pl)" denotes the Bethe-Salpeter point-like-nucleus approximation and "Dirac(fs)" the exact wave function solved from the Dirac equation taking into account the finite size of the nucleus. The value $g_{\mathrm{pp}}^{(T=0)} = 0.7$ is adopted for particle-particle interaction parameter. **(A)** Basis: "Adj.". **(B)** Basis: "WS".

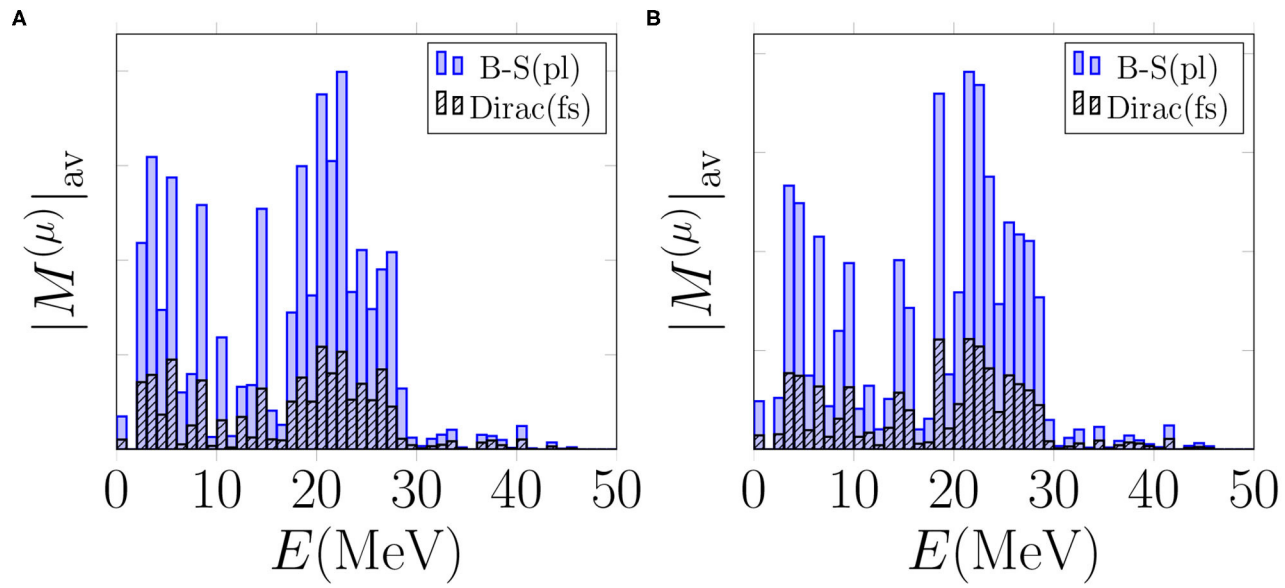

FIGURE 10 | Average OMC matrix elements for the captures to $J^\pi = 2^+$ states computed with different bound-muon wave functions. "B-S(pl)" denotes the Bethe-Salpeter point-like-nucleus approximation and "Dirac(fs)" the exact wave function solved from the Dirac equation taking into account the finite size of the nucleus. The value $g_{\mathrm{pp}}^{(T=0)} = 0.7$ is adopted for particle-particle interaction parameter. **(A)** Basis: "Adj.". **(B)** Basis: "WS".

element is more evenly distributed to a few leading multipoles. The multipoles $J^\pi = 1^+$ and 2^+ play a major role in both processes, hence we have studied the transitions involving those multipoles in more detail: we have studied the effect of different particle-particle parameter values on both the $0\nu\beta^+\beta^+$-decay and the OMC matrix elements, and the effect of different bound-muon wave functions on the OMC matrix elements in these cases.

Our studies indicate that the $0\nu\beta^+\beta^+$-decay matrix element of ^{106}Cd strongly depends on the value of the isovector

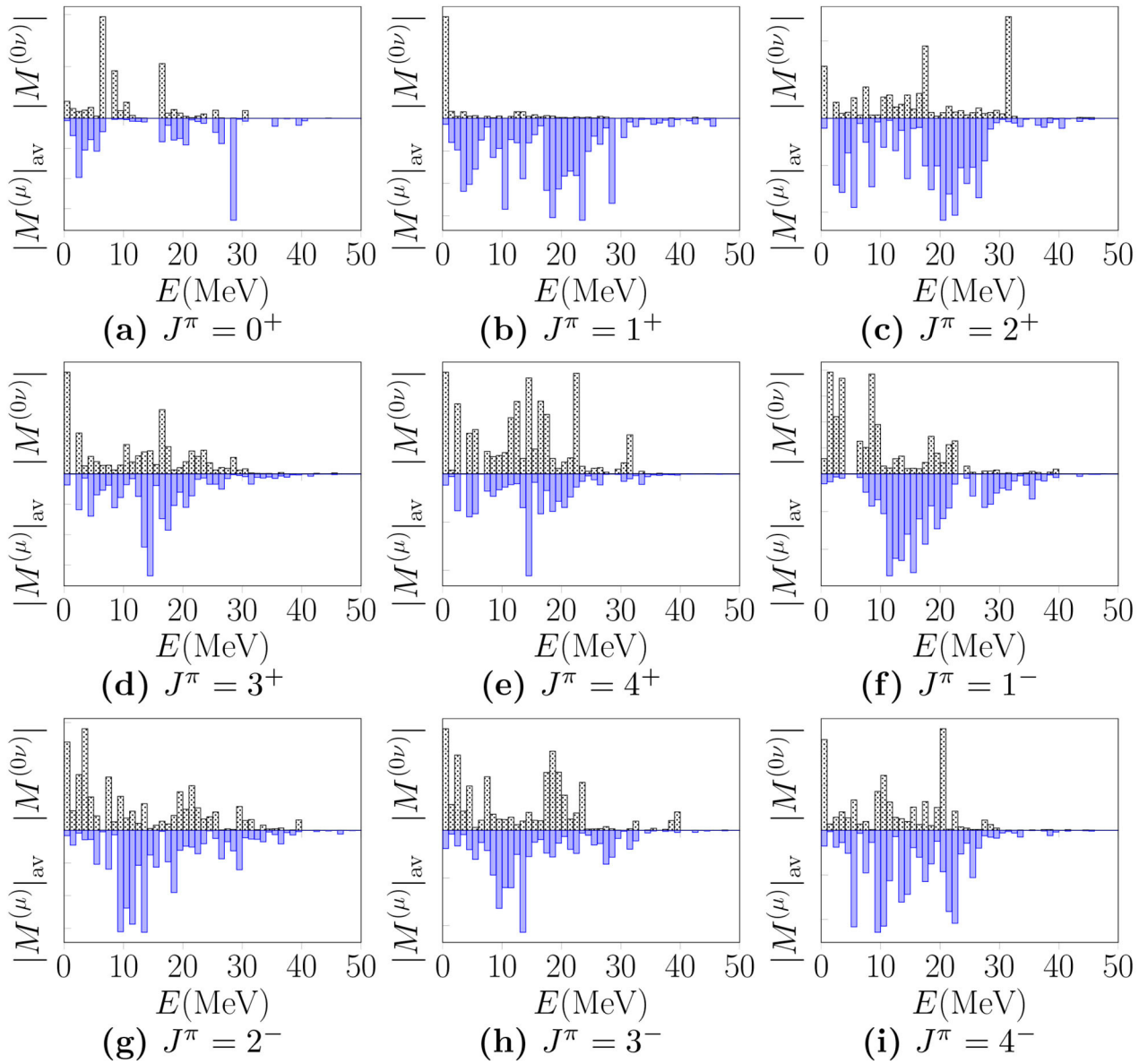

FIGURE 11 | Multipole decompositions in terms of relative $0\nu\beta^+\beta^+$-decay matrix elements (positive y axes) and average matrix elements of the OMC (negative y axes) for ^{106}Cd as functions of the excitation energy E in the intermediate nucleus (^{106}Ag) of the $0\nu\beta^+\beta^+$ decay of ^{106}Cd. These matrix elements correspond the adjusted Woods-Saxon basis and $g_{\text{pp}}^{(T=0)} = 0.7$. For the bound-muon wave function we have used the realistic exact wave function solved from the Dirac equation. Here J^π refer to the angular momenta and parities of the virtual states in ^{106}Ag and all quantities have been summed within 1 MeV energy bins. The subfigures represent different J^π values. The scale values of the y axes have been omitted, since they are not relevant for the current analysis. For more information see the text.

part $g_{\text{pp}}^{(T=0)}$ of the particle-particle interaction parameter of pnQRPA. Contrary to this, the average value of the OMC matrix element is less dependent on the $g_{\text{pp}}^{(T=0)}$. However, near the pnQRPA breaking point the average OMC matrix element becomes unstable and grows fast in magnitude. Furthermore, when comparing the $0\nu\beta^+\beta^+$-decay matrix elements of the present work with those computed in (much) smaller single-particle bases in [14], we noticed that the matrix elements are sensitive to the size of the single-particle basis. This observation is in accordance with our earlier work on the $\beta^-\beta^-$ type of decays [13].

Finally, we compared the energy distributions of the multipole-decomposed $0\nu\beta^+\beta^+$-decay matrix elements and the average OMC matrix elements, computed in the adjusted Woods-Saxon single-particle basis. We identified a clear correspondence between the absolute values of the $0\nu\beta^+\beta^+$-decay and OMC multipole contributions, especially in the cases of the J^π =

$3^+, 4^+$, and 4^- multipoles. This finding is in accordance with our previous work [13], where we compared the energy distributions of the multipole-decomposed $0\nu\beta^-\beta^-$-decay and OMC matrix elements for several $0\nu\beta^-\beta^-$-decay triplets in a similar manner.

DATA AVAILABILITY STATEMENT

The raw data supporting the conclusions of this article will be made available by the authors, without undue reservation.

AUTHOR CONTRIBUTIONS

All authors listed have made a substantial, direct and intellectual contribution to the work, and approved it for publication.

FUNDING

This work has been partially supported by the Academy of Finland under the Academy project no. 318043. JK has been supported by the Academy of Finland, Grant Nos. 314733 and 320062.

REFERENCES

1. Blaum K, Eliseev S, Danevich FA, Tretyak VI, Kovalenko S, Krivoruchenko MI, et al. Neutrinoless double-electron capture. *Rev Mod Phys*. (2020) 92:045007. doi: 10.1103/RevModPhys.92.045007
2. Aharmin B, Ahmed SN, Amsbaugh JF, Anthony AE, Banar J, Barros N, et al. Independent measurement of the total active 8B solar neutrino flux using an array of 3He proportional counters at the sudbury neutrino observatory. *Phys Rev Lett*. (2008) 101:111301. doi: 10.1103/PhysRevLett.101.111301
3. Abe K, Haga Y, Hayato Y, Ikeda M, Iyogi K, Kameda J, et al. Solar neutrinomeasurements in Super-Kamiokande-IV. *Phys Rev D*. (2016) 94:052010. doi: 10.1103/PhysRevD.94.052010
4. Abe K, Amey J, Andreopoulos C, Antonova M, Aoki S, Ariga A, et al. Combined analysis of neutrino and antineutrino oscillations at T2K. *Phys Rev Lett*. (2018) 118:151801. doi: 10.1103/PhysRevLett.118.151801
5. Ebert J, Fritts M, Gling C, Gfert T, Gehre D, Hagner C, et al. Current status and future perspectives of the COBRA experiment. *Adv High Energy Phys*. (2013) 2013:703572. doi: 10.1155/2013/703572
6. Ebert J, Fritts M, Gehre D, Gling C, Hagner C, Heidrich N, et al. Results of a search for neutrinoless double-β decay using the COBRA demonstrator. *Phys Rev C*. (2016) 94:024603. doi: 10.1103/PhysRevC.94.024603
7. Rukhadze NI, Brianon C, Brudanin VB, ermk P, Egorov VG, Klimenko AA, et al. Experiment TGV-2-search for double beta decay of ^{106}Cd. *Nucl Phys B*. (2012) 229:232–478. doi: 10.1016/j.nuclphysbps.2012.09.115
8. Belli P, Bernabei R, Brudanin VB, Cappella F, Caracciolo V, Cerulli R, et al. Search for double beta decay of ^{106}Cd with an enriched $^{106}CdWO_4$ crystal scintillator in coincidence with $CdWO_4$ scintillation counters. *Universe*. (2020) 2020:182. doi: 10.3390/universe6100182
9. Zinatulina D, Brudanin V, Egorov V, Petitjean C, Shirchenko M, Suhonen J, et al. Ordinary muon capture studies for the matrix elements in $\beta\beta$ decay. *Phys Rev C*. (2019) 99:024327. doi: 10.1103/PhysRevC.99.024327
10. Hashim IH, Ejiri H, Shima T, Takahisa K, Sato A, Kuno Y, et al. Muon capture reaction on ^{100}Mo to study the nuclear response for double-β decay and neutrinos of astrophysics origin. *Phys Rev C*. (2018) 97:014617. doi: 10.1103/PhysRevC.97.014617
11. Hashim IH, Ejiri H. New research project with muon beams for neutrino nuclear responses and nuclear isotopes production. *AAPPS Bull*. (2019) 29:21–6. doi: 10.22661/AAPPSBL.2019.29.3.21
12. Kortelainen M, Suhonen J. Nuclear muon capture as a powerful probe of double-beta decays in light nuclei. *J Phys G Nucl Part Phys*. (2004) 30:2003–18. doi: 10.1088/0954-3899/30/12/017
13. Jokiniemi L, Suhonen J. Comparative analysis of muon-capture and $0\nu\beta\beta$-decay matrix elements. *Phys Rev C*. (2020) 102:024303. doi: 10.1103/PhysRevC.102.024303
14. Suhonen J. Neutrinoless double beta decays of ^{106}Cd revisited. *Phys Lett B*. (2011) 701:490–5. doi: 10.1016/j.physletb.2011.06.016
15. Kotila J, Iachello F. Phase-space factors for double-β decay. *Phys Rev C*. (2012) 85:034316. doi: 10.1103/PhysRevC.85.034316
16. Kotila J, Iachello F. Phase space factors for $\beta^+\beta^+$ decay and competing modes of double-β decay. *Phys Rev C*. (2013) 87:024313. doi: 10.1103/PhysRevC.87.024313
17. Hyvärinen J, Suhonen J. Nuclear matrix elements for $0\nu\beta\beta$ decays with light or heavy Majorana-neutrino exchange. *Phys Rev C*. (2015) 91:024613. doi: 10.1103/PhysRevC.91.024613
18. Miller GA, Spencer JE. A survey of pion charge-exchange reactions with nuclei. *Ann Phys*. (1976) 100:562. doi: 10.1016/0003-4916(76)90073-7
19. Kortelainen M, Civitarese O, Suhonen J, Toivanen J. Short-range correlations and neutrinoless double beta decay. *Phys Lett B*. (2007) 647:128. doi: 10.1016/j.physletb.2007.01.054
20. Šimkovic F, Faessler A, Müther H, Rodin V, Stauf M. $0\nu\beta\beta$-decay nuclear matrix elements with self-consistent short-range correlations. *Phys Rev C*. (2009) 79:055501. doi: 10.1103/PhysRevC.79.055501
21. Morita M, Fujii A. Theory of allowed and forbidden transitions in Muon capture reactions. *Phys Rev*. (1960) 118:606–18. doi: 10.1103/PhysRev.118.606
22. Bethe HA, Salpeter EE. *Quantum Mechanics of One- and Two-Electron Atoms*. New York, NY: Academic Press Inc. (1959).
23. Tsoulos IG, Kosmas OT, Stavrou VN. DiracSolver: a tool for solving the Dirac Equation (2018). *arXiv:1810.13042 [physics.comp-ph]*. doi: 10.1016/j.cpc.2018.10.010
24. Kotila J, Barea J, Iachello F. Neutrinoless double-electron capture. *Phys Rev C*. (2014) 89:064319. doi: 10.1103/PhysRevC.89.064319
25. Salvat F, Fernández-Varea J, Williamson W Jr. Accurate numerical solution of the radial Schrödinger and Dirac wave equations. *Comput Phys Commun*. (1995) 90:151–68. doi: 10.1016/0010-4655(95)00039-I
26. Jokiniemi L. *Probing neutrinoless double-beta decay by charge-exchange reactions and muon capture* (JYU Dissertations). University of Jyväskylä, Jyväskylä, Finland (2020).
27. Ejiri H, Suhonen J, Zuber K. Neutrino-nuclear responses for astro-neutrinos, single beta decays and double beta decays. *Phys Rep*. (2019) 797:1–102. doi: 10.1016/j.physrep.2018.12.001
28. Goldberger ML, Treiman SB. Form factors in β decay and μ capture. *Phys Rev*. (1958) 111:354. doi: 10.1103/PhysRev.111.354
29. Ejiri H. Nuclear matrix elements for β and $\beta\beta$ decays and quenching of the weak coupling g_A in QRPA. *Front Phys*. (2019) 7:30. doi: 10.3389/fphy.2019.00030
30. Suhonen JT. Value of the axial-vector coupling strength in β and $\beta\beta$ decays: a review. *Front Phys*. (2017) 5:55. doi: 10.3389/fphy.2017.00055
31. Kolbe E, Langanke K, Vogel P. Muon capture, continuum random phase approximation, and in-medium renormalization of the axial-vector coupling constant. *Phys Rev C*. (1994) 50:2576. doi: 10.1103/PhysRevC.50.2576
32. Johnson BL, Gorringe TP, Armstrong DS, Bauer J, Hasinoff MD, Kovash MA, et al. Observables in muon capture on ^{23}Na and the effective weak couplings ga and gp. *Phys Rev C*. (1996) 54:2714. doi: 10.1103/PhysRevC.54.2714
33. Bohr A, Mottelson BR. *Nuclear Structure*. Vol. 1. New York, NY: Benjamin (1969). doi: 10.1063/1.3022342
34. Suhonen J, Civitarese O. Theoretical results on the double positron decay of ^{106}Cd. *Phys Lett B*. (2001) 497:221–7. doi: 10.1016/S0370-2693(00)01324-1
35. Jokiniemi L, Suhonen J. Isovector spin-multipole strength distributions in double-β-decay triplets. *Phys Rev C*. (2017) 96:034308. doi: 10.1103/PhysRevC.96.034308
36. Holinde K. Two-nucleon forces and nuclear matter. *Phys Rep*. (1981) 68:121. doi: 10.1016/0370-1573(81)90188-5

37. Šimkovic F, Rodin V, Faessler A, Vogel P. $0\nu\beta\beta$ and $2\nu\beta\beta$ nuclear matrix elements, quasiparticle random-phase approximation, and isospin symmetry restoration. *Phys Rev C*. (2013) 87:045501. doi: 10.1103/PhysRevC.87.045501
38. Kortelainen M, Suhonen J. Ordinary muon capture as a probe of virtual transitions of $\beta\beta$ decay. *Europhys Lett*. (2002) 58:666–72. doi: 10.1209/epl/i2002-00401-5
39. Šimkovic F, Dvornický R, Vogel P. Muon capture rates: evaluation within the quasiparticle random phase approximation. *Phys Rev C*. (2020) 102:034301. doi: 10.1103/PhysRevC.102.034301
40. Jokiniemi L, Ejiri H, Frekers D, Suhonen J. Neutrinoless $\beta\beta$ nuclear matrix elements using isovector spin-dipole $J^\pi = 2^-$ data. *Phys Rev C*. (2018) 98:024608. doi: 10.1103/PhysRevC.98.024608
41. Jokiniemi L, Suhonen J, Ejiri H, Hashim IH. Pinning down the strength function for ordinary muon capture on ^{100}Mo. *Phys Lett B*. (2019) 794:143–7. doi: 10.1016/j.physletb.2019.05.037
42. Jokiniemi L, Suhonen J. Muon-capture strength functions in intermediate nuclei of $0\nu\beta\beta$ decays. *Phys Rev C*. (2019) 100:014619. doi: 10.1103/PhysRevC.100.014619
43. Primakoff H. Theory of muon capture. *Rev Mod Phys*. (1959) 31:802–22. doi: 10.1103/RevModPhys.31.802

Conflict of Interest: The authors declare that the research was conducted in the absence of any commercial or financial relationships that could be construed as a potential conflict of interest.

frontiers in Physics

PERSPECTIVE
published: 05 April 2021
doi: 10.3389/fphy.2021.650421

Experimental Approaches to Neutrino Nuclear Responses for $\beta\beta$ Decays and Astro-Neutrinos

Hiroyasu Ejiri *

Research Center for Nuclear Physics, Osaka University, Osaka, Japan

Fundamental properties of neutrinos are investigated by studying double beta decays ($\beta\beta$-decays), while atro-neutrino nucleo-syntheses and astro-neutrino productions are investigated by studying inverse beta decays (inverse β-decays) induced by astro-neutrinos. Neutrino nuclear responses for these $\beta\beta$ and β-decays are crucial for these neutrino studies in nuclei. This reports briefly perspectives on experimental studies of neutrino nuclear responses (square of nuclear matrix element) for $\beta\beta$-decays and astro-neutrinos by using nuclear and leptonic (muon) charge-exchange reactions

Keywords: double beta decay, nuclear matrix element, charge exchange reaction, supernova neutrino, quenching of axial vector coupling

OPEN ACCESS

Edited by:
Filipe Rafael Joaquim, University of Lisbon, Portugal

Reviewed by:
Frank Franz Deppisch, University College London, United Kingdom
Carlo Giunti, Ministry of Education, Universities and Research, Italy

***Correspondence:**
Hiroyasu Ejiri
ejiri@rcnp.osaka-u.ac.jp

Specialty section:
This article was submitted to High-Energy and Astroparticle Physics, a section of the journal Frontiers in Physics

Received: *07 January 2021*
Accepted: *01 February 2021*
Published: *05 April 2021*

Citation:
Ejiri H (2021) Experimental Approaches to Neutrino Nuclear Responses for ββ Decays and Astro-Neutrinos. Front. Phys. 9:650421. doi: 10.3389/fphy.2021.650421

1 NEUTRINOLESS $\beta\beta$-DECAYS AND ASTRO-NEUTRINO NUCLEAR INTERACTIONS

Fundamental properties of neutrinos such as the Majorana nature and the neutrino masses, which are beyond the standard electro-weak model, are well investigated by studying neutrinoless double beta decays ($\beta\beta$-decays) in nuclei. Inverse beta decays (inverse β-decays) induced by neutrino nuclear interactions are used to study astro-neutrino nucleo-syntheses and astro-neutrino productions [1–3].

The $\beta\beta$ rate $T^{0\nu}$ for the light Majorana-neutrino mass mode is expressed as [4–6].

$$T^{0\nu} = g_A^4 G^{0\nu} \left| M^{0\nu} m^{eff} \right|^2, B^{0\nu} = \left| M^{0\nu} \right|^2, \tag{1}$$

where $G^{0\nu}$ is the phase space, $B^{0\nu}$ is the nuclear response and m^{eff} is the effective neutrino mass. $M^{0\nu}$ is the nuclear matrix element (NME). The axial vector weak coupling is $g_A = 1.27$ in units of the vector coupling for a free nucleon. The $\beta\beta$ nuclei to be considered are even-even nuclei.

Astro-neutrino (supernova- and solar-neutrinos) nuclear interaction rate $T^{\nu}(i)$, i.e., the inverse β-decay rate, for the ith nuclear state is given as [1, 2].

$$T^{\nu}(i) = \int g_A^2 G^{\nu}(i, E_{\nu}) B_i^{\nu} f_{\nu}(E_{\nu}) dE_{\nu}, B_i^{\nu} = \left| M_i^{\nu} \right|^2 (2J+1)^{-1}, \tag{2}$$

where $G^{\nu}(i, E_{\nu})$ is the phase space volume, B_i^{ν} is the nuclear response, and $f_{\nu}(E_{\nu})$ is the neutrino flux. B_i^{ν} is expressed in terms of the NME M_i^{ν} and the initial state spin J.

The $\beta\beta$ NME $M^{0\nu}$ and the inverse β-decay NME M_i^{ν} are crucial for extracting the effective neutrino-mass of the particle physic interest and the neutrino flux of the astro-physics interest from the experimental $\beta\beta$ rate and the inverse β-decay rate, respectively. They are important to design the $\beta\beta$ and astro-neutrino detectors since the nuclear isotopes used in $\beta\beta$ and astro-neutrino detectors depend on their NMEs [2, 3]. Accurate theoretical calculations for the $\beta\beta$ and inverse β-decay NMEs,

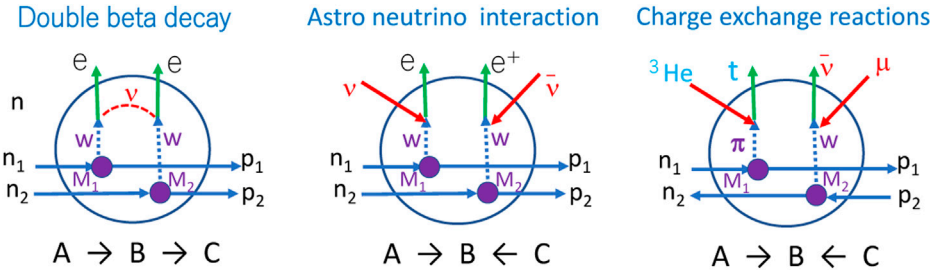

FIGURE 1 | Decay and interaction schemes. **(A)**: Double beta decay. **(B)**: Astro-neutrino and astro-antineutrino interactions. **(C)**: Nuclear (^{3}He) and leptonic (muon) charge-exchange reactions (CERs). W and π are weak boson and pion involved in the weak and nuclear CERs, respectively.

however, are very hard since they depend much on models and parameters used for the calculations [1, 2, 7–9].

Recently, nuclear and muon (lepton) charge-exchange reactions (CERs) have been shown to be used to provide experimentally single-$\beta^{\pm}$ NMEs associated with the $\beta\beta$ and astro-neutrino NMEs [1–3, 6]. The present report aims at critical reviews on perspectives of experimental approaches to the $\beta\beta$ and astro-neutrino nuclear responses by means of the nuclear and leptonic (muon) CERs and others.

We consider mainly the ground-state to ground-state ($0^+ \rightarrow 0^+$) $\beta\beta$ decay of ${}^A_Z\mathrm{X} \leftrightarrow {}^A_{Z+2}\mathrm{X}$, the ground-state to the ith state astro-neutrino transition of ${}^A_Z\mathrm{X} \rightarrow {}^A_{Z+1}\mathrm{X}_i$ and the ground-state to the ith state astro-antineutrino transition of ${}^A_{Z+1}\mathrm{X} \leftarrow {}^A_{Z+2}\mathrm{X}$. The $\beta\beta$ decay and astro-neutrino transition schemes are illustrated in **Figure 1**. Hereafter $\beta\beta$ and astro-neutrino stand for, respectively, neutrinoless $\beta\beta$ and astro-neutrino and astro-antineutrino unless specified. The $\beta\beta$ NME is expressed as [1, 2, 6].

$$M^{0\nu} = \sum_{\alpha} g_{\alpha}^2 M^{0\nu}(\alpha), M^{0\nu}(\alpha) = \sum_i M_i^{0\nu}(\alpha), \tag{3}$$

where α = GT, T, F stand for the Gamow-Teller, tensor and Fermi transitions and g_α is the weak coupling in units of g_A and $M_i^{0\nu}(\alpha)$ is the α mode $\beta\beta$ NME via the ith state in the intermediate nucleus of ${}^A_{Z+1}\mathrm{X}$. The $\beta\beta$ NME $M_i^{0\nu}(\alpha)$ associated with the ν-exchange between two neutrons is expressed as $M_i^{0\nu}(\alpha) = < T_\alpha h_i(\alpha) >_i$ with T_α and $h_i(\alpha)$ being the α mode transition operator and the neutrino potential for the $\beta\beta$ decay via the ith intermediate state [2, 4, 6, 7]. T_α operators for α = GT. F and T are given, respectively, by $\tau\tau\sigma\sigma, \tau\tau$, and $\tau\tau(\sigma r\sigma r - \sigma\sigma/3)$ where τ, σ are the isospin and spin operators and r is the distance between the two neutrons. Among GT, F, and T NMEs, the GT and F NMEs are dominant. Experimental measurements of the $\beta\beta$ NMEs are not possible unless the $\beta\beta$ rates and the neutrino-masses are measured, while two-neutrino $\beta\beta$ ($2\nu\beta\beta$) NMEs have been derived from the measured rates.

The astro-neutrino NME for the ith state is expressed as [1, 2].

$$M_i^{\nu} = \sum_{\alpha'} M_i^{\pm}(\alpha'), \tag{4}$$

where $M_i^{\pm}(\alpha')$ is the α'-mode single-$\beta^{\pm}$ NME for the ith state. Here β^+ and β^- refer to the anti-neutrino τ^+ transition of ${}^A_{Z+1}\mathrm{X} \leftarrow {}^A_{Z+2}\mathrm{X}$ and the neutrino τ^- transition of ${}^A_Z\mathrm{X} \rightarrow {}^A_{Z+1}$ respectively, as shown in **Figure 1**. The transition modes include the allowed F transition, the allowed GT transition, the first-forbidden unique transition, the first forbidden non-unique transition, and so on.

2 NEUTRINO NUCLEAR RESPONSES FOR $\beta\beta$-DECAYS AND ASTRO-NEUTRINOS

So far, neutrino nuclear responses and their NMEs have been measured mainly by $\beta^{\pm}$ and electron capture, and thus they are limited mostly to ground-state and low-momentum GT (1^+) transitions. There are several specific features of $\beta\beta$ and astro-neutrino nuclear responses (NMEs) to be considered [1, 2].

1. $\beta\beta$ and astro-neutrino NMEs involve wide ranges of momentum, spin and excitation energy [2, 6, 7]. In case of the light neutrino-mass mode $\beta\beta$, the Majorana neutrino is exchanged between two nucleons with distance r in the nucleus. Then the linear and angular momenta and the excitation energy involved in $\beta\beta$ are around $1/r$ = 30–120 MeV/c, $l\hbar \approx 0$–$5\,\hbar$ and E_i = 0–30 MeV. Supernova neutrinos are in the wide energy range of 10–50 MeV, depending on the temperature. Then the energetic neutrinos may excite final states up to around 40 MeV with spin transfers of $\Delta J^{\pi} = 0^{\pm}, 1^{\pm}, 2^{\pm}$ and so on.
2. $\beta\beta$ and astro-neutrino interactions are expressed in terms of the isospin (τ) and spin (σ) operators. Thus the NMEs are necessarily very sensitive to nucleonic and non-nucleonic τ and $\tau\sigma$ interactions and correlations. Nuclear τ and $\tau\sigma$ interactions are repulsive in nature, and thus most τ and $\tau\sigma$ strengths are pushed up to the τ and $\tau\sigma$-type giant resonances in the high excitation region, leaving little strengths in the low-lying quasi-particle states involved in the DBDs and astro-neutrinos [1–3].
3. The τ and $\tau\sigma$ interactions and correlations are associated with both the nucleons (protons and neutrons) and non-nucleonic hadrons (mesons, Δ-baryons). The $\beta\beta$ and astro-neutrino NMEs are sensitive to nuclear medium changes from the initial to final states, resulting in the reduction of the NMEs.
4. Axial-vector NMEs for nuclear $\beta\gamma$ transitions are quenched with respect to the NMEs calculated by the proton-neutron quasi-particle random-phase approximation, which includes nucleonic $\tau\sigma$

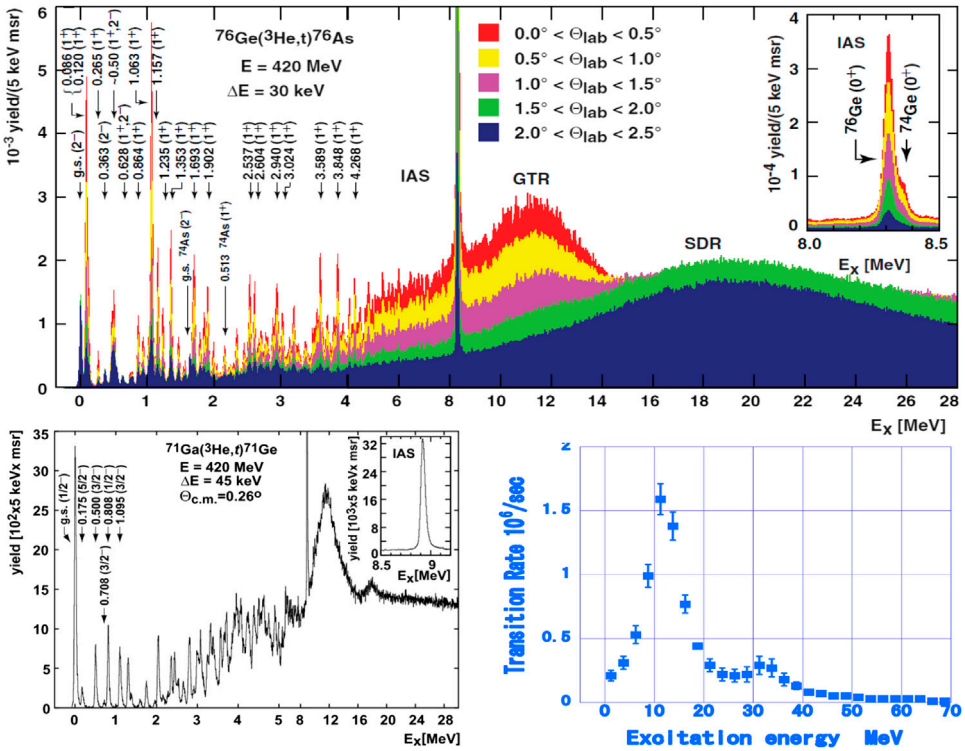

FIGURE 2 | CER strengths as a function of the excitation energy. Top: The ^{76}Ge(^{3}He,t)^{76}As reaction for $\beta\beta$ responses, where the GT s-wave strengths (red lines) are preferentially excited at the forward angles, while SD p-wave strengths (blue lines) at larger angles [13]. Bottom left-panel: The ^{71}Ga(^{3}He,t) ^{71}Ge reaction for solar neutrino responses [14]. Bottom right-panel: The ^{100}Mo (μ, ν_μ) Nb reactions [20]. The strong GT and SD giant resonances, GTR and SDR, at around 12 and 20 MeV are seen in the spectrum of ^{76}Ge(^{3}He,t)^{76} As.

interactions and correlations but not explicitly the non-nucleonic correlations and nuclear medium effects [1, 2, 10, 11]. Such quenching effect is incorporated by using the effective axial-vector coupling $g_A^{eff} = kg_A$, where g_A = 1.27 is the coupling for a free nucleon and k is the quenching coefficient [1–3].

5. Accurate theoretical calculations for the $\beta\beta$ and astro-neutrino NMEs are very hard since the medium heavy nuclei involved in the NMEs are very complex many-body strongly interacting hadron (nucleon, meson, Δ-baryon, and others) systems [2, 7, 8]. Then the NMEs are very sensitive to all kinds of nucleonic, non-nucleonic and nuclear medium effects. Furthermore, the NMEs themselves are only a very tiny (10^{-2}–10^{-3}) fraction of the total strength. Actually, theoretical $\beta\beta$ NMEs scatter over an order of magnitude depending on the models and the parameters such as g_A^{eff} and nuclear interactions [2, 6].

3 EXPERIMENTAL APPROACHES TO $\beta\beta$ AND ASTRO-NEUTRINO RESPONSES

The $\beta\beta$ and astro-neutrino NMEs have recently been studied by using nuclear and muon CERs as given in the reviews and references there in [1, 2]. Here we discuss mainly the single β^- NME $M_i^-(\alpha')$ for ${}^A_Z\mathrm{X} \rightarrow {}^A_{Z+1}\mathrm{X}$ and single β^+NME $M_i^+(\alpha_I)$ for ${}^A_{Z+1}\mathrm{X} \leftarrow {}^A_{Z+2}\mathrm{X}$ (see **Figure 1**). They are the τ^- and τ^+-side NMEs, which the $\beta\beta$ NME for the ith intermediate state is associated with through the neutrino potential, and are the NMEs relevant to the astro-neutrino and astro-antineutrino reactions for the ith state in ${}^A_{Z+1}\mathrm{X}$, respectively. The M_i^- (GT) and M_i^+ (GT) for low-lying quasi-particle states have been used to evaluate the $2\nu\beta\beta$ NMEs, and the evaluated NMEs agree with the NMEs derived from the observed $2\nu\beta\beta$ rates [12].

Medium energy (^{3}He,t) reactions with $E(^3\mathrm{He})$ = 0.42 GeV at Research Center for Nuclear Physics (RCNP) are shown to be powerful for studying τ^--side $\tau\sigma$ responses in the wide momentum (0–120 MeV/c) and excitation energy (0–30 MeV) regions [1, 2]. The axial-vector α' = GT (1^+) and α' = SD (spin dipole 2^-) NMEs in nuclei of $\beta\beta$ and astro-neutrino interests are measured [1, 2, 13–17]. The measured spectrum for ^{76}Ge [13] is shown in **Figure 2**. GT NMEs are the NMEs involved mainly in the $2\nu\beta\beta$ decays and the low-energy astro-neutrinos, while SD NMEs are major components associated with the neutrinoless DBDs and medium energy astro-neutrinos [2].

The measured GT and SD NMEs are quenched by the coefficient $k = g_A^{eff}/g_A \approx 0.4$–$0.6$ with respect to the NMEs by the quasi-particle random-phase approximation [1, 2, 11]. The measured GT and SD responses (square of NME) for low excitation region are only a few % of the total strength and most of them are located at the highly

excited giant resonances, as shown in **Figure 2**. The giant resonances are coherent $\tau\sigma$ excitations with the large NMEs. They mix in the low-lying GT and SD states with the negative (out-phase) mixing coefficient via the repulsive interaction. Thus the GT and SD NMEs for the low-lying states are quenched by the mixing effect of the high-lying GT and SD giant resonances, respectively.

Ordinary muon capture (OMC) [18] is a muon charge-exchange reaction (μ-CER). It is used for studying the $M_i^+(\alpha')$ NMEs [2]. A negative muon trapped in an inner atomic orbit is captured into the nucleus. The process is a lepton CER of $\mu + {}^{A}_{Z+2}\mathrm{X} \rightarrow \nu_\mu + {}^{A}_{Z+1}\mathrm{X}_i$. The momentum and energy transferred to the nucleus are around 95–50 MeV/c and 5–50 MeV, which are the regions of DBDs and astro-neutrinos.

μ-CERs on Mo isotpes [19] and $\beta\beta$ nuclei have been studied by using low-momentum muons from the MuSIC beam line at RCNP [2, 20]. The *i*th excited state of ${}^{A}_{Z+1}\mathrm{X}_i$ produced by the μ-CER on ${}^{A}_{Z+2}\mathrm{X}$ decays by emitting a number (x) of neutrons and gamma rays to the ground state of ${}^{A-x}_{Z+1}\mathrm{X}$. The number x depends on the excitation energy E_i. The residual nuclei are identified by measuring γ rays characteristic of them. Then the μ-CER strength distribution in ${}^{A}_{Z+1}\mathrm{X}$ as a function of the excitation energy E_i is obtained from the measured mass-number $(A-x)$ distribution by using the neutron cascade-emission model [20]. The μ-CER strength distribution for ^{100}Mo [20] show a strong μ-giant resonance around $E_i \approx 12$ MeV, as shown in **Figure 2**. Since μ-CER excites mainly states with $J^\pi = 0^\pm, 1^\pm, 2^\pm$, and $3^\pm$, the giant resonance is a composite of the resonances with these spins. The observed strength distribution agrees with the calculation using the quasi-particle random-phase approximation [21]. The muon-capture rate is smaller by a factor around 5 with respect to the calculated rate, suggesting the quenching coefficient of $g_A^{eff}/g_A \approx 0.5$ [21].

4 PERSPECTIVES AND REMARKS ON NEUTRINO NUCLEAR RESPONSES

The high energy-resolution (^{3}He,t) CERs at RCNP are well used for studying the τ^--side $M_i^-(\alpha')$ NMEs with $\alpha' = \mathrm{GT}(1^+)$ and SD (2^-) in the wide momentum and energy regions involved in $\beta\beta$-decays and astro-neutrinos. They are extended to higher-multipole NMEs $M_i^-(\alpha')$ with $\alpha' = $ SQ (spin quadra-pole 3^+) and SO (spin octa-pole 4^-). The τ^+-side NMEs of $M_i^+(\alpha')$ are studied by using (d,^{2}He) [22] and (t,^{3}He) CERs [1]. Higher energy-resolution studies of unbound ^{2}He from the (d,^{2}He) CER is interesting to study the τ^+-side NMEs for individual states.

The axial-vextor (GT, SD, and higher multi-pole) strength distributions in the wide excitation region are interesting to see how the axial vector NMEs at the low lying quasi-particle states are quenched due to the destructive interference with the high-lying giant resonances, and how the summed strengths over the giant resonances are somewhat reduced by the possible effects of the Δ baryons [2, 11].

Double charge-exchange reactions explore double τ and $\tau\sigma$ responses for $\beta\beta$ responses [2, 3, 23]. The RCNP (^{11}B, ^{11}Li) data indicate a large strength at the high excitation region and little one at the low-lying states. Extensive studies of double charge-exchange reactions are under progress at INFN-LNS [23].

μ-CERs are used to study the NME $M_i^+(\alpha')$ in wide momentum and energy regions relevant to $\beta\beta$-decays and astro-neutrinos. The observed μ giant resonance around $E_i \approx 12$ MeV suggests concentration of the τ^+-strengths at the highly excited giant resonance, resulting in the quenching of the NMEs at low-lying states, as in case of the τ^--side responses. In fact, the absolute μ-CER strength is much smaller than the calculated one [21, 24], suggesting the severe quenching as in case of τ^- responses. The recent calculations, however, reproduce the observed rates with the bare g_A [25]. The two calculations are based on the quasi-particle random-phase approximation, but use different nuclear parameters. Thus the calculated strength distributions and the calculated multipole components are different between the two calculations. So the origins of the differences are open questions. Actually, the μ-CER rate is a product of the phase space factor and the neutrino nuclear response (square of the NME). It is important to compare the experimental μ-CER NME with the theoretical NME to see if one needs a quenched g_A^{eff} as in case of the NMEs studied in single $\beta^\pm$. Further experimental and theoretical studies of the μ-CERs for nuclei of $\beta\beta$ and astro-neutrino interests are interesting to investigate the NMEs $M_i^+(\alpha')$ up to around 50 MeV.

Medium-energy neutrinos are of potential interest for direct measurements of neutrino nuclear responses [26]. High-intensity medium-energy (1–3 GeV) proton accelerators at SNS ORNL and MLF KEK and others are used to produce intense pions, and neutrinos of the order of 10^{15}/sec are obtained from the $\pi - \mu$ decays. Neutrino and anti-neutrino CERs of $\nu(\bar{\nu}) \rightarrow \mathrm{e}^-(\mathrm{e}^+)$ are used to study $(M_i^+(\alpha'))$ NMEs. Neutrino nuclear cross-sections are of the order of 10^{-40} cm^2. Then one may use multi-ton scale isotopes as used for $\beta\beta$ experiments to study neutrino nuclear responses.

Electro-magnetic interaction includes isovector and isoscalar components. They are analogous to the charged and neutral current responses of the neutrino (weak) interaction, respectively. Thus one gets information of the neutrino NME by studying the isovector component of the EM transition [2, 9]. The special case is the photo-nuclear excitation of the isobaric analogue state of $\mathrm{T}^-|\mathrm{i}>$ with T^- being the isosin lowering operator [1, 2, 27]. The NME for the weak transition of $|\mathrm{i}> \rightarrow |\mathrm{f}>$ is obtained from the analogous EM NME for the γ transition from the isobaric analogue state to $|\mathrm{f}>$ [2].

Nucleon transfer reactions are used to measure single quasi-particle occupation probabilities. The summed probability is quenched by 0.5–0.6 with respect to the nucleon-based model value [28]. This suggests some non-nucleonic and nuclear medium effects as in the neutrino responses [2].

DATA AVAILABILITY STATEMENT

The original contributions presented in the study are included in the article/Supplementary Material, further inquiries can be directed to the corresponding author.

AUTHOR CONTRIBUTIONS

The author confirms being the sole contributor of this work and has approved it for publication.

REFERENCES

1. Ejiri H. Nuclear spin isospin responses for low-energy neutrinos. *Phys Rep* (2000) 338:265. doi:10.1016/s0370-1573(00)00044-2
2. Ejiri H, Suhonen J, Zuber K. Neutrino-nuclear responses for astro-neutrinos, single beta decays and double beta decays. *Phys Rep* (2019) 797:1. doi:10.1016/j.physrep.2018.12.001
3. Ejiri H. Neutrino-mass sensitivity and nuclear matrix element for neutrinoless double beta decay. *Universe* (2020) 6:225. doi:10.3390/universe6120225
4. Doi M, Kotani T, Takasugi E. Double beta decay and majorana neutrino. *Prog Theor Phys Suppl* (1985) 83:1–175. doi:10.1143/ptps.83.1
5. Avignone FT, Elliott SR, Engel J. Double beta decay, majorana neutrinos, and neutrino mass. *Rev Mod Phys* (2008) 80:481. doi:10.1103/revmodphys.80.481
6. Vergados JD, Ejiri H, Šimkovic F. Theory of neutrinoless double-beta decay. *Rep Prog Phys* (2012) 75:106301. doi:10.1088/0034-4885/75/10/106301
7. Suhonen J, Civitarese O. Double-beta decay nuclear matrix elements in the QRPA framework. *J Phys G Nucl Part Phys* (2012) 39:035105. doi:10.1088/0954-3899/39/8/085105
8. Engel J, Menéndez J. Status and future of nuclear matrix elements for neutrinoless double-beta decay: a review. *Rep Prog Phys* (2017) 80:046301. doi:10.1088/1361-6633/aa5bc5
9. Jokiniemi L, Ejiri H, Frekers D, Suhonen J. Neutrinoless nuclear matrix elements using isovector spin-dipole data. *Phys Rev C* (2018) 98:024608. doi:10.1103/physrevc.98.024608
10. Suhonen J. Impact of the quenching of the on the sensitivities of 0 experiments. *Phys Rev C* (2017) 96:05501. doi:10.1103/physrevc.96.055501
11. Ejiri H. Nuclear matrix elements for β and decays and quenching of the weak coupling in QRPA. *Front Phys* (2019).2165:020007.doi:10.1063/1.5130968
12. Ejiri H. Fermi surface quasi particle model nuclear matrix elements for two neutrino double beta decays. *J Phys Nucl Part Phys* (2017) 44:15201. doi:10.1088/1361-6471/aa8a1f
13. Thies JH, Frekers D, Adachi T, Dozono M, Ejiri H, Fujita H, et al. The (^{3}He,t) reaction on ^{76}Ge, and double-β decay matrix element. *Phys Rev C* (2012) 86:014304. doi:10.1103/physrevc.86.014304
14. Frekers D, Ejiri H, Akimune H, Adachi T, Bilgier B, Brown BA, et al. The ^{71}Ga(^{3}He,t) reaction and the low-lying neutrino response. *Phys Lett B* (2011) 706:134–8. doi:10.1016/j.physletb.2011.10.061
15. Ejiri H, Frekers D. Spin dipole nuclear matrix elements for double beta decay nuclei by charge-exchange reactions. *J Phys G: Nucl Part Phys* (2016) 43:11LT01. doi:10.1088/0954-3899/43/11/11lt01
16. Akimune H, Ejiri H, Hattori F, Agodi C, Alanssari M, Cappuzzello F, et al. Spin-dipole nuclear matrix element for double beta decay of ^{76}Ge by the (^{3}He,t) charge-exchange reaction. *J Phys G Nucl Part Phys* (2020) 47:05LT01. doi:10.1088/1361-6471/ab7a87
17. Ejiri H. Axial-vector weak coupling at medium momentum for astro neutrinos and double beta decays. *J Phys G: Nucl Part Phys* (2019) 46:125202. doi:10.1088/1361-6471/ab4dcb
18. Measday DF. The nuclear physics of muon capture. *Phys Rep* (2001) 354:243–409. doi:10.1016/s0370-1573(01)00012-6
19. Ejiri H, Engel J, Hazama R, Krastev P, Kudomi N, Robertson RGH. Spectroscopy of double-beta and inverse-beta decays from ^{100}Mo for neutrinos. *Phys Rev Lett* (2000) 85:2917. doi:10.1103/physrevlett.85.2917
20. Hashim I, Ejiri H, Shima T, Takahisa K, Sato A, Kuno Y, et al. Muon capture reaction on Mo to study neutrino nuclear responses for double-β decays and neutrinos of astro-physics origins. *Phys Rev C* (2018) 97:014617. doi:10.1103/physrevc.97.014617
21. Jokiniemi L, Suhonen J, Ejiri H, Hashim IH. Pinning down the strength function for ordinary muon capture on ^{100}Mo. *Phys Lett B* (2019) 794:143–7. doi:10.1016/j.physletb.2019.05.037
22. Dohmann H, Bǎmer C, Frekers D, Grewe E -W, Harakeh MN, Hollstein S, et al. The (d,^{2}He) reaction on Mo and the double-β decay matrix elements for Zr. *Phys Rev C* (2008) 78:041602. doi:10.1103/physrevc.78.041602
23. Cappuzzello F, Cavallaro M, Agodi C, Bondì M, Carbone D, Cunsolo A, et al. Heavy ion double charge exchange reactions: a tool toward 0 nuclear matrix elements. *Eur Phys J* (2015) 51:145. doi:10.1140/epja/i2015-15145-5
24. Jokiniemi L, Suhonen J. Muon-capture strength functions in intermediate nuclei of 0 decays. *Phys Rev C* (2019) 100:014619. doi:10.1103/physrevc.100.014619
25. Simkovic F, Dvornieky R, Vogel P. Muon capture rates: evaluation within the quasiparticle random phase approximation. *Phys Rev C* (2020) 102:034301. doi:10.1103/PhysRevC.102.034301
26. Ejiri H. Neutrino studies in nuclei and intense neutrino sources. *Nucl Instr Methods Phys Res Sec. A* (2003) 503:276–8. doi:10.1016/s0168-9002(03)00695-8
27. Ejiri H, Titov A, Bosewell M, Yang A. Neutrino nuclear response and photonuclear reactions. *Phys Rev C* (2013) 88:054610. doi:10.1103/physrevc.88.054610
28. Kay BP, Schiffer JP, Freeman SJ. Quenching of cross sections in nuclear transfer reactions. *Phys Rev Lett* (2013) 111:042502. doi:10.1103/physrevlett.111.042502

Conflict of Interest: The author declares that the research was conducted in the absence of any commercial or financial relationships that could be construed as a potential conflict of interest.

frontiers in Astronomy and Space Sciences

ORIGINAL RESEARCH
published: 20 April 2021
doi: 10.3389/fspas.2021.668587

The NUMEN Project: An Update of the Facility Toward the Future Experimental Campaigns

Francesco Cappuzzello[1,2], Luis Acosta[3], Clementina Agodi[2], Ismail Boztosun[4], Giuseppe A. Brischetto[1,2], Salvatore Calabrese[2], Luciano Calabretta[2], Daniela Calvo[5], Luigi Campajola[6,7], Vittoria Capirossi[5,8], Diana Carbone[2], Manuela Cavallaro[2], Efrain Chávez[3], Irene Ciraldo[1,2], Franck Delaunay[1,2,9], Haris Djapo[10], Carlo Ferraresi[5,11], Paolo Finocchiaro[2], Maria Fisichella[2], Elisa M. Gandolfo[6,7], Felice Iazzi[5,8], Mauricio Moralles[12], Lorenzo Neri[2], Josè R. B. Oliveira[13], Luciano Pandola[2], Horia Petrascu[14], Federico Pinna[5,8], Antonio D. Russo[2], Diego Sartirana[5], Onoufrios Sgouros[2], S. O. Solakci[4], Vasileios Soukeras[2], Alessandro Spatafora[1,2], Domenico Torresi[2], Salvatore Tudisco[2] and Aydin Yildirim[4] on behalf of the NUMEN collaboration*

[1] Dipartimento di Fisica e Astronomia "Ettore Majorana", Università di Catania, Catania, Italy, [2] Istituto Nazionale di Fisica Nucleare–Laboratori Nazionali del Sud, Catania, Italy, [3] Instituto de Física, Universidad Nacional Autónoma de México, Mexico City, Mexico, [4] Physics Department, Akdeniz University, Antalya, Turkey, [5] Istituto Nazionale di Fisica Nucleare–Sezione di Torino, Turin, Italy, [6] Dipartimento di Fisica–Università di Napoli Federico II, Napoli, Italy, [7] Istituto Nazionale di Fisica Nucleare–Sezione Napoli, Napoli, Italy, [8] Dipartimento Scienza Applicata e Tecnologia, Politecnico di Torino, Torino, Italy, [9] LPC Caen, Normandie Université, ENSICAEN, UNICAEN, CNRS/IN2P3, Caen, France, [10] Institute of Accelerator Laboratory, Ankara University, Ankara, Turkey, [11] Dipartimento di Ingegneria Meccanica e Aerospaziale, Politecnico di Torino, Turin, Italy, [12] Instituto de Pesquisas Energéticas e Nucleares, Instituto de Pesquisas Energéticas e Nucleares, Comissão Nacional de Energia Nuclear, São Paulo, Brazil, [13] Instituto de Física da Universidade de São Paulo, São Paulo, Brazil, [14] Institutul National de Cercetare-Dezvoltare pentru Fizica si Inginerie Nucleara Horia Hulubei (IFIN-HH), Măgurele, Romania

OPEN ACCESS

Edited by:
Giuseppe Mandaglio,
University of Messina, Italy

Reviewed by:
Michał Silarski,
Jagiellonian University, Poland
Andrea Celentano,
Universities and Research, Italy

***Correspondence:**
Francesco Cappuzzello
cappuzzello@lns.infn.it

Specialty section:
This article was submitted to Nuclear Physics, a section of the journal Frontiers in Astronomy and Space Sciences

Received: 16 February 2021
Accepted: 18 March 2021
Published: 20 April 2021

Citation:
Cappuzzello F, Acosta L, Agodi C, Boztosun I, Brischetto GA, Calabrese S, Calabretta L, Calvo D, Campajola L, Capirossi V, Carbone D, Cavallaro M, Chávez E, Ciraldo I, Delaunay F, Djapo H, Ferraresi C, Finocchiaro P, Fisichella M, Gandolfo EM, Iazzi F, Moralles M, Neri L, Oliveira JRB, Pandola L, Petrascu H, Pinna F, Russo AD, Sartirana D, Sgouros O, Solakci SO, Soukeras V, Spatafora A, Torresi D, Tudisco S and Yildirim A (2021) The NUMEN Project: An Update of the Facility Toward the Future Experimental Campaigns. Front. Astron. Space Sci. 8:668587. doi: 10.3389/fspas.2021.668587

The goal of NUMEN project is to access experimentally driven information on Nuclear Matrix Elements (NME) involved in the neutrinoless double beta decay ($0\nu\beta\beta$) by accurate measurements of the cross sections of heavy-ion induced double charge-exchange reactions. In particular, the (^{18}O, ^{18}Ne) and (^{20}Ne, ^{20}O) reactions are adopted as tools for $\beta^+\beta^+$ and $\beta^-\beta^-$ decays, respectively. The experiments are performed at INFN–Laboratory Nazionali del Sud (LNS) in Catania using the Superconducting Cyclotron to accelerate the beams and the MAGNEX magnetic spectrometer to detect the reaction products. The measured cross sections are very low, limiting the present exploration to few selected isotopes of interest in the context of typically low-yield experimental runs. In order to make feasible a systematic study of all the candidate nuclei, a major upgrade of the LNS facility is foreseen to increase the experimental yield by more than two orders of magnitude. To this purpose, frontier technologies are being developed for both the accelerator and the detection systems. An update description of the NUMEN project is presented here, focusing on recent achievements from the R&D activity.

Keywords: double beta decay, nuclear matrix elements, double charge exchange, heavy ion multidetector, MAGNEX spectrometer

INTRODUCTION

Neutrinoless double beta decay ($0\nu\beta\beta$) is a nuclear process where a parent nucleus decays into a daughter isobar differing by two units of charge and two electrons (or positrons) are emitted. Although not yet observed, this phenomenon is nowadays widely investigated since, if discovered in the experiments, it would allow to directly determine the Majorana nature of neutrino and unveil that the total lepton number is not necessarily conserved in nature (Suhonen and Civitarese, 2012; Vergados et al., 2012; Gouvea and Vogel, 2013). Moreover, the neutrino effective mass could be extracted from decay rate measurements, with foreseen sensitivity to normal or inverted hierarchy scenarios in the neutrino mass distribution. Presently, this physics case is leading the research "beyond the standard model" as it could help to explain the matter–antimatter asymmetry observed in the Universe and open new perspectives toward a grand unified theory of fundamental interactions.

Double beta decay occurs in atomic nuclei, making nuclear structure issues essential for its proper description. The $0\nu\beta\beta$ decay rate is typically expressed as the product of three main factors: (i) a phase-space parameter, describing the motion of the electrons (or positrons); (ii) the square of a nuclear matrix element (NME), connected to the overlap between the initial and final nuclear states; (iii) a factor describing the emission and reabsorption of the neutrino, containing physics beyond the standard model. Thus, if the NMEs are established with sufficient precision, new physics can be accessed from $0\nu\beta\beta$ decay rate measurements.

A deeper knowledge of the NMEs is thus crucial to set the strategies of future experiments of direct search for $0\nu\beta\beta$ decay. However, an updated comparison of the results of NMEs calculations, obtained within various nuclear structure frameworks (Barea et al., 2013; Dell'Oro et al., 2016; Ejiri et al., 2019), indicates that significant differences (about a factor three) are indeed found, which makes the present situation not satisfactory. To date the determination of the NMEs, based on different calculation schemes, is still controversial, also due to the lack of experimental constraints.

Over the last few years, major interest has raised for heavy-ion induced Double Charge-Exchange (DCE) studies, especially because of their possible connection to $0\nu\beta\beta$ decay. Exploratory studies have been started at RIKEN in Tokyo and at RCNP in Osaka (Matsubara et al., 2013; Kisamori et al., 2016; Takahisa et al., 2017). An intense activity is also being pursued at the Istituto Nazionale di Fisica Nucleare–Laboratori Nazionali del Sud (INFN-LNS) in Catania, in the frame of the NUMEN project. A new DCE reaction, the (^{20}Ne,^{20}O), has been recently studied for the first time, looking for $\beta^-\beta^-$-like transitions. In addition, important results have been achieved on the $\beta^+\beta^+$ side by the renewed use of the (^{18}O,^{18}Ne) reaction in upgraded experimental conditions. NUMEN and the synergic NURE (ERC Starting Grant 2016) project at INFN-LNS (Agodi et al., 2015; Cappuzzello et al., 2015a, 2018; Cavallaro et al., 2017; Cappuzzello and Agodi, 2021) aim at extracting nuclear structure information relevant for $0\nu\beta\beta$ NMEs by measuring cross sections of DCE and Single Charge Exchange (SCE) reactions. Recent theoretical developments suggest that besides the transition to the ground state of the residual nucleus, the whole double Gamow-Teller strength could, in principle, be connected to $0\nu\beta\beta$-NME (Sagawa and Uesaka, 2016; Santopinto et al., 2018; Shimizu et al., 2018). In particular, results from state-of-art shell-model calculations indicate that a simple relation is expected between the $0\nu\beta\beta$ NME for ^{48}Ca and the centroid energy of the still not observed double Gamow-Teller giant resonance (DGTGR) (Shimizu et al., 2018). In addition, an interesting linear correlation is found between the DGT transition to the ground state of the final nucleus and the $0\nu\beta\beta$ decay NME, even adopting other nuclear structure models.

Since the DGTGR is expected to almost exhaust the corresponding model independent sum rule (Sagawa and Uesaka, 2016), the experimental determination of its strength will also give quantitative access to the quenching of the nuclear response to second order spin-isospin operators. This is particularly interesting because of its connection to long debated problem of the quenching of the axial coupling constant in $0\nu\beta\beta$ decay (Suhonen, 2017). A renormalization of the coupling constant (quenching) of second order spin-isospin (GT-like) operators is indeed expected, due to limitations of the model spaces adopted in the NME calculations and to the typical neglect of two-body currents (Engel and Menendez, 2017; Cappuzzello and Cavallaro, 2020). The exact value of this quenching is still controversial despite it enters to the fourth power in the determination of the $0\nu\beta\beta$ decay rates and could drastically impact on the sensitivity of different experiments searching for that. No experimental evidence of the DGTGR has been reported until now, which makes the possible discovery of this mode a ground-breaking result by itself. Thus, it is not surprising that NUMEN as well as the projects at RIKEN are also targeting the DGTGR resonance.

The aim of the NUMEN project is to measure the absolute cross section for heavy-ion induced DCE reactions on nuclei candidates for the $0\nu\beta\beta$ decay and find a connection between the NMEs of the two processes. Even if $0\nu\beta\beta$ decays and DCE reactions are mediated by different interactions, there are a number of similarities among them: the key aspects are that initial and final nuclear states are the same and the transition operators in both cases are a superposition of short-range isospin, spin-isospin and rank-two tensor components with a relevant available momentum (100 MeV/c or so). The strong interaction mediating the HIDCE makes these processes much more likely to occur compared to $0\nu\beta\beta$ decay. In this way the many body nuclear states involved in the $0\nu\beta\beta$ decay can be explored under controlled laboratory conditions.

In DCE reactions the nuclear matrix elements enter in the expression of the cross section, which is the observable deserving the main interest. However, the DCE reaction channel competes with other nuclear processes activated by the projectile-target collision, many of which are much more likely to occur. As a consequence, the experimental challenge is to isolate and measure a very rare nuclear transition among a very high rate of reaction products generated by the beam-target interaction. In Cappuzzello et al. (2015b) the ^{40}Ca(^{18}O,^{18}Ne)^{40}Ar reaction was studied at 15 MeV/u at the MAGNEX facility of INFN-LNS laboratory (Cappuzzello et al., 2016), showing that

high mass, angular and energy resolution energy spectra and accurate absolute cross sections can be measured, even at very forward scattering angles. With respect to this pilot experiment, additional difficulties are foreseen for the exploration of DCE on nuclei of interest for 0νββ research. As discussed in Cappuzzello et al. (2018), the present limits of the facility in terms of beam power for the Superconducting Cyclotron accelerator and the acceptable rate of few kHz for the MAGNEX focal plane detector (FPD) have limited so far the exploration of DCE to only few cases (e.g., ^{12}C, ^{40}Ca,^{48}Ti, ^{76}Ge, ^{76}Se, ^{116}Cd, ^{116}Sn, ^{130}Te) with beam power of few W. The systematic exploration of all the nuclei of interest for 0νββ decay, foreseen in the NUMEN project, needs an upgraded set-up able to work with kW beam power (Agodi et al., 2021).

NUMEN is also fostering the development of a specific theory program to allow an accurate extraction of nuclear structure information from the measured cross sections. Heavy ion induced SCE reactions have been analyzed in detail in Cappuzzello et al. (2004), Lenske et al. (2018), Lenske et al. (2019) in view of the connection to single beta decay NME. It was shown that the surface localization of the SCE, due the strong absorption of the target-projectile nucleus-nucleus potential, allows for a decisive simplification of the reaction description, making the isovector meson exchange mechanism dominant at forward detection angles. The development of a second order perturbation scheme for DCE cross section is being accomplished relying on quantum mechanical scattering theory, within the Distorted Wave Born Approximation. The theory is focused on the development of microscopic models for DCE reactions, employing several approaches (QRPA, shell model, IBM) for inputs connected to nuclear structure quantities. The link between the theoretical description of the 0νββ decay and DCE reactions is also under study (Santopinto et al., 2018; Lenske et al., 2019; Bellone et al., 2020; Magana Vsevolodovna et al., 2021).

Part of the plans and activities in view of the upgrade of the experimental facility is described in Cappuzzello et al. (2018), Finocchiaro et al. (2020), Agodi et al. (2021), while recent experimental results from NUMEN are cited in Section Experimental activity with accelerated beams during numen phase 2. In this manuscript an update of the NUMEN R&D activity is given, with special emphasis on recent advances on technical aspects not presented elsewhere.

EXPERIMENTAL ACTIVITY WITH ACCELERATED BEAMS DURING NUMEN PHASE 2

Experimental Setup

The NUMEN experiments have been performed at INFN-LNS, using the available high performing experimental facilities, mainly constituted by the K800 superconducting cyclotron (CS) and the MAGNEX magnetic spectrometer.

The CS accelerates the required ion beams, namely ^{18}O, ^{20}Ne, at energies ranging from 15 to 30 MeV/u with high energy resolution (1/1,000) (Cappuzzello et al., 2014) and low emittance (∼2π mm mr) (Rifuggiato et al., 2013). So far, the maximum cyclotron beam power could not exceed ∼100 W, which has not been an issue for the NUMEN Phase 2 experiments, due to more stringent limitations from the present detectors installed at the MAGNEX focal plane. Both facilities need to be upgraded in view of the future experimental campaign (NUMEN Phase 4), where beam power of few kW on target are demanded. An overview of the ongoing upgrade of the CS is found in Agodi et al. (2021).

The MAGNEX spectrometer is a large acceptance magnetic device consisting of a large aperture vertically focusing quadrupole and a horizontally bending dipole magnet (Cappuzzello et al., 2016). A picture of the MAGNEX spectrometer is shown in **Figure 1**. MAGNEX was designed to investigate heavy-ion induced reactions down to very low cross sections allowing the identification of the reaction products with good mass ($\Delta A/A \sim 1/160$), angle ($\Delta\theta \sim 0.2^{\circ}$), and energy resolution ($\Delta E/E \sim 1/1{,}000$), within a large solid angle ($\Omega \sim 50$ msr) and momentum range ($-14\% < \Delta p/p < +10\%$). High-resolution measurements for quasi-elastic processes, characterized by differential cross sections falling down to tens of nb/sr, were already performed with this setup (Pereira et al., 2012; Oliveira et al., 2013; Cappuzzello et al., 2015b,c; Calabrese et al., 2018) even at very forward scattering angles. A crucial feature is the implementation of the powerful technique of trajectory reconstruction, based on differential algebra, which solves the equation of motion of each detected particle up to 10th order (Cappuzzello et al., 2011). This is a unique characteristic of MAGNEX, which guarantees the above-mentioned performances and its relevance in the worldwide scenario of heavy-ion physics also taking advantage of its coupling to the EDEN neutron detector array (Cavallaro et al., 2016).

The MAGNEX FPD consists of a large (active volume 1,360 × 200 × 96 mm) low-pressure gas-filled tracker followed by a wall of 60 silicon pad sensors stopping the detected ions (Cavallaro et al., 2012; Torresi et al., 2021). A set of wire-based drift chambers measures the vertical position and angle of the reaction ejectiles, while the horizontal position and angle are extracted from the induced charge distributions on a set of segmented pads (Carbone et al., 2012). The energy loss measured by the multiplication wires and the residual energy at the silicon

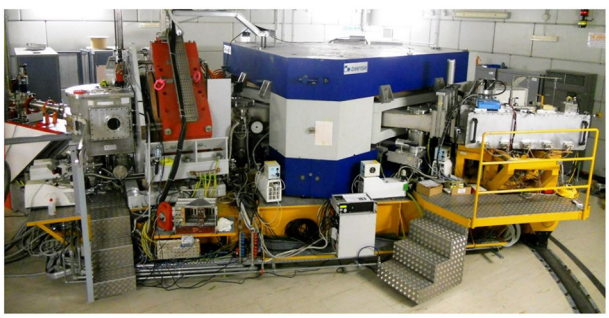

FIGURE 1 | View of the MAGNEX spectrometer at INFN-LNS.

TABLE 1 | List of the reactions explored during NUMEN Phase 2 together with references.

Projectile-Ejectile system	Reaction channel	References
(^{18}O,^{18}O)	Elastic and inelastic scattering	Carbone et al., 2021; Cavallaro et al., 2021; La Fauci et al., 2021
(^{18}O,^{18}Ne)	DCE reaction	Cappuzzello et al., 2015b
(^{18}O,^{18}F)	SCE reaction	Cavallaro et al., 2021
(^{18}O,^{17}O)	One-Neutron stripping reaction	(Ciraldo et al., in preparation)
(^{18}O,^{16}O)	Two-Neutron stripping reaction	Cappuzzello et al., 2021
(^{18}O,^{19}F)	One-Proton pickup reaction	(Ciraldo and Nuovo Cimento, submitted)
(^{18}O,^{20}Ne)	Two-Proton pickup reaction	Ferreira et al., 2021
(^{20}Ne,^{20}Ne)	Elastic and inelastic scattering	Spatafora et al., 2019; Carbone et al., 2021
(^{20}Ne,^{20}O)	DCE reaction	Calabrese et al., 2018, 2020
(^{20}Ne,^{20}F)	SCE reaction	(Burrello et al., in preparation)
(^{20}Ne,^{21}Ne)	One-Neutron pickup reaction	–
(^{20}Ne,^{22}Ne)	Two-Neutron pickup reaction	Carbone et al., 2020
(^{20}Ne,^{19}F)	One-Proton stripping reaction	(Burrello et al., in preparation)
(^{20}Ne,^{18}O)	Two-Proton stripping reaction	Carbone et al., 2020

detectors are used for atomic number (Z) identification of the ions. The ratio m/q between the ion mass (m) and charge (q) is determined by correlating the measured energy and impact position in the spectrometer horizontal (dispersive) direction, as described in Cappuzzello et al. (2010). The present FPD is a suitable detector to discriminate ions with 0.6% resolution in m/q and 2% in Z. The tracking measurement sensitivity guarantees an overall energy resolution of about 1/1,000, which is close to the limit of the optics for the used beams. The performances of the present FPD are described in Torresi et al. (2021).

Experimental Activity

The Phase 2 of NUMEN has been recently concluded with the last experiment performed at INFN LNS in June 2020 before the shutdown of the accelerator machines needed for the planned facility upgrade (Agodi et al., 2021).

The Phase 2 in-beam experimental activity targeted two classes of measurements, characterized by the acceleration of CS beams and the detection of specific reaction ejectiles with the MAGNEX spectrometer. The two classes correspond to the exploration of the two directions of isospin lowering and raising operators, characteristic of $\beta^-\beta^-$ and $\beta^+\beta^+$ decay, respectively. In particular, the investigation of the isospin raising transitions in the target has been performed using ^{18}O beams and studying the (^{18}O,^{18}Ne) double charge exchange transitions in the projectile, while the isospin lowering direction in the target has been explored using ^{20}Ne beams via the (^{20}Ne,^{20}O) DCE reaction (Cavallaro et al., 2020). For both classes of experiments, besides the DCE reaction channel, other scattering and reactions channels characterized by the same projectile and target at the same dynamical conditions have been studied. **Table 1** lists the reactions investigated in NUMEN Phase 2, together with the already available references to publication. **Figure 2** gives a comprehensive schematic representation of the already explored reactions, where also the involved target and residual nuclei are indicated.

A limited number of isotopes were selected as target systems in the Phase 2 experiments as result of a compromise between the interest of the scientific community to specific ββ emitter candidates and technical issues. These latter are also connected with the complex target production technologies and the expected energy resolution necessary to isolate the ground-to ground state transition in the DCE measured energy spectra.

The target isotopes explored via the (^{18}O,^{18}Ne) reaction at 15 MeV/u are ^{48}Ti, ^{76}Se, ^{116}Sn with the aim of studying the ^{48}Ti $\rightarrow$ ^{48}Ca, ^{76}Se $\rightarrow$ ^{76}Ge and ^{116}Sn $\rightarrow$ ^{116}Cd DCE transitions, respectively, together with the competing channels listed in **Table 1**. The ^{40}Ca $\rightarrow$ ^{40}Ar and ^{12}C $\rightarrow$ ^{12}Be transitions were also studied as test cases for the experimental and theoretical analyses at two different energies, 15 and 22 MeV/u. The measurements at very forward angles, including zero degree, were performed by placing the spectrometer optical axis at $+3^\circ$ with respect to the incident beam axis. Thanks to its large angular acceptance, the $-2^\circ < \theta_{lab} < +9^\circ$ range was explored. A specifically designed Faraday cup, located in a region aside the FPD, stopped the beam and measured the incident charge in each run for the determination of the absolute cross section.

The target isotopes explored by the (^{20}Ne,^{20}O) DCE reaction at 15 MeV/u are ^{116}Cd (to study the ^{116}Cd $\rightarrow$ ^{116}Sn transition), ^{130}Te (for ^{130}Te $\rightarrow$ ^{130}Xe) and ^{76}Ge (for ^{76}Ge $\rightarrow$ ^{76}Se). For these experiments, the spectrometer optical axis was typically placed at -3°, covering an angular range $-8^\circ < \theta_{lab} < +3^\circ$. A different Faraday cup, located in the high-magnetic-rigidity region aside the FPD was used in these experiments, as described in Cavallaro et al. (2020).

RECENT TECHNICAL ACHIEVEMENTS

Several recent accomplishments have been achieved by NUMEN, while it is moving from the intense experimental and R&D activity of Phase 2 toward the construction of the new upgraded elements. The evolution of the different aspects of the project, by means of laboratory tests on prototypes, simulations and the development of technical drawings is allowing for the continuous fine tuning of all the elements under study. In this section some of the most relevant new results are briefly presented.

Target Characterization

The NUMEN target system must face two main requirements: the first is related to the heat dissipation, the second is related to the energy resolution constraints (Cappuzzello et al., 2018).

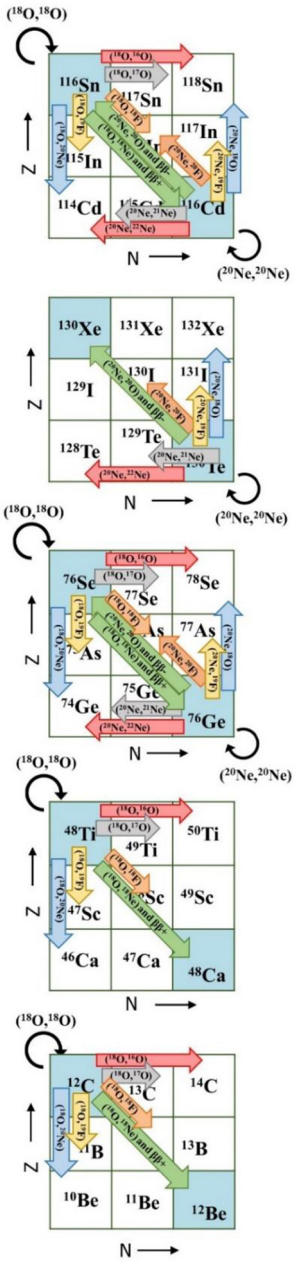

FIGURE 2 | Diagram of the reactions explored by the NUMEN project so far. The labels inside the arrows indicate the projectile-ejectile systems for each nuclear reaction channel, while the nuclei indicated in the squares are the target and residual systems populated by the reaction of the corresponding arrow.

The necessity of quickly dissipating the heat generated by the intense ion beam (up to 10^{13} pps) in the target led to a composite design of the target system. The isotopic material, required to build the target for DCE reactions, will be deposited on a substrate of Highly Oriented Pyrolytic Graphite (HOPG) (Iazzi et al., 2017; Pinna et al., 2020a). This type of graphite has a very high in-plane thermal conductivity, making this substrate

TABLE 2 | Target parameters extracted from RBS and APT measurements. See text.

Sample	$\bar{x}_{APT}$[nm]	*R* (APT) %	$\bar{x}_{RBS}$[nm]	Δ%
A25 (Ge)	530	6	535	1
B22 (Ge)	405	16	385	5
C11 (Ge)	350	6	535	1
A14 (Te)	430	6	425	1
B10 (Te)	435	11	415	4
C4 (Te)	435	1	420	4
A20 (Sn)	235	44	250	6
B4 (Sn)	230	68	260	12
C7 (Sn)	170	62	160	7

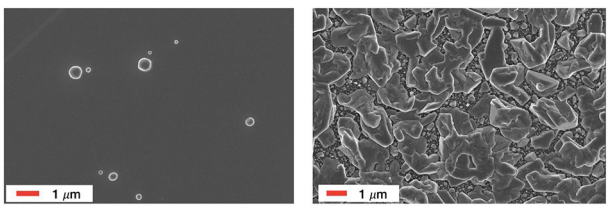

FIGURE 3 | FESEM images of the B22 (∼400 nm natural Germanium evaporated on 5 μm HOPG backing) (left) and B4 (∼250 nm natural Tin evaporated on 5 μm HOPG backing) (right) target samples.

able to quickly transfer the heat from the target center, hit by the ion beam, to the target extremities in contact with a cooled frame.

The energy resolution requirements of the NUMEN experiments limit the target thickness. Due to the interaction of the incident ions and the ejectiles produced by the nuclear reactions with the target material, energy dispersion and straggling occur proportionally to the target thickness. For this reason, the targets, including possible substrates, should be made as thin and uniform as possible. In addition, as discussed in Lo Presti et al. (2020) and in Section Radiation level, the amount of target material impacts on the overall radiation level in the MAGNEX experimental hall, during beam time operations and on the remnant activation afterward. Thus, a thinner target would be helpful also to mitigate this drawback. However, the reduction of the target thickness directly suppresses the yield collected in the experiments, which is a relevant issue especially for suppressed reaction channels such as DCE. A search for the optimal compromise depends on several aspects also connected to the chemical and thermodynamical properties of the involved materials. An extensive investigation of the problem leads us to target thickness in the range 250–450 nm for almost all the isotopes of interest and a few micrometers for the HOPG substrate.

The determination of the thickness of target and substrate is of crucial importance, as well as the knowledge of their thickness uniformity: the target system characterization is thus very important and has been subject of R&D study (Capirossi et al., 2020). In order to get as much information

as possible on the target samples and characterize the NUMEN target system, several analysis techniques have been adopted. In particular, Rutherford Backscattering Spectroscopy (RBS) and Alpha Particle Transmission (APT) techniques have been exploited to measure the thickness and the uniformity of target layer and substrate.

Both the techniques can provide precise evaluations of the average thickness of the sample, but only with APT the thickness uniformity can be quantified. The thickness obtained by APT can be verified with the RBS, while the quality of the isotopic layer deposition can be evaluated by studying the sample surface by Field Emission Scanning Electron Microscopy, which provides images of the sample surface topography.

The target thickness measurements with RBS and APT are listed in **Table 2**, together with the uniformity parameter R, defined as $R = \frac{\sigma_{nu}}{\overline{x}}$, where σ_{nu} is the standard deviation and $\overline{x}$ is the average value of the peak in the thickness distribution. The first column shows the labels of the target system prototypes. The first three rows are related to natural Germanium targets, the following three to natural Tellurium and the last three to natural Tin. The targets with labels beginning with the letter A, B and C have a HOPG substrate 10 μm, 5 μm and 2 μm thick, respectively. The fifth column indicates the parameter, calculated as the ratio $\Delta = \frac{\delta}{x}$, where δ is the difference and x is the average between the thickness measured by APT and RBS.

Table 2 shows that the agreement on the thickness evaluation between APT and RBS techniques is within 5% for all the Ge and Te targets. The stronger deviation for Sn targets is explained by their larger non-uniformity (from 44 to 68%), as confirmed by the comparison of the FESEM microscopies of B4 (Sn) and B22 (Ge) samples shown in **Figure 3**. From these images the better uniformity of the Germanium deposition in B22 can be easily appreciated if compared with the topography of the Tin deposition of B4. This difference is confirmed by the R values measured by APT, that highlight the good thickness uniformity of the B22 Germanium deposition.

To evaluate how the target characteristics affect the NUMEN energy resolution, a Monte Carlo code has been implemented, which simulates the DCE events and estimates the ejectiles energy distribution using the experimental measurements as input (Pinna et al., 2020b).

Uncertainties on the average target thickness will affect the measured DCE cross section while the non-uniformity will affect the energy resolution on the DCE reaction products. A typical thickness uncertainty of 5% can be expected from the thickness measurement itself, performed with APT or RBS. An additional systematic uncertainty of typically a few % from the energy loss model should also be considered. A total uncertainty on the average thickness of 6–7% can therefore be foreseen, which will affect directly the measured cross section. However, since the cross section is proportional to the square of the NME, the corresponding contribution to the NME uncertainty will be about a factor two smaller.

To illustrate the effects of the target non-uniformity on the energy resolution of the DCE reaction products, we consider depositions on a 2 μm thick HOPG backing and DCE reactions at 15 MeV/u. With the characteristics of the Ge and Te target prototypes presented in **Table 2**, i.e., an average thickness of ≈ 400 nm and a non-uniformity R ≈ 10%, the contribution to the energy resolution due to the target non-uniformity would be quite small [≈80 keV Full Width at Half Maximum (FWHM)] leading to an overall FWHM of ≈460 keV. Therefore, the present Ge and Te uniformity appears to be acceptable. Considering a Sn target with a thickness of ≈200 nm, the contribution to the resolution due to the measured non-uniformity (R ≈ 60%) would be ≈300 keV, for an overall estimated resolution of ≈ 510 keV. The latter value is comparable to the excitation energy of the first excited state of the residual nucleus, thus increasing the Sn thickness to typical values of 600–700 nm would not be feasible. Additional investigations are required to improve the uniformity of the Sn depositions.

More studies are currently ongoing, on one side, to improve the deposition technique of Sn and, on the other side, to extend the APT and RBS tests to the other targets of the NUMEN foreseen experiments.

Enhancement of MAGNEX Magnetic Elements

A key item for the accomplishment of the NUMEN project is the upgrade of MAGNEX optical elements to higher magnetic rigidity to allow the transport of ions at higher energy. In particular, to match the request of the NUMEN experimental program, the magnetic field has to be increased of about 20% from the presently achievable highest values, preserving the present magnetic field maps, important for the application of ray reconstruction techniques (Lazzaro et al., 2007, 2008a,b, 2009). The expected new maximum fields will be 1.380 T (+20%) for the dipole magnet and 1.139 T (+20%) for the quadrupole one.

The evaluated field in the central region of the medium plane of the dipole magnet is plotted in **Figure 4** as a function of the excitation current. The first blue dot represents the field at the maximum current supplied by the present power supply (920 A), while the red dot is the new maximum field of 1.38 T achievable with a circulating current of 1,160 A (+26%) in the existing pair of coils (120 turn per coils). The higher circulating current means about 59% more power dissipation with respect to the present. A significant upgrade of the cooling of the magnets coils is thus needed. The usual constraint to maintain the coils at maximum temperature of 70°C requires the increase of the water inlet pressure up to 8 bar, preserving the present cooling circuit. In this way, the water flow is enough to dissipate the higher thermal power and keep the water temperature rise below the safe value of 20°. Nonetheless, the higher pressure also means a higher speed of the water flow, which could reduce the coils life due to the mechanical abrasion of the copper from the inner surface of the coil. To mitigate this problem, a dedicated cooling circuit at 8 bar will be used only when higher current is needed while the existing circuit at 5 bar is used at lower currents.

An inspection of **Figure 4** makes it clear that raising the excitation current in the dipole coils does not generate a linear increase of the magnetic field, due to the saturation of parts of the magnet iron. Finite element calculations of the magnetic fields generated by the bending magnet show that almost all

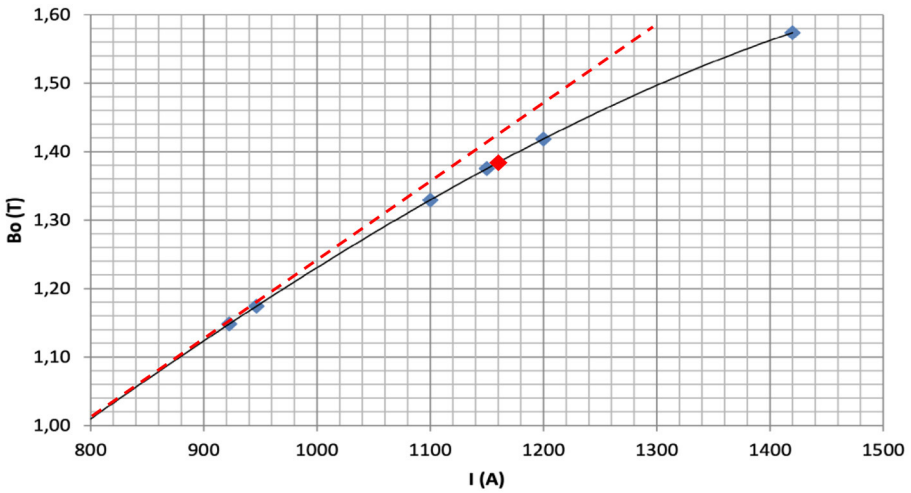

FIGURE 4 | Simulated field in the center of the dipole magnet as function of the excitation current. The red straight line emphasizes the deviation from linearity of the excitation curve.

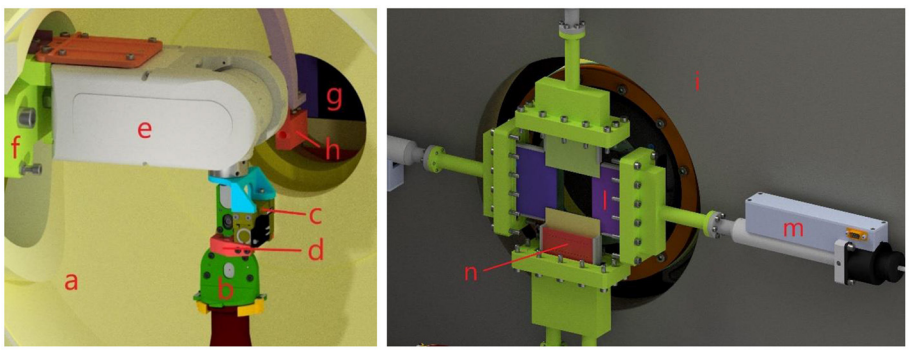

FIGURE 5 | Left: detail of the target manipulator end-effector. Inside the scattering chamber (a) the target-holder is connected to the cryo-cooler (b). A gripper (c) with its fingers (d) is used to disconnect the target-holder, which is rotated by a wrist (e) in horizontal position, then a pneumatic cylinder (f) moves the structure outside the chamber. During the automatic procedure, the Faraday cup (h) is aligned to the direction of the beam line in front of the slits system (g). Right: detail of the motorized slits system defining the MAGNEX acceptance at the entrance of the quadrupole magnet. The slits system is positioned upstream of the quadrupole shield (i) and it is composed by four screens (l) each one equipped with a linear drive (m). The "pepperpot" (n) is included in the lower part of this system.

the corners of the pole and part of the outer return yoke reach the saturation value of about 2 T. Because of saturation, the magnetic field over the pole surface is less uniform than at lower excitation. The existing MAGNEX surface coils will be used (Cunsolo et al., 2002; Cappuzzello et al., 2016) to compensate for the quadrupole (surface α-coil) and sextupole (surface β-coil) effects of the magnetic field at higher fields.

As also discussed in Section The new focal plane detector chamber, the MAGNEX surface α-coil has a key role for NUMEN, as it can generate a tunable positive or negative quadrupole-like field which effectively changes the focusing properties of the spectrometer, thus guaranteeing the fine focusing of the ejectiles onto the fixed FPD, according to the reaction kinematics (Cunsolo et al., 2002). However, due to the enhancement of the main field, also the surface coils need to be upgraded by allowing more current to flow through them and consequently more cooling. A detailed project for surface coils refurbishing in under way.

Finite elements simulations of the field distribution on the quadrupole magnet indicate that increasing the excitation current to 1,500 A (+50% with respect to the present maximum value), so as to achieve the requested gradient of 5.98 T/m (+20%), a sizable increase of the saturation is found. A further analysis of the high-order harmonics ($n > 2$) content in the field generated by the quadrupole magnet reveals that the main contribution comes from the $n = 6$ component, whose integrated strength is about 0.26% compared to the $n = 2$ and the trend is decreasing at increasing currents. Resembling the situation presented for the dipole magnet, also for the quadrupole an upgraded cooling system is demanded to remove the extra heat from the coils. A similar solution will be adopted with a complementary cooling system working at inlet pressure of 8 bar,

to maintain the water temperature increase below 20°C, to be used only when the experimental conditions require the highest excitation currents.

Due to the high-power request by the power supplies for the dipole and quadrupole magnets, 350 and 540 kW respectively, the overall electromagnetic noise induced by these elements could significantly interfere with sensitive electronic devices working in the MAGNEX hall. In particular, high sensitive charge pre-amplifiers coupled to the FPD detectors, are affected by high frequency components (>10 kHz) of the noise. Specific tests with different kinds of power supplies have been performed to characterize different sources of high-frequency electromagnetic induced and conducted noise. Results compliant with NUMEN specifications were found only with linear power supplies with series transistor banks. Based on these results, new power supplies with currents and voltages of 1,250 A, 280 V and 1,500 A, 360 V need to be built for the dipole and quadrupole magnets, respectively.

A New Scattering Chamber

A new scattering chamber matching the physics goal of the NUMEN experiment is under design according to the requirements coming from the upgrade of the MAGNEX spectrometer. As a main condition the chamber must cope with high intensity beam (10^{13} pps) still leaving the possibility to work with lower intensity beams (10^{11} pps).

To meet this request, two alternative beam lines, positioned at an angle of 70° to each other and pointing to the object point of the spectrometer, are foreseen. The scattering chamber, installed on the MAGNEX rotating platform, can be alternatively connected to each of the beam lines.

Additional rotations of the MAGNEX spectrometer with respect to the two beam line directions are obtained with two different mechanical systems according to the angular range to be explored in the NUMEN experiments. In the case of high intensity beams, a suitable mechanical bellows guarantees small rotations around two fixed angles (+3° and −3°) of the spectrometer optical axis. For low intensity beams, a sliding seal window allows continuous rotation of the optical axis in the −5–+25° angular range. Both systems guarantee to keep the high vacuum (10^{-6} mbar) in the chamber requested by the experiments. Inside the chamber, the target is supported by a holder, about 100 mm height, made of copper and shaped to include also slots for the beam monitoring devices. It should be noticed that the axis of the scattering chamber corresponds to the MAGNEX supporting platform fulcrum and, whatever chamber rotation is obtained, the target will be keeping its position, offering its surface to the normal incidence of the ion beam.

The target holder (Sartirana et al., 2020) is mounted over the cold finger of a vertical cryo-cooler, which maintains it at low temperature (∼40 K). A specific actuator below the cryo-cooler guarantees the movement of the target holder and fine alignment of the target to the beam axis (<200 μm).

Since a not negligible radiation level is foreseen in the scattering chamber, a significant activation of the target and its frame is expected, making its automatic handling necessary. A manipulator has been studied (Sartirana et al., 2020) in order to be placed outside the chamber at 90° with respect the beam line. The device is provided with a wrist featuring two degrees of freedom and when in position it clamps the target holder by the help of a pneumatic gripper and rotates it to disconnect from the cold finger (**Figure 5**-left). A bayonet coupling between the target holder and the cold finger facilitates the automatic procedure. A temporary storage outside the scattering chamber is used to collect up to 6 different targets.

The products from beam-target interactions are preferentially emitted in the forward direction together with the unreacted beam. A dedicated system, downstream the target, composed of two pairs of motorized slits, is implemented to further define the aperture of the spectrometer both in vertical and horizontal directions by limiting its acceptance within a maximum of ±7.5° in vertical direction and ±6.5° in horizontal one. The slits are made of 2 mm thick tantalum, each one controlled by a dedicated linear driver. The right panel of **Figure 5** shows the 3D CAD drawing of the motorized slit system. In addition, immediately upstream of the slit system, a "pepperpot" screen can be inserted by a dedicated linear driver along the beam for trajectory calibration purposes. It is made of tantalum and it features a matrix of holes 13 x 5, each of 1 mm diameter.

A Faraday cup (**Figure 5**-Left) has to be installed in the chamber for beam diagnostics purposes and to measure the integrated charge of the ion beam in the low intensity configuration. The system is inserted by the top of the scattering chamber and it is rotated in the measurement position (i.e., 0°) only if needed, otherwise it is kept at one side.

To keep the vacuum inside the chamber, the described components require static or dynamic sealing, with the further condition to guarantee an adequate radiation tolerance. This is obtained by applying rings of copper, elastomer or specific solutions as Helicoflex seals.

The New Focal Plane Detector Chamber

A challenging mechanical component for NUMEN is the new vacuum chamber containing the new FPD. A 3D model of these elements is shown in **Figure 6**. The chamber is coupled to the dipole magnet chamber by a large rectangular gate valve (800 × 230 mm internal clearance) to separate the magnets and focal plane volumes when different residual pressures are needed. This component also ensures the interchangeability of the new chamber with the existing one in MAGNEX.

Resembling the present chamber of the MAGNEX FPD (Torresi et al., 2021), the height of the new one will be kept larger than 230 mm to avoid interference with ion trajectories. On the other hand, the new chamber will have a larger width to allow both the ^{18}O and ^{20}Ne unreacted ion beams to be transported out of the spectrometer toward the beam dump lines, located besides the FPD. To guarantee the transmission of heavy ions toward the FPD and of the beam toward the beam dump lines a residual pressure in the range 10^{-5}-10^{-6} mbar has to be preserved.

The vacuum chamber houses the FPD that is filled with isobutane, featuring an absolute pressure of few tens of mbar. Specific internal walls separate the gas-filled region of the FPD from the chamber lateral regions under vacuum where the unreacted ion beams are directed toward the beam dump lines. A

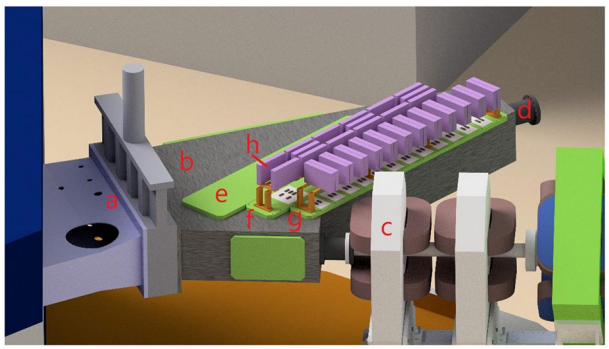

FIGURE 6 | The new design of the MAGNEX FPD. The gate valve at the dipole exit **(a)** is connected to the new FPD chamber **(b)**. This structure connects alternatively with ^{20}Ne and ^{18}O beam dump lines [**(c,d)**, respectively]; here the ^{20}Ne beam dump line configuration **(c)** is shown. On the top of the chamber three different flanges are present: one for the FPD Mylar window maintenance **(e)**, the second for the tracker and its electronics **(f)**, the last one for the PID wall **(g)**. The boxes on the top of these flanges contain the preamplifier circuits **(h)**.

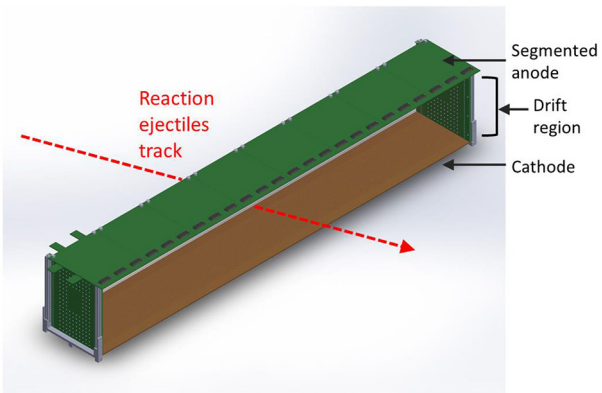

FIGURE 7 | Rendering of the full-size tracker cage that will be installed in FPD chamber.

very thin (few μm) Mylar window contains the isobutane within the FPD minimizing the material along the paths of the ions entering in the FPD. The FPD entrance window is tilted with an angle of 59° from the rectangular gate valve.

The window will be 150 mm high, and 920 mm large, thus slightly shorter than for the present detector (200 × 920 mm) (Torresi et al., 2021), reducing the overall ejectile transmission efficiency by about 10%. This guarantees compliance with the new FPD geometry (see Section The FPD gas tracker), and with the constraint from the beam transport outside the FPD chamber.

Contrary to the present FPD, the new one is not designed to move along the optical axis due to the mechanical limitation imposed by the first magnetic elements of the two beam dump lines. This prevents the possible fine focusing of the reaction products, by moving the FPD along the optical axis direction depending on the specific reaction kinematics (Cunsolo et al., 2002). Instead, as discussed in Section Enhancement of MAGNEX magnetic elements, the fine focusing of the reaction products is performed using the MAGNEX dipole surface α-coil (Cunsolo et al., 2002).

The new gas tracker and PID system, which constitute the active elements of the FPD (see Sections The FPD gas tracker and The particle identification system) are suspended to metal flanges sealed on the vacuum chamber top. Short coaxial cables are routed toward the detectors inside the FPD through SAMTEC multipin connectors, soldered on PCB boards present on each flange. This allows for independent and fast extraction and insertion of both systems from the chamber in case of need. Pre-amplifiers (CAEN MOD. 1429) are positioned on the top of these supporting flanges, outside the vacuum region. Long coaxial cables connect the front-end electronics to the read-out based on CAEN VX2740 multichannel digitizers (Finocchiaro et al., 2020). For the maintenance, each flange with pre-amplifiers circuits and suspended detectors will be hooked and lifted by a dedicated lifting system, positioned on board of the MAGNEX platform, in order to be placed on a stand near the spectrometer. The same lifting system will work on a third flange on the top of the vacuum chamber that allows the installation of the mylar window.

The FPD Gas Tracker

The aim of the FPD-gas tracker is to provide a precise and accurate three-dimensional tracking of the particles crossing the focal plane. Two characteristics for the gas tracker are required by the NUMEN project.

The first is a high resolution measurement of the phase space parameters of the ion tracks at the focal plane: X_{foc}, Y_{foc}, θ_{foc}, ϕ_{foc}, where X_{foc} is the horizontal coordinate (dispersive direction in the focal plane), θ_{foc} the horizontal angle, Y_{foc} the vertical coordinate and ϕ_{foc} the vertical angle. The required resolution is lower than 0.6 mm that for X_{foc} and Y_{foc} and lower than 5 mr for θ_{foc} and ϕ_{foc}. This requirement is of fundamental importance because the precise and accurate particle ray reconstruction is mandatory for the determination of the momentum vector at the target position that, in turn, translates in scattering angle and particle energy.

The second requirement is to withstand the expected high rate of impinging particles. The particle rate density along the 92 cm horizontal aperture of the FPD at full intensity is foreseen to be about 50 kHz/cm. The tracker should be able to cope with such a high rate managing to disentangle the track of each detected particle and maintain the required resolutions on the phase space parameters. For that reason, particular care has been devoted to the choice of the multiplication stage. Among all the Micro-Pattern Gas Detector types (MPGD), the multiple THick Gas Electron Multipliers (THGEM) have been chosen because, based on PCB technology, they are mechanically robust, easy to build and to handle, and economical. Moreover, the choice of multiple THGEM in place of a single one is motivated by the higher gain achievable at fixed operational voltage, which allows to reduce the voltage thus ensuring a better stability and longer average life.

The working principles of the adopted solution and first results from a reduced size prototype of the tracker can be found in Finocchiaro et al. (2020). As the focus of the present article is on recent advancements, two aspects need to be specifically

considered. First, a new full-scale project of the tracker assembly, based on the prototype adopted solutions, is now available, as shown in **Figure 7**.

The volume of the new detector, filled with gas (e.g., isobutane at a typical pressure of few tens of mbar), will be 1,200 × 185 × 118 mm^3. When an ionizing particle crosses the volume it generates a track of primary electrons and positive ions. Under the effect of a uniform electric field, the electrons drift, at constant velocity, toward the multiplication stage that is based on multiple THGEM (Sauli, 2016; Cortesi et al., 2017) that can easily cope with the expected rate of particles. The strong electric field inside the THGEM induces charge multiplication, generating electron jets, which are directed toward the anode.

Second, a new anode, segmented in small pads with size of 5 × 10 mm^2 was designed and is presently under construction. Compared to the previous anode the new one allows for an easier track reconstruction, especially at high rate, where ambiguities to the assignment of the detector signals to a specific event could be an important issue. **Figure 8** shows a sketch of one of the four modules which will be mounted side-by side in the new anode. The pads are arranged in five rows each one made of more than 200 units. Neighboring rows of pads are spaced by 10 mm. In this way the ion track is sampled in five positions inside the tracker. Knowing which pads are hit by the electrons and the total collected charge it is possible to extract the two-dimensional projection of the track on the horizontal plane X-Z with a submillimeter precision. The vertical coordinate Y_{foc} is determined by the measurement of the electron drift times. This corresponds to the interval between the signal-over-threshold time generated by the ion on a SiC detector (see Section The particle identification system) and the signal-over-threshold time generated by secondary electrons on the anodic pads. In this way a full three-dimensional track is obtained on an event-by-event basis.

The Particle Identification System

The ejectiles to be identified in the NUMEN experiments are typically in the mass region $10 < A < 25$ and atomic number $4 < Z < 12$. Due to the interaction with the target (Cavallaro et al., 2019), ions characterized by different charge states (q) are distributed at the focal plane for each isotope species, making the ion identification more challenging. The adopted technique for particle identification (PID) with MAGNEX, described in Cappuzzello et al. (2010), Calabrese et al. (2018), guarantees a clear selection of the ions of interest in the whole range of A and Z produced in the collision, provided that precise measurements of the energy loss (ΔE), the residual energy (E_r) and the horizontal position at the focus (X_{foc}) are available.

In the new MAGNEX FPD, the gas tracker will provide accurate measurement of the X_{foc} parameter, while ΔE and E_r are obtained from a dedicated array of two-stage telescopes of Silicon Carbide (SiC) (Tudisco et al., 2018) and Tallium doped Cesium Iodide CsI(Tl) detectors. The active area of each element is 1.5 × 1.5 cm, with 0.2 mm dead space between adjacent cells. The SiC detector is 100 μm thick and measures ΔE. The CsI(Tl) inorganic scintillator is 5 mm thick and is coupled to a Hamamatsu S3590 photodiode of 1 × 1 cm area to measure E_r.

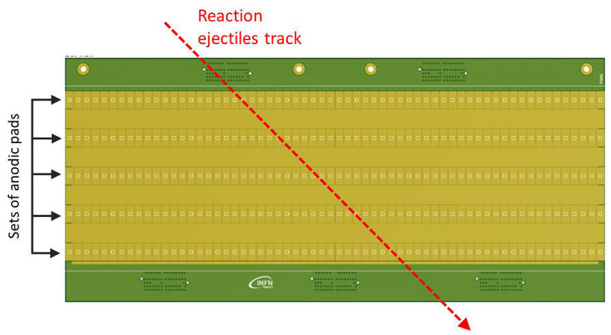

FIGURE 8 | CAD drawing of one module of the new anode of the MAGNEX FPD for NUMEN.

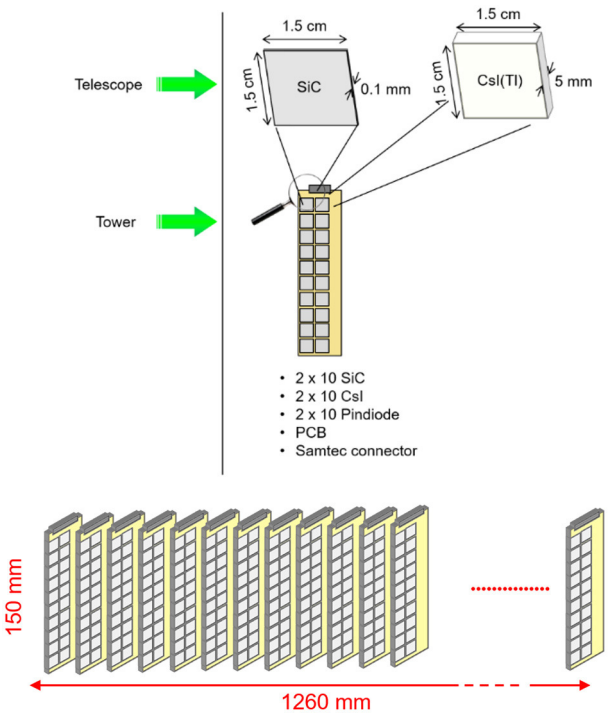

FIGURE 9 | Top: mechanical arrangement of the PID detector telescopes. The telescopes are arranged into *towers*, each one consisting of 20 units. Bottom: mechanical arrangement of the PID *towers*. The full focal plane is covered by 36 towers rotated by 35° around the vertical axis (see text).

The capabilities of the system in terms of radiation hardness and mass resolution are discussed in Finocchiaro et al. (2020). A new mechanical arrangement of the telescopes is presented here, as a result of optimization of the detection efficiency and the mechanical integration. Indeed, in the configuration shown in Finocchiaro et al. (2020), the central region of the vertical coordinate (Y_{foc}∼0) was not covered as it corresponded to the dead region between two vertical modules. This would have determined a relevant efficiency loss, since close to the MAGNEX symmetry plane ($Y_{foc} \sim 0$) the ion rate is maximum (see for e.g.,

Cappuzzello et al., 2014; Carbone, 2015). For this reason, in the new geometry, shown in **Figure 9**, the telescopes are arranged in *towers* (10 rows and 2 columns each) in order to avoid efficiency losses for $Y_{foc} \sim 0$. From the mechanical point of view, with this new configuration the towers can be precisely mounted and easily attached on the top flange of the FPD chamber (see Section The new focal plane detector chamber) by means of a mechanical stand, making also the mounting and maintenance procedures more comfortable. A PCB board houses the pin diodes on top of which CsI(Tl) crystals are glued. A copper grid is placed on the top of the crystals over which the SiC detectors can be glued. The signals are collected and sent to the front-end electronics (Caen V1429 64-channel pre-amplifiers) by means of a connector on the top of each tower (see **Figure 9**-top). The readout is performed using 64-channel digitizers (Caen VX2740), as described in Ref. (Finocchiaro et al., 2020). Since the MAGNEX FPD is rotated around the vertical axis by 59° with respect to the plane normal to the optical (Cunsolo et al., 2002), the towers are also rotated of about 35° around the vertical axis, in order to minimize the differences in the path length inside the detectors. GEANT4 simulations show that such an arrangement moreover avoids that unwanted neutron and γ-ray fluxes, produced by the interaction of the ejectiles with one SiC-CsI(Tl) telescope, could interfere with the telescope beyond. With the present geometry the full length of the FPD will be covered by 36 PID towers, placed downstream of the tracker, for a total of 720 telescopes.

The G-NUMEN Gamma Spectrometer Array

The typical energy resolution for a NUMEN experiment is around 500 keV (FWHM) at 15 MeV/u beam energies, which is sufficient for the separation of the low-lying excited states and ground state of the fragments of the DCE reaction in some near-spherical target mass regions. However, this is not the case for deformed nuclei, for which the low-lying states appear well-below 500 keV, and for all cases at high beam energies (around 30 MeV/u or above) since there is a significant contribution from the accelerated beam energy resolution itself (0.1%) and from the MAGNEX optics (0.1%). To allow for the separate determination of the cross sections of the ground-state and first excited states of both the projectile (PLF) and the target (TLF) fragments of the DCE nuclear reaction, an array of gamma-ray detectors will be used (Oliveira et al., 2018). The gamma rays will be detected in coincidence with the PLF, identified at the MAGNEX focal plane. With an energy resolution at least one order of magnitude better than the best ones achievable with MAGNEX under NUMEN experiment conditions, it should be possible to separate the close-to-ground state transitions and therefore measure their cross sections.

This gamma array must fulfill a series of requirements, besides guaranteeing sufficient energy resolution. It should have a high photo-peak detection efficiency, due to the minute DCE cross sections expected, the detectors should be tolerant to a high radiation field of gamma rays and neutrons, due to the interaction of high intensity beam with the target and tolerate high counting rates. The timing resolution should also be high enough to clearly separate events from subsequent accelerated beam bunches. In order to meet those requirements, an inorganic scintillator array

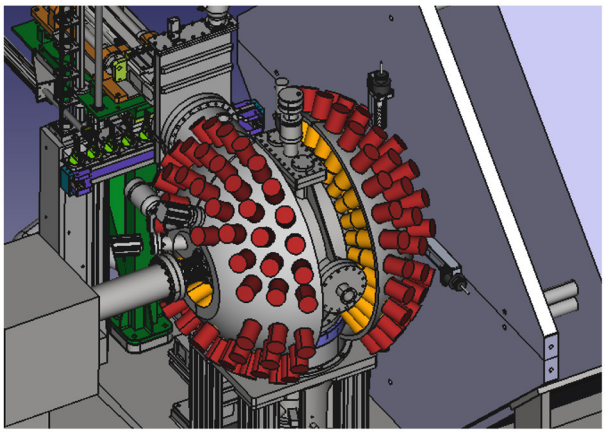

FIGURE 10 | The G-NUMEN gamma spectrometer disposed around the MAGNEX scattering chamber.

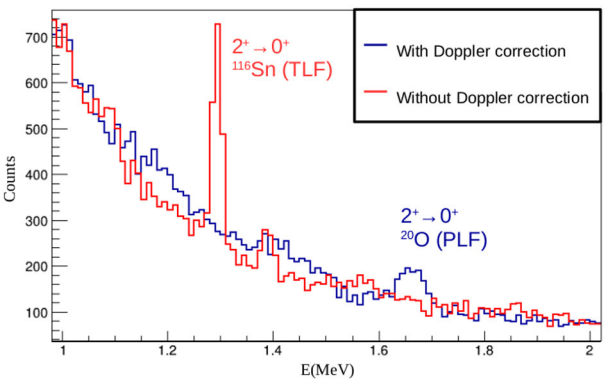

FIGURE 11 | Simulation of the G-NUMEN γ-ray spectra for transitions to low-lying states of a typical DCE experiment.

with large angular coverage (as high as possible, given the limitations imposed by the peripheral equipment around the scattering chamber) and high granularity, to control pulse pile up, was envisaged. The $LaBr_3$(Ce) scintillator was chosen among inorganic scintillators due to its high radiation tolerance and fast timing response, high photopeak intrinsic efficiency and excellent energy resolution. The scintillator crystals will be coupled to standard photomultiplier tubes due to the fast response and good radiation tolerance of these devices. **Figure 10** presents a CAD sketch of the gamma detector array, mounted around the scattering chamber.

The dimensions of the crystals will be 38 mm diameter and 50 mm length, and their faces will be at about 245 mm distance from the target. The detectors will be disposed in rings between 43 and 149 degrees to the beam direction, covering a total solid angle of 20% of the unit sphere. The expected total photopeak efficiency of the array will be near 4%, and the energy resolution around 3%, at 1.3 MeV gamma-ray energy. The expected timing resolution should be under 1 ns. This is important to separate

the PLF-gamma coincident events from the huge background of gamma rays from all other nuclear reactions with the beam and target combination of the experiment.

Extensive GEANT4 simulations (Agostinelli et al., 2003; Folger et al., 2004; Allison et al., 2006, 2016; Oliveira et al., 2020), based on the BIC (binary intra-nuclear cascade) model of the reaction were performed in order to evaluate this background. The results indicate that cross sections as low as 1 nb, can be measured with uncertainties of the order of 10%, using a beam intensity of the order of 10^{12} beam particles per second on typical targets with tenths of mg/cm^2 surface density in month-long experiments. Typical gamma count rates of 300 kHz are expected for each detector. The beam intensity is limited to that order of magnitude by pile-up effects and simultaneous occurrence of more than one nuclear reaction within the same beam pulse, which makes the gamma event time virtually undistinguishable.

Figure 11 presents the simulated gamma-ray spectra for the reaction case of ^{116}Cd(^{20}Ne,^{20}O) at 300 MeV. It illustrates the presence of background under the transitions from the first excited states of the target-like fragment (TLF) and the projectile-like fragment (PLF—with Doppler correction which is quite significant for this case), at the high beam current conditions. This background is comparatively negligible at low beam currents. The data acquisition will be performed with CAEN digitizers (VX2740). The possibility to do on-line particle-gamma coincidences with these modules is being explored in view of possible mitigation of data storage space issues during experiments.

Radiation Level

The knowledge of the radiation level expected inside the MAGNEX experimental hall is of paramount importance since high rates of neutron and gamma-rays could spoil the performance of the electronic devices and of the detectors used in the MAGNEX FPD. Dedicated Monte Carlo simulations for the radiation background at the MAGNEX facility have been performed using the FLUKA code (Ferrari et al., 2005; Vlachoudis, 2009; Bohlen et al., 2014). A schematic geometry of the experimental room was implemented in the simulations as shown in **Figure 12**. In the present study, three main radiation sources were considered, namely:

- The interaction of the beam particles with the target material
- The interaction of beam particles with the beam stopper inside the beam dump
- A hypothetical 10W power loss in the beam intensity along the beam line. This is a conservative assumption (0.5% of the maximum beam power) to describe the possible source of radiation represented by the interaction of beam halos with the vacuum pipes of the magnetic elements located at the exit of the FPD (see Section The new focal plane detector chamber).

The simulation was performed following the prescription of Ref. (Lo Presti et al., 2020). In more details, a ^{20}Ne^{10+} beam at the energy of 60 MeV/u with an intensity of 2 kW ($\sim 1 \times 10^{13}$ pps) was directed onto a 214 μg/cm^2 thick ^{76}Ge target followed by a 2 μm thick ^{12}C layer. The simulated neutron flux, measured at the FPD (see **Figure 12**), is presented in **Figure 13** with the dashed green-line. Further on, a loss of 10 W along the beam line toward the beam dump was also considered in our simulations. This loss is assumed to occur at the position where the second steerer magnet will be installed (indicated with a blue cross in **Figure 12**). In this case, a substantial increase in the radiation level in the vicinity of the FPD is found. In the last part of our simulations, the ^{20}Ne beam was directed into the beam dump, stopped in a thick Ag target. The beam dump is confined into a (5 × 5 × 3) m^3 Portland concrete cube, providing thus an effective shield against neutron and gamma radiation.

Considering the contribution of the radiation sources mentioned above, the distribution of the simulated neutron flux

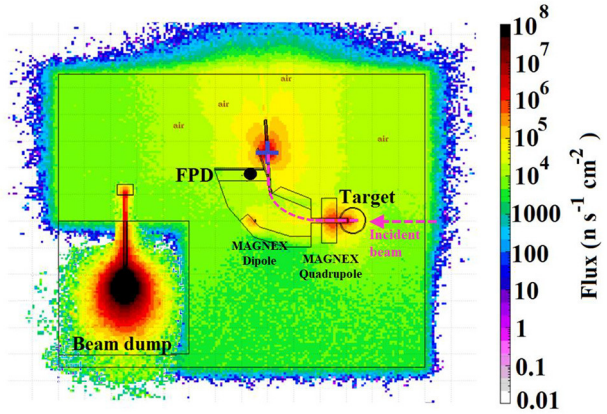

FIGURE 12 | Estimated neutron flux inside the MAGNEX experimental hall via FLUKA simulations. The result is obtained considering three radiation sources namely the beam-target interaction, the beam dump and a 10W loss of the beam power close to the MAGNEX FPD. The detector used in the simulation is indicated by a filled black circle, while the position where the 10 W loss occurs is indicated with the blue cross (see text for details).

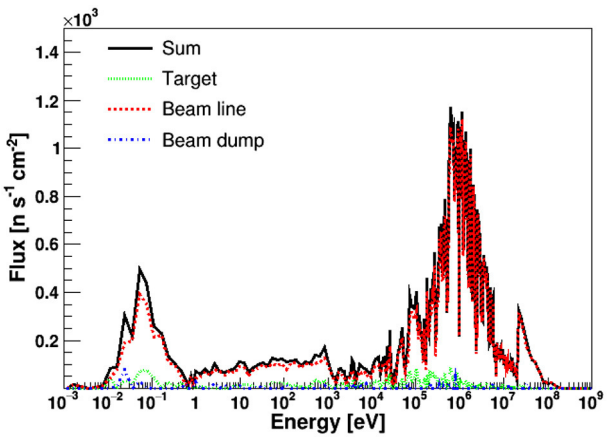

FIGURE 13 | Simulated neutron energy spectra at the MAGNEX FPD region. The contributions from the beam-target interaction, the beam dump and the 10W loss along the beam line are denoted by the dotted green, dotted-dashed blue and dashed red lines, respectively. The sum of the three contributions is presented with the solid black line.

inside the experimental hall is given in **Figure 12**, while the corresponding energy spectra are shown in **Figure 13**. The total integrated neutron flux is $7.2*10^4$ $n*s^{-1}*cm^{-2}$, dominated by fast neutrons above 100 keV.

Both **Figures 12**, **13** show that the main contribution to the neutron flux in the FPD region comes from the possible scattering of the beam into the beam pipe close to the FPD. Therefore, a detailed study of the beam transport is in progress in order to quantify the beam losses in such area and reduce them to tolerable values. Moreover, a substantial reduction of the neutron flux is expected by the introduction of proper shields to the detectors and electronics, which are also presently under study.

CONCLUSION AND PERSPECTIVES

Pioneering experimental campaigns, using the (^{18}O,^{18}Ne) and (^{20}Ne,^{20}O) DCE reactions on a few isotope candidates for 0νββ-decay, have been recently performed at INFN-LNS Laboratory by the NUMEN collaboration. The data analysis is ongoing, with preliminary results showing that accurate DCE cross sections measurements can be extracted at very forward angles for the ground-to-ground state transitions. In the experiments a wide net of direct reactions, generated by the beam-target interaction was also explored, providing additional information useful to characterize the complicated many-body nature of the involved nuclei as well as the reaction mechanisms.

The measurement of DCE absolute cross sections and the extraction of relevant NMEs is the main objective of the NUMEN project. An ambitious goal of NUMEN is to investigate the link between NMEs extracted from DCE reactions and those characterizing 0νββ decay. In this perspective, NUMEN is proposing an original experimental and theoretical approach to 0νββ decay NMEs that could contribute to the extraction of the absolute value of neutrino average mass from the expected observation of this rare decay.

The systematic exploration of all 0νββ decay candidate isotopes is highly desirable for neutrino physics and NUMEN is fully committed to pursue this ambitious goal. However, despite the first promising results achieved to date, much remains to be done toward the determination of NME for 0νββ decay, with the necessary accuracy to foster the neutrino physics.

As described in this paper, the project promotes a major and widely distributed upgrade of the INFN–LNS research facility in view of a significant increase of the beam intensity. As a consequence, several aspects of the technology involved in heavy ion collision experiments demand for challenging R&D.

The acceleration of heavy ion beams required by the NUMEN experiments in the regime of kW power and at energies from 15 to 70 MeV/u leads to substantial changes in the adopted technologies to extract the beam from the INFN-LNS Superconducting Cyclotron. The transport of such beams poses important radioprotection issues which requires a careful evaluation of radiation levels also involving the effects on detectors, electronics and various equipment. A critical aspect is the design of isotopically-enriched, thin and uniform targets for DCE experiments, considering the deterioration due to the dissipation of the enormous amount of heat deposited by the ion beam. The copious production of reaction products emerging from the target makes the present detectors of the MAGNEX spectrometer unfit for this application. A dedicated study of new classes of detectors, coping with the expected high rate and high fluency, still preserving the high resolution and sensitivity of the present ones is mandatory. This includes the search of new materials, the study of new electronics and DAQ systems, matching the rather stringent experimental requests and a complex mechanical integration of all parts, accounting for the limitation on human activities in the experimental hall due to radioprotection issues. Such R&D activity is a fundamental aspect of the NUMEN project, already supported by INFN to move to its construction phase.

In perspective, NUMEN aims at giving an innovative contribution in one of the most promising fields of fundamental physics. It indicates also a new avenue for heavy ion physics in synergy with neutrino physics with possible fallout in other research fields as well as in technological developments.

DATA AVAILABILITY STATEMENT

The raw data supporting the conclusions of this article will be made available by the authors, without undue reservation.

AUTHOR CONTRIBUTIONS

All authors listed have made a substantial, direct and intellectual contribution to the work, and approved it for publication.

FUNDING

The NUMEN project is mainly funded by INFN. Additional funds come from the Italian Ministry of University and Research (MIUR) under the *FARE Ricerca in Italia* program, with grant number R16HXFTMCT and acronym TEBE (SC and MF contracts are paid under TEBE). This project has also received funding from the European Research Council (ERC) under the European Union's Horizon 2020 research and innovation program, NURE project, grant agreement No. 714625 (The contracts of DT and FD are totally paid under NURE. The contracts of MC and FC are partly paid under NURE). JO acknowledges support from Fundação de Amparo à pesquisa no Estado de São Paulo, (FAPESP SPRINT grant proc. 2017/50160-5). LA and EC acknowledge support from DGAPA-UNAM IN107820, AG101120, and CONACyT 314857.

REFERENCES

Agodi, C., Cappuzzello, F., Cavallaro, M., Bondì, M., Carbone, D., Cunsolo, A., et al. (2015). Heavy ions double charge exchange reactions: towards the 0νββ nuclear matrix element determination. *Nucl. Part Phys. Proc*. 265, 28–30. doi: 10.1016/j.nuclphysbps.2015.06.007

Agodi, C., Russo, A. D., Calabretta, L., D'Agostino, G., Cappuzzello, F., Cavallaro, M., et al. (2021). The NUMEN project towards new experiments with high intensity beams. *Universe* 7:72. doi: 10.3390/universe7030072

Agostinelli, S., Allison, J., Amako, K., Apostolakis, J., Araujo, H., Arce, P., et al. (2003). Geant4—a simulation toolkit. *Nucl. Instr. Method A* 506:250. doi: 10.1016/S0168-9002(03)01368-8

Allison, J., Amako, K., Apostolakis, J., Araujo, H., Arce Dubois, P., Asai, M., et al. (2006). Geant4 developments and applications. *IEEE Trans. Nucl. Sci*. 53:270. doi: 10.1109/TNS.2006.869826

Allison, J., Amako, K., Apostolakis, J., Arce, P., Asai, M., Aso, T., et al. (2016). Recent developments in Geant4. *Nucl. Instr. Method A* 835:186. doi: 10.1016/j.nima.2016.06.125

Barea, J., Kotila, J., and Iachello, F. (2013). Nuclear matrix elements for double-β decay. *Phys. Rev. C* 87:014315. doi: 10.1103/PhysRevC.87.014315

Bellone, J. I., Burrello, S., Colonna, M., Lay, J.-A., and Lenske, H. (2020). Two-step description of heavy ion double charge exchange reactions. *Phys. Lett. B* 807:135528. doi: 10.1016/j.physletb.2020.135528

Bohlen, T. T., Cerutti, F., Chin, M. P. W., Fassò, A., Ferrari, A., Ortega, P. G., et al. (2014). The FLUKA code: developments and challenges for high energy and medical applications. *Nucl. Data Sheets* 120:211. doi: 10.1016/j.nds.2014.07.049

Calabrese, S., Cappuzzello, F., Carbone, D., Cavallaro, M., Agodi, C., Acosta, L., et al. (2018). First measurement of the 116Cd(20Ne,20O)116Sn. *Acta Phys. Pol. B* 49:275. doi: 10.5506/APhysPolB.49.275

Calabrese, S., Cappuzzello, F., Carbone, D., Cavallaro, M., Agodi, C., Torresi, D., et al. (2020). Analysis of the background on cross section measurements with the MAGNEX. *Nucl. Inst. Method Phys. Res. A* 980:164500. doi: 10.1016/j.nima.2020.164500

Capirossi, V., Delaunay, F., Iazzi, F., Pinna, F., Calvo, D., Fisichella, M., et al. (2020). Thickness and uniformity characterization of thin targets for intense ion beam experiments. *Acta Phys. Pol. B* 51:661. doi: 10.5506/APhysPolB.51.661

Cappuzzello, F., and Agodi, C. (2021). The NUMEN project: shedding light on neutrinoless double beta decay by heavy-ion nuclear reactions. *Nucl. Phys. News*. 31. doi: 10.1080/10619127.2021.1881368

Cappuzzello, F., Agodi, C., Bondì, M., Carbone, D., Cavallaro, M., Cunsolo, A., et al.. (2014). A broad angular-range measurement of elastic and inelastic scatterings in the 16O on 27Al reaction at 17.5 MeV/u. *Nucl. Instr. Method A* 763:314. doi: 10.1016/j.nima.2014.06.058

Cappuzzello, F., Agodi, C., Bondì, M., Carbone, D., Cavallaro, M., and Foti, A. (2015a). The role of nuclear reactions in the problem of 0νββ decay and the NUMEN project at INFN-LNSJ. *Phys. Conf. Ser*. 630:012018. doi: 10.1088/1742-6596/630/1/012018

Cappuzzello, F., Agodi, C., Carbone, D., and Cavallaro, M. (2016). The MAGNEX spectrometer: results and perspectives. *Eur. Phys. J. A* 52:167. doi: 10.1140/epja/i2016-16167-1

Cappuzzello, F., Agodi, C., Cavallaro, M., Carbone, D., Tudisco, S., Lo Presti, D., et al.. (2018). The NUMEN project: NUclear matrix elements. *Eur. Phys. J. A* 54:72. doi: 10.1140/epja/i2018-12509-3

Cappuzzello, F., Carbone, D., and Cavallaro, M. (2011). Measuring the ions momentum vector with a large acceptance magnetic spectrometer. *Nucl. Instr. Method A* 638:74. doi: 10.1016/j.nima.2011.02.045

Cappuzzello, F., Carbone, D., Cavallaro, M., Bondì, M., Agodi, C., Azaiez, F., et al. (2015c). Signatures of the giant pairing vibration in the 14C and 15C atomic nuclei. *Nat. Comm*. 6:6743. doi: 10.1038/ncomms7743

Cappuzzello, F., Carbone, D., Cavallaro, M., Spatafora, A., Ferreira, J. L., Agodi, C., et al. (2021). Confirmation of giant pairing vibration evidence in 12,13C(18O,16O)14,15C reactions at 275 MeV. *Eur. Phys. J. A* 57:34. doi: 10.1140/epja/s10050-021-00345-7

Cappuzzello, F., and Cavallaro, M. (2020). Nuclear response to second-order isospin probes in connection to double beta decay. *Universe*. 6:217. doi: 10.3390/universe6110217

Cappuzzello, F., Cavallaro, M., Agodi, C., Bondì, M., Carbone, D., Cunsolo, A., et al. (2015b). Heavy-ion double charge exchange reactions: a tool toward 0nbb nuclear matrix elements. *Eur. Phys. J. A* 51:145. doi: 10.1140/epja/i2015-15145-5

Cappuzzello, F., Cavallaro, M., Cunsolo, A., Foti, A., Carbone, D., Orrigo, S. E. A., et al. (2010). A particle identification technique for large acceptance spectrometers. *Nucl. Instr. Method A* 621:419. doi: 10.1016/j.nima.2010.05.027

Cappuzzello, F., Lenske, H., Cunsolo, A., Beaumel, D., et al.. (2004). Analysis of the 11B(7Li, 7Be)11Be reaction at 57 MeV in a microscopic approach. *Nucl. Phys. A* 739, 30–56. doi: 10.1016/j.nuclphysa.2004.03.221

Carbone, D. (2015). Signals of the giant pairing vibration in 14C and 15C nuclei populated by (18O,16O) two-neutron transfer reactions. *Eur. Phys. J. Plus* 130:43. doi: 10.1140/epjp/i2015-15143-0

Carbone, D., Cappuzzello, F., and Cavallaro, M. (2012). Universal algorithm for the analysis of charge distributions in segmented electrodes of gas detectors. *Euro. Phys. J. A*. 48:60. doi: 10.1140/epja/i2012-12060-3

Carbone, D., Ferreira, J. L., Calabrese, S., Cappuzzello, F., Cavallaro, M., Hacisalihoglu, A., et al. (2020). Analysis of two-nucleon transfer reactions in the 20Ne+116Cd system at 306 MeV. *Phys. Rev. C* 102:044606. doi: 10.1103/PhysRevC.102.044606

Carbone, D., Linares, R., Amador-Valenzuela, P., Calabrese, S., Cappuzzello, F., Cavallaro, M., et al. (2021). Initial state interaction for the 20Ne + 130Te and 18O + 116Sn systems at 15.3 AMeV from elastic and inelastic scattering measurements. *Universe* 7:58. doi: 10.3390/universe7030058

Cavallaro, M., Aciksoz, E., Acosta, L., Agodi, C., Auerbach, N., Bellone, J. I., et al. (2017). "NURE: an ERC project to study nuclear reactions," in *Proceedings, 55th International Winter Meeting on Nuclear Physics Bormio*, (Bormio). doi: 10.22323/1.302.0015

Cavallaro, M., Agodi, C., Assie, M., Azaiez, F., Cappuzzello, F., Carbone, D., et al. (2016). Neutron decay of 15C resonances by measurements of neutron time-of-flight. *Phys. Rev. C* 93:064323. doi: 10.1103/PhysRevC.93.064323

Cavallaro, M., Agodi, C., Brischetto, G. A., Calabrese, S., Cappuzzello, F., Carbone, D., et al. (2020). The MAGNEX magnetic spectrometer for double charge exchange reactions. *Nucl. Inst. Method Phys. Res. B* 463, 334–338. doi: 10.1016/j.nimb.2019.04.069

Cavallaro, M., Bellone, J. I., Calabrese, S., Agodi, C., Burrello, S., Cappuzzello, F., et al. (2021). A constrained analysis of the 40Ca(18O,18F)40K direct charge exchange reaction mechanism at 275 MeV. *Front. Space Sci. Astron.*

Cavallaro, M., Cappuzzello, F., Carbone, D., Cunsolo, A., Foti, A., Khouaja, A., et al. (2012). The low-pressure focal plane detector of the MAGNEX spectrometer. *Eur. Phys. J. A* 48:59. doi: 10.1140/epja/i2012-12059-8

Cavallaro, M., Santagati, G., Cappuzzello, F., Carbone, D., Linares, R., Torresi, D., et al. (2019). Charge-state distributions of 20 Ne ions emerging from thin foils. *Res. in Phys*. 13, 102191. doi: 10.1016/j.rinp.2019.102191

Cortesi, M., Rost, S., Mittig, W., Ayyad-Limonge, Y., Bazin, D., Yurkon, J., et al. (2017). Multi-layer thick gas electron multiplier (M-THGEM): a new MPGD structure for high-gain operation at low-pressure. *Rev. Sci. Instr*. 88:013303. doi: 10.1063/1.4974333

Cunsolo, A., Cappuzzello, F., Foti, A., Lazzaro, A., and Melita, A. L. (2002). Ion optics for large-acceptance magnetic spectrometers. *Nucl. Instr. Method A* 484:56. doi: 10.1016/S0168-9002(01)02004-6

Dell'Oro, S., Marcocci, S., Viel, M., and Vissani, F. (2016). Neutrinoless double beta decay: 2015 review. *Adv. High Ener. Phys*. 2016:2162659. doi: 10.1155/2016/2162659

Ejiri, H., Suhonen, J., and Zuber, K. (2019). Neutrino-nuclear responses for astro-neutrinos, single beta decays and double beta decays. *Phys. Rep*. 797, 1–102. doi: 10.1016/j.physrep.2018.12.001

Engel, J., and Menendez, J. (2017). Status and future of nuclear matrix elements for neutrinoless double-beta: a review. *Rep. Progr. Phys*. 80:046301. doi: 10.1088/1361-6633/aa5bc5

Ferrari, A., Sala, P. R., Fassò, A., and Ranft, J. (2005). *CERN-2005-10, INFN/TC_05/11, SLAC-R-773*.

Ferreira, J. L., Carbone, D., Cavallaro, M., Deshmukh, N. N., Agodi, C., Brischetto, G. A., et al. (2021). Analysis of two-proton transfer in the 40Ca(18O,20Ne)38Ar reaction at 270 MeV. *Phys. Rev. C*.

Finocchiaro, P., Acosta, L., Agodi, C., Altana, C., Amador-Valenzuela, P., Boztosun, I., et al. (2020). The NUMEN heavy ion multidetector for a complementary approach to the neutrinoless double beta decay. *Universe* 6:129. doi: 10.3390/universe6090129

Folger, G., Ivanchenko, V. N., and Wellisch, J. P. (2004).The binary cascade. *Eur. Phys. J. A* 21:407. doi: 10.1140/epja/i2003-10219-7

Gouvea, A., and Vogel, P. (2013). Lepton flavor and number conservation and physics beyond the standard model. *Prog. Part. Nucl. Phys.* 71:75. doi: 10.1016/j.ppnp.2013.03.006

Iazzi, F., Ferrero, S., Introzzi, R., Pinna, F., Scaltrito, L., Calvo, D., et al. (2017). A new cooling technique for targets operating under very intense beams. *WIT Trans. Engin. Sci*. 116:61. doi: 10.2495/MC170071

Kisamori, K., Shimoura, S., Miya, H., Michimasa, S., Ota, S., Assie, M., et al. (2016). Candidate resonant tetraneutron state populated by the 4He(8He,8Be) reaction. *Phys. Rev. Lett*. 116:052501. doi: 10.1103/PhysRevLett.116.052501

La Fauci, L., Spatafora, A., Cappuzzello, F., Agodi, C., Carbone, D., Cavallaro, M., et al. (2021). 18O + 76Se elastic and inelastic scattering at 275 MeV. *Phys. Rev. C*.

Lazzaro, A., Cappuzzello, F., Cunsolo, A., Cavallaro, M., Foti, A., Khouaja, A., et al. (2007). Field simulations for large dipole magnets. *Nucl. Instr. Method A* 570:192. doi: 10.1016/j.nima.2006.10.055

Lazzaro, A., Cappuzzello, F., Cunsolo, A., Cavallaro, M., Foti, A., Orrigo, S. E. A., et al. (2008a). Field measurement for large quadrupole magnets. *Nucl. Instr. Method A* 591:394. doi: 10.1016/j.nima.2008.02.103

Lazzaro, A., Cappuzzello, F., Cunsolo, A., Cavallaro, M., Foti, A., Orrigo, S. E. A., et al. (2008b). Field measurement for large bending magnets. *Nucl. Instr. and Meth. A*. 585, 136. doi: 10.1016/j.nima.2007.10.046

Lazzaro, A., Cappuzzello, F., Cunsolo, A., Cavallaro, M., Foti, A., Orrigo, S. E. A., et al. (2009). Field reconstruction in large aperture quadrupole magnets. *Nucl. Instr. Method A* 602:494. doi: 10.1016/j.nima.2009.01.019

Lenske, H., Bellone, J. I., Colonna, M., and Lay, J. A. (2018). Theory of single-charge exchange heavy-ionreactions. *Phys. Rev. C* 98:044620. doi: 10.1103/PhysRevC.98.044620

Lenske, H., Cappuzzello, F., Cavallaro, M., and Colonna, M. (2019). Heavy ion charge exchange reactions as probes for nuclear beta-decay. *Prog. Part Nucl. Phys*. 109:103716. doi: 10.1016/j.ppnp.2019.103716

Lo Presti, D., Medina, N. H., Guazzelli, M. A., Moralles, M., Aguiar, V. A. P., Oliveira, J. R. B., et al. (2020). Neutron radiation effects on an electronic system on module. *Rev. Sci. Instr*. 91:083301. doi: 10.1063/5.0010968

Magana Vsevolodovna, R., Santopinto, E., and Bijker, R. (2021). Transfer reactions between odd-odd and even-even nuclei by using IBFFM. *arXiv* arXiv:2101.05659v05651.

Matsubara, H., Takaki, M., Uesaka, T., Shimoura, S., Aoi, N., Dozono, M., et al. (2013). Spectroscopic Measurement in 9He and 12Be. *Few Body Syst*. 54, 1433–1436. doi: 10.1007/s00601-012-0586-9

Oliveira, J. R. B., Cappuzzello, F., Chamon, L. C., Pereira, D., Agodi, C., Bondì, M., et al. (2013). Study of the rainbow-like pattern in the elastic scattering of 16O on 27Al at Elab. = 100 MeV. *J. Phys. G Nucl. Part Phys*. 40:105101. doi: 10.1088/0954-3899/40/10/105101

Oliveira, J. R. B., Finocchiaro, P., Agodi, C., Boztosun, I., Cappuzzello, F., De Faria, P. N., et al. (2018). New spectrometer projects for challenging particle-gamma measurements of nuclear reactions. *J. Phys. Conf. Ser*. 1056:012040. doi: 10.1088/1742-6596/1056/1/012040

Oliveira, J. R. B., Moralles, M., Flechas, D., Carbone, D., Cavallaro, M., Torresi, D., et al. (2020). First comparison of GEANT4 hadrontherapy physics model with experimental data for a NUMEN project reaction case. *Eur. Phys. J. A* 56:153. doi: 10.1140/epja/s10050-020-00152-6

Pereira, D., Linares, R., Oliveira, J. R. B., Lubian, J., Chamon, L. C., Gomes, P. R. S., et al.. (2012). Nuclear rainbow in the 16O+27AL system: the role of couplings at energies far above the barrier. *Phys. Lett. B* 710, 426–429. doi: 10.1016/j.physletb.2012.03.032

Pinna, F., Calvo, D., Campostrini, M., Capirossi, V., Delaunay, F., Fisichella, M., et al. (2020b). Evaluation of target non-uniformity and dispersion effects on energy measurement resolution in NUMEN experiment. *Phys. Scripta*. 95:094002. doi: 10.1088/1402-4896/aba779

Pinna, F., Capirossi, V., Delaunay, F., Iazzi, F., Brunasso, O., Calvo, D., et al. (2020a). Tests of a cooling system for thin targets submitted to intense ions beams for the NUMEN experiment. *Acta Phys. Pol. B* 51:665. doi: 10.5506/APhysPolB.51.655

Rifuggiato, D., Calabretta, L., Cosentino, L., and Cuttone, G. (2013). "Variety of beam production at the infn lns superconducting cyclotron," in *Proceedings of Cyclotrons 2013*. (Vancouver, BC: Canada).

Sagawa, H., and Uesaka, T. (2016). Sum rule study for double gamow-teller states. *Phys. Rev. C* 94:064325. doi: 10.1103/PhysRevC.94.064325

Santopinto, E., Garcia-Tecocoatzi, H., Magana Vsevolodovna, R. I., and Ferretti, J. (2018). Heavy-ion double-charge-exchange and its relation to neutrinoless double-beta decay. *Phys. Rev. C* 98:061601. doi: 10.1103/PhysRevC.98.061601

Sartirana, D., Calvo, D., Capirossi, V., Ferraresi, C., Iazzi, F., and Pinna, F. (2020). Target manipulation in nuclear physics experimentwith ion beams. *Adv. Serv. Indust. Robot.* 84, 533–543. doi: 10.1007/978-3-030-48989-2_57

Sauli, F. (2016). The gas electron multiplier (GEM). Operating principles and applications. *Nucl. Instr. Meth. Phys. Res. A* 805, 2–24. doi: 10.1016/j.nima.2015.07.060

Shimizu, N., Menendez, J., and Yako, K. (2018). Double gamow-teller transitions and its relation to neutrinoless decay. *Phys. Rev. Lett*. 120:142502. doi: 10.1103/PhysRevLett.120.142502

Spatafora, A., Cappuzzello, F., Carbone, D., Cavallaro, M., Lay, J.-A., Acosta, L., et al. (2019). 20Ne + 76Ge elastic and inelastic scattering at 306 MeV. *Phys. Rev. C* 100:034620. doi: 10.1103/PhysRevC.100.034620

Suhonen, J., and Civitarese, O. (2012). Review of the properties of the 0νβ-β- nuclear matrix elements. *J. Phys. G* 39:124005. doi: 10.1088/0954-3899/39/12/124005

Suhonen, J. T. (2017). Value of the axial-vector coupling strength in β and ββ decays: a review. *Front. Phys*. 5:55. doi: 10.3389/fphy.2017.00055

Takahisa, K., Ejiri, H., Akimune, H., Fujita, H., Matumiya, R., Ohta, T., et al. (2017). Double charge exchange (11B,11Li) reaction for double beta decay response. *arrive* arXiv 1703.08264.

Torresi, D., Sgouros, O., Soukeras, V., Cavallaro, M., Cappuzzello, F., Carbone, D., et al. (2021). An upgraded focal plane detector for the MAGNEX spectrometer. *Nucl. Instr. Method A* 989:164918. doi: 10.1016/j.nima.2020.164918

Tudisco, S., La Via, F., Agodi, C., Altana, C., Borghi, G., Boscardin, M., et al. (2018). SiCILIA—silicon carbide detectors for intense luminosity investigations and applications. *Sensors* 18:2289. doi: 10.3390/s18072289

Vergados, J. D., Ejiri, H., and Simkovic, F. (2012). Theory of neutrinoless double-beta decay. *Rep. Prog. Phys*. 75:106301. doi: 10.1088/0034-4885/75/10/106301

Vlachoudis, V. (2009). "A Powerful But User Friendly Graphical Interface For FLUKA," in *Proceeding International Conference on Mathematics, Computational Methods and Reactor Physics, Saratoga.* (New York, NY: Springs)

Conflict of Interest: The authors declare that the research was conducted in the absence of any commercial or financial relationships that could be construed as a potential conflict of interest.

frontiers in Astronomy and Space Sciences

ORIGINAL RESEARCH
published: 07 May 2021
doi: 10.3389/fspas.2021.659815

A Constrained Analysis of the $^{40}Ca(^{18}O,^{18}F)^{40}K$ Direct Charge Exchange Reaction Mechanism at 275 MeV

Manuela Cavallaro[1], Jessica I. Bellone[1], Salvatore Calabrese[1], Clementina Agodi[1], Stefano Burrello[2], Francesco Cappuzzello[1,3], Diana Carbone[1], Maria Colonna[1], N. Deshmukh[4], H. Lenske[5], A. Spatafora[1,3], L. Acosta[6], P. Amador-Valenzuela[7], T. Borello-Lewin[8], G. A. Brischetto[1,3], D. Calvo[9], V. Capirossi[9,10], E. Chávez[6], I. Ciraldo[1,3], M. Cutuli[1,3], F. Delaunay[11], H. Djapo[12], C. Eke[13], P. Finocchiaro[1], S. Firat[14], M. Fisichella[1], A. Foti[15], M. A. Guazzelli[16], A. Hacisalihoglu[17], F. Iazzi[9,10], L. La Fauci[1,3], R. Linares[18], J. Lubian[18], N. H. Medina[8], M. Moralles[19], J. R. B. Oliveira[8], A. Pakou[20], Luciano Pandola[1], H. Petrascu[21], F. Pinna[9,10], G. Russo[15], O. Sgouros[1], S. O. Solakci[14], V. Soukeras[1], G. Souliotis[22], D. Torresi[1], Salvatore Tudisco[1], A. Yildirin[14] and V. A. B. Zagatto[18] for the NUMEN collaboration*

[1] Istituto Nazionale di Fisica Nucleare, Laboratori Nazionali del Sud, Catania, Italy, [2] Université Paris-Saclay, CNRS/IN2P3, IJCLab, Orsay, France, [3] Dipartimento di Fisica e Astronomia "Ettore Majorana," Università di Catania, Catania, Italy, [4] School of Sciences, Auro University, Surat, India, [5] Department of Physics, University of Giessen, Giessen, Germany, [6] Instituto de Física, Universidad Nacional Autónoma de México, Mexico City, Mexico, [7] Departamento de Aceleradores y Estudio de Materiales, Instituto Nacional de Investigaciones Nucleares—Ocoyoacac, Mexico City, Mexico, [8] Instituto de Fisica, Universidade de São Paulo, São Paulo, Brazil, [9] Istituto Nazionale di Fisica Nucleare, Sezione di Torino, Turin, Italy, [10] Dipartimento Scienza Applicata e Tecnologia, Politecnico di Torino, Turin, Italy, [11] LPC Caen, Normandie Université, ENSICAEN, UNICAEN, CNRS/IN2P3, Caen, France, [12] Institute of Accelerator Technologies, Ankara University, Ankara, Turkey, [13] Department of Mathematics and Science Education, Akdeniz University, Antalya, Turkey, [14] Department of Physics, Akdeniz University, Antalya, Turkey, [15] Istituto Nazionale di Fisica Nucleare, Sezione di Catania, Catania, Italy, [16] Centro Universitario FEI, São Bernardo do Campo, Brazil, [17] Institute of Natural Science, Karadeniz Teknik Universitesi, Trabzon, Turkey, [18] Instituto de Fisica, Universidade Federal Fluminense, Niterói, Brazil, [19] Instituto de Pesquisas Energeticas e Nucleares IPEN/CNEN, São Paulo, Brazil, [20] Department of Physics, University of Ioannina and Hellenic Institute of Nuclear Physics, Ioannina, Greece, [21] IFIN-HH, Bucharest, Romania, [22] Department of Chemistry, University of Athens and Hellenic Institute of Nuclear Physics, Athens, Greece

The $^{40}Ca(^{18}O,^{18}F)^{40}K$ single charge exchange (SCE) reaction is explored at an incident energy of 275 MeV and analyzed consistently by collecting the elastic scattering and inelastic scattering data under the same experimental conditions. Full quantum-mechanical SCE calculations of the direct mechanism are performed by including microscopic nuclear structure inputs and adopting either a bare optical potential or a coupled channel equivalent polarization potential (CCEP) constrained by the elastic and inelastic data. The direct SCE mechanism describes the magnitude and shape of the angular distributions rather well, thus suggesting the suppression of sequential multi-nucleon transfer processes.

Keywords: nuclear physics, charge exchange reactions, elastic scattering, magnetic spectrometer, neutrinoless double beta (0νββ) decay

OPEN ACCESS

Edited by:
Nunzio Itaco,
University of Campania Luigi Vanvitelli, Italy

Reviewed by:
Mengoni Daniele,
National Institute of Nuclear Physics of Padova, Italy
Pierre Descouvemont,
Université libre de Bruxelles, Belgium

****Correspondence:***
Manuela Cavallaro
manuela.cavallaro@lns.infn.it

Specialty section:
This article was submitted to Nuclear Physics, a section of the journal Frontiers in Astronomy and Space Sciences

Received: *28 January 2021*
Accepted: *30 March 2021*
Published: *07 May 2021*

Citation:
Cavallaro M, Bellone JI, Calabrese S, Agodi C, Burrello S, Cappuzzello F, Carbone D, Colonna M, Deshmukh N, Lenske H, Spatafora A, Acosta L, Amador-Valenzuela P, Borello-Lewin T, Brischetto GA, Calvo D, Capirossi V, Chávez E, Ciraldo I, Cutuli M, Delaunay F, Djapo H, Eke C, Finocchiaro P, Firat S, Fisichella M, Foti A, Guazzelli MA, Hacisalihoglu A, Iazzi F, Fauci LL, Linares R, Lubian J, Medina NH, Moralles M, Oliveira JRB, Pakou A, Pandola L, Petrascu H, Pinna F, Russo G, Sgouros O, Solakci SO, Soukeras V, Souliotis G, Torresi D, Tudisco S, Yildirin A and Zagatto VAB (2021) A Constrained Analysis of the $^{40}Ca(^{18}O,^{18}F)^{40}K$ Direct Charge Exchange Reaction Mechanism at 275 MeV. Front. Astron. Space Sci. 8:659815. doi: 10.3389/fspas.2021.659815

INTRODUCTION

Single charge exchange (SCE) reactions are considered to be the best probe to explore the isospin and spin–isospin nuclear response to the strong interaction. Light-ion-induced SCE reactions have been widely investigated (Taddeucci et al., 1987; Osterfeld, 1992; Alford and Spicer, 1998) especially thanks to the high energy resolution (30 keV) achieved in (^{3}He,t) experiments (Fujita et al., 1997, 2007; Douma et al., 2020) which have allowed to study the details of the populated energy spectra, including their relationships with beta decay transition strengths (Fujita et al., 2011; Frekers et al., 2013; Diel et al., 2019). The use of light-ion-induced SCE reactions for the spectroscopic studies of Fermi ($J^\pi = 0^+$; $L = 0$, $T = 1$, $S = 0$) and Gamow–Teller ($J^\pi = 1^+$; $L = 0$, $T = 1$, $S = 1$) excitations is well-established. Recent studies have also shown a sensitivity of (^{3}He,t) reactions to higher multipoles, such as the spin dipole ($J^\pi = 2^-$; $L = 1$, $T = 1$, $S = 1$) (Ejiri et al., 2014; Akimune et al., 2020). The isospin response at high multipolarity has attracted interest in the last few years in view of its possible connection to neutrinoless double beta decay ($0\nu\beta\beta$) nuclear matrix elements (NMEs), where indeed higher multipoles are expected to play a relevant role in an intermediate virtual state (Ejiri et al., 2019). Ordinary muon capture (OMC) techniques, despite the moderate energy resolution of the order of few MeV, have been recently developed to explore nuclear high multipoles stimulated by isospin weak interaction operators (Ejiri, 2005; Jokiniemi et al., 2019).

In this perspective, heavy-ion-induced SCE reactions are particularly interesting because of their enhanced probability to populate high-spin states, due to the large momentum transferred from the heavy projectile to the target even at forward scattering angles. Hence, heavy-ion SCE reactions are expected to provide a relevant contribution to our understanding of the matrix elements of nuclear multipole transitions (Lenske et al., 2018, 2019). In this case, the achievable energy resolution is a few hundred keV, mainly limited by energy straggling due to the projectile–target interaction, which is often enough to allow the separation of low-lying states in the inclusive spectra. Different heavy-ion probes have been proposed in the years, mainly induced by ^{6,7}Li, ^{12,13}C, ^{48}Ti beams at energies above the Coulomb barrier (Lenske et al., 2019). The main findings concern the competition between direct meson exchange and sequential nucleonic transfer mechanisms depending on the specific dynamical conditions. When the direct mechanism is dominant, a proportionality of SCE cross sections with beta decay strengths is found and a general trend to favor the population of unnatural parity transitions is observed (Cappuzzello et al., 2004a). Not much is known about the (^{18}O,^{18}F) SCE reaction, which is discussed in the present paper. Such a probe has been studied on the ^{28}Si and ^{36}S targets from 3 to 19.6 A MeV (Kim et al., 1979; Horen et al., 1986; Fifield et al., 1993). In all cases, a significant role of the direct mechanism has been deduced, especially at the highest beam energies, but uncertainties in the adopted models for the nuclear structure and reaction inputs did not allow to draw any firm conclusion.

The study of such SCE reactions is of crucial importance in the NUMEN and NURE projects (Cappuzzello et al., 2015a, 2018; Cavallaro et al., 2017) at the INFN-LNS laboratory, which aims at investigating double-charge exchange (DCE) reactions (^{18}O,^{18}Ne) and (^{20}Ne,^{20}O) to an unprecedented level of accuracy, both from the experiment and theory side, in view of their connections with $0\nu\beta\beta$ decay. The key aspects of this research program are the similarities between the two classes of processes, DCE and $0\nu\beta\beta$, both characterized by the exchange of two units of isospin between the initial state and the final state, although mediated by the strong interaction and the weak interaction, respectively (Cappuzzello and Cavallaro, 2020).

A theory for heavy-ion SCE and DCE reactions, describing the two kinds of reaction in a unified manner, was missing up to few years ago and is presently under development within the NUMEN activities (Lenske et al., 2018, 2019; Santopinto et al., 2018; Bellone et al., 2020; Carbone et al., 2020; Ferreira et al., 2021; Burrello et al., in preparation). The competition between the direct mechanisms, mediated by the exchange of one (SCE) or two (DCE) charged mesons between the projectile and target and probing the isospin structure of the ions, and the sequential transfer of protons and neutrons, probing the mean field structure of the involved nuclei, is one of the topics of this research. In particular, Bellone et al. (2020) demonstrated that the (^{18}O,^{18}F) cross section is fundamental to constrain the DCE sequential meson exchange mechanism along the ^{18}O $\rightarrow$ ^{18}F $\rightarrow$ ^{18}Ne transition. Moreover, the experimental measurement and analysis of the elastic scattering and inelastic scattering cross sections for the same projectile–target system is crucial to constrain the SCE and DCE calculations. Indeed, the projectile–target nucleus-nucleus potential needs to be accurately modeled both in the entrance [initial state interaction (ISI)] and exit [final state interaction (FSI)] channels (Spatafora et al., 2019; Carbone et al., 2021; La Fauci et al., submitted).

A case of interest for a description of charge exchange cross sections is the ^{40}Ca(^{18}O,^{18}F)^{40}K reaction at an incident energy of 275 MeV for which the theoretical formalism and the details of a microscopic quantum-mechanical calculation were reported by Lenske et al. (2018). Such an approach includes a nuclear structure part modeled by quasi-particle random phase approximation- (QRPA-) based transition densities, and a reaction part via distorted wave Born approximation (DWBA) cross section calculations. Here, we provide for the first time the experimental cross section angular distribution data and discuss their comparison with the theoretical calculations. Contextually, the elastic and inelastic scattering of ^{18}O beam on ^{40}Ca target at the same bombarding energy were measured in a wide momentum transfer range and studied to extract the optical potential to be used in the SCE calculations. The importance of experimental constraints coming from the elastic scattering data to the determination of the ion–ion interaction was already stressed by Lenske et al. (2018). However, such information was missing in that work and is available here for the first time. The effect of the couplings with inelastic excitations is also explored here.

EXPERIMENT AND DATA REDUCTION

The ^{40}Ca(^{18}O,^{18}F)^{40}K charge exchange reaction was measured at INFN-Laboratori Nazionali del Sud in Catania (Italy). A beam of $^{18}O^{4+}$ ions, extracted by the K800 Superconducting Cyclotron accelerator, bombarded a 280 ± 14 μg/cm^2 natural calcium (96.9% ^{40}Ca) target at an incident energy of 275 MeV. The calcium material for the target was evaporated on a carbon backing of 25 μg/cm^2 thick, and a further carbon layer of 15 μg/cm^2 was evaporated on the top of the calcium layer to reduce oxidation processes. The ^{18}O + ^{40}Ca elastic scattering and inelastic scattering were measured in a dedicated run using a 250 ± 12 μg/cm^2 thick calcium target evaporated on 47 μg/cm^2 carbon backing. A Faraday cup located inside a scattering chamber and 15 cm downstream of the target was used to collect the beam charge. An electron suppressor polarized at −200 V and a low-noise charge integrator allowed a charge collection accuracy better than 10%. The ejectiles produced in the collisions were selected by the MAGNEX large acceptance spectrometer (Cappuzzello et al., 2016) and identified by its focal plane detector (Cavallaro et al., 2012; Torresi et al., 2021). For the charge exchange measurement, the optical axis of the spectrometer was located at $\theta_{opt} = +7^\circ$ with respect to the beam direction. Thanks to the MAGNEX angular acceptance, an angular range of $3^\circ < \theta_{lab} < 9^\circ$ in the laboratory reference frame was explored in a single angular setting. For the measurement of elastic scattering and inelastic scattering, the optical axis of MAGNEX was set at $\theta_{opt} = +8^\circ$, $+14^\circ$, and $+18^\circ$ in three different acquisition runs, exploring an overall angular range of $3^\circ < \theta_{lab} < 19^\circ$. The procedure to reduce the collected data and extract the energy spectra and the cross section angular distributions for the measured transitions is described in detail by Cappuzzello et al. (2010), Cappuzzello et al. (2011), Cappuzzello et al. (2014), Calabrese et al. (2020), Cavallaro et al. (2011), and Carbone (2015).

In **Figure 1**, an example of a measured spectrum is shown as a function of excitation energy $E_x = Q_0 - Q$ (where Q is the reaction Q-value, $Q_0 = 0$ for elastic scattering) for the ^{18}O+^{40}Ca scattering in the angular region $8.2^\circ < \theta_{lab} < 9.0^\circ$. The peaks related to the transition to the 0^+ ^{40}Ca ground state and to

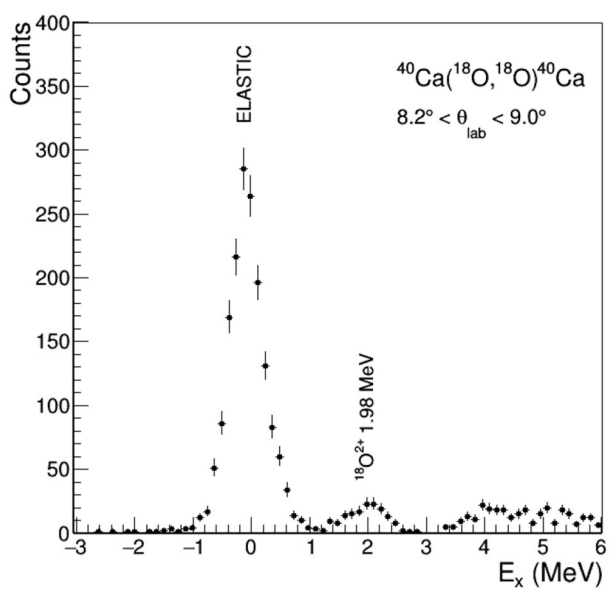

FIGURE 1 | Excitation energy spectrum of ^{40}Ca obtained in the ^{18}O + ^{40}Ca elastic scattering and inelastic scattering at an incident energy of 275 MeV and $8.2^\circ < \theta_{lab} < 9.0^\circ$.

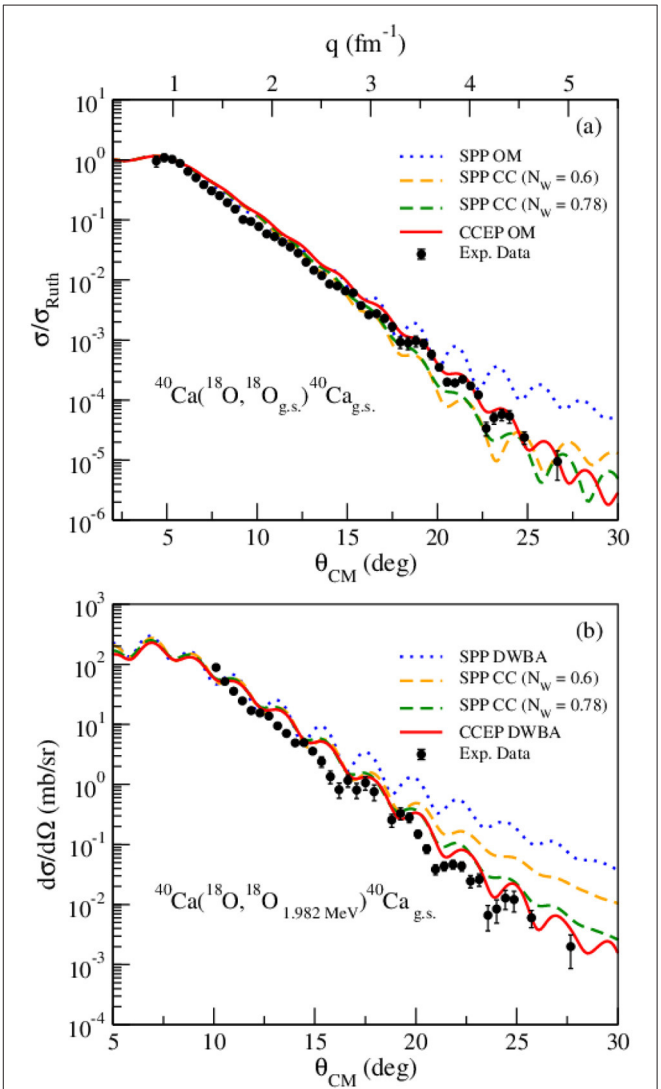

FIGURE 2 | (A) Cross section angular distribution of the ^{18}O + ^{40}Ca elastic scattering at 275 MeV in terms of its ratio to the Rutherford cross section σ_{Ruth}. **(B)** Angular distribution of the inelastic channel ^{40}Ca(^{18}O,^{18}O$_{1.982}$)^{40}Ca$_{g.s.}$. In both plots, the blue dotted line shows the optical model (OM; for elastic) and distorted wave Born approximation (DWBA; for inelastic) calculations with São Paulo potential (SPP), the orange dashed line shows the coupled channel (CC) calculations with SPP and $N_W = 0.6$, the green dashed line shows the CC calculations with SPP and $N_W = 0.78$, and the red solid line shows the OM and DWBA calculations with coupled channel equivalent polarization potential (CCEP).

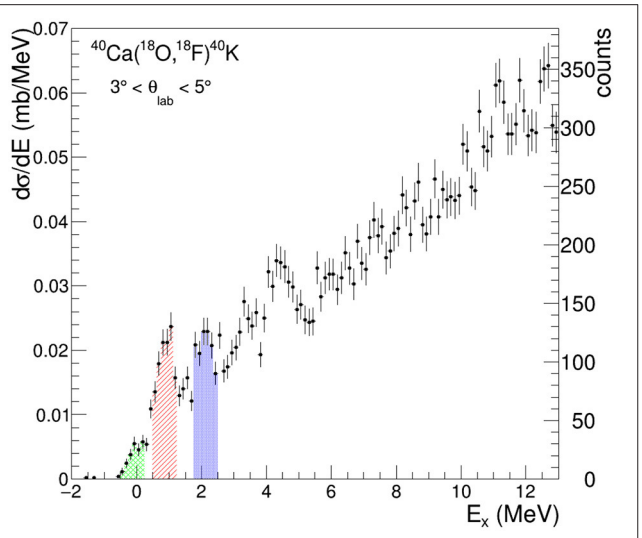

FIGURE 3 | Excitation energy spectrum of the ^{40}Ca(^{18}O, ^{18}F)^{40}K charge exchange reaction at 275 MeV and $3^\circ < \theta_{lab} < 5^\circ$. The three hatched areas indicate the regions of interest for the study of the angular distributions.

the first 2^+ ^{18}O excited state at $E_x = 1.982$ MeV are clearly visible. The structures above $E_x = 3$ MeV are due to unresolved excitations of both ejectile and residual nuclei. The contributions arising due to the carbon and oxygen impurities in the target are expected at $E_x > 6$ and $E_x > 4$ MeV, respectively, so not present in the range of the explored transitions. An energy resolution of about 500 keV (full width at half maximum) is measured.

The cross section angular distribution for the ^{18}O + ^{40}Ca elastic scattering, expressed in terms of its ratio to the Rutherford cross section, is shown in **Figure 2A**. The corresponding scale of transferred linear momentum q is also given. The angular distribution for the inelastic scattering to the first excited state of ^{18}O at 1.982 MeV is shown in **Figure 2B**.

The ^{40}K excitation energy spectrum $E_x = Q_0 - Q$ (where Q is the reaction Q-value and Q_0 the ground state to ground state Q-value) extracted from the ^{40}Ca(^{18}O,^{18}F)^{40}K SCE measurement in the angular region of $3^\circ < \theta_{lab} < 5^\circ$ is shown in **Figure 3**. Both counts and energy differential cross section $d\sigma/dE$ in the absolute value (mb/MeV) are indicated in two scales. Some structures are observed in the low excitation energy region; however, the limited resolution and the high-level density do not allow to isolate single transitions. The groups of levels belonging to the three energy regions indicated in **Figure 3** as well as the corresponding integrated cross sections in the angular interval of $4.8^\circ < \theta_{CM} < 11.3^\circ$ are listed in **Table 1**.

The angular distributions for the SCE cross section extracted in the three regions of interest of the ^{18}F+^{40}K excitation energy sketched in **Figure 3** are shown in **Figure 4**. In particular, the ground state region (including the unresolved transitions to the ground state and the first excited state of ^{40}K at 0.029 MeV), the region at energies of 0.5 MeV $< E_x <$ 1.2 MeV and the region at energies of 1.7 MeV $< E_x <$ 2.6 MeV are explored. For the extraction of the cross section in the ground state region, a Gaussian fitting procedure was performed for each angular bin.

The error bars reported in the experimental data in **Figures 2**, **4** include the statistical contribution and the uncertainties coming from the determination of the solid angle intervals. An overall uncertainty of about 10%, due to the determination of charge collection and target thickness, is not shown in **Figures 2**, **4** as it is common to all data points in the angular distributions.

ANALYSIS OF THE ELASTIC AND INELASTIC SCATTERING AND DETERMINATION OF THE OPTICAL POTENTIAL

The measured angular distributions of the elastic and inelastic experimental cross section are compared with the quantum-mechanical optical model (OM), DWBA, and coupled channel (CC) calculations, using the FRESCO code (Thompson, 1988). The double-folding São Paulo potential (V_{SPP}) (Chamon et al., 2002) is adopted as the real part of a complex optical potential $U(r) = V_{SPP}(r) + i\,N_W\,V_{SPP}(r)$. The imaginary part is assumed with the same shape of the real one scaled by a factor $N_W = 0.78$, as typically done, for example, in Alvarez et al. (2003), Spatafora et al. (2019), and Oliveira et al. (2013). For the CC calculations, the results obtained by using a smaller scaling factor, $N_W = 0.6$ (Pereira et al., 2009), are also shown and commented in the following. In the double-folding procedure, two-parameter Fermi distributions are adopted to describe the projectile and target matter densities, with radius and diffuseness obtained from systematic analyses (Chamon et al., 2002). In particular, the diffuseness of the matter density of the projectile is set to $a_p = 0.61$ fm, which is increased by 10% with respect to SPP systematics ($a_p = 0.56$ fm), as commonly done for ^{18}O projectile (Crema et al., 2011; Cavallaro et al., 2013; Cappuzzello et al., 2015b; Ermamatov et al., 2016, 2017; Carbone et al., 2017; Paes et al., 2017; Cardozo et al., 2018; Linares et al., 2018; Fonseca et al., 2019).

The couplings introduced in the DWBA and CC calculations account for the collective low-lying quadrupole and octupole transitions. Namely, we consider the first ^{18}O(2^+) excited state at $E_x = 1.982$ MeV, and the first ^{40}Ca(3^-) and ^{40}Ca(2^+) excited states, at 3.737 MeV and 3.904 MeV, respectively. The adopted coupling scheme is sketched in **Figure 5**.

Both DWBA and CC calculations are performed within a rotational model. Calculations within a vibrational model do not give relevant differences in the results. Reduced transition probabilities B(E2; $0^+ \rightarrow 2^+$) = 0.0043 e^2b^2 for ^{18}O, B(E3 $0^+ \rightarrow 3^-$) = 0.0184 e^2b^3 and B(E2; $0^+ \rightarrow 2^+$) = 0.00924 e^2b^2 for ^{40}Ca are taken from Pritychenko et al. (2016), Pritychenko et al. (2017), and Kibedi and Spear (2002) and used to describe the strength of Coulomb deformation of both the projectile and target (Satchler, 1983; Khoa and Satchler, 2000).

Nuclear deformations (for the multipolarity λ) are described in terms of a first-order derivative of the potential $U(r)$, which is used to describe the corresponding elastic channel:

TABLE 1 | Transitions expected for the three regions of interest of the $^{40}Ca(^{18}O,^{18}F)^{40}K$ energy spectrum as indicated in **Figure 3**.

Excitation energy region (MeV)	Final channel	Calculated cross section (μb)	Sum of calculated cross section (μb)	Experimental cross section (μb)
−0.5 – 0.2	$^{18}F_{g.s.}(1^+) + ^{40}K_{g.s.}(4^-)$	0.51	0.92	5.6 ± 0.6
	$^{18}F_{g.s.}(1^+) + ^{40}K_{0.029}(3^-)$	0.41		
0.5 – 1.2	$^{18}F_{g.s.}(1+) + ^{40}K_{0.800}(2^-)$	8.7	9.6	25 ± 2
	$^{18}F_{g.s.}(1^+) + ^{40}K_{0.891}(5^-)$	$4.7{\cdot}10^{-2}$		
	$^{18}F_{0.937}(3^+) + ^{40}K_{g.s.}(4^-)$	0.42		
	$^{18}F_{0.937}(3^+) + ^{40}K_{0.029}(3^-)$	$8.9{\cdot}10^{-2}$		
	$^{18}F_{1.042}(0^+) + ^{40}K_{0.029}(3^-)$	0.19		
	$^{18}F_{1.121}(5^+) + ^{40}K_{g.s.}(4^-)$	$9.6{\cdot}10^{-2}$		
	$^{18}F_{1.121}(5^+) + ^{40}K_{0.029}(3^-)$	$8.2{\cdot}10^{-3}$		
1.7 – 2.6	$^{18}F_{g.s.}(1^+) + ^{40}K_{1.959}(2^+)$	$1.3{\cdot}10^{-2}$	23	31 ± 2
	$^{18}F_{g.s.}(1^+) + ^{40}K_{2.047}(2^-)$	4.2		
	$^{18}F_{g.s.}(1^+) + ^{40}K_{2.070}(3^-)$	0.18		
	$^{18}F_{g.s.}(1^+) + ^{40}K_{2.104}(1^-)$	3.8		
	$^{18}F_{g.s.}(1^+) + ^{40}K_{2.260}(3^+)$	$3.5{\cdot}10^{-2}$		
	$^{18}F_{g.s.}(1^+) + ^{40}K_{2.290}(1^+)$	0.13		
	$^{18}F_{g.s.}(1^+) + ^{40}K_{2.290}(3^-)$	1.2		
	$^{18}F_{g.s.}(1^+) + ^{40}K_{2.397}(4^-)$	1.8		
	$^{18}F_{g.s.}(1^+) + ^{40}K_{2.419}(2^-)$	6.8		
	$^{18}F_{g.s.}(1^+) + ^{40}K_{2.543}(7^+)$	$4.1{\cdot}10^{-4}$		
	$^{18}F_{g.s.}(1^+) + ^{40}K_{2.576}(2^+)$	$4.6{\cdot}10^{-3}$		
	$^{18}F_{g.s.}(1^+) + ^{40}K_{2.626}(0^-)$	1.2		
	$^{18}F_{0.937}(3^+) + ^{40}K_{0.800}(2^-)$	2.1		
	$^{18}F_{0.937}(3^+) + ^{40}K_{0.891}(5^-)$	$4.3{\cdot}10^{-2}$		
	$^{18}F_{1.041}(0^+) + ^{40}K_{0.891}(5^-)$	0.26		
	$^{18}F_{1.121}(5^+) + ^{40}K_{0.800}(2^-)$	0.17		
	$^{18}F_{1.121}(5^+) + ^{40}K_{0.891}(5^-)$	$1.7{\cdot}10^{-2}$		
	$^{18}F_{1.701}(1^+) + ^{40}K_{g.s.}(4^-)$	$3.7{\cdot}10^{-2}$		
	$^{18}F_{1.701}(1^+) + ^{40}K_{0.029}(3^-)$	$2.8{\cdot}10^{-2}$		
	$^{18}F_{1.701}(1^+) + ^{40}K_{0.800}(2^-)$	1.0		
	$^{18}F_{1.701}(1^+) + ^{40}K_{0.891}(5^-)$	$1.7{\cdot}10^{-3}$		
	$^{18}F_{2.101}(2^-) + ^{40}K_{g.s.}(4^-)$	$2.4{\cdot}10^{-4}$		
	$^{18}F_{2.101}(2^-) + ^{40}K_{0.029}(3^-)$	$1.1{\cdot}10^{-4}$		
	$^{18}F_{2.523}(2^+) + ^{40}K_{g.s.}(4^-)$	$6.8{\cdot}10^{-5}$		
	$^{18}F_{2.523}(2^+) + ^{40}K_{0.029}(3^-)$	$4.8{\cdot}10^{-2}$		

The third and fourth columns give the calculated cross sections in the angular region of $4.8^\circ < \theta_{CM} < 11.3^\circ$ for each individual transition and summed over the three energy intervals, respectively. The last column gives the measured cross sections integrated in the same angular interval.

$$V_\lambda(r) = -\frac{\delta_\lambda}{\sqrt{4\pi}}\frac{dU(r)}{dr} \quad (1)$$

The strength of the deformation is embedded in the deformation length δ_λ (Satchler, 1983):

$$\delta_\lambda = \beta_\lambda R_V = \frac{4\pi}{3Ze}\frac{\sqrt{(2I+1)\,B(E\lambda; I \to I')}}{R_V^{\lambda-1}} \quad (2)$$

where β_λ is the deformation parameter characterizing the transition (of multipole λ) of the given nucleus of charge Ze and is deduced from the electric reduced transition probability $B(E\lambda; I \to I')$ from a state of spin I to a state of spin I', and $R_V = 3.73$ fm is the radius of the real part of the adopted optical potential $U(r)$, extracted from its fit with a Woods–Saxon shape (Satchler, 1983). For the imaginary coupling potentials, the same radial form factors are assumed. Exploratory calculations changing the method for the determination of R_V or introducing a N/Z correction factor in Equation (2) to account for possible differences in the density profiles for neutrons and protons (Satchler, 1983), give very similar results, within the quoted uncertainty of $B(E_\lambda; I \to I')$ (Kibedi and Spear, 2002; Pritychenko et al., 2016, 2017).

The results of the calculations are compared with the experimental data in **Figure 2**, where all the theoretical curves are folded with the experimental angular resolution (∼0.9° in the center of mass reference frame). The OM and DWBA calculations including São Paulo-derived optical potential

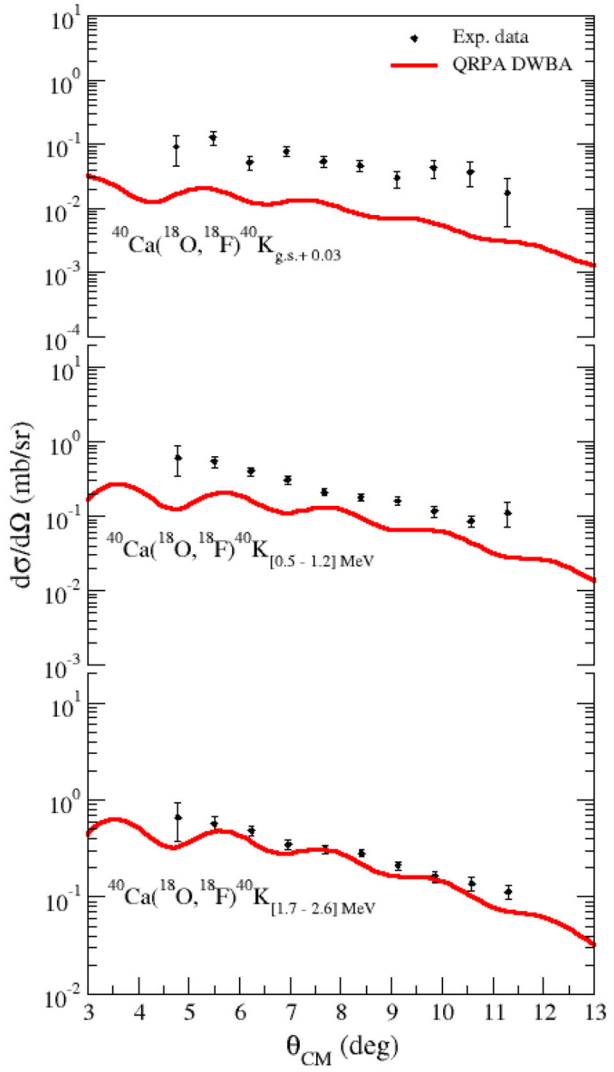

FIGURE 4 | Angular distributions for the ^{40}Ca(^{18}O,^{18}F)^{40}K transitions corresponding to the three selected regions in the single charge exchange (SCE) spectrum sketched in **Figure 3**. The red curves are the sum of the cross sections associated to the different transitions belonging to the three regions resulting from the quasi-particle random phase approximation (QRPA) DWBA calculations.

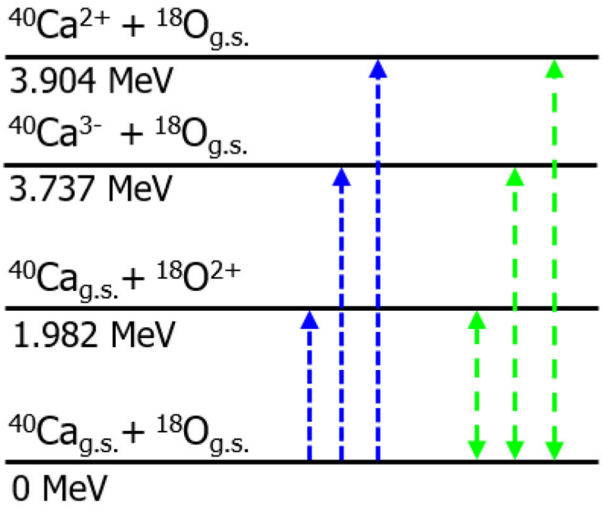

FIGURE 5 | Coupling scheme adopted in the DWBA (blue dotted single arrows) and CC (green dashed double arrows) calculations in the present work. In DWBA, the single arrows sketch that back coupling effects are not included.

describe reasonably well the experimental cross sections at small angles, showing an oscillatory pattern, which is more pronounced than the experimental data and a general overestimation of the data especially at larger angles and momentum transfer ($q >$ 4 fm^{-1}). This behavior resembles the one found in the similar analyses (Zagatto et al., 2018; Spatafora et al., 2019; Carbone et al., 2021; La Fauci et al., submitted; Burrello et al., in preparation) and is due to the lack of important couplings of elastic channel with inelastic channels.

The results of the CC calculations, also reported in **Figure 2**, show that the explored cross sections are affected by the couplings among the selected channels. The main effect is to reduce the cross section, especially at a large momentum transfer. Moreover, the couplings damp the oscillations and slightly shift the positions of the minima toward larger scattering angles, thus improving the description of the data. The coupling to the first 2^+ excited state of the ^{18}O projectile, keeping the target in its ground state, gives a main contribution to the elastic channel. Nonetheless, the explicit inclusion of the coupling to the first 3^- state of ^{40}Ca, keeping the projectile in its ground state, improves the description of the slope of the inelastic cross section (Ohkubo and Hirabayashi, 2014; Cappuzzello et al., 2016; Zagatto et al., 2018). We note that the calculations with N_W = 0.78 better describe the experimental data both in absolute cross section and shape of the angular distributions compared to those obtained assuming N_W = 0.6, which is often used in large-scale CC calculations (Pereira et al., 2009). The larger value for the N_W scaling factor, also reported by Spatafora et al. (2019) and Zagatto et al. (2018), may be explained due to the few states included in the present coupling scheme (see **Figure 5**) and it is compatible with uncertainties in the adopted B(E2) and B(E3) strengths.

As mentioned above, a proper description of the experimental elastic scattering and inelastic scattering data in the fully explored transferred momentum range is achieved, thanks to the introduction of couplings to inelastic channels. This result indicates that also the optical potential necessary for the description of the other quasi-elastic reaction channels induced by the same projectile and target at the same incident energy and angular momentum transfer should account for these couplings. However, it is evident that higher-order effects as introduced by CC calculations are most important for strong channel couplings as, e.g., the coupling of low-lying vibrational or rotational inelastic excitations to the elastic ground state channel. Since the SCE channels are rather weakly coupled to the other configurations, they are well-described already in a first-order DWBA approach. Moreover, in a CC description, the form

TABLE 2 | Volume integrals per interacting pair and root mean square radii for the real (V) part and imaginary (W) part of the São Paulo potential (SPP) and coupled channel equivalent polarization potential (CCEP) optical potentials adopted in the calculations.

	J_v (MeV fm^3)	J_W (MeV fm^3)	$\sqrt{\langle R_V^2 \rangle}$ (fm)	$\sqrt{\langle R_W^2 \rangle}$ (fm)
SPP	−346.1	−269.9	4.75	4.75
CCEP	−233.7	−205.6	4.38	4.59

factors describing each considered reaction channel should come from consistent nuclear structure models. Developments in that direction are the subject of ongoing theory projects and will be discussed elsewhere.

In this view, following the approach of Thompson et al. (1989), we have implicitly incorporated the effect of channel couplings in the elastic optical potential by means of an effective polarization potential term. In general, the formal theory gives a polarization potential, which is not only complex and energy dependent but also non-local and angular momentum dependent. The approach of Thompson et al. (1989), instead, produces an average local and L-independent polarization potential named trivially equivalent local potential (TELP). Adding the TELP to the São Paulo bare optical potential ($V_{\rm SPP}$) used in CC calculations, we get a CCEP (Thompson et al., 1985; Rangel et al., 2016). Such CCEP has been used herein in the OM and DWBA calculations for the elastic scattering and inelastic scattering, respectively, and in the DWBA calculations for the SCE channel described in Section The Charge Exchange Reaction Channel. We emphasize that, in the TELP approach, the effect of couplings is derived from a CC solution of the scattering problem, guaranteeing that the physics of coupling on average is accounted for. Thus, this method is more accurate than the common procedure to scale the imaginary part or slightly modify the geometry of the optical potential (Lubian and Nunes, 2007).

The elastic scattering and inelastic scattering experimental data are compared with the OM and DWBA calculations, respectively, using the CCEP optical potential in **Figure 2**. It is evident that the introduction of the polarization potential is essential to reproduce the experimental cross section even in an OM and a DWBA approach. We stress that in the present work the use of a CCEP has been introduced in view of its application to the SCE and DCE analyses. For the elastic scattering and inelastic scattering studies, it would not be necessary, since CC calculations are feasible and, indeed, have been performed.

The volume integrals and root mean square radii obtained for the SPP and CCEP potentials here adopted are listed in **Table 2**. The results agree with the values known from systematic studies (Satchler, 1983), confirming a very satisfactory description of the optical potential properties.

THE CHARGE EXCHANGE REACTION CHANNEL

As discussed in the introduction, the ^{40}Ca(^{18}O,^{18}F)^{40}K SCE reaction could proceed via two mechanisms: one mediated by charged meson exchange (direct SCE) and one governed by mean field interaction among the interacting nucleons (sequential multi-nucleon transfer). In the present work, we show the calculations performed for the former mechanism, which is the one of main interest in view of DCE studies. Calculations are performed within a framework of DWBA, where the cross section in a center of mass rest frame is given by the expression:

$$\frac{d^2\sigma}{dE_x d\Omega} = \frac{E_\alpha E_\beta}{\left(2\pi\hbar^2 c^2\right)^2}\frac{k_\beta}{k_\alpha}\frac{1}{(2J_A+1)\,(2J_a+1)} \sum_{M_A,\,M_a,M_B,M_b}\left|\int d^3r\,\chi^*_{\beta,\mathbf{k}_\beta}(r)\,F^{(SCE)}_{\alpha\beta}(\mathbf{r})\,\chi_{\alpha,\mathbf{k}_\alpha}(\mathbf{r})\right|^2 \tag{3}$$

where E_α (E_β) and k_α (k_β) denote the energy and relative momentum in the entrance $\alpha = a + A$ (exit $\beta = b + B$) channel; χ_α (χ_β) is the distorted wave, accounting for the initial (final) state interaction, i.e., it is the solution of the Schroedinger equation for the Hamiltonian including Coulomb and optical potential (CCEP in the present study) of the entrance (exit) channel. $F^{(SCE)}_{\alpha\beta}(\mathbf{r})$ is the SCE form factor, given by the folding of the nucleon–nucleon effective local interaction potential $V_{\rm NN}(r)$ and the one-body transition densities of projectile and target nuclei $\rho(r)$.

The effective local nucleon–nucleon direct and exchange interaction potential $V_{\rm NN}(r)$ contains both central and tensor components. It is parameterized by the sum of three Yukawa functions, with parameters coming from a proper interpolation procedure (Lenske, 1988) between two different parameterizations: (i) the G-matrix calculated by solving the Bethe–Salpeter equation with Paris nucleon–nucleon potential for E/A $\leq$ 10 MeV (Anantaraman et al., 1983) and (ii) the Franey–Love parameterization of effective nucleon–nucleon T-matrix for E/A $\geq$ 50 MeV (Franey and Love, 1985). The one-body transition densities $\rho(r)$ are the matrix elements of the one-body operator describing SCE transitions in the projectile and target nuclei (Lenske et al., 2018). These transition densities are calculated within an extended QRPA framework, going beyond the standard approach by accounting for the coupling of the two-quasi-particle configurations to core excitations by polarization self-energies. Residual interactions are determined self-consistently in the context of Fermi-liquid theory. The single quasi-particle states are derived from Hartree–Fock–Bogoliubov (HFB) calculations with state-dependent pairing gaps, describing the ground state properties of the involved nuclei very accurately (Lenske and Tsoneva, 2019). The HFB wave functions and the QRPA configuration amplitudes are used to construct the radial transitions densities, entering finally into the charge exchange transition form factors.

Calculations are performed in terms of the partial wave decomposition of distorted waves and the multipole expansion of the form factor, which is a quite standard procedure (Satchler, 1983). Detailed information on the adopted theoretical modeling is given by Lenske et al. (2018). This approach has been successfully used to also study other heavy-ion-induced SCE

reactions (Cappuzzello et al., 2004a,b; Nociforo et al., 2006; Cavallaro, 2011).

On the reaction side, we performed the DWBA calculations using the CCEP optical potential defined in Section 3 for the three excitation energy ranges for which experimental angular distributions have been extracted. The cross sections corresponding to transitions to different excited states are calculated by using the HIDEX code (Lenske, private communication). The calculations shown in **Figure 4** represent the sum of the angular distributions of the SCE reactions leading to all the possible excited states experimentally populated both by the ejectile and residual nucleus with total excitation energy within the above-mentioned three ranges. These exit channels are listed in **Table 1**, together with the corresponding values of the calculated cross section integrated in the same angular range explored by the data.

Table 1 shows that in the first region of interest, the transitions to the 4^- ground state and 3^- excited state of ^{40}K at 0.029 MeV, with the ^{18}F ejectile at its 1^+ ground state, give comparable contributions. In the [0.5, 1.7] MeV region, the transition to the first 2^- state of ^{40}K at 0.800 MeV and to $^{18}F_{g.s.}(1^+)$ dominates over the other transitions. Conversely, in the [1.7, 2.6] MeV energy range, several multipolarities are comparable in magnitude, even if the cross sections of the transitions to the 2^- states of ^{40}K at 2.047 and 2.419 MeV, with ejectile $^{18}F_{g.s.}(1^+)$, are somewhat larger than the others.

An interesting result comes out from a comparison of the calculated cross sections for the 2^-,3^-,4^-, and 5^- multiplet of states at 0.800, 0.029, 0.0, and 0.891 MeV, respectively. Although these states refer to the same particle-hole structure with one neutron in the $1f_{7/2}$ orbital coupled to a $1d_{3/2}$ proton hole, the calculated cross sections strongly enhance the 2^-. Indeed, the 2^- cross section is larger than the 3^-, 4^-, and 5^-, by a factor of 21, 17, and 185, respectively. A close inspection of the calculated form factors reveals that the $(L = 1, S = 1)$-component of the 2^- transition carries a certain amount of collectivity, reminiscent of the spin-dipole collectivity seen in other reactions, see Lenske et al. (2019) and Austin et al. (2001). The $L = 3$ multipoles entering in the 2^-, 3^-, 4^-, and 5^- transitions are comparable, while the $L = 5$ components, contributing to the excitations of the 4^- and 5^- states, are the smallest. Thus, an interesting selectivity of the smallest L transfer for this SCE reaction is found. Similar behavior is observed in (^{3}He,t) (Ajzenberg-Selove et al., 1985) and (^{12}C,^{12}N) reactions (von Oertzen, 1988) on the same target, where again the 2^- state is the most populated, thus suggesting a universal property of the nuclear response to the nucleon–nucleon isovector interaction.

The plots in **Figure 4** tell us that the direct SCE mechanism allows the reproduction of the shape of the measured angular distribution. Regarding the absolute cross sections, the data are slightly underestimated in the regions of low excitation, while a good agreement is found in the excitation energy region between 1.7 and 2.6 MeV.

Simple semiclassical estimates for the energy and angular momentum matching for the transfer processes (Brink, 1972) suggest that a cross section of a relevant magnitude may be expected in the region of the ground state, progressively decreasing at higher excitation energies. Thus, the multi-nucleon transfer mechanism is expected to play a major role in the low excitation energy region of the spectrum explaining the larger experimental cross section with respect to the direct mechanism calculations.

CONCLUSIONS

The ^{40}Ca(^{18}O,^{18}F)^{40}K charge exchange reaction, together with the elastic scattering and inelastic scattering of ^{18}O on ^{40}Ca, has been studied at an incident energy of 275 MeV and at forward angles using the MAGNEX spectrometer. The availability of this complete set of data, where the absolute cross section at different angles has been measured with high precision, has allowed a constrained and reliable description of the direct reaction mechanism for the charge exchange process. Charge exchange cross section calculations have been performed in DWBA using a CCEP tested against the elastic and inelastic scattering data and form factors extracted from double folding of a nucleon–nucleon isovector interaction with QRPA transition densities. Such full quantum-mechanical calculations with microscopic nuclear structure inputs describe the order of magnitude and shape of the observed cross sections. Selectivity of this reaction to the different angular momentum transfer components is revealed, making this probe an interesting tool to explore the nuclear response to isovector operators with high momentum as those entering the $0\nu\beta\beta$ NME.

It is worthwhile to emphasize that the above-mentioned calculations are based on a quite involved approach, starting from microscopic nuclear response functions, combined with free-space nucleon–nucleon interactions to derive the transition form factors and fixing ion–ion ISI and FSI by elastic scattering and inelastic scattering. The advantage of such a demanding program is evident from the fact that the data are quite well-described without the need to introduce additional scaling factors, as it was found necessary in the former heavy-ion-induced SCE reactions on the same target such as the ^{40}Ca(^{7}Li,^{7}Be)^{40}K reaction at 35 MeV (Williams-Norton et al., 1979) or the pioneering studies on (^{18}O,^{18}F) on different targets (Kim et al., 1979; Horen et al., 1986; Fifield et al., 1993).

The origin of the remaining difference between the theoretical and experimental results is not easy to access. On a nuclear structure side, there is some room left for refinements of the nuclear response functions by going deeper into the dynamics of polarization effects, e.g., in the multi-phonon approach of Lenske and Tsoneva (2019) or by second RPA methods of Gambacurta et al. (2020). On the reaction side, the competing sequential nucleon transfer mechanism should be studied, mainly for reasons of completeness. Based on the presently available results, a rather successful description of the higher excitation energy region by the direct SCE mechanism strongly hints at a rather insignificant role of nucleon transfer, at least in that spectral region, as indeed it is expected from the matching conditions for transfer processes (Brink, 1972). Nevertheless, the contribution of the transfer mechanism to the SCE process would not prevent any extrapolation to DCE reactions, where transfer processes

are expected to be safely negligible as experimentally checked (Cappuzzello et al., 2015a; Ferreira et al., in preparation) and because they are processes of a higher order than a direct DCE.

DATA AVAILABILITY STATEMENT

The raw data supporting the conclusions of this article will be made available by the authors, without undue reservation.

AUTHOR CONTRIBUTIONS

MCa, JB, SC, CA, SB, FC, DCar, and MCo contributed to conception and design of the study. MCa, SC, CA, FC, DCar, AS, LA, PA-V, TB-L, GB, DCal, VC, EC, IC, FD, HD, CE, PF, SF, MF, AF, MG, AH, FI, RL, NM, MM, JO, AP, LP, HP, FP, GR, OS, SS, VS, GS, DT, ST, AY, and VZ participated to the data taking. SC, ND, and DCar performed the data reduction. JB, SC, HL, JL, and AS performed the calculations. MCa wrote the first draft of the manuscript. JB wrote a section of the manuscript. All authors contributed to manuscript revision, read, and approved the submitted version.

FUNDING

This project has received funding from the European Research Council (ERC) under the European Union's Horizon 2020 Research and Innovation Program (Grant Agreement No. 714625). Partial funding by the European Union's Horizon 2020 research and innovation program under Grant No. 654002 is acknowledged. The grants DGAPA-UNAM IN107820, AG101120, and CONACyT 314857, Mexico, FAPESP (Fundação de Amparo à Pesquisa do Estado de São Paulo, proc. 2019/07767-1), and INCT: Instituto Nacional de Ciência e Tecnologia-Física Nuclear e Aplicações (INCT-FNA, research project 464898/2014-5), Brazil are also acknowledged. HL acknowledges support by INFN and DFG, Grant Le439/16.

REFERENCES

Ajzenberg-Selove, F., Brown, R. E., Flynn, E. R., and Sunier, J. W. (1985). (t,3He) reactions on 40,42,44Ca, 46,48,50Ti, 54Cr, and 54Fe. *Phys. Rev. C* 32, 756–780. doi: 10.1103/PhysRevC.32.756

Akimune, H., Ejiri, H., Hattori, F., Agodi, C., Alanssari, M., Cappuzzello, F., et al. (2020). Spin-dipole nuclear matrix element for the double beta decay of 76Ge by the (He3,t) charge-exchange reaction. *J. Phys. G: Nucl. Part. Phys.* 47:05LT01. doi: 10.1088/1361-6471/ab7a87

Alford, W. P., and Spicer, B. M. (1998). Nucleon charge-exchange reactions at intermediate energy. *Adv. Nucl. Phys.* 1:24. doi: 10.1007/0-306-47073-X_1

Alvarez, M. A. G., Chamon, L. C., Hussein, M. S., Pereira, D., Gasques, L. R., Rossi, J.r., et al. (2003). A parameter-free optical potential for the heavy-ion elastic scattering process. *Nucl. Phys. A* 723, 93–103. doi: 10.1016/S0375-9474(03)01158-8

Anantaraman, N.,Toki, H., and Bertsch, G. F. (1983). An effective interaction for inelastic scattering derived from the Paris potential. *Nucl. Phys. A* 398, 269–278. doi: 10.1016/0375-9474(83)90487-6

Austin, S. M., Adamides, E., Galonsky, A., Nees, T., Sterrenburg, W. A., Bainum, D. E., et al. (2001). Splitting of the dipole and spin-dipole resonances. *Phys. Rev. C* 63:034322. doi: 10.1103/PhysRevC.63.034322

Bellone, J. I., Burrello, S., Colonna, M., Lay, J.-A., and Lenske, H. (2020). Two-step description of heavy ion double charge exchange reactions. *Phys. Lett. B*, 807:135528. doi: 10.1016/j.physletb.2020.135528

Brink, D. M. (1972). Kinematical effects in heavy-ion reactions. *Phys. Lett. B* 40, 37–40. doi: 10.1016/0370-2693(72)90274-2

Calabrese, S., Cappuzzello, F., Carbone, D., and Cavallaro, M. (2020). Analysis of the background on cross section measurements with the MAGNEX spectrometer:The (20Ne,20O) Double Charge Exchange case. *Nucl. Inst. Meth. Phys. Res. A* 980:164500. doi: 10.1016/j.nima.2020.164500

Cappuzzello, F., Agodi, C., Bondì, M., Carbone, D., Cavallaro, M., Cunsolo, A., et al. (2014). A broad angular-range measurement of elastic and inelastic scatterings in the 16O on 27Al reaction at 17.5 MeV/u. *Nucl. Instr. Meth. A* 763, 314–319. doi: 10.1016/j.nima.2014.06.058

Cappuzzello, F., Agodi, C., Carbone, D., and Cavallaro, M. (2016). The MAGNEX spectrometer: Results and perspectives. *Eur. Phys. J. A* 52:169. doi: 10.1140/epja/i2016-16167-1

Cappuzzello, F., Agodi, C., Cavallaro, M., Carbone, D., Tudisco, S., Lo Presti, D., et al. (2018). The NUMEN project: NUclear Matrix Elements for neutrinoless double beta decay. *Eur. Phys. J. A* 54:72. doi: 10.1140/epja/i2018-12509-3

Cappuzzello, F., Carbone, D., and Cavallaro, M. (2011). Measuring the ions momentum vector with a large acceptance magnetic spectrometer. *Nucl. Instrum. Methods A* 638, 74–82. doi: 10.1016/j.nima.2011.02.045

Cappuzzello, F., Carbone, D., Cavallaro, M., Bond,ì, M., Agodi, C., Azaiez, F., et al. (2015b). Signatures of the giant pairing vibration in the 14C and 15C atomic nuclei. *Nat. Commun.* 6:6743. doi: 10.1038/ncomms7743

Cappuzzello, F., and Cavallaro, M. (2020). Nuclear response to second-order isospin probes in connection to double beta decay. *Universe* 6:217. doi: 10.3390/universe6110217

Cappuzzello, F., Cavallaro, M., Agodi, C., Bond,ì, M., Carbone, D., et al. (2015a). Heavy-ion double charge exchange reactions: a tool toward 0nbb nuclear matrix elements. *Eur. Phys. J. A* 51:145. doi: 10.1140/epja/i2015-15145-5

Cappuzzello, F., Cavallaro, M., Cunsolo, A., Foti, A., Carbone, D., et al. (2010). A particle identification technique for large acceptance spectrometers. *Nucl. Instrum. Methods A* 621, 419–423. doi: 10.1016/j.nima.2010.05.027

Cappuzzello, F., Lenske, H., Cunsolo, A., Beaumel, D., Fortier, S., Foti, A., et al. (2004a). Analysis of the 11B(7Li, 7Be)11Be reaction at 57 MeV in a microscopic approach. *Nuclear Phys. A* 739, 30–56. doi: 10.1016/j.nuclphysa.2004.03.221

Cappuzzello, F., Orrigo, S. E. A., Cunsolo, A., Lenske, H., Allia, M. C., Beaumel, D., et al. (2004b). Excited states of 15C. *Europhys. Lett.* 65, 766–772. doi: 10.1209/epl/i2003-10197-8

Carbone, D. (2015). Signals of the Giant Pairing Vibration in 14C and 15C nuclei populated by (18O,16O) two-neutron transfer reactions. *Eur. Phys. J. Plus.* 130 143. doi: 10.1140/epjp/i2015-15143-0

Carbone, D., Ferreira, J. L., Calabrese, S., Cappuzzello, F., Cavallaro, M., Hacisalihoglu, A., et al. (2020). Analysis of two-nucleon transfer reactions in the 20Ne+116Cd system at 306 MeV. *Phys. Rev. C* 102:044606. doi: 10.1103/PhysRevC.102.044606

Carbone, D., Ferreira, J. L., Cappuzzello, F., Lubian, J., Agodi, C., et al. (2017). Microscopic cluster model for the description of new experimental results on the 13C(18O,16O)15C two-neutron transfer at 84 MeV incident energy. *Phys. Rev. C* 95:034603. doi: 10.1103/PhysRevC.95.034603

Carbone, D., Linares, R., Amador-Valenzuela, P., Calabrese, S., Cappuzzello, F., Cavallaro, M., et al. (2021). Initial state interaction for the 20Ne+130Te and 18O+116Sn Systems at 15.3 AMeV from elastic and inelastic scattering. *Measur. Univ.* 7:58. doi: 10.3390/universe7030058

Cardozo, E. N., Lubian, J., Linares, R., Cappuzzello, F., Carbone, D., Cavallaro, M., et al. (2018). Competition between direct and sequential two-neutron transfers in the 18O + 28Si collision at 84 MeV. *Phys. Rev. C* 97:064611. doi: 10.1103/PhysRevC.97.064611

Cavallaro, M. (2011). Preliminary study of the 19F(7Li, 7Be)19O reaction at 52MeV with MAGNEX. *Nuovo Cimento* 34, 1–9. doi: 10.1393/ncc/i2011-10924-8

Cavallaro, M., Aciksoz, E., Acosta, L., Agodi, C., Auerbach, N., Bellone, J., et al. (2017). NURE: an ERC project to study nuclear reactions for neutrinoless double beta decay. *Proc. Sci.* 302:015. doi: 10.22323/1.302.0015

Cavallaro, M., Cappuzzello, F., Bond,ì, M., Carbone, D., Garcia, V. N., Gargano, A., et al. (2013). Quantitative analysis of two-neutron correlations in the 12C(18O,16O)14C reaction. *Phys. Rev. C* 88:054601. doi: 10.1103/PhysRevC.88.054601

Cavallaro, M., Cappuzzello, F., Carbone, D., Cunsolo, A., Foti, A., Khouaja, A., et al. (2012). The low-pressure focal plane detector of the MAGNEX spectrometer. *Eur. Phys. J. A* 48:59. doi: 10.1140/epja/i2012-12059-8

Cavallaro, M., Cappuzzello, F., Carbone, D., Cunsolo, A., Foti, A., Linares, R., et al. (2011). Transport efficiency in large acceptance spectrometers. *Nucl. Instr. Meth. A* 637, 77–87. doi: 10.1016/j.nima.2011.01.078

Chamon, L. C., Carlson, B. V., Gasques, L. R., Pereira, D., De Conti, C., Alvarez, M. A. G., et al. (2002). Toward a global description of the nucleus-nucleus interaction. *Phys. Rev. C* 66:014610. doi: 10.1103/PhysRevC.66.014610

Crema, E., Otomar, D. R., Simões, R. F., Barioni, A., Monteiro, D. S., Ono, L. K., et al. (2011). Near-barrier quasielastic scattering as a sensitive tool to derive nuclear matter diffuseness. *Phys. Rev. C* 84:024601. doi: 10.1103/PhysRevC.84.024601

Diel, F., Fujita, Y., Fujita, H., Cappuzzello, F., Ganioglu, E., Greweet, E.-W., et al. (2019). High-resolution study of the Gamow-Teller strength in the 64Zn(3He,t)64Ga reaction. *Phys. Rev. C* 99:054322. doi: 10.1103/PhysRevC.99.054322

Douma, C. A., Agodi, C., Akimune, H., Alanssari, M., Cappuzzello, F., Carbone, D., et al. (2020). Gamow–Teller strength distributions of 116Sb and 122Sb using the (3He, t) charge-exchange reaction. *Eur. Phys. J. A* 56:51. doi: 10.1140/epja/s10050-020-00044-9

Ejiri, H. (2005). Double beta decays and neutrino masses. *Phys. Soc. Jpn*. 74, 2101–2127. doi: 10.1143/JPSJ.74.2101

Ejiri, H., Soukouti, N., and Suhonen, J. (2014). Spin-dipole nuclear matrix elements for double beta decays and astro-neutrinos. *Phys. Lett. B* 729, 27–32. doi: 10.1016/j.physletb.2013.12.051

Ejiri, H., Suhonen, J., and Zuber, K. (2019). Neutrino–nuclear responses for astro-neutrinos, single beta decays and double beta decays. *Phys. Rep*. 1:797. doi: 10.1016/j.physrep.2018.12.001

Ermamatov, M. J., Cappuzzello, F., Lubian, J., Cubero, M., Agodi, C., Carbone, D., et al. (2016). Two-neutron transfer analysis of the 16O(18O,16O)18O reaction. *Phys. Rev. C* 94:024610. doi: 10.1103/PhysRevC.94.024610

Ermamatov, M. J., Linares, R., Lubian, J., Ferreira, L., Cappuzzello, F., Carbone, D., et al. (2017). Comprehensive analysis of high-lying states in 18O populated with (t, p) and (18O,16O) reactions. *Phys. Rev. C* 96:044603. doi: 10.1103/PhysRevC.96.044603

Ferreira, J. L., Carbone, D., Cavallaro, M., Deshmukh, N. N., Agodi, C., and Brischetto, G. A. (2021). Analysis of two-proton transfer in the 40Ca(18O,20Ne)38Ar reaction at 270 MeV. *Phys. Rev. C.*

Fifield, L. K., Catford, W. N., Orr, N. A., Ophel, T. R., Etchegoyen, A., and Etchegoyen, M. C. (1993). Charge-exchange reactions on 36S. *Nucl. Phys. A* 552, 125–139. doi: 10.1016/0375-9474(93)90335-U

Fonseca, L. M., Linares, R., Zagatto, V. A. B., Cappuzzello, F., Carbone, D., Cavallaro, M., et al. (2019). Elastic and inelastic scattering of 16O on 27Al and 28Si at 240 MeV. *Phys. Rev. C* 100:014604. doi: 10.1103/PhysRevC.100.014604

Franey, M. A., and Love, W. G. (1985). Nucleon-nucleon t-matrix interaction for scattering at intermediate energies. *Phys. Rev. C* 31:488. doi: 10.1103/PhysRevC.31.488

Frekers, D., Puppe, P., Thies, J. H., and Ejiri, H. (2013). Gamow–Teller strength extraction from (3He, t) reactions. *Nuclear Phys A* 916, 219–240. doi: 10.1016/j.nuclphysa.2013.08.006

Fujita, H., Fujita, Y., Adachi, T., Bacher, A. D., Berg, G. P. A., et al. (2007). Isospin structure of Jπ =1+states in 58Ni and 58Cu studied by 58Ni(p,p') and 58Ni(3He,t)58Cu measurements. *Phys. Rev. C* 75:034310. doi: 10.1103/PhysRevC.75.034310

Fujita, Y., Hatanaka, K., Berg, G. P. A., Hosono, K., Matsuo, N., Morinobu, S., et al. (1997). Matching of a beam line and a spectrometer New beam line project at RCNP. *Nucl. Instrum. Methods Phys. Res. B* 126, 274–278. doi: 10.1016/S0168-583X(96)01008-7

Fujita, Y., Rubio, B., and Gelletly, W. (2011). Spin–isospin excitations probed by strong, weak and electro-magnetic interactions. *Progr. Particle Nuclear Phys.* 66, 549–606. doi: 10.1016/j.ppnp.2011.01.056

Gambacurta, D., Grasso, M., and Engel, J. (2020). Gamow-teller strength in 48Ca and 78Ni with the charge-exchange subtracted second random-phase approximation. *Phys. Rev. Lett*. 125:212501. doi: 10.1103/PhysRevLett.125.212501

Horen, D. J., Burks, B. L., Fernandes, M. A. G., Auble, R. L., Bertrand, F. E., Blankenship, J. L., et al. (1986). Investigation of the one-step direct contribution to the 28Si (18O, 18F) 28Al reaction at 19.6 MeV/nucleon. *Phys. Lett. B* 181, 38–42. doi: 10.1016/0370-2693(86)91250-5

Jokiniemi, L., Suhonen, J., Ejiri, H., and Hashim, I. H. (2019). Pinning down the strength function for ordinary muon capture on 100Mo. *Phys. Lett. B*, 794, 143–147. doi: 10.1016/j.physletb.2019.05.037

Khoa, D. T., and Satchler, G. R. (2000). Generalized folding model for elastic and inelastic nucleus–nucleus scattering using realistic density dependent nucleon–nucleon interaction. *Nucl. Phys. A* 668, 3–41. doi: 10.1016/S0375-9474(99)00680-6

Kibedi, T., and Spear, R. H. (2002). Atomic data and nuclear data *Tables* 80, 35–82. doi: 10.1006/adnd.2001.0871

Kim, B. T., Greiner, A., Fernandes, M. A. G., Lisbona, N., Low, K. S., and Mermaz, M. C. (1979). Heavy-ion charge exchange reaction 28Si(18O,18F)28Al. *Phys. Rev. C* 20:1396–1407. doi: 10.1103/PhysRevC.20.1396

Lenske, H. (1988). Theory of heavy ion charge exchange scattering at low and intermediate energies. *Nucl. Phys. A* 482, 343c–356c. doi: 10.1016/0375-9474(88)90595-7

Lenske, H., Bellone, J. I., Colonna, M., and Lay, J.-A. (2018). Theory of single-charge exchange heavy-ion reactions. *Phys. Rev. C* 98:044620. doi: 10.1103/PhysRevC.98.044620

Lenske, H., Cappuzzello, F., Cavallaro, M., and Colonna, M. (2019). Heavy ion charge exchange reactions as probes for nuclear beta-decay. *Progress Part. Nuclear Phys.* 109:103716. doi: 10.1016/j.ppnp.2019.103716

Lenske, H., and Tsoneva, N. (2019). Dissolution of shell structures and the polarizability of dripline nuclei. *Eur. Phys. J. A* 55:238. doi: 10.1140/epja/i2019-12811-6

Linares, R., Ermamatov, M. J., Lubian, J., Cappuzzello, F., Carbone, D., Cardozo, E. N., et al. (2018). Analysis of the one-neutron transfer to 16O, 28Si, and 64Ni induced by the (18O,17O) reaction at 84 MeV. *Phys. Rev C*. 98:054615. doi: 10.1103/PhysRevC.98.054615

Lubian, J., and Nunes, F. M. (2007). Searching for a polarization potential in the breakup of ^{8}B. *J. Phys. G: Nucl. Part. Phys*. 34, 513–521. doi: 10.1088/0954-3899/34/3/009

Nociforo, C., Cappuzzello, F., Cunsolo, A., Foti, A., Orrigo, S. E. A., Winfield, J. S., et al. (2006). Exploring the Nα+3n light nuclei via the (7Li,7Be) reaction. *Eur. Phys. J. A* 27, 283–288. doi: 10.1007/3-540-32843-2_43

Ohkubo, S., and Hirabayashi, Y. (2014). Evidence for a secondary bow in Newton's zero-order nuclear rainbow. *Phys. Rev. C* 89:051601(R). doi: 10.1103/PhysRevC.89.051601

Oliveira, J. R. B., Cappuzzello, F., Chamon, L. C., Pereira, D., Agodi, C., Bond,í M., et al. (2013). Study of the rainbow-like pattern in the elastic scattering of 16O on 27Al at Elab.= 100 MeV. *J. Phys. G: Nucl. Part. Phys*. 40:105101. doi: 10.1088/0954-3899/40/10/105101

Osterfeld, F. (1992). Nuclear spin and isospin excitation. *Rev. Modern Phys.* 64, 491–557. doi: 10.1103/RevModPhys.64.491

Paes, B., Santagati, G., Magana Vsevolodovna, R., Cappuzzello, F., Carbone, D., Cardozo, E. N., et al. (2017). Long-range versus short-range correlations in the two-neutron transfer reaction 64Ni(18O,16O)66Ni. *Phys. Rev. C* 96:044612. doi: 10.1103/PhysRevC.96.044612

Pereira, D., Lubian, J., Oliveira, J. R. B., de Sousa, D. P., Chamon, L. C., et al. (2009). An imaginary potential with universal normalization for dissipative processes in heavy-ion reactions. *Phys. Lett. B* 670, 330–335. doi: 10.1016/j.physletb.2008.10.066

Pritychenko, B., Birch, M., Singh, B., and Horoi, M. (2016). Tables of E2 transition probabilities from the first 2+ states in even–even nuclei. *At. Data Nucl. Data Tables* 107:1. doi: 10.1016/j.adt.2015.10.001

Pritychenko, B., Birch, M., Singh, B., and Horoi, M. (2017). Erratum to Tables of E2 transition probabilities from the first 2+ states in even-even nuclei. *At. Data Nucl. Data Tables* 114:371. doi: 10.1016/j.adt.2016.08.002

Rangel, J., Lubian, J., Canto, L. F., and Gomes, P. R. S. (2016). Effect of Coulomb breakup on the elastic cross section of the 8B proton-halo projectile on a heavy, 208Pb target. *Phys. Rev. C* 93:054610. doi: 10.1103/PhysRevC.93.054610

Santopinto, E., García-Tecocoatzi, H., Magaña Vsevolodovna, R. I., and Ferretti, J. (2018). Heavy-ion double-charge-exchange and its relation to neutrinoless double-beta decay. *Phys. Rev. C* 98:061601. doi: 10.1103/PhysRevC.98.061601

Satchler, G. R. (1983). *Direct Nuclear Reactions*. Oxford: Oxford University Press.

Spatafora, A., Cappuzzello, F., Carbone, D., Cavallaro, M., Lay, J. A., Acosta, L., et al. (2019). 20Ne+76Ge elastic and inelastic scattering at 306 MeV. *Phys. Rev. C* 100:034620. doi: 10.1103/PhysRevC.100.034620

Taddeucci, T. N., Goulding, C. A., Carey, T. A., Byrd, R. C., Goodman, D. C., Gaarde, C., et al. (1987). The (p, n) reaction as a probe of beta decay strength. *Nucl. Phys. A* 469, 125–172. doi: 10.1016/0375-9474(87)90089-3

Thompson, I. J. (1988). Getting started with FRESCO. *Comput. Phys. Rep.* 7, 167–211. doi: 10.1016/0167-7977(88)90005-6

Thompson, I. J., Nagarajan, M. A., Lilley, J. S., and Fulton, B. R. (1985). Contribution of multistep transfers to low-energy elastic and reaction cross sections. *Phys. Lett. B* 157:250. doi: 10.1016/0370-2693(85)90660-4

Thompson, I. J., Nagarajan, M. A., Lilley, J. S., Smithson, M. J., et al. (1989). The threshold anomaly in 16O+208Pb scattering. *Nucl. Phys. A* 505,84–102. doi: 10.1016/0375-9474(89)90417-X

Torresi, D., Sgouros, O., Soukeras, V., Cavallaro, M., Cappuzzello, F., Carbone, D., et al. (2021). An upgraded focal plane detector for the MAGNEX spectrometer. *Nucl. Instr. and Meth. A* 989:164918. doi: 10.1016/j.nima.2020.164918

von Oertzen, W. (1988). Excitation of isovector modes in heavy ion induced charge exchange reactions. *Nucl. Phys. A* 482, 357c–372c. doi: 10.1016/0375-9474(88)90596-9

Williams-Norton, M. E., Petrovich, F., Kemper, K. W., Puigh, R. J., Stanley, D., et al. (1979). Charge exchange study with the 40Ca(7Li, 7Be)40K reaction. *Nucl. Phys. A* 313, 477–484. doi: 10.1016/0375-9474(79)90514-1

Zagatto, V. A. B., Cappuzzello, F., Lubian, J., Cavallaro, M., Linares, R., Carbone, D., et al. (2018). Important role of projectile excitation in 16O + 60Ni and 16O + 27Al scattering at intermediate energies. *Phys. Rev. C* 97:054608. doi: 10.1103/PhysRevC.97.054608

Conflict of Interest: The authors declare that the research was conducted in the absence of any commercial or financial relationships that could be construed as a potential conflict of interest.

frontiers in Physics

MINI REVIEW
published: 21 May 2021
doi: 10.3389/fphy.2021.666591

Brief Review of the Results Regarding the Possible Underlying Mechanisms Driving the Neutrinoless Double Beta Decay

Andrei Neacsu[1,2]*, *Vasile Alin Sevestrean*[1,2] *and Sabin Stoica*[1,2]

[1] International Centre for Advanced Training and Research in Physics, Mgurele, Romania, [2] Horia Hulubei National Institute for R&D in Physics and Nuclear Engineering, Department of Theoretical Physics, Mgurele, Romania

Since the experimental discovery of neutrino oscillations, the search for the neutrinoless double beta ($0\nu\beta\beta$) decay has intensified greatly, as this particular decay mode, if experimentally discovered, could offer a testing ground for Beyond Standard Model (BSM) theories related to the yet hidden fundamental properties of neutrinos and the possibility of violating of some fundamental symmetries. In this work we make a brief review of the nuclear matrix elements and phase space factors calculations performed mainly by our group. Next, using these calculations and the most recent experimental half-life limits, we revise the constraints on the BSM parameters violating the lepton number corresponding to four mechanisms that could contribute to $0\nu\beta\beta$ decay. Finally, using the values obtained for the BSM parameters from one of the most sensitive double-beta decay experiments, we provide a comparison with the sensitivities of other experiments.

Keywords: double beta decay, nuclear matrix elements, phase-space factors, shell model, beyond standard model, neutrino

OPEN ACCESS

Edited by:
Theocharis S. Kosmas, University of Ioannina, Greece

Reviewed by:
Bhupal Dev, Washington University in St. Louis, United States
Carlo Giunti, Ministry of Education, Universities and Research, Italy

***Correspondence:**
Andrei Neacsu
nandrei@theory.nipne.ro

Specialty section:
This article was submitted to High-Energy and Astroparticle Physics, a section of the journal Frontiers in Physics

Received: *10 February 2021*
Accepted: *16 April 2021*
Published: *21 May 2021*

Citation:
Neacsu A, Sevestrean VA and Stoica S (2021) Brief Review of the Results Regarding the Possible Underlying Mechanisms Driving the Neutrinoless Double Beta Decay. Front. Phys. 9:666591. doi: 10.3389/fphy.2021.666591

1. INTRODUCTION

Two decades ago, the successful experimental measurement of neutrino oscillations [1, 2] established that neutrinos have a mass different from zero. Although this discovery was a significant one, many of the neutrino properties still remain unknown to this day. Because in neutrino oscillation experiments only squared mass differences can be measured, we still have unanswered questions regarding their absolute masses, the mass hierarchy, the underlying mechanism that gives neutrinos mass, and even the very nature of the neutrinos (whether they are Dirac or Majorana particles). While there are many experimental and theoretical endeavors to bring clear answers to some of these questions, like high-precision calculations, measurements of different single-β decays, cosmological observations, the double-beta decay (DBD) and particularly the $0\nu\beta\beta$ decay mode are still considered the most appealing approaches to study the yet unknown properties of neutrinos. However, even if one $0\nu\beta\beta$ transition event would be experimentally observed, not all of the desired information about neutrinos would be immediately revealed. Recording such an event would demonstrate that the lepton number conservation is violated by two units, but cannot indicate the mechanism that dominates this process. Many large-scale experiments dedicated to the discovery of this lepton number violating (LNV) decay are already collecting data, with up-dates and new ones planned for the future, but so far there is

no experimental proof of $0\nu\beta\beta$ transitions, only reports of lower limits for the corresponding half-lives. Experimentally, DBD of the isotopes ^{76}Ge and ^{136}Xe are currently the most accurately measured, but others like ^{48}Ca, ^{82}Se, and ^{130}Te are also investigated, with ^{124}Sn being considered for the future. There are advantages and disadvantages to studying each of these isotopes (costs, purity, Q-value, background signals, etc.), but the fact that different ones are being investigated is of great importance if an experimental confirmation is obtained for any of them. Theoretical studies of $0\nu\beta\beta$ involve the computation of nuclear matrix elements (NME) and phase space factors (PSF) appearing in the half-life expressions, whose precise calculation is essential for predicting the neutrino properties and interpretation of the DBD experimental data. Particularly, the NME computation is the subject of the largest uncertainties, so much effort is devoted to their accurate estimation. The most commonly used nuclear structure approaches for the NME calculation are proton-neutron Quasi Random Phase Approximation (pnQRPA) [3–11], Interacting Shell Model (ISM) [12–30], Interacting Boson Model (IBM-2) [31–35], Projected Hartree Fock Bogoliubov method (PHFB) [36], Energy Density Functional method (EDF) [37], and the Relativistic Energy Density Functional method (REDF) [38]. Each of these methods presents various advantages and disadvantages when compared to each other, especially when dealing with the nuclear structure of particular isotopes. Once experimentally confirmed, it is also important to establish the underlying mechanism(s) that may contribute to the $0\nu\beta\beta$ decay, as to properly extend the Standard Model. For the longest time, studies only addressed the so called "mass mechanism" that involves the exchange of light left-handed (LH) Majorana neutrinos. Presently, more scenarios are being considered and their investigation consists of calculating of the NME associated to each mechanism and the corresponding PSF. For example, possible contributions to $0\nu\beta\beta$ decay may come via the exchange of the right-handed (RH) heavy neutrinos [39]. Other contributions from possible RH components of the weak currents, through the so-called "λ" and "η" mechanisms could also be taken into account [40]. One of the most popular model that includes these mechanisms is the left-right symmetric model (LRSMM) [41–45]. In this work we consider several of these scenarios for $0\nu\beta\beta$ decay, following the prescriptions of [46]. We present and discuss the NME and PSF calculations that were recently published by our group. For the nuclear structure calculations our group and collaborators use Shell Model (ShM) techniques and codes [19–29]. For the PSF calculations we use our results from [47, 48] for the light neutrino and the heavy neutrino exchange mechanisms, and results from [49] for the other mechanisms. Using the latest experimental limits for the half-lives reported in literature, we up-date the constraints on the LNV parameters corresponding to each mechanism. Finally, we use the calculated values of the LNV parameters deduced with the half-life limits taken from the ^{76}Ge experiment [50], to evaluate the half-lives of the other four isotopes that should be achieved by their experiments to reach the sensitivity of the Ge experiment.

2. BRIEF FORMALISM OF THE $0\nu\beta\beta$ DECAY

For a long time, most of the $0\nu\beta\beta$ decay literature has focused its interest mainly on the mass mechanism, that assumes that this decay mode occurs via the exchange of light LH Majorana neutrinos between two nucleons inside the nucleus. The inclusion of contributions coming from RH components of the weak currents has also been discussed (for example in [40, 51]), but very few papers presented theoretical results considering these contributions. However, any mechanism/scenario that violates with two units the lepton number conservation may, in principle, contribute to the decay rate. Considering several mechanisms, the $0\nu\beta\beta$ decay half-life can be written in a factorized compact form, as a sum of products of PSF, NME, and the BSM parameters, corresponding to each mechanism [52], as follows:

$$\left[T^{0\nu}_{1/2}\right]^{-1} = g_A^4 \left[\sum_i |\mathcal{E}_i|^2 \mathcal{M}_i^2 + Re \sum_{i\neq j} \mathcal{E}_i \mathcal{E}_j \mathcal{M}_{ij}\right]. \quad (1)$$

Here, the $\mathcal{E}_i$ contain the BSM parameters associated with the following mechanisms: $\mathcal{E}_1 = \mathcal{E}_{0\nu} = \sum_k^{light} U_{ek}^2 \frac{m_k}{m_e}$ the exchange of light LH neutrinos, $\mathcal{E}_2 = \mathcal{E}_\lambda = \left(\frac{M_{WL}}{M_{WR}}\right)^2 \left|\sum_k^{light} U_{ek} V_{ek}\right|$ corresponds to the "λ mechanism" with RH leptonic and LH hadronic currents, $\mathcal{E}_3 = \mathcal{E}_\eta = \xi \left|\sum_k^{light} U_{ek} V_{ek}\right|$ is associated to the "η mechanism" with RH leptonic and RH hadronic currents, and $\mathcal{E}_4 = \mathcal{E}_{0N} = \left(\frac{M_{W_L}}{M_{W_R}}\right)^4 \sum_k^{heavy} V_{ek}^2 \frac{m_p}{M_k}$ comes from the exchange of heavy RH neutrinos, with m_e being the electron mass and m_p the proton mass. M_{WL} and M_{WR} denote the masses of the LH and the RH W bosons, respectively. We assume that the neutrino mass eigenstates are separated as light, $m_k (m_k \ll 1\ eV)$, and heavy, $M_k (M_k \gg 1\ GeV)$. U_{ek} and V_{ek} are electron neutrino mixing matrices for the light LH and heavy RH neutrino, respectively [14, 44]. Following [4–6, 39, 46], $\mathcal{M}_i^2$ are factors expressed in a standardized form as combinations of NME described in Equation (2) and integrated PSF denoted with $G_{01} - G_{09}$. Values for the PSF used in this paper can be seen in **Table 1**, together with our ShM values for the individual NME M_α (with $\alpha = GTq, Fq, Tq, GT\omega, F\omega, P, R, M_{GTN}, M_{FN}$, and M_{TN}). Assuming that only one mechanism dominates the $0\nu\beta\beta$ transition, we can perform a so called "on-axis" analysis where the interference terms $\mathcal{E}_i \mathcal{E}_j \mathcal{M}_{ij}$ are no longer taken into account.

$$\mathcal{M}_{0\nu}^2 = G_{01}\left[M_{GT} - \left(\frac{g_V}{g_A}\right)^2 M_F + M_T\right]^2, \quad (2a)$$

$$\mathcal{M}_{0N}^2 = G_{01}\left[M_{GTN} - \left(\frac{g_V}{g_A}\right)^2 M_{FN} + M_{TN}\right]^2, \quad (2b)$$

$$\mathcal{M}_\lambda^2 = G_{02}\mathcal{M}_{2+}^2 - \frac{2}{9} G_{03}\mathcal{M}_{1-}\mathcal{M}_{2+} + \frac{1}{9} G_{04}\mathcal{M}_{1-}^2 - G_{07} M_P M_R + G_{08} M_P^2 + G_{09} M_R^2, \quad (2c)$$

TABLE 1 | In the upper part we present the $Q_{\beta\beta}$ values and the calculated PSF ($G_{01} - G_{09}$) in years^{-1} for all five isotopes currently under investigation.

	^{48}Ca	^{76}Ge	^{82}Se	^{130}Te	^{136}Xe
$Q_{\beta\beta}$[MeV]	4.272/4.271	2.039/2.041	2.995/3.005	2.527/2.533	2.458/2.481
$G_{01} \cdot 10^{14}$	2.46/2.61	0.24/0.26	1.01/1.15	1.42/1.82	1.45/1.94
$G_{02} \cdot 10^{14}$	16.2/17.1	0.39/0.43	3.53/4.04	3.76/4.84	3.68/4.99
$G_{03} \cdot 10^{15}$	18.9/19.8	1.30/1.44	6.91/7.82	8.97/11.4	9.05/11.9
$G_{04} \cdot 10^{15}$	5.33/5.55	0.47/0.51	2.14/2.39	3.02/3.72	3.10/3.96
$G_{05} \cdot 10^{13}$	3.01/3.81	0.57/0.76	2.00/2.76	3.79/5.81	4.02/6.36
$G_{06} \cdot 10^{12}$	3.98/4.18	0.53/0.59	1.73/1.96	2.23/2.82	2.28/2.98
$G_{07} \cdot 10^{10}$	2.63/3, 35	0.27/0.36	1.16/1.59	1.76/2.69	1.81/2.88
$G_{08} \cdot 10^{11}$	1.11/1.64	0.15/0.24	0.71/1.17	1.55/2.85	1.66/3.16
$G_{09} \cdot 10^{10}$	16.2/17.1	1.22/1.35	4.78/5.41	4.97/6.33	4.96/6.56
M_{GT}	0.807	3.206	3.005	1.662	1.505
M_F	−0.233	−0.674	−0.632	−0.438	−0.400
M_T	0.080	0.011	0.012	−0.007	−0.008
M_{GTq}	0.709	3.228	3.034	1.587	1.440
M_{Fq}	−0.121	−0.383	−0.362	−0.249	−0.230
M_{Tq}	−0.173	−0.059	−0.058	−0.013	−0.012
$M_{GT\omega}$	0.930	3.501	3.287	1.855	1.682
$M_{F\omega}$	−0.232	−0.659	−0.618	−0.427	−0.391
M_P	0.395	−2.466	−2.332	−1.729	−1.617
M_R	1.014	3.284	3.127	2.562	2.341
M_{GTN}	58.5	162.3	150.1	107.6	96.6
M_{FN}	−22.9	−62.6	−58.1	−41.0	−36.9
M_{TN}	9.42	−0.8	0.4	−2.1	1.4

The s-wave electron PSF (G_{01}) are from [48] and the p-wave electron PSF ($G_{02} - G_{09}$) are from [49] are on the left side of each column, while the older, less rigorous values with the point-like formalism of [40] are on the right side for comparison. The lower part shows the M_α NME calculated by our group.

$$\mathcal{M}_\eta^2 = G_{02}\mathcal{M}_{2-}^2 - \frac{2}{9}G_{03}\mathcal{M}_{1+}\mathcal{M}_{2-} + \frac{1}{9}G_{04}\mathcal{M}_{1+}^2, \quad \text{(2d)}$$

$$\text{with } \mathcal{M}_{1\pm} = M_{GTq} \pm 3\left(\frac{g_V}{g_A}\right)^2 M_{Fq} - 6M_{Tq},$$

$$\text{and } \mathcal{M}_{2\pm} = M_{GT\omega} \pm \left(\frac{g_V}{g_A}\right)^2 M_{F\omega} - \frac{1}{9}\mathcal{M}_{1\pm}.$$

Detailed equations of individual NME M_α can be found in the Appendix of [46], where they have been expressed in a consistent form. The expressions for the PSF can be found in [47, 49]. We note that Equations (2a, 2b) contain combinations of NME and PSF coming from contributions of only s-wave electron wave functions, while Equations (2c, 2d) present combinations of NME and PSF with contributions only from p-wave electron wavefunctions.

To use the expressions in Equation (2), we need accurate calculations of both the PSF that embed the distortion of the motion of outgoing electrons by the electric field of the daughter nucleus, and of the NME that depend on the nuclear structure of the parent and the daughter nuclei. Thus, the theoretical investigation of $0\nu\beta\beta$ transitions is a complex task that involves knowledge of physics at the atomic level for the PSF, nuclear level when calculating the NME, and at the fundamental particle level dealing with the LNV couplings.

2.1. Phase Space Factors

For a long time, PSF that enter the $\beta\beta$ half-life equations were considered to be calculated accurately enough [40, 53]. However, more recent reevaluations of their values using methods that use improved Fermi functions and more accurate integration routines have shown relevant differences in several cases, when compared to the previous results. Within these new methods of PSF calculation, the Fermi functions are constructed with "exact" electron wave functions (w.f.) obtained by solving the Dirac equation and consider finite nuclear size (FNS) and screening effects [47–49, 54]. In addition, in [47, 48] a Coulomb potential built from a realistic proton distribution in the daughter nucleus is used and the most recent Q-values [55] are taken into account.

In the upper part of **Table 1**, we present our choice of values for the nine PSF that enter Equation (2) for the five nuclei of interest. The PSF values obtained with s-electron w.f. (G_{01}) are taken from [48], while the PSF values obtained with the p-electron w.f. ($G_{02} - G_{09}$) are from [49]. Both references provide consistently very similar values for the PSF needed in this study. Also, these current PSF values are compared to the previous calculations of [40] that relied on older $Q_{\beta\beta}$ values and where the proton distribution in the daughter nucleus, FNS, or electron screening effects were not considered. This comparison is meant to emphasize the need to use the results of newer calculations for more reliable analyzes.

TABLE 2 | The first line shows the experimental lower half-life limits $T_{1/2}$ in years.

	^{48}Ca	^{76}Ge	^{82}Se	^{130}Te	^{136}Xe
$T_{1/2}$	$2.0 \cdot 10^{22}$ [61]	$1.8 \cdot 10^{26}$ [50]	$2.5 \cdot 10^{23}$ [62]	$4.0 \cdot 10^{24}$ [63]	$1.07 \cdot 10^{26}$ [64]
$\mathcal{M}^2_{0\nu} \cdot 10^{14}$	2.62	3.13	11.8	5.29	4.43
$\mathcal{M}^2_{\lambda} \cdot 10^{13}$	1.14	0.44	3.74	1.29	1.04
$\mathcal{M}^2_{\eta} \cdot 10^{9}$	1.57	1.55	5.56	4.09	3.45
$\mathcal{M}^2_{0N} \cdot 10^{10}$	1.79	0.96	3.53	2.44	1.99
$\mathcal{E}_{0\nu}$	$2.71 \cdot 10^{-5}$	$2.61 \cdot 10^{-7}$	$3.61 \cdot 10^{-6}$	$1.35 \cdot 10^{-6}$	$2.85 \cdot 10^{-7}$
$\mathcal{E}_{\lambda}$	$1.3 \cdot 10^{-5}$	$2.21 \cdot 10^{-7}$	$2.03 \cdot 10^{-6}$	$8.62 \cdot 10^{-7}$	$1.86 \cdot 10^{-7}$
$\mathcal{E}_{\eta}$	$1.11 \cdot 10^{-7}$	$1.18 \cdot 10^{-9}$	$1.66 \cdot 10^{-8}$	$4.85 \cdot 10^{-9}$	$1.02 \cdot 10^{-9}$
$\mathcal{E}_{0N}$	$3.28 \cdot 10^{-7}$	$4.71 \cdot 10^{-9}$	$6.6 \cdot 10^{-8}$	$1.99 \cdot 10^{-8}$	$4.24 \cdot 10^{-9}$
$\langle m_{0\nu} \rangle$	13.85	0.133	1.845	0.69	0.146
$T^{\mathcal{E}_{0\nu}}_{1/2} \cdot 10^{-26}$	2.15	1.80	0.48	1.07	1.27
$T^{\mathcal{E}_{\lambda}}_{1/2} \cdot 10^{-26}$	0.69	1.80	0.21	0.61	0.75
$T^{\mathcal{E}_{\eta}}_{1/2} \cdot 10^{-26}$	1.78	1.80	0.50	0.68	0.81
$T^{\mathcal{E}_{0N}}_{1/2} \cdot 10^{-26}$	0.97	1.80	0.49	0.71	0.87

In the upper part, we present the $\mathcal{M}^2_i$ factors of Equation (2) using the NME and PSF from ***Table 1****. Displayed in the middle section are the values of the LNV parameters $\mathcal{E}_\alpha$ that can be extracted and the corresponding light left-handed Majorana neutrino mass $m_{0\nu}$ in units of eV. In the lower part, we estimate the $0\nu\beta\beta$ that are expected for all the 5 isotopes when the LNV parameters of ^{76}Ge are used in Equation (1).*

2.2. Nuclear Matrix Elements

We choose our NME values from [46]. These were calculated using ShM techniques in the closure approximation with optimal closure energies $\langle E \rangle$ taken from [21, 23, 26]. These values were found to reproduce the NME results obtained in non-closure calculations. The Hamiltonians specific for each model space are chosen such that good agrements with experimental spectroscopic observables is achieved. The testing of these Hamiltonians can be found in [27, 28], where we performed calculations of $2\nu\beta\beta$ NME, the energy spectra for the first $\left[0^+ - 6^+\right]$ states, $B(E2) \uparrow$ transition probabilities, occupation probabilities and the Gamow-Teller strengths, which were compared to the experimental data available. For ^{48}Ca in the *pf* model space $(0f_{7/2}, 1p_{3/2}, 0f_{5/2}, 1p_{1/2})$ we use the GXPF1A [56] effective Hamiltonian and $\langle E \rangle$ 0.5 MeV, for ^{76}Ge and ^{82}Se in the *jj*44 model space $(0f_{5/2}, 1p_{3/2}, 1p_{1/2}, 0g_{9/2})$ we choose the JUN45 [57] effective Hamiltonian and $\langle E \rangle$ 3.4 MeV, and for ^{130}Te and ^{136}Xe in the *jj*55 model space $(0g_{7/2}, 1d_{5/2}, 1d_{3/2}, 1s_{1/2}, 0h_{11/2})$ we use the SVD [58] effective Hamiltonian and $\langle E \rangle$ 3.5 MeV. For the calculation of our two-body NME, we use finite size effects and higher order corrections of the nucleon current (with the vector and axial-vector form factors $\Lambda_V = 850$ MeV and $\Lambda_A = 1086$ MeV, respectively), and we include short-range correlations by multiplying the harmonic oscillator wave functions $\psi_{nl}(lr)$ and the Jastrow correlation function $\psi_{nl}(r) \rightarrow \left[1 + f(r)\right] \psi_{nl}(r)$ with the CD-Bonn parametrization $(f(r) = -c \cdot e^{-ar^2} \left(1 - br^2\right)$, with $a = 1.59, b = 1.45$, and $c = 0.46)$ [19, 27–29].

The lower part of **Table 1** shows the ShM individual NME that enter Equation (2) which were calculated by our group using the effective Hamiltonians and ingredients listed above. In the values presented, the sign convention is that the Gamow-Teller NME M_{GT} is taken positive, with the other contributions having their sign listed as relative to that of M_{GT}.

3. DISCUSSIONS

This brief review summarizes our recent calculations of the PSF and NME involved in $0\nu\beta\beta$ decay for four possible decay mechanisms, namely the light LH neutrino exchange, heavy RH neutrino exchange, $\lambda-$mechanism involving RH leptonic and RH hadronic currents, and the $\eta-$mechanism involving RH leptonic and LH hadronic currents. The PSF are calculated with Fermi functions built with exact electron w.f. solutions of the Dirac equation with a Coulomb-type potential obtained from a realistic distribution of protons in the daughter nucleus. FNS and screening effects were taken into account, as well. G_{01} that include s-w.f. are taken from [48], while $G_{(02-09)}$ that include p-w.f. are taken from [49]. Between the newer and the older PSF values, one can observe numerous differences in the range of 5–30%, with some rising of up to 90% (see G_{08} of ^{136}Xe in **Table 1**). Such differences would impact the LNV values and the conclusions regarding the sensitivity of the experiments with various isotopes to the possible $0\nu\beta\beta$ mechanisms. In passing, we mention that in addition to the development of the new PSF codes, our group has also developed a very fast effective method [59] that is still based on the formalism of [40], but is fitted and tweaked to replicate the current results obtained with the most rigorous methods. Within reasonable precision, this method can be used for rapid PSF estimations and for plotting the un-integrated angular and energy electron distributions.

The NME are calculated within a ShM approach with the ingredients presented in section 2.2. ShM calculations are attractive because they consider all the correlations around the Fermi surface, respect all symmetries, and take into account consistently the effects of the missing single particle space via many-body perturbation theory (the effects were shown to be small, about 20%, for ^{82}Se [60]). In the case of closed-shell nuclei, ShM calculations using optimized Hamiltonians

for nucleon-nucleon interactions are very reliable and compare well with the spectroscopic data available from experiments. Another advantage of this approach, important for reliable calculations, is that the calculated nucleon occupancies are close to the experimental ones. ShM calculations were successful in predicting the $2\nu\beta\beta$ decay half-life of ^{48}Ca [12] before experimental measurements. Calculations of different groups largely agree with each other without the need to adjust model parameters.

From Equation (2), using the NME and PSF in **Table 1**, we calculate the $\mathcal{M}_i^2$ factors that enter the half-life in Equation (1). Using these factors and the most recent experimental half-life limits, we re-evaluate the LNV parameters corresponding to the four mechanisms. These results are presented in **Table 2**.

Table 2 first presents in the top section the experimental lower half-life limits $T_{1/2}$ in years. The next rows list the $\mathcal{M}_i^2$ factors that contain combinations of PSF and NME for the five nuclei of current experimental interest, in the case of four possible $0\nu\beta\beta$ decay mechanisms described in Equation (2). In the middle section are found the values of the LNV parameters $\mathcal{E}_i$ deduced from the experimental $T_{1/2}$ and the $\mathcal{M}_i^2$ factors. For the mass mechanism, we also show the electron neutrino mass parameters $\langle m_{0\nu}\rangle$ in units of eV that are obtained by the multiplication of $\mathcal{E}_{0\nu}$ with the electron mass m_e. This extracted $\langle m_{0\nu}\rangle$ is what is most commonly reported in the literature and is presented here for the convenience of the reader and an easier comparison with other references.

Lastly, we perform predictions of the half-lives for each isotope that would correspond to the LNV parameters extracted from one experiments of the highest sensitivity. Choosing the $\mathcal{E}_i$ LNV deduced from the ^{76}Ge experiment [50], we estimate the half-lives of the other four isotopes. These values are displayed in the lower section of **Table 2** and offer an indication about the relative sensitivity between DBD experiments.

AUTHOR CONTRIBUTIONS

All authors listed have made a substantial, direct and intellectual contribution to the work, and approved it for publication.

FUNDING

This work has been supported by the grants of Romanian Ministry of Research Innovation and Digitalization through the projects No. PN19-030102-INCDFM and CNCS - UEFISCDI No. PN-III-P4-ID-PCE-2020-2374, within PNCDI III.

ACKNOWLEDGMENTS

The authors thank Prof. Mihai Horoi for useful discussions and comments.

REFERENCES

1. Fukuda Y, Hayakawa T, Ichihara E, Inoue K, Ishihara K, Ishino H, et al. Evidence for oscillation of atmospheric neutrinos. *Phys Rev Lett.* (1998) 81:1562–7. doi: 10.1103/PhysRevLett.81.1562
2. Ahmad QR, Allen RC, Andersen TC, Anglin JD, Bühler G, Barton JC, et al. Measurement of the rate of $\nu_e + d \rightarrow p + p + e^-$ interactions produced by ^8B solar neutrinos at the sudbury neutrino observatory. *Phys Rev Lett.* (2001) 87:071301. doi: 10.1103/PhysRevLett.87.071301
3. Hirsch M, Klapdor-Kleingrothaus HV, Kovalenko SG. On the SUSY accompanied neutrino exchange mechanism of neutrinoless double beta decay. *Phys Lett B.* (1996) 372:181–6. doi: 10.1016/0370-2693(96)00050-0
4. Pas H, Hirsch M, Klapdor-Kleingrothaus HV, Kovalenko SG. Towards a superformula for neutrinoless double beta decay. *Phys Lett B.* (1999) 453:194–8. doi: 10.1016/S0370-2693(99)00330-5
5. Pas H, Hirsch M, Klapdor-Kleingrothaus HV, Kovalenko SG. A Superformula for neutrinoless double beta decay. 2. The Short range part. *Phys Lett B.* (2001) 498:35–9. doi: 10.1016/S0370-2693(00)01359-9
6. Deppisch FF, Hirsch M, Pas H. Neutrinoless double-beta decay and physics beyond the standard model. *J Phys G.* (2012) 39:124007. doi: 10.1088/0954-3899/39/12/124007
7. Simkovic F, Pantis G, Vergados JD, Faessler A. Additional nucleon current contributions to neutrinoless double-beta decay. *Phys Rev C.* (1999) 60:055502. doi: 10.1103/PhysRevC.60.055502
8. Suhonen J, Civitarese O. Effects of orbital occupancies and spin-orbit partners on 0v beta beta-decay rates. *Nucl Phys A.* (2010) 847:207. doi: 10.1016/j.nuclphysa.2010.08.003
9. Faessler A, Meroni A, Petcov ST, Simkovic F, Vergados J. Uncovering multiple CP-nonconserving mechanisms of (beta beta)(0v) decay. *Phys Rev D.* (2011) 83:113003. doi: 10.1103/PhysRevD.83.113003
10. Mustonen MT, Engel J. Large-scale calculations of the double-beta decay of Ge-76, Te-130, Xe-136, and Nd-150 in the deformed self-consistent Skyrme quasiparticle random-phase approximation. *Phys Rev C.* (2013) 87:064302. doi: 10.1103/PhysRevC.87.064302
11. Faessler A, Gonzalez M, Kovalenko S, Simkovic F. Arbitrary mass Majorana neutrinos in neutrinoless double beta decay. *Phys Rev D.* (2014) 90:096010. doi: 10.1103/PhysRevD.90.096010
12. Retamosa J, Caurier E, Nowacki F. Neutrinoless double-beta decay of CA-48. *Phys Rev C.* (1995) 51:371. doi: 10.1103/PhysRevC.51.371
13. Caurier E, Nowacki F, Poves A, Retamosa J. Shell model studies of the double beta decays of ^{76}Ge, ^{82}Se, and ^{136}Xe. *Phys Rev Lett.* (1996) 77:1954. doi: 10.1103/PhysRevLett.77.1954
14. Horoi M. Shell model analysis of competing contributions to the double-beta decay of Ca-48. *Phys Rev C.* (2013) 87:014320. doi: 10.1103/PhysRevC.87.014320
15. Neacsu A, Stoica S. Constraints on heavy neutrino and SUSY parameters derived from the study of neutrinoless double beta decay. *Adv High Energy Phys.* (2014) 2014:724315. doi: 10.1155/2014/724315
16. Caurier E, Menendez J, Nowacki F, Poves A. Influence of pairing on the nuclear matrix elements of the neutrinoless beta beta decays. *Phys Rev Lett.* (2008) 100:052503. doi: 10.1103/PhysRevLett.100.052503
17. Menendez J, Poves A, Caurier E, Nowacki F. Disassembling the nuclear matrix elements of the neutrinoless beta beta decay. *Nucl Phys A.* (2009) 818:139. doi: 10.1016/j.nuclphysa.2008.12.005
18. Caurier E, Martinez-Pinedo G, Nowacki F, Poves A, Zuker AP. The shell model as a unified view of nuclear structure. *Rev Mod Phys.* (2005) 77:427. doi: 10.1103/RevModPhys.77.427
19. Horoi M, Stoica S. Shell model analysis of the neutrinoless double-beta decay of Ca-48. *Phys Rev C.* (2010) 81:024321. doi: 10.1103/PhysRevC.81.024321
20. Neacsu A, Stoica S, Horoi M. Fast, efficient calculations of the two-body matrix elements of the transition operators for neutrinoless double-beta decay. *Phys Rev C.* (2012) 86:067304. doi: 10.1103/PhysRevC.86.067304
21. Sen'kov RA, Horoi M. Neutrinoless double-beta decay of Ca-48 in the shell model: closure versus nonclosure approximation. *Phys Rev C.* (2013) 88:064312. doi: 10.1103/PhysRevC.88.064312
22. Horoi M, Brown BA. Shell-model analysis of the Xe-136 double Beta Decay Nuclear Matrix Elements. *Phys Rev Lett.* (2013) 110:222502. doi: 10.1103/PhysRevLett.110.222502

23. Sen'kov RA, Horoi M, Brown BA. Neutrinoless double-beta decay of Se-82 in the shell model: Beyond the closure approximation. *Phys Rev C*. (2014) 89:054304. doi: 10.1103/PhysRevC.89.054304
24. Brown BA, Horoi M, Sen'kov RA. Nuclear structure aspects of neutrinoless double-beta decay. *Phys Rev Lett*. (2014) 113:262501. doi: 10.1103/PhysRevLett.113.262501
25. Neacsu A, Stoica S. Study of nuclear effects in the computation of the 0 nu beta beta decay matrix elements. *J Phys G*. (2014) 41:015201. doi: 10.1088/0954-3899/41/1/015201
26. Sen'kov RA, Horoi M. Accurate shell-model nuclear matrix elements for neutrinoless double-beta decay. *Phys Rev C*. (2014) 90:051301(R). doi: 10.1103/PhysRevC.90.051301
27. Neacsu A, Horoi M. Shell model studies of the ^{130}Te neutrinoless double-beta decay. *Phys Rev C*. (2015) 91:024309. doi: 10.1103/PhysRevC.91.024309
28. Horoi M, Neacsu A. Shell model predictions for ^{124}Sn double-β decay. *Phys Rev C*. (2016) 93:024308. doi: 10.1103/PhysRevC.93.024308
29. Horoi M, Stoica S, Brown BA. Shell-model calculations of two-neutrino double-beta decay rates of ^{48}Ca with the GXPF1A interaction. *Phys Rev C*. (2007) 75:034303. doi: 10.1103/PhysRevC.75.034303
30. Blennow M, Fernandez-Martinez E, Lopez-Pavon J, Menendez J. Neutrinoless double-beta decay in seesaw models. *JHEP*. (2010) 07:096. doi: 10.1007/JHEP07(2010)096
31. Barea J, Iachello F. Neutrinoless double-beta decay in the microscopic interacting boson model. *Phys Rev C*. (2009) 79:044301. doi: 10.1103/PhysRevC.79.044301
32. Barea J, Kotila J, Iachello F. Limits on neutrino masses from neutrinoless double-beta decay. *Phys Rev Lett*. (2012) 109:042501. doi: 10.1103/PhysRevLett.109.042501
33. Barea J, Kotila J, Iachello F. Nuclear matrix elements for double-beta decay. *Phys Rev C*. (2013) 87:014315. doi: 10.1103/PhysRevC.87.014315
34. Barea J, Kotila J, Iachello F. $0\nu\beta\beta$ and $2\nu\beta\beta$ nuclear matrix elements in the interacting boson model with isospin restoration. *Phys Rev C*. (2015) 91:034304. doi: 10.1103/PhysRevC.91.034304
35. Deppisch FF, Graf L, Iachello F, Kotila J. Analysis of light neutrino exchange and short-range mechanisms in $0\nu\beta\beta$ decay. *Phys Rev D*. (2020) 102:095016. doi: 10.1103/PhysRevD.102.095016
36. Rath PK, Chandra R, Chaturvedi K, Lohani P, Raina PK, Hirsch JG. Neutrinoless beta beta decay transition matrix elements within mechanisms involving light Majorana neutrinos, classical Majorons, and sterile neutrinos. *Phys Rev C*. (2013) 88:064322. doi: 10.1103/PhysRevC.88.064322
37. Rodriguez TR, Martinez-Pinedo G. Energy density functional study of nuclear matrix elements for neutrinoless beta beta decay. *Phys Rev Lett*. (2010) 105:252503. doi: 10.1103/PhysRevLett.105.252503
38. Song LS, Yao JM, Ring P, Meng J. Relativistic description of nuclear matrix elements in neutrinoless double-beta decay. *Phys Rev C*. (2014) 90:054309. doi: 10.1103/PhysRevC.90.054309
39. Vergados JD, Ejiri H, Simkovic F. Theory of neutrinoless double-beta decay. *Rep Prog Phys*. (2012) 75:106301. doi: 10.1088/0034-4885/75/10/106301
40. Doi M, Kotani T, Takasugi E. Double-beta decay and Majorana neutrino. *Prog Theor Phys Suppl*. (1985) 83:1. doi: 10.1143/PTPS.83.1
41. Pati JC, Salam A. Lepton number as the fourth color. *Phys Rev D*. (1974) 10:275.
42. Keung WY, Senjanovic G. Majorana neutrinos and the production of the right-handed charged gauge boson. *Phys Rev Lett*. (1983) 50:1427.
43. Rodejohann W. Neutrinoless double-beta decay and neutrino physics. *J Phys G*. (2012) 39:124008. doi: 10.1088/0954-3899/39/12/124008
44. Barry J, Rodejohann W. Lepton number and flavor violation in TeV-scale left-right symmetric theories with large left-right mixing. *J High Energy Phys*. (2013) 9:153. doi: 10.1007/JHEP09(2013)153
45. Bhupal Dev PS, Goswami S, Mitra M. TeV-scale left-right symmetry and large mixing effects in neutrinoless double beta decay. *Phys Rev D*. (2015) 91:113004. doi: 10.1103/PhysRevD.91.113004
46. Horoi M, Neacsu A. Shell model study of using an effective field theory for disentangling several contributions to neutrinoless double-β decay. *Phys Rev C*. (2018) 98:035502. doi: 10.1103/PhysRevC.98.035502
47. Stoica S, Mirea M. New calculations for phase space factors involved in double-beta decay. *Phys Rev C*. (2013) 88:037303. doi: 10.1103/PhysRevC.88.037303
48. Mirea M, Pahomi T, Stoica S. Values of the phase space factors involved in double beta decay. *Rom Rep Phys*. (2015) 67:035503.
49. Stefanik D, Dvornicky R, Simkovic F, Vogel P. Reexamining the light neutrino exchange mechanism of the $0\nu\beta\beta$ decay with left- and right-handed leptonic and hadronic currents. *Phys Rev C*. (2015) 92:055502. doi: 10.1103/PhysRevC.92.055502
50. Agostini M, Araujo GR, Bakalyarov AM, Balata M, Barabanov I, Baudis L, et al. Final results of GERDA on the search for neutrinoless double-β decay. *Phys Rev Lett*. (2020) 125:252502. doi: 10.1103/PhysRevLett.125.252502
51. Doi M, Kotani T, Nishiura H, Takasugi E. Double beta-decay. *Progr Theor Exp Phys*. (1983) 69:602. doi: 10.1143/PTP.69.602
52. Horoi M, Neacsu A. Analysis of mechanisms that could contribute to neutrinoless double-beta decay. *Phys Rev D*. (2016) 93:113014. doi: 10.1103/PhysRevD.93.113014
53. Suhonen J, Civitarese O. Weak-interaction and nuclear-structure aspects of nuclear double beta decay. *Phys Rep*. (1998) 300:123. doi: 10.1016/S0370-1573(97)00087-2
54. Kotila J, Iachello F. Phase-space factors for double-beta decay. *Phys Rev C*. (2012) 85:034316. doi: 10.1103/PhysRevC.85.034316
55. Kondev FG, Wang M, Audi G, Wapstra AH, MacCormick M, Xu X, et al. The AME2012 atomic mass evaluation: (II). Tables, graphs and references. *Chinese Phys C*. (2012) 36:12. doi: 10.1088/1674-1137/36/12/003
56. Honma M, Otsuka T, Brown BA, Mizusaki T. New effective interaction for pf-shell nuclei and its implications for the stability of the N=Z=28 closed core. *Phys Rev C*. (2004) 69:034335. doi: 10.1103/PhysRevC.69.034335
57. Honma M, Otsuka T, Mizusaki T, Hjorth-Jensen M. New effective interaction for f5pg9-shell nuclei. *Phys Rev C*. (2009) 80:064323. doi: 10.1103/PhysRevC.80.064323
58. Qi C, Xu ZX. Monopole-optimized effective interaction for tin isotopes. *Phys Rev C*. (2012) 86:044323. doi: 10.1103/PhysRevC.86.044323
59. Horoi M, Neacsu A. An effective method to accurately calculate the phase space factors for $\beta^-\beta^-$ decay. *Adv High Energy Phys*. (2016) 2016:7486712. doi: 10.1155/2016/7486712
60. Holt JD, Engel J. Effective double-beta-decay operator for Ge-76 and Se-82. *Phys Rev C*. (2013) 87:064315. doi: 10.1103/PhysRevC.87.064315
61. Arnold R, Augier C, Bakalyarov AM, Baker JD, Barabash AS, Basharina-Freshville A, et al. Measurement of the double-beta decay half-life and search for the neutrinoless double-beta decay of ^{48}Ca with the NEMO-3 detector. *Phys Rev D*. (2016) 93:112008. doi: 10.1103/PhysRevD.93.112008
62. *Latest Results From NEMO-3 and Status of the SuperNEMO Experiment*. (2016). Available online at: http://neutrino2016.iopconfs.org/IOP/media/uploaded/EVIOP/event_948/10.25__5__waters.pdf
63. Alfonso K, Artusa DR, Avignone FT, Azzolini O, Balata M, Banks TI, et al. Search for neutrinoless double-beta decay of ^{130}Te with CUORE-0. *Phys Rev Lett*. (2015) 115:102502. doi: 10.1103/PhysRevLett.115.102502
64. Gando A, Gando Y, Hachiya T, Hayashi A, Hayashida S, Ikeda H, et al. Search for majorana neutrinos near the inverted mass hierarchy region with KamLAND-Zen. *Phys Rev Lett*. (2016) 117:082503. doi: 10.1103/PhysRevLett.117.082503

Conflict of Interest: The authors declare that the research was conducted in the absence of any commercial or financial relationships that could be construed as a potential conflict of interest.

frontiers in Astronomy and Space Sciences

ORIGINAL RESEARCH
published: 24 May 2021
doi: 10.3389/fspas.2021.652180

Comparison of Microscopic Interacting Boson Model and Quasiparticle Random Phase Approximation $0\nu\beta\beta$ Decay Nuclear Matrix Elements

Jenni Kotila [1,2]*

[1] Finnish Institute for Educational Research, University of Jyväskylä, Jyväskylä, Finland, [2] Center for Theoretical Physics, Sloane Physics Laboratory Yale University, New Haven, CT, United States

The fundamental nature of the neutrino is presently a subject of great interest. A way to access the absolute mass scale and the fundamental nature of the neutrino is to utilize the atomic nuclei through their rare decays, the neutrinoless double beta ($0\nu\beta\beta$) decay in particular. The experimentally measurable observable is the half-life of the decay, which can be factorized to consist of phase space factor, axial vector coupling constant, nuclear matrix element, and function containing physics beyond the standard model. Thus reliable description of nuclear matrix element is of crucial importance in order to extract information governed by the function containing physics beyond the standard model, neutrino mass parameter in particular. Comparison of double beta decay nuclear matrix elements obtained using microscopic interacting boson model (IBM-2) and quasiparticle random phase approximation (QRPA) has revealed close correspondence, even though the assumptions in these two models are rather different. The origin of this compatibility is not yet clear, and thorough investigation of decomposed matrix elements in terms of different contributions arising from induced currents and the finite nucleon size is expected to contribute to more accurate values for the double beta decay nuclear matrix elements. Such comparison is performed using detailed calculations on both models and obtained results are then discussed together with recent experimental results.

Keywords: double beta decay, nuclear matrix element, microscopic interacting boson model, quasiparticle random phase approximation, physics beyond the standard model

OPEN ACCESS

Edited by:
Theocharis S. Kosmas, University of Ioannina, Greece

Reviewed by:
Sabin Stoica, Horia Hulubei National Institute for Research and Development in Physics and Nuclear Engineering (IFIN-HH), Romania
Carlo Giunti, National Institute of Nuclear Physics, Ministry of Education, Universities and Research, Italy

***Correspondence:**
Jenni Kotila
jenni.kotila@jyu.fi

Specialty section:
This article was submitted to High-Energy and Astroparticle Physics, a section of the journal Frontiers in Astronomy and Space Sciences

Received: *11 January 2021*
Accepted: *10 March 2021*
Published: *24 May 2021*

Citation:
Kotila J (2021) Comparison of Microscopic Interacting Boson Model and Quasiparticle Random Phase Approximation $0\nu\beta\beta$ Decay Nuclear Matrix Elements. Front. Astron. Space Sci. 8:652180. doi: 10.3389/fspas.2021.652180

1. INTRODUCTION

The question of whether neutrinos are Majorana or Dirac particles and what is the neutrino mass parameter remains one of the most fundamental problems in physics today. Even though the neutrino oscillation experiments can investigate the neutrino mass differences and neutrino mixing amplitudes to high precision already, a complementary way is needed to access the absolute neutrino mass and the fundamental nature of the neutrino (see, e.g., de Salas et al., 2021). Observation of neutrinoless double beta decay ($0\nu\beta\beta$), hypothesized extremely rare second-order process of weak interaction, would verify the Majorana nature of the neutrino, constrain the absolute scale of the neutrino mass spectrum, and provide proof of lepton-number violation. It would have fundamental implications for neutrino physics, theories beyond the standard model, and cosmology. The $0\nu\beta\beta$ decay experiments aim to obtain the half-life of the process and

information to be extracted from the experiments is subject to uncertainties arising from the uncertainties in the related nuclear matrix elements (NMEs). Hence, the reliable calculation of these NMEs is of utmost importance.

The inverse $0\nu\beta\beta$ decay half-life in a given isotope is conventionally expressed as

$$T_{1/2}^{-1} = \left|f(m_i, U_{ei})\right|^2 G_\nu |\mathcal{M}_\nu|^2, \tag{1}$$

with the phase space factor (PSF) G_ν and the nuclear matrix element (NME) $\mathcal{M}_\nu$. In particular, the mass mechanism of $0\nu\beta\beta$ decay is sensitive to the neutrino mass parameter. In older calculations, PSFs were evaluated using approximate wave functions for electrons (Furry, 1939; Primakoff and Rosen, 1959; Molina and Pascual, 1977; Doi et al., 1981, 1985; Haxton and Stephenson, 1984; Tomoda, 1991; Suhonen and Civitarese, 1998) and in more recent calculations exact Dirac electron wave functions have been used (Kotila and Iachello, 2012, 2013; Stoica and Mirea, 2013; Kotila et al., 2014, 2015; Mirea et al., 2015; Graf et al., 2018; Deppisch et al., 2020). The $0\nu\beta\beta$ NMEs have been computed by a number of different models: the quasiparticle random-phase approximation (QRPA), in its proton-neutron version (Šimkovic et al., 2008, 2013; Fang et al., 2011, 2018; Faessler et al., 2012; Suhonen and Civitarese, 2012; Mustonen and Engel, 2013; Hyvärinen and Suhonen, 2015), the interacting shell model (ISM) (Caurier et al., 2005, 2007; Menéndez et al., 2009a,b; Horoi and Brown, 2013; Neacsu and Stoica, 2014; Neacsu and Horoi, 2015; Coraggio et al., 2020), the microscopic interacting boson model (IBM-2) (Barea and Iachello, 2009; Barea et al., 2013a,b, 2015a,b; Kotila et al., 2014, 2015; Graf et al., 2018; Deppisch et al., 2020), the energy density functional approach (EDF) along with density functional theory (Rodríguez and Martínez-Pinedo, 2010; Song et al., 2014, 2017; Yao et al., 2015), and the projected Hartree–Fock–Bogoliubov mean-field scheme (PHFB) (Rath et al., 2010, 2019) to name some most frequently used. In principle, the calculation of NME is straightforward but in practice the values predicted by different nuclear models differ by factors of up to three, causing a large uncertainty in the half-life for a given value of neutrino mass parameter (Rath et al., 2010). A way to avoid the model dependence and thus the uncertainties that are caused by model assumptions and approximation made in different models is to calculate the NMEs from first principles, which is currently the goal of several theoretical groups. However, applying modern *ab initio* methods to $0\nu\beta\beta$ decay is challenging and the $0\nu\beta\beta$ candidate nuclei are generally more complicated and heavier than those treated so far (Hergert et al., 2016; Pastore et al., 2018; Wang et al., 2019; Basili et al., 2020). Thus, traditional nuclear model calculations for $0\nu\beta\beta$ NMEs are still very much needed for the interpretation of the experimental results as well as for the planning of the future experiments. It is therefore important to try to understand the similarities and differences of different models. In this paper, the focus is on elaborate comparison between IBM-2 and QRPA nuclear matrix elements. For both of these models detailed calculations of individual NMEs that contribute to the full $0\nu\beta\beta$ NME are available.

The paper is organized as follows: The theoretical background is reviewed in section 2 and numerical results are summarized in section 3 for both light and heavy neutrino exchange. Differences and similarities of the two models are then discussed in section 4 along with possible explanations for the obtained results. Section 5 concludes the discussion with a summary and an outlook.

2. THEORETICAL BACKGROUND

The theory of $0\nu\beta\beta$ decay was first formulated by Furry (1939) and further developed by Primakoff and Rosen (1959), Molina and Pascual (1977), Doi et al. (1981), Doi et al. (1983), Haxton and Stephenson (1984), and, more recently, by Tomoda (1991) and Šimkovic et al. (1999). All these formulations often differ by factors of 2, by the number of terms retained in the non-relativistic expansion of the current and by their contribution. Adopting the formulation of Šimkovic et al. (1999), which is the one used in most recent calculations, the transition operator for $0\nu\beta\beta$ in momentum space, $p = \left|\vec{q}\right|$, can be written as

$$T(p) = H(p) f(m_i, U_{ei}) \tag{2}$$

where for light neutrino exchange

$$f(m_i, U_{ei}) = \frac{\langle m_\nu \rangle}{m_e}, \quad \langle m_\nu \rangle = \sum_{k=light} (U_{ek})^2 m_k, \tag{3}$$

while for heavy neutrino exchange

$$\begin{aligned} f(m_i, U_{ei}) &= m_p \left\langle m_{\nu_h}^{-1} \right\rangle, \\ \left\langle m_{\nu_h}^{-1} \right\rangle &= \sum_{k=heavy} \left(U_{ek_h}\right)^2 \frac{1}{m_{k_h}}. \end{aligned} \tag{4}$$

The (two-body) operator $H(p)$ can be written as

$$H(p) = \sum_{n,n'} \tau_n^\dagger \tau_{n'}^\dagger \left[-h^F(p) + h^{GT}(p) \vec{\sigma}_n \cdot \vec{\sigma}_{n'} \; -h^T(p) S_{nn'}^p \right], \tag{5}$$

with the tensor operator defined as

$$S_{nn'}^p = 3\left[\left(\vec{\sigma}_n \cdot \hat{p}\right)\left(\vec{\sigma}_{n'} \cdot \hat{p}\right)\right] - \vec{\sigma}_n \cdot \vec{\sigma}_{n'}. \tag{6}$$

The Fermi (F), Gamow-Teller (GT), and tensor (T) contributions are further divided into $h_{VV}^F(p)$, $h_{AA}^{GT}(p)$, $h_{AP}^{GT}(p)$, $h_{PP}^{GT}(p)$, $h_{WW}^{GT}(p)$, $h_{AP}^T(p)$, $h_{PP}^T(p)$, and $h_{WW}^T(p)$ terms. The terms AP, PP, and WW are higher order corrections (HOC) arising from weak magnetism (W) and induced pseudoscalar terms (P) in the weak nucleon current. Finally, the terms $h^\circ(p)$ can be further factorized as

$$h^\circ(p) = \nu(p) \tilde{h}^\circ(p) \tag{7}$$

where $\nu(p)$ is called the neutrino potential and $\tilde{h}^\circ(p)$ are the form factors given in **Table 1**. The finite nucleon size (FNS) is

TABLE 1 | Double beta decay Fermi ($\mathcal{M}_F$), Gamow–Teller ($\mathcal{M}_{GT}$), and tensor ($\mathcal{M}_T$) NMEs appearing in Equation (12), with the associated reduced form factor product $\tilde{h}(q^2)$.

NME	$\tilde{h}_\circ(q^2)$
$\mathcal{M}_F = \langle h_{XX}(q^2)\rangle$	$\tilde{h}_{XX}(q^2) = \frac{1}{(1+q^2/m_V^2)^4}$
$\mathcal{M}_{GT}^{AA} = \langle h_{AA}(q^2)(\boldsymbol{\sigma}_a\cdot\boldsymbol{\sigma}_b)\rangle$	$\tilde{h}_{AA}(q^2) = \frac{1}{(1+q^2/m_A^2)^4}$
$\mathcal{M}_{GT}^{\prime AP} = \left\langle \frac{q^2}{m_p^2} h_{AP}(q^2)(\boldsymbol{\sigma}_a\cdot\boldsymbol{\sigma}_b)\right\rangle$	$\tilde{h}_{AP}(q^2) = \frac{1}{(1+q^2/m_A^2)^4}\frac{1}{1+q^2/m_\pi^2}$
$\mathcal{M}_T^{\prime AP} = \left\langle \frac{q^2}{m_p^2} h_{AP}(q^2) S_{ab}\right\rangle$	$\tilde{h}_{AP}(q^2)$
$\mathcal{M}_{GT}^{\prime WW} = \left\langle \frac{q^2}{m_p^2} h_{XX}(q^2)(\boldsymbol{\sigma}_a\cdot\boldsymbol{\sigma}_b)\right\rangle$	$\tilde{h}_{XX}(q^2)$
$\mathcal{M}_T^{\prime WW} = \left\langle \frac{q^2}{m_p^2} h_{XX}(q^2) S_{ab}\right\rangle$	$\tilde{h}_{XX}(q^2)$
$\mathcal{M}_{GT}^{\prime\prime PP} = \left\langle \frac{q^4}{m_p^4} h_{PP}(q^2)(\boldsymbol{\sigma}_a\cdot\boldsymbol{\sigma}_b)\right\rangle$	$\tilde{h}_{PP}(q^2) = \frac{1}{(1+q^2/m_A^2)^4}\frac{1}{(1+q^2/m_\pi^2)^2}$
$\mathcal{M}_T^{\prime\prime PP} = \left\langle \frac{q^4}{m_p^4} h_{PP}(q^2) S_{ab}\right\rangle$	$\tilde{h}_{PP}(q^2)$

taken into account by taking the coupling constants g_V and g_A as momentum dependent

$$g_V(p^2) = g_V \frac{1}{\left(1+\frac{p^2}{M_V^2}\right)^2},$$
$$g_A(p^2) = g_A \frac{1}{\left(1+\frac{p^2}{M_A^2}\right)^2}. \tag{8}$$

The value of M_V is well fixed by the electromagnetic form factor of the nucleon, $M_V^2 = 0.71(\mathrm{GeV}/c^2)^2$ (Dumbrajs et al., 1983) and $g_V = 1$ by the hypothesis of conserved vector current (CVC). The value of M_A is estimated to be $M_A = 1.09(\mathrm{GeV}/c^2)$ (Schindler and Scherer, 2007) and free value of $g_A = 1.269$ (Yao et al., 2006).

The neutrino potential $v(p)$ is written, in the closure approximation, for light neutrino exchange as

$$v(p) = \frac{2}{\pi}\frac{1}{p\left(p+\tilde{A}\right)}. \tag{9}$$

In non-closure calculations, an average energy $\tilde{A}$ is replaced with the actual intermediate state energies making the calculation more accurate but also much more complicated. For heavy neutrino exchange, the neutrino potential is given by

$$v(p) = \frac{2}{\pi}\frac{1}{m_e m_p}. \tag{10}$$

Short-range correlations (SRC) are taken into account by multiplying the potential $V(r)$ in coordinate space by a correlation function $f(r)$ squared. The most commonly used correlation function is the Jastrow function

$$f_J(r) = 1 - ce^{-ar^2}(1-br^2) \tag{11}$$

with $a = 1.1\ \mathrm{fm}^{-2}$, $b = 0.68\ \mathrm{fm}^{-2}$ and $c = 1$ for the phenomenological Miller–Spencer parameterization (Miller and Spencer, 1976), and, in recent years, the Argonne/CD-Bonn parameterizations (Šimkovic et al., 2009) $a = 1.59/1.52\ \mathrm{fm}^{-2}$, $b = 1.45/1.88\ \mathrm{fm}^{-2}$ and $c = 0.92/0.46$. Since the formulation is in momentum space, SRC is taken into account by using the Fourier–Bessel transform of $f_J(r)$.

From these ingredients, one can calculate the individual contributing NMEs listed also in **Table 1**. Furthermore, from these one can calculate the final NMEs for the standard mass mechanism, $\mathcal{M}_\nu$ and heavy neutrino exchange $\mathcal{M}_{\nu_h}$. To allow the analysis to be performed in section 3, it is convenient to introduce the quantities

$$\mathcal{M}_{GT} = \mathcal{M}_{GT}^{AA} - \frac{g_P}{6g_A}\mathcal{M}_{GT}^{\prime AP} + \frac{(g_V+g_W)^2}{6g_A^2}\mathcal{M}_{GT}^{\prime WW} + \frac{g_P^2}{48g_A^2}\mathcal{M}_{GT}^{\prime\prime PP}$$
$$\mathcal{M}_T = \frac{g_P}{6g_A}\mathcal{M}_T^{\prime AP} + \frac{(g_V+g_W)^2}{12g_A^2}\mathcal{M}_T^{\prime WW} - \frac{g_P^2}{48g_A^2}\mathcal{M}_T^{\prime\prime PP} \tag{12}$$

and write $\mathcal{M}_\nu$ as

$$\mathcal{M}_\nu = g_A^2\left[-\left(\frac{g_V}{g_A}\right)^2\mathcal{M}_F + \mathcal{M}_{GT} - \mathcal{M}_T\right], \tag{13}$$

and similarly for $\mathcal{M}_{\nu_h}$.

The obtained NMEs, both individual and compound, are compared in two different models IBM-2 and QRPA. The method of evaluation $0\nu\beta\beta$ NMEs in IBM-2 is discussed in detail in Barea and Iachello (2009); Barea et al. (2015a). For QRPA calculations, see Suhonen and Civitarese (2012), Hyvärinen and Suhonen (2015) and references therein. For both models, versions with isospin restoration are used. In the case of $2\nu\beta\beta$ decay, if isospin is a good quantum number, the Fermi matrix elements should identically vanish. By a similar argument, the Fermi matrix elements in $0\nu\beta\beta$ are expected to be small, although not zero, the main difference between $2\nu\beta\beta$ and $0\nu\beta\beta$ being the neutrino potential, which for $2\nu\beta\beta$ is $v_{2\nu}(p) = \frac{\delta(p)}{p^2}$, being the Fourier–Bessel transform of the configuration space potential $V(r) = 1$. The method for isospin restoration is similar in spirit for both models but different in practice and is discussed further in section 4.1.

3. RESULTS

The matrix elements of the operator $H(p)$ have dimension fm^{-1}. In the following, NMEs are multiplied by nuclear radius in fm, $R = R_0 A^{1/3}$, with $R_0 = 1.2$ fm in order to make them dimensionless, which is the way they are usually quoted.

3.1. Light Neutrino Exchange

The individual IBM-2 nuclear matrix elements were recently calculated in Deppisch et al. (2020) in order to study the potential interplay of non-standard short-range operators of $0\nu\beta\beta$ decay with standard light Majorana neutrino exchange. A selection of those NMEs is compared with QRPA nuclear matrix elements reported in Hyvärinen and Suhonen (2015). To avoid the differences arising from the use of different form factor charges, they are explicitly factored out for both models

TABLE 2 | Nuclear matrix elements (NMEs) for the standard light neutrino exchange $0\nu\beta\beta$ decay mechanism evaluated in the interacting boson model (IBM-2) and quasiparticle random phase approximation (QRPA) as described in the text.

		$\mathcal{M}_F$	$\mathcal{M}_{GT}^{AA}$	$\mathcal{M}_{GT}^{'AP}$	$\mathcal{M}_{T}^{'AP}$	$\mathcal{M}_{GT}^{'WW}$	$\mathcal{M}_{T}^{'WW}$	$\mathcal{M}_{GT}^{''PP}$	$\mathcal{M}_{T}^{''PP}$
^{76}Ge	IBM-2	−0.780	6.062	0.036	−0.010	0.089	−0.035	3.4×10^{-4}	-1.4×10^{-4}
	QRPA	−1.743	5.972	0.068	−0.011	0.224	−0.032	9.8×10^{-4}	-1.4×10^{-4}
^{82}Se	IBM-2	−0.667	4.928	0.030	−0.010	0.073	−0.034	4.1×10^{-4}	-1.3×10^{-4}
	QRPA	−1.291	4.262	0.049	−0.008	0.161	−0.025	7.1×10^{-4}	-1.1×10^{-4}
^{96}Zr	IBM-2	−0.361	4.317	0.027	0.009	0.065	0.032	3.1×10^{-4}	1.2×10^{-4}
	QRPA	−1.441	3.890	0.050	−0.010	0.173	−0.032	7.5×10^{-4}	-1.4×10^{-4}
^{100}Mo	IBM-2	−0.511	5.553	0.038	0.012	0.096	0.041	4.7×10^{-4}	1.6×10^{-4}
	QRPA	−1.634	4.306	0.056	−0.011	0.195	−0.039	8.4×10^{-4}	-1.6×10^{-4}
^{110}Pd	IBM-2	−0.425	4.432	0.032	0.009	0.080	0.036	3.9×10^{-4}	1.4×10^{-4}
	QRPA	−2.315	7.769	0.084	−0.011	0.273	−0.040	12.0×10^{-4}	-1.7×10^{-4}
^{116}Cd	IBM-2	−0.335	3.173	0.023	0.005	0.058	0.023	2.9×10^{-4}	8.7×10^{-5}
	QRPA	−1.496	4.238	0.047	−0.007	0.153	−0.027	6.7×10^{-4}	-1.1×10^{-4}
^{124}Sn	IBM-2	−0.572	3.370	0.021	−0.005	0.053	−0.018	2.5×10^{-4}	-7.5×10^{-5}
	QRPA	−2.332	7.519	0.083	−0.017	0.273	−0.055	11.9×10^{-4}	-2.4×10^{-4}
^{128}Te	IBM-2	−0.718	4.321	0.027	−0.005	0.067	−0.023	3.1×10^{-4}	-9.1×10^{-5}
	QRPA	−1.777	5.232	0.066	−0.018	0.230	−0.060	9.9×10^{-4}	-2.5×10^{-4}
^{130}Te	IBM-2	−0.651	3.894	0.024	−0.006	0.061	−0.021	2.8×10^{-4}	-8.3×10^{-5}
	QRPA	−1.523	4.878	0.060	−0.015	0.205	−0.053	8.9×10^{-4}	-2.2×10^{-4}
^{136}Xe	IBM-2	−0.522	3.203	0.019	−0.005	0.048	−0.016	2.2×10^{-4}	-6.3×10^{-5}
	QRPA	−0.894	3.338	0.040	−0.009	0.133	−0.030	5.7×10^{-4}	-1.3×10^{-4}

and NMEs are presented in the notation given in Deppisch et al. (2020). The individual QRPA nuclear matrix elements given in **Tables 2**, **4**, for light and heavy neutrino exchange, respectively, are obtained from the values reported in Tables 2, 4 of Hyvärinen and Suhonen (2015) as follows: F and AA contributions are taken as they are; AP contributions are divided by $\mp(4 * m_p^2/m_\pi^2)/6$, where $-$ sign corresponds to $\mathcal{M}_{GT}^{'AP}$ and $+$ sign to $\mathcal{M}_{T}^{'AP}$; WW contributions (in Hyvärinen and Suhonen (2015) these are called MM contributions): GT NMEs are divided by $(\mu_p - \mu_n)^2/6$ and T NMEs by $(\mu_p - \mu_n)^2/12$ with $\mu_p - \mu_n = 3.7$; finally PP contributions are divided by $\pm(4 * m_p^2/m_\pi^2)^2/48$, where $+$ sign corresponds to $\mathcal{M}_{GT}^{''PP}$ and $-$ sign to $\mathcal{M}_{T}^{''PP}$. The thus obtained numerical values of individual ground state to ground state NMEs are given in **Table 2** for ^{76}Ge, ^{82}Se, ^{96}Zr, ^{100}Mo, ^{110}Pd, ^{116}Cd, ^{124}Sn, ^{128}Te, ^{130}Te, and ^{136}Xe.

Since nuclei from $A = 76$ to $A = 136$ are covered, there are two classes of nuclei: those in which protons and neutrons occupy the same major shell ($A = 76, 82, 124, 128, 130, 136$) and those in which they occupy different major shells ($A = 96, 100, 110, 116$). Clearly notable difference between the two models is shown for the tensor matrix elements in these two classes. For QRPA, the sign of tensor NMEs is always negative. For IBM-2, it is negative if the protons and neutrons occupy the same major shell and positive when they occupy different major shells. This behavior can be traced to the fact that the neutrino potential $V(r)$ is different for the tensor contribution than for Fermi and Gamow–Teller contributions. In the notation of Table 8 of Barea and Iachello (2009), $V(r) = H(r)$ for Fermi and Gamow–Teller matrix elements and $V(r) = -rH'(r)$ for tensor matrix elements.

Another considerable difference is the magnitude of $\mathcal{M}_F$ matrix elements. They appear twice or more larger in QRPA than in IBM-2 for most of the studied nuclei, ^{136}Xe being a notable exception. On the other hand, the $\mathcal{M}_{GT}^{AA}$, giving the biggest contribution to the full NME, have rather similar magnitudes in both models, exceptions being ^{110}Pd and ^{124}Sn which are much larger in QRPA. The other contributions, *AP*, *PP*, and *WW*, are orders of magnitude smaller. $\mathcal{M}_{GT}^{'AP}$, as well as, $\mathcal{M}_{GT}^{''PP}$, have comparable magnitudes in both models, the exceptions again being ^{110}Pd and ^{124}Sn, which are much larger in QRPA. $\mathcal{M}_{GT}^{'WW}$, however, is twice or more larger in QRPA in all the studied nuclei. The contributions of tensor matrix elements are the smallest and their magnitudes are fairly similar in both models.

To analyze further the similarities and differences in these two models, it is useful to calculate the compound NMEs $\mathcal{M}_{GT}$, and $\mathcal{M}_T$ given in Equation (12) using the individual NMEs of **Table 2**. In the calculation, values $g_V = 1.0$ and $g_W = 3.7$ and quenched values for $g_A = 1.0$, $g_P = 4g_A \frac{m_p^2}{m_\pi^2}\left(1 - \frac{m_\pi^2}{m_A^2}\right) = 182$ are used in order to allow straightforward use of other values of g_A using Equation (13) for the full matrix element. $\mathcal{M}_F$, $\mathcal{M}_{GT}$, $\mathcal{M}_T$, and full matrix element $\mathcal{M}_\nu$ are listed in **Table 3**, along with their ratios in the two studied models. The ratio $\chi_F = \mathcal{M}_F/\mathcal{M}_{GT}$ is also shown for each model.

If we first look at the ratio $\chi_F = \mathcal{M}_F/\mathcal{M}_{GT}$, we note that QRPA gives larger absolute value in all studied nuclei. For QRPA, this value varies between -0.30 and -0.42, largest absolute values

TABLE 3 | Comparison between interacting boson model (IBM-2) and quasiparticle random phase approximation (QRPA) light neutrino exchange Fermi (F), Gamow–Teller (GT), tensor (T), and full $\mathcal{M}_\nu$ NMEs as defined in Equations (12) and (13) calculated using quenched value $g_A = 1.0$.

Isotope		$\mathcal{M}_F$	$\mathcal{M}_{GT}$	$\mathcal{M}_T$	χ_F	$\mathcal{M}_\nu$	$\frac{\mathcal{M}_F^{QRPA}}{\mathcal{M}_F^{IBM-2}}$	$\frac{\mathcal{M}_{GT}^{QRPA}}{\mathcal{M}_{GT}^{IBM-2}}$	$\frac{\mathcal{M}_T^{QRPA}}{\mathcal{M}_T^{IBM-2}}$	$\frac{\mathcal{M}_\nu^{QRPA}}{\mathcal{M}_\nu^{IBM-2}}$
^{76}Ge	IBM-2	−0.78	5.58	−0.28	−0.14	6.64	2.23	0.97	1.05	1.12
	QRPA	−1.74	5.41	−0.30	−0.32	7.45				
^{82}Se	IBM-2	−0.67	4.52	−0.27	−0.15	5.46	1.94	0.85	0.83	0.98
	QRPA	−1.29	3.85	−0.22	−0.33	5.37				
^{96}Zr	IBM-2	−0.36	3.95	0.25	−0.09	4.07	3.99	0.89	−1.01	1.28
	QRPA	−1.44	3.52	−0.25	−0.41	5.22				
^{100}Mo	IBM-2	−0.51	5.08	0.32	−0.10	5.27	3.20	0.77	−0.92	1.11
	QRPA	−1.63	3.91	−0.29	−0.42	5.84				
^{110}Pd	IBM-2	−0.43	4.03	0.24	−0.11	4.21	5.45	1.75	−1.22	2.29
	QRPA	−2.32	7.04	−0.30	−0.33	9.66				
^{116}Cd	IBM-2	−0.34	2.89	0.12	−0.12	3.11	4.47	1.33	−1.58	1.77
	QRPA	−1.50	3.84	−0.19	−0.39	5.52				
^{124}Sn	IBM-2	−0.57	3.10	−0.12	−0.18	3.79	4.08	2.20	3.72	2.53
	QRPA	−2.33	6.83	−0.44	−0.34	9.60				
^{128}Te	IBM-2	−0.72	3.97	−0.12	−0.18	4.80	2.47	1.20	4.07	1.46
	QRPA	−1.78	4.75	−0.47	−0.37	6.99				
^{130}Te	IBM-2	−0.65	3.59	−0.16	−0.18	4.40	2.34	1.24	2.56	1.45
	QRPA	−1.52	4.43	−0.41	−0.34	6.37				
^{136}Xe	IBM-2	−0.52	2.96	−0.12	−0.18	3.60	1.71	1.02	1.90	1.15
	QRPA	−0.89	3.02	−0.23	−0.30	4.15				

being for ^{100}Mo and ^{96}Zr. For IBM-2 χ_F, values are between −0.09 and −0.18 and smallest absolute values are obtained for ^{100}Mo and ^{96}Zr. This shows that in addition to the absolute magnitude of $\mathcal{M}_F$ being larger in QRPA than in IBM-2 also the relative magnitude of $\mathcal{M}_F$ to $\mathcal{M}_{GT}$ is larger in QRPA.

The ratios of compound NMEs $\mathcal{M}_{GT}$ and $\mathcal{M}_T$ in QRPA and IBM-2 are shown in the last two columns of **Table 3**. $\mathcal{M}_{GT}$ gives the biggest contribution to the full matrix element defined in Equation (13). For ^{76}Ge and ^{136}Xe, $\mathcal{M}_{GT}$ are in very close correspondence in QRPA and IBM-2. For ^{82}Se and ^{96}Zr, the difference is 15% or less, and for ^{100}Mo, ^{116}Cd, ^{128}Te, and ^{130}Te, the difference is 33% or less. The largest differences are for ^{110}Pd and ^{124}Sn, as was the case also for individual NMEs. For $\mathcal{M}_T$, the situation is a bit different. Also for these nuclear matrix elements QRPA and IBM-2 give very similar results for ^{76}Ge and ^{82}Se. In ^{96}Zr, ^{100}Mo, ^{110}Pd, and ^{116}Cd, the magnitude is comparable but since these nuclei have protons and neutrons occupying different shells there is the sign difference. For ^{124}Sn, ^{128}Te, ^{130}Te, and ^{136}Xe, the difference is as large or larger than 90%. However, it is good to keep in mind that tensor contribution is an order of magnitude smaller than GT contribution.

The numerical values of full matrix element $\mathcal{M}_\nu$ are discussed in sections 4.3 and 4.4.

3.2. Heavy Neutrino Exchange

The matrix elements for heavy neutrino exchange can be simply calculated by replacing the potential $v(p) = 2\pi^{-1}[p(p+\tilde{A})]^{-1}$ of Equation (9) with the potential $v_h(p) = 2\pi^{-1}(m_e m_p)^{-1}$ of Equation (10). **Table 4** gives the corresponding individual nuclear matrix elements. The index h is added to distinguish these matrix elements from those with light neutrino exchange. As can be seen from **Table 4**, the situation is much more complicated than in the case of light neutrino exchange. In addition to Fermi matrix elements being larger in QRPA and tensor matrix elements having sign that varies depending whether neutrons and protons occupy the same shell in IBM-2 also the $\mathcal{M}_{GT}^{AA}$ are much larger in QRPA and the sign of $\mathcal{M}_{GT}^{\prime WW}$ is negative for all studied nuclei in IBM-2 and positive in QRPA. Furthermore, $\mathcal{M}_{GT}^{\prime WW}$ is also much larger in magnitude in QRPA than in IBM-2.

Table 5 presents the $\mathcal{M}_F$, $\mathcal{M}_{GT}$, $\mathcal{M}_T$, and full matrix element $\mathcal{M}_{\nu_h}$ along with their ratios in the two studied models in case of heavy neutrino exchange. Again, also the ratio $\chi_{\nu_h,F} = \mathcal{M}_{\nu_h,F}/\mathcal{M}_{\nu_h,GT}$ is shown. Now we see that the absolute value of $\chi_{\nu_h,F}$ is larger for IBM-2 in all studied nuclei on the contrary to light neutrino exchange. On the other hand, $\chi_{\nu_h,F}$ ratios are rather close to each other: for QRPA, they vary from −0.30 to −0.39, and for IBM-2, they vary from −0.43 to −0.48. In addition to the Fermi matrix element being ∼2 − 5 times larger in QRPA, the compound GT matrix elements are also ∼3 − 7 larger in QRPA. As in the case of light neutrino exchange, the difference is largest for ^{110}Pd and ^{124}Sn. If those two systems are disregarded, variation is much smaller, in average 2.8 and 3.6, for F and GT, respectively. The

TABLE 4 | Nuclear matrix elements (NMEs) for the heavy neutrino exchange $0\nu\beta\beta$ decay mechanism evaluated in the interacting boson model (IBM-2) and quasiparticle random phase approximation (QRPA) as described in the text.

		$\mathcal{M}_F$	$\mathcal{M}_{GT}^{AA}$	$\mathcal{M}_{GT}^{'AP}$	$\mathcal{M}_{T}^{'AP}$	$\mathcal{M}_{GT}^{'WW}$	$\mathcal{M}_{T}^{'WW}$	$\mathcal{M}_{GT}^{''PP}$	$\mathcal{M}_{T}^{''PP}$
^{76}Ge	IBM-2	−48.89	170.0	2.110	−1.310	−2.945	−6.541	0.028	−0.022
	QRPA	−139.4	458.1	7.101	−1.104	17.75	−4.821	0.117	−0.018
^{82}Se	IBM-2	−41.22	140.7	1.758	−1.249	−2.456	−6.206	0.024	−0.021
	QRPA	−102.0	329.3	5.084	−0.834	12.32	−3.506	0.083	−0.013
^{96}Zr	IBM-2	−35.31	124.3	1.523	1.090	−3.116	5.436	0.020	0.019
	QRPA	−114.2	359.1	5.698	−1.201	15.65	−5.698	0.095	−0.021
^{100}Mo	IBM-2	−51.96	181.9	2.273	1.590	−4.590	8.055	0.029	0.027
	QRPA	−127.1	405.5	6.441	−1.438	17.53	−6.925	0.108	−0.025
^{110}Pd	IBM-2	−43.52	151.2	1.892	1.356	−3.945	6.816	0.024	0.023
	QRPA	−167.6	557.5	8.552	−1.503	20.64	−7.100	0.139	−0.026
^{116}Cd	IBM-2	−32.45	110.5	1.374	0.843	−3.069	4.222	0.017	0.015
	QRPA	−102.1	314.1	4.818	−1.016	11.35	−4.909	0.078	−0.018
^{124}Sn	IBM-2	−33.19	104.2	1.321	−0.723	−1.701	−3.655	0.018	−0.012
	QRPA	−168.7	561.4	8.691	−1.994	21.74	−9.379	0.143	−0.034
^{128}Te	IBM-2	−41.82	131.7	1.667	−0.890	−2.439	−4.519	0.023	−0.015
	QRPA	−138.5	471.9	7.481	−2.156	20.07	−10.256	0.125	−0.037
^{130}Te	IBM-2	−38.05	119.7	1.514	−0.807	−1.951	−4.105	0.021	−0.014
	QRPA	−119.9	419.5	6.620	−1.909	17.62	−9.116	0.110	−0.033
^{136}Xe	IBM-2	−29.83	94.18	1.177	−0.620	−1.625	−3.158	0.016	−0.011
	QRPA	−61.0	235.8	3.734	−1.214	9.95	−5.873	0.062	−0.021

TABLE 5 | Comparison between interacting boson model (IBM-2) and quasiparticle random phase approximation (QRPA) heavy neutrino exchange Fermi (F), Gamow–Teller (GT), tensor (T), and full $\mathcal{M}_{\nu_h}$ nuclear matrix elements (NMEs) as defined in Equations (12) and (13) and calculated using quenched value $g_A = 1.0$.

Isotope		$\mathcal{M}_{\nu_h,F}$	$\mathcal{M}_{\nu_h,GT}$	$\mathcal{M}_{\nu_h,T}$	$\chi_{\nu_h,F}$	$\mathcal{M}_{\nu_h}$	$\frac{\mathcal{M}_{\nu_h,F}^{QRPA}}{\mathcal{M}_{\nu_h,F}^{IBM-2}}$	$\frac{\mathcal{M}_{\nu_h,GT}^{QRPA}}{\mathcal{M}_{\nu_h,GT}^{IBM-2}}$	$\frac{\mathcal{M}_{\nu_h,T}^{QRPA}}{\mathcal{M}_{\nu_h,T}^{IBM-2}}$	$\frac{\mathcal{M}_{\nu_h}^{QRPA}}{\mathcal{M}_{\nu_h}^{IBM-2}}$
^{76}Ge	IBM-2	−48.9	115	−36.3	−0.43	200	2.85	3.38	0.82	2.79
	QRPA	−139.4	388.5	−29.8	−0.36	557.6				
^{82}Se	IBM-2	−41.2	94.7	−34.5	−0.44	171	2.47	2.93	0.64	2.35
	QRPA	−102.0	277.6	−22.2	−0.37	401.9				
^{96}Zr	IBM-2	−35.3	80.2	30.2	−0.44	85.4	3.23	3.86	−1.08	5.34
	QRPA	−114.2	309.5	−32.7	−0.37	456.3				
^{100}Mo	IBM-2	−52.0	116	44.1	−0.45	124	2.45	3.01	−0.89	4.16
	QRPA	−127.1	348.9	−39.2	−0.36	515.2				
^{110}Pd	IBM-2	−43.5	96.2	37.5	−0.45	102	3.85	4.89	−1.09	6.65
	QRPA	−167.6	470.3	−40.8	−0.36	678.7				
^{116}Cd	IBM-2	−32.5	69.6	23.3	−0.47	78.8	3.15	3.79	−1.19	5.00
	QRPA	−102.1	263.9	−27.7	−0.39	393.6				
^{124}Sn	IBM-2	−33.2	70.3	−20.0	−0.47	124	5.08	6.77	2.71	5.64
	QRPA	−168.8	476.2	−54.1	−0.35	699.2				
^{128}Te	IBM-2	−41.8	87.9	−24.7	−0.48	154	3.31	4.61	2.38	3.91
	QRPA	−138.5	404.8	−58.7	−0.34	602.0				
^{130}Te	IBM-2	−38.1	80.8	−22.4	−0.47	141	3.15	4.45	2.33	3.77
	QRPA	−119.9	359.5	−52.1	−0.33	531.5				
^{136}Xe	IBM-2	−29.8	63.5	−17.2	−0.47	111	2.05	3.18	1.93	2.67
	QRPA	−61.0	202.1	−33.2	−0.30	296.3				

tensor matrix elements, however, behave similarly as in the case of light neutrino exchange and the ratios are comparable to those.

The numerical values of full matrix element $\mathcal{M}_{\nu_h}$ are discussed in sections 4.3 and 4.4.

4. DISCUSSION

There are several ingredients that go into the calculation of nuclear matrix elements. In the following, some of these are discussed in view of explaining similarities and differences obtained in the results of the two models studied, IBM-2 and QRPA. Various discussed assumptions are interrelated with each other.

4.1. Model Assumptions

4.1.1. Microscopic Interacting Boson Model

The IBM-2 is based on presentation of nucleon pairs as bosons with certain quantum numbers and features a truncation of the full shell-model space to a subspace. The procedure to obtaining wavefunctions is typically more phenomenological than in QRPA, and relies more on adjusting the model parameters to match available observables. However, there are no data on $0\nu\beta\beta$ matrix elements and the associated operators therefore must be derived from the shell model, at least approximately. The mapping is approximate since it involves only two- and four-nucleon states (which are mapped to one- and two-boson states) and a schematic surface-delta interaction (SDI) that is not fully consistent with the phenomenological boson interaction. In addition to three fundamental assumptions in IBM-2, those being a shell-model assumption, a mapping assumption, and a truncation assumption, all of which enter in a microscopic derivation of the parameters of the IBM-2 Hamiltonian, there are several assumptions specifically related to description of $0\nu\beta\beta$ decay, such as closure approximation, method of isospin restoration, and inclusion of short-range correlations.

- *The shell model assumption and single particle energies*

  It is generally accepted that the shell model provides an appropriate microscopic framework for the description of the low-lying states of nuclei. The basic assumption is that nuclei contain a relatively inert doubly magic core and additional valence nucleons (or nucleon holes) restricted to a small number of valence shells. Interactions between the valence nucleons scatter them over the valence orbits, thereby dictating spectroscopic properties in the region of low excitation energies. In practice, this means that one major shell is active for neutrons and one for protons and corresponding single particle energies (SPEs) play considerable role. In Kotila and Barea (2016), the single-particle and single-hole energies and strengths of interaction were evaluated and discussed in connection to IBM-2. Furthermore, the occupancies of the single particle levels were calculated and compared to QRPA at BCS level and available experimental data in order to satisfy a two-fold goal: to assess the goodness of the single particle energies and check the reliability of the used wave functions. Both tests are particularly important in the case of nuclei involved in double beta decay, as they affect the evaluation of the NMEs and then their reliability (Engel, 2015).

  In principle, the single particle energies can be considered as input parameters that can be fitted to reproduce the experimental occupancies. Instead of fitting, the single particle energies can also be calculated using, e.g., Woods–Saxon potential or extracted from experimental data on nuclei with a particle more or one particle less than a shell closure as is used in IBM-2. As part of the study reported in Kotila and Barea (2016), the single particle energies used in IBM-2 calculations were updated and in Deppisch et al. (2020), a notable increase for $0\nu\beta\beta$ NMEs was obtained particularly for ^{76}Ge, ^{82}Se and ^{96}Zr, and ^{100}Mo for which the SPEs changed the most. The obtained increase, $\sim 20-40\%$, is mainly due GT contribution. One should note that in IBM-2 the number of the valence orbitals is dictated by magic numbers. The corresponding single particle energies enter the calculation through mapping procedure and the only parameter that is changed when SPEs change is the SDI strength parameter. Also, in the IBM-2 calculation the same single particle energies and SDI strength parameters for both initial and final states are used.

- *The mapping and truncation assumption*

  Formally, any fermion problem can be transformed into an equivalent boson problem by carrying out a mapping from the original fermion space (the shell model space) onto space composed of many-boson states. Those states, which properly reflect the Pauli principle, define the so-called physical boson space. To avoid violating the suppressed effects of the Pauli principle, the boson operators that arise in such mappings will, in general, involve infinite expansions. Their use in practical applications requires that only low orders in the series expansion be maintained. Implicit in the IBM-2 is the assumption that the original fermion shell model Hamiltonian can be mapped to a good approximation onto a boson Hamiltonian which contains, at most, two-boson interactions.

  In the current double beta decay calculations, the Otsuka–Arima–Iachello (OAI) mapping (Otsuka et al., 1978) is employed, where first the dominant, collective degrees of freedom in the fermion space are isolated and then only this collective subspace is mapped onto a boson space. In the zeroth-order OAl mapping, the series expansion for the boson Hamiltonian is truncated so that only one- and two-body terms are kept. One should note that for strongly deformed nuclei different mapping could be more suitable [e.g., the generalized Holstein–Primakoff (GHP) expansion, Marshalek, 1980]. Boson mapping procedures, in principle, map the entire fermion space onto a boson space. Practical application of any such procedure requires truncation to a small set of collective bosons: in IBM-2, this is two collective bosons ($I = 0$ and $I = 2$) for neutrons and likewise two collective bosons for protons.

  In Barea and Iachello (2009), the role of approximations in the boson calculation was assessed by comparing generalized seniority (GS), IBM-2, and IBM-2 with next to leading order (NLO) calculation. It was observed that there was a systematic reduction of the matrix elements by about 20% when going from GS to IBM-2, while the effect of NLO terms was found

to be very small. It was also found that the contribution of *s* bosons is dominant, the contribution of *d* bosons is sizable and of opposite sign, whereas NLO corrections are small and with random sign. It was concluded that NLO corrections appear to be small, they are henceforth neglected in the calculations of Deppisch et al. (2020).

- *Isospin restoration*

  Isospin restoration was already briefly mentioned in section 2. The need for this improvement was obvious: the Fermi matrix elements $\mathcal{M}_F^{(2\nu)}$ for $2\nu\beta\beta$ decay in IBM-2 did not vanish in cases where protons and neutrons occupy the same major shell. Similarly, the Fermi matrix elements $\mathcal{M}_F^{(0\nu)}$ for $0\nu\beta\beta$ decay were large when protons and neutrons are in the same major shell, as can be seen from Table 7 of Barea et al. (2013a), where the quantity χ_F is reported. In IBM-2, the isospin is restored by modifying the mapped operator by imposing the condition that $\mathcal{M}_F^{(2\nu)} = 0$. This condition is simply implemented in the calculation by replacing the radial integrals of Appendix A of Barea and Iachello (2009) with ones given in Equations (9) and (10) in Barea et al. (2015a) that guarantee that the F matrix elements vanish for $2\nu\beta\beta$ as given in Barea et al. (2015a), and they also reduce the F matrix elements for $0\nu\beta\beta$ by subtraction of the monopole term in the expansion of the matrix element into multipoles. Even though the method of isospin restoration is similar in spirit in QRPA, it is different in practice. In IBM-2, the isospin restoration does not affect any model parameters in contrary to QRPA. When compared with the matrix elements without the isospin restoration in IBM-2 (Barea et al., 2013a), a considerable reduction of the F matrix elements to values comparable to those of the shell model (Caurier et al., 2007; Menéndez et al., 2009a), where isospin is a good quantum number by definition, and uniformly small ($\chi_F \sim -0.15$), are found. The overall reduction in full matrix element for light neutrino exchange $\mathcal{M}^{(0\nu)}$ due isospin restoration is ∼15%.
- *Closure approximation*

  A standard way to consider a double beta decay process is to present it as a transitional process from an initial nucleus to an intermediate nucleus and then to a final nucleus, so that the corresponding nuclear matrix elements can be presented as a sum over the intermediate nuclear states. To calculate these matrix elements, one needs to calculate all the intermediate states, which could be a very challenging task. However, this can be avoided using closure approximation. The main idea behind the closure approximation is to replace the energies of the intermediate states with an average energy, and then the sum over the intermediate states can be found explicitly by using the completeness relation. In IBM-2, calculations closure approximation is assumed. In Barea et al. (2013a), the sensitivity to the closure energy (∼10 MeV) is estimated to be 5%. This uncertainty in the value of the nuclear matrix elements is related to the ability to derive accurately enough the average energy associated with the closure approximation. Fortunately, the $0\nu\beta\beta$ nuclear matrix elements are not very sensitive to the value of closure energy since the typical, large value of momentum of the virtual neutrino is $\sim 100 - 200$ MeV, i.e., much larger than the typical nuclear excitations. In Yoshida and Iachello (2013), IBM-2 was employed without closure approximation in the description of $2\nu\beta\beta$ for $A = 128, 130$ systems. The results were found to be comparable with the ones using closure approximation, even though $2\nu\beta\beta$ is much more sensitive to the choice of closure energy. In $2\nu\beta\beta$ decay, the typical neutrino momentum is of the same order than nuclear excitations. Further IBM-2 calculations without closure approximations for $2\nu\beta\beta$ and $0\nu\beta\beta$ are in progress.

4.1.2. Quasiparticle Random Phase Approximation

The QRPA is a standard method for describing collective excitations in open-shell nuclei with stable mean-field solutions, either spherical or deformed. The advantage of the QRPA is the number of single-particle orbits that can be included in the calculation. In most QRPA calculations, all the orbitals within one, two, or even more oscillator shells of the Fermi surface are treated explicitly, with those further below assumed to be fully occupied and those further above completely empty. The cost for such large single-particle spaces in the QRPA is a restricted set of correlations. To compensate this, the effective nucleon–nucleon interaction used to generate the nuclear states needs to be modified. The original interaction is typically a realistic nucleon–nucleon potential adapted to the QRPA configuration space through many-body perturbation theory.

- *Parameter fitting and isospin restoration*

  The interaction is usually modified independently in the particle-hole and pairing channels. The strengths of the pairing interaction are renormalized independently for protons, g_p^{pair}, and neutrons, g_n^{pair}, to reproduce the pairing gaps. The strengths of the interaction in the proton–neutron particle-hole channels are usually renormalized to properly reproduce the energies of the Gamow–Teller and spin-dipole giant resonances, altering both the $2\nu\beta\beta$ and $0\nu\beta\beta$ matrix elements somewhat. The particle–particle channel is used to cure the problem of isospin violation obtained in $2\nu\beta\beta$ decay. This is done by adjusting the renormalization constant $g_{pp}^{T=1}$ to make $\mathcal{M}_F^{(2\nu)}$ vanish (Šimkovic et al., 2013). In order to restore the isospin symmetry, $g_{pp}^{T=1}$ should approximately equal to g^{pair}'s (Rodin and Faessler, 2011). Then this adjusted value of $g_{pp}^{T=1}$ is used in further calculations for the $0\nu\beta\beta$ decay. The parameter $g_{pp}^{T=0}$ is usually independently fitted to reproduce the measured $2\nu\beta\beta$-decay half-life and thus obtained value is then used in the calculation of the $0\nu\beta\beta$ NMEs. The fitted g_{pp}'s depend naturally on the chosen nucleon–nucleon interaction. However, in Fang et al. (2018), it was found that even though the parameters that lead to same $2\nu\beta\beta$ NME are different for different interactions, they lead also basically to the same $0\nu\beta\beta$ NME.

  When comparing the matrix elements without and with the restoration, the reduction is found to be smaller for QRPA (Hyvärinen and Suhonen, 2015) than for IBM-2. The effect on light neutrino exchange Fermi matrix elements is found to be very small or negligible and Gamow–Teller and tensor parts are found to be hardly affected in disagreement with

QRPA calculations reported in Šimkovic et al. (2013). This deviation with different QRPA calculations is discussed further in section 4.4. For heavy neutrino exchange, the effect on F NMEs is less than 5% and very small or negligible for GT and T nuclear matrix elements. It should also be noted that for $A = 110$ and $A = 124$ systems, there are no $2\nu\beta\beta$-decay data available, and in the QRPA calculation beta decay data were used for $A = 110$ and for $A = 124$ $2\nu\beta\beta$ nuclear matrix element proposed in Šimkovic et al. (2013) was taken. These two nuclear systems are exactly the ones were nuclear matrix elements in **Tables 2**–**5** for QRPA and IBM-2 differ the most. However, in Šimkovic et al. (2013), for these nuclei QRPA results are presented that are much closer to IBM-2 values.

- *Size of the model space*

  Size of the model space and SPEs play considerable role in QRPA $0\nu\beta\beta$ calculations as was pointed out in Suhonen and Civitarese (2008). In QRPA calculations, the valence space usually spans more than just one harmonic oscillator shell. In Suhonen and Civitarese (2010), the effects of different orbital occupancies and model-space sizes on the magnitudes of $0\nu\beta\beta$ nuclear matrix elements were studied. It was found that the contributions coming from beyond the simple shell-model space are essential in obtaining a reliable value of the nuclear matrix element. Furthermore, inclusion of spin-orbit partners in the single particle basis is not only possible in QRPA but also found necessary in order to avoid underestimation of the $0\nu\beta\beta$ NMEs. Also, in QRPA rather different sets of single particle energies are employed for initial and final nucleus (Suhonen and Civitarese, 2010).

  The size of the model space and SPEs affect also the fitting of g_{pp} parameters. Usually larger values of parameters g_{pp} are needed to obtain agreement for the $2\nu\beta\beta$ transition probabilities when smaller model space is considered and the $2\nu\beta\beta$ NMEs decrease with increasing particle–particle strength.

- *Non-closure approach*

  In QRPA, the use of closure approximation is avoided when evaluating $0\nu\beta\beta$ NMEs. In this so-called non-closure approach, one needs to calculate the sum through all intermediate states explicitly, which is an obvious challenge due to the large number of intermediate states. As noted earlier, use of closure approximation in the description of $0\nu\beta\beta$ decay is much more justified than in the case of $2\nu\beta\beta$ decay. However, in QRPA $2\nu\beta\beta$ NMEs are needed to fit the g_{pp} parameters and thus the use of non-closure approximation is essential.

  The QRPA calculations have also been used to estimate the difference between closure vs. non-closure and the validity of used closure energy. For example, results from Pantis and Vergados (1990) indicate a deviation of about up to 10% between closure and non-closure NMEs, but its magnitude and sign depend on the choice of g_{pp}. In Muto (1994), very small differences between closure and non-closure is reported, and in most cases the magnitude of the non-closure results is slightly smaller than the magnitude of the closure result.

4.2. Short Range Correlations

The short range correlation is important issue in the actual calculation of $0\nu\beta\beta$ NMEs. Early calculations use the Miller-Spencer SRC, which gives rather large reductions to the final results. More modern Argonne and CD-Bonn SRC behave much milder.

The short-range correlations affect heavy neutrino exchange, $0\nu_h\beta\beta$, decay differently than light neutrino exchange, $0\nu\beta\beta$. This is because the neutrino potential for heavy neutrino exchange is a contact interaction in configuration space and thus strongly influenced by SRC. For light neutrino exchange, the effect is very small, especially when going from Argonne SRC to CD-Bonn SRC, which are the SRC parameterizations used in IBM-2 and QRPA calculations of interest here, respectively. For heavy neutrino exchange, however, the effect is considerable. In Hyvärinen and Suhonen (2015), effect of changing from Argonne to CD-Bonn SRC in case of heavy neutrino exchange in QRPA was studied and CD-Bonn NMEs were found to be roughly 1.5 larger than Argonne NMEs. Similar result is found also for IBM-2 (Barea et al., 2013a). Taking this into account, the difference between the results for heavy neutrino exchange obtained in IBM-2 and QRPA is reduced to factor $\sim$1.9 for F nuclear matrix elements and $\sim$2.5 for GT nuclear matrix elements and full matrix element.

4.3. Sign of the Tensor Matrix Element and Full $0\nu\beta\beta$ Nuclear Matrix Element

In recent papers (Graf et al., 2018; Deppisch et al., 2020), the mapping of the quark current products to nucleon matrix elements and finally to nuclear matrix elements was performed in detail. A different relative sign between GT and T matrix element was found than in previous papers available in literature. In case of light neutrino exchange, the tensor contribution is rather small, $\sim$1%. However, for heavy neutrino exchange the sign affects the final $0\nu_h\beta\beta$ NMEs considerably. In **Figures 1**, **2**, total NMEs obtained with IBM-2 and QRPA using the same form factor charges, same overall sign for tensor matrix elements, and the convention that $\mathcal{M}_\nu > 0$, $\mathcal{M}_{\nu_h} > 0$, are plotted for light and heavy neutrino exchange, respectively. The numerical values are also given in **Tables 3**, **5**. Total nuclear matrix element are found to be systematically larger in QRPA. However, for light neutrino exchange the correspondence is very good for $A = 76, 82, 100$, and 136 systems where the deviation is less or equal to 15%. For heavy neutrino exchange, the situation is more complicated and a factor up to 6.65 difference is found between the two models when ^{110}Pd and ^{124}Sn are included. When ^{110}Pd and ^{124}Sn are not included and different parameterization of short range correlation is taken into account, the factor reduces to $\sim 2-3$. However, even for the heavy neutrino exchange, the trend is found to be similar for IBM-2 and QRPA. The difference also seems to be rather regular and systematic.

The matrix elements $\mathcal{M}_\nu$ attain their smallest values at the closed proton and neutron shells due to the form of the transition operator, which for $\beta^-\beta^-$ decay annihilates a neutron pair and creates a proton pair. These shell effects are very clear in **Figure 1**

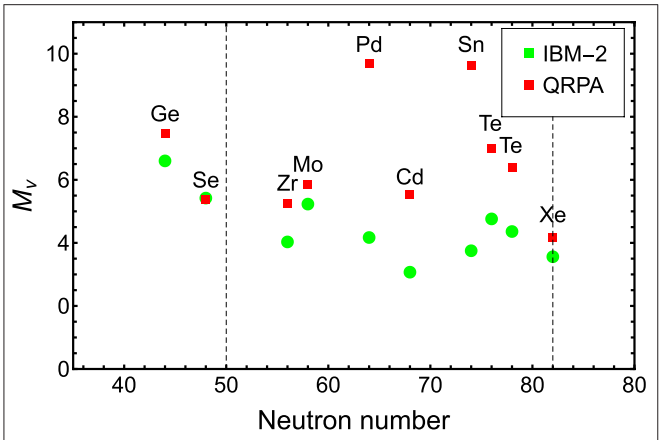

FIGURE 1 | Total light neutrino exchange $0\nu\beta\beta$ nuclear matrix elements $\mathcal{M}_\nu$ obtained with interacting boson model (IBM-2) and quasiparticle random phase approximation (QRPA) using same form factor charges, same overall sign for tensor matrix elements, and the convention that $\mathcal{M}_\nu > 0$.

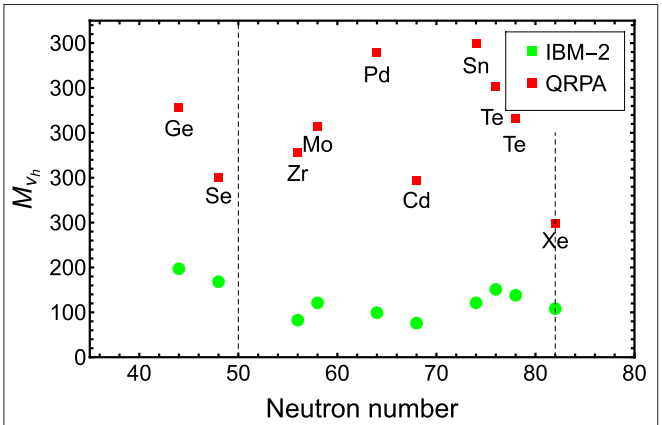

FIGURE 2 | Total heavy neutrino exchange $0\nu_h\beta\beta$ nuclear matrix elements $\mathcal{M}_{\nu_h}$ obtained with interacting boson model (IBM-2) and quasiparticle random phase approximation (QRPA) using same form factor charges, same overall sign for tensor matrix elements, and the convention that $\mathcal{M}_{\nu_h} > 0$.

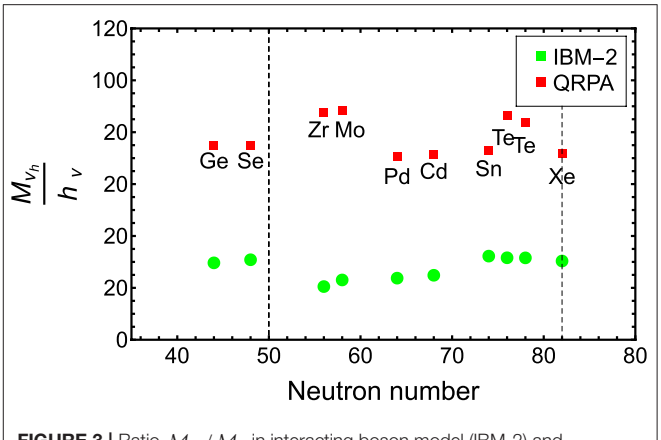

FIGURE 3 | Ratio $\mathcal{M}_{\nu_h}/\mathcal{M}_\nu$ in interacting boson model (IBM-2) and quasiparticle random phase approximation (QRPA) using same form factor charges, same overall sign for tensor matrix elements, and the convention that $\mathcal{M}_\nu, \mathcal{M}_{\nu_h} > 0$.

and it even seems that both calculations suggest a kind of shell closure at $A = 116$ system, i.e., around $N = 66$. Shell effects are also responsible for the ratio of the matrix elements of two different isotopes of the same element. For example, a simple calculation using the pair operators of Equation (42) of Barea and Iachello (2009) gives $\mathcal{M}_\nu(^{128}\text{Te})/\mathcal{M}_\nu(^{130}\text{Te}) = 1.11$, which is nicely reproduced by both models.

4.4. Other QRPA Calculations

As already noted, there are also several other calculations available using QRPA in the description of double beta decay. In Šimkovic et al. (2013), a significant reduction in the Fermi matrix element was observed when comparing results without and with isospin restoration. On the other hand, the values of Fermi NMEs without isospin restoration were considerably higher than in the QRPA calculation analyzed here. As a consequence, after the isospin restoration the Fermi NMEs for light neutrino exchange of these two QRPA calculations (Šimkovic et al., 2013; Hyvärinen and Suhonen, 2015) are rather close to each other. Also the GT NMEs are generally in good agreement in these two calculations, exceptions being ^{110}Pd and ^{124}Sn, where (Šimkovic et al., 2013) reports much smaller values that in fact are in good correspondence with IBM-2 results. In Šimkovic et al. (2013), the T NMEs are also found to be reduced slightly once isospin restoration is taken into account. Nonetheless, T nuclear matrix elements obtained in Šimkovic et al. (2013) are roughly twice as large compared to Hyvärinen and Suhonen (2015).

The nuclear matrix elements for heavy neutrino exchange with isospin restoration in QRPA were also calculated in Faessler et al. (2014) where only full matrix elements are given. The results of this calculation are somewhere between IBM-2 (Deppisch et al., 2020) and QRPA of Hyvärinen and Suhonen (2015). The results obtained with CD-Bonn parameterization of SRC are about 67% of those given in Hyvärinen and Suhonen (2015) obtained with the same SRC parameterization, exceptions being ^{110}Pd and ^{124}Sn. Faessler et al. (2014) also gives results with Argonne parameterization of short range correlations and those are very similar to the ones obtained with IBM-2 (Deppisch et al., 2020) and calculated with same SRC parameterization.

Double beta decay nuclear matrix elements for ^{76}Ge, ^{82}Se, ^{130}Te, ^{136}Xe, and ^{150}Nd have also been calculated using deformed QRPA in Fang et al. (2018), where the results are presented for both CD-Bonn and Argonne parameterization of SRC. It is thus convenient to compare spherical and deformed QRPA calculations with CD-Bonn parameterization, where as the comparison with IBM-2 and deformed QRPA is made using Argonne parameterization. Compared to spherical QRPA calculations a reduction of ∼30% was found for ^{76}Ge, ^{82}Se, and ^{130}Te, and about 60% for ^{136}Xe, which has a magic neutron number and different Fermi surfaces of initial non-paired and final paired neutrons.The reduction was concluded to be mainly

TABLE 6 | Upper limits on $|m_{\beta\beta}||\mathcal{M}_\nu|$ from current experimental bounds $T^{\text{exp}}_{1/2}$ at 90% CL and taking $g_A = 1.0$.

Isotope	$T^{\text{exp}}_{1/2}$ [yr]		G_ν 10^{-15}yr^{-1}	$\lvert m_{\beta\beta}\rvert\lvert\mathcal{M}_\nu\rvert$ [eV]
76Ge	$>1.8\times10^{26}$	Agostini et al., 2020	2.36	<0.78
^{82}Se	$>2.4\times10^{24}$	Azzolini et al., 2018	10.19	<3.27
^{96}Zr	$>9.2\times10^{21}$	Argyriades et al., 2010	20.58	<37.14
^{100}Mo	$>1.1\times10^{24}$	Arnold et al., 2015	15.91	<3.86
^{116}Cd	$>2.2\times10^{23}$	Barabash et al., 2018	16.69	<8.43
^{128}Te	$>1.1\times10^{23}$	Arnaboldi et al., 2003	0.59	<63.43
^{130}Te	$>3.2\times10^{25}$	Adams et al., 2020	14.20	<0.76
^{136}Xe	$>1.1\times10^{26}$	Gando et al., 2016	14.56	<0.40

due the presence of BCS overlap factor between the initial and ground states. This reduction leads to light neutrino exchange NMEs that are roughly half of those obtained with IBM-2 and spherical QRPA except for ^{136}Xe, where the reduction is larger. This holds also for heavy neutrino exchange between the QRPA calculations. The IBM-2 NMEs, however, are very close to those obtained with deformed QRPA when sign of the tensor matrix element is taken into account (exception again being ^{136}Xe).

4.5. Correlation of Light and Heavy Neutrino Exchange Matrix Elements

It has been suggested that measurement of $0\nu\beta\beta$ decay in different nuclei could be used to distinguish between the two mechanisms, light or heavy neutrino exchange. Unfortunately, the results in **Tables 3**, **5** are highly correlated as is evident from the fact that they are obtained one from the other just by replacing the potential $v(p)$ with $v_h(p)$. Therefore, this criterion cannot be used to distinguish between the two mechanisms (Lisi, 2011). The situation is further illustrated in **Figure 3**. For QRPA, the heavy neutrino nuclear matrix elements are roughly 80 times larger than light neutrino ones. For IBM-2, this factor is roughly 30.

4.6. Experimental Half-Life Limits

Table 6 summarizes current bounds for $T^{\text{exp}}_{1/2}$ at 90% CL from different experiments. For ^{76}Ge and ^{136}Xe, limit of 10^{26}yr has already been exceeded. Experimental half-life limits can be converted to limits on product of neutrino mass parameter $|m_{\beta\beta}|$ and nuclear matrix element as shown in the last column of **Table 6**. Once the nuclear matrix element is known accurately enough, these can be converted to limits on neutrino mass parameter $|m_{\beta\beta}|$. As mentioned, the stringent limits are currently found for ^{76}Ge and ^{136}Xe. For these two systems the IBM-2 and QRPA give rather good correspondence as can be seen from **Figure 1**, deviation being ∼15%. As a result, limits of $|m_{\beta\beta}|$ ∼100 meV are deduced for both ^{76}Ge and ^{136}Xe.

5. SUMMARY

In this paper, a comparison between QRPA and IBM-2 calculations for $0\nu\beta\beta$ NMEs with isospin restoration in both models was presented in detailed level, i.e., looking at the individual NMEs that contribute to F, GT, and T matrix elements and finally to total $0\nu\beta\beta$ NME when multiplied with appropriate form factor charges. Possible explanations, including method of isospin restoration, short range correlations, single particle energies, and closure approximation, for obtained similarities and differences were then discussed. The agreement is found to be quite good in most cases for light neutrino exchange. However, there seems to be larger deviations for the $A = 110, 124$ systems. In these cases, there is no $2\nu\beta\beta$ data available that is used in the QRPA to fit parameter $g_{pp}^{T=1}$. For heavy neutrino exchange, the trend is found to be similar, but a factor of ∼3 difference is obtained even when the effect of different short range correlation parameterization, which affects heavy neutrino exchange considerably, is taken into account. This suggest a need for a further investigation on heavy neutrino exchange $0\nu\beta\beta$ nuclear matrix elements. Once the origin of this systematic and rather regular difference is better understood, and perhaps solved, the connection between IBM-2 and QRPA could be used to combine the strengths of each model, in particular the large model space and non-closure of QRPA and capability to describe deformed nuclei of IBM-2.

DATA AVAILABILITY STATEMENT

The original contributions presented in the study are included in the article/supplementary material, further inquiries can be directed to the corresponding author/s.

AUTHOR CONTRIBUTIONS

The author confirms being the sole contributor of this work and has approved it for publication.

FUNDING

This research was funded by the Academy of Finland, Grant Nos. 314733 and 320062.

REFERENCES

Adams, D. Q., Alduino, C., Alfonso, K., Avignone, III, F. T., Azzolini, O., Bari, G., et al. (2020). Improved limit on neutrinoless double-beta decay in ^{130}Te with CUORE. *Phys. Rev. Lett.* 124:122501. doi: 10.1103/PhysRevLett.124.122501

Agostini, M., Araujo, G. R., Bakalyarov, A. M., Balata, M., Barabanov, I., Baudis, L., et al. (2020). Final results of GERDA on the search for neutrinoless double-β decay. *Phys. Rev. Lett.* 125:252502. doi: 10.1103/PhysRevLett.125.252502

Argyriades, J., Arnold, R., Augier, C., Baker, J., Barabash, A. S., Basharina-Freshville, A., et al. (2010). Measurement of the two neutrino double beta decay half-life of Zr-96 with the NEMO-3 detector. *Nuclear Phys. A* 847, 168–179. doi: 10.1016/j.nuclphysa.2010.07.009

Arnaboldi, C., Brofferio, C., Bucci, C., Capelli, S., Cremonesi, O., Fiorini, E., et al. (2003). A Calorimetric search on double beta decay of Te-130. *Phys. Lett. B* 557, 167–175. doi: 10.1016/S0370-2693(03)00212-0

Arnold, R., Augier, C., Baker, J. D., Barabash, A. S., Basharina-Freshville, A., Blondel, S., et al. (2015). Results of the search for neutrinoless double-β decay in ^{100}Mo with the NEMO-3 experiment. *Phys. Rev. D* 92:072011. doi: 10.1103/PhysRevD.92.072011

Azzolini, O., Beeman, J.W., Bellini, F., and Barrera, M. T. (2018). First result on the neutrinoless double-β decay of ^{82}Se with CUPID-0. *Phys. Rev. Lett.* 120:232502. doi: 10.1103/PhysRevLett.120.232502

Barabash, A. S., Belli, P., Bernabei, R., Cappella, F., Caracciolo, V., Cerulli, R., et al. (2018). Final results of the Aurora experiment to study 2β decay of ^{116}Cd with enriched $^{116}CdWO_4$ crystal scintillators. *Phys. Rev. D* 98:092007. doi: 10.1103/PhysRevD.98.092007

Barea, J., and Iachello, F. (2009). Neutrinoless double-β decay in the microscopic interacting boson model. *Phys. Rev. C* 79:044301. doi: 10.1103/PhysRevC.79.044301

Barea, J., Kotila, J., and Iachello, F. (2013a). Nuclear matrix elements for double-β decay. *Phys. Rev. C* 87:014315. doi: 10.1103/PhysRevC.87.014315

Barea, J., Kotila, J., and Iachello, F. (2013b). Neutrinoless double-positron decay and positron-emitting electron capture in the interacting boson model. *Phys. Rev. C* 87:057301. doi: 10.1103/PhysRevC.87.057301

Barea, J., Kotila, J., and Iachello, F. (2015a). $0\nu\beta\beta$ and $2\nu\beta\beta$ nuclear matrix elements in the interacting boson model with isospin restoration. *Phys. Rev. C* 91:034304. doi: 10.1103/PhysRevC.91.034304

Barea, J., Kotila, J., and Iachello, F. (2015b). Limits on sterile neutrino contributions to neutrinoless double beta decay. *Phys. Rev. D* 92:093001. doi: 10.1103/PhysRevD.92.093001

Basili, R. A. M., Yao, J. M., Engel, J., Hergert, H., Lockner, M., Maris, P., et al. (2020). Benchmark neutrinoless double-β decay matrix elements in a light nucleus. *Phys. Rev. C* 102:014302. doi: 10.1103/PhysRevC.102.014302

Caurier, E., Martínez-Pinedo, G., Nowacki, F., Poves, A., and Zuker, A. (2005). The shell model as a unified view of nuclear structure. *Rev. Mod. Phys.* 77:427. doi: 10.1103/RevModPhys.77.427

Caurier, E., Nowacki, F., and Poves, A. (2007). Beta beta decay and nuclear structure. *Int. J. Mod. Phys. E* 16, 552–560. doi: 10.1142/S0218301307005983

Coraggio, L., Itaco, N., De Gregorio, G., Gargano, A., Mancino, R., and Pastore, S. (2020). Present status of nuclear shell-model calculations of $0\nu\beta\beta$ decay matrix elements. *Universe* 6:233. doi: 10.3390/universe6120233

de Salas, P. F., Forero, D. V., Gariazzo, S., Martínez-Miravé, P., Mena, O., Ternes, C. A., et al. (2021). 2020 global reassessment of the neutrino oscillation picture. *J. High Energ. Phys.* 2021:71. doi: 10.1007/JHEP02(2021)071

Deppisch, F. F., Graf, L., Iachello, F., and Kotila, J. (2020). Analysis of light neutrino exchange and short-range mechanisms in $0\nu\beta\beta$ decay. *Phys. Rev. D* 102:095016. doi: 10.1103/PhysRevD.102.095016

Doi, M., Kotani, T., Nishiura, H., Okuda, K., and Takasugi, E. (1981). Neutrino mass, the right-handed interaction and the double beta decay. I: formalism. *Prog. Theor. Phys.* 66:1739. doi: 10.1143/PTP.66.1739

Doi, M., Kotani, T., Nishiura, H., Okuda, K., and Takasugi, E. (1983). Double beta decay. *Prog. Theor. Phys.* 69:602. doi: 10.1143/PTP.69.602

Doi, M., Kotani, T., and Takasugi, E. (1985). Double beta decay and Majorana neutrino. *Prog. Theor. Phys. Suppl.* 83, 1–175. doi: 10.1143/PTPS.83.1

Dumbrajs, O., Koch, R., Pilkuhn, H., Oades, G. C., Behrens, H., de Swart, J. J., et al. (1983). Compilation of coupling constants and low-energy parameters. *Nuclear Phys. B* 216, 277–335. doi: 10.1016/0550-3213(83)90288-2

Engel, J. (2015). Uncertainties in nuclear matrix elements for neutrinoless double-beta decay. *J. Phys. G Nuclear Phys.* 42:034017. doi 10.1088/0954-3899/42/3/034017

Faessler, A., González, M., Kovalenko, S., and Šimkovic, F. (2014). Arbitrary mass Majorana neutrinos in neutrinoless double beta decay. *Phys. Rev. D* 90:096010. doi: 10.1103/PhysRevD.90.096010

Faessler, A., Rodin, V., and Šimkovic, F. (2012). Nuclear matrix elements for neutrinoless double-beta decay and double-electron capture. *J. Phys. G Nuclear Phys.* 39:124006. doi: 10.1088/0954-3899/39/12/124006

Fang, D. L., Faessler, A., Rodin, V., and Šimkovic, F. (2011). Neutrinoless double-β decay of deformed nuclei within quasiparticle random-phase approximation with a realistic interaction. *Phys. Rev. C* 83:034320. doi: 10.1103/PhysRevC.83.034320

Fang, D. L., Faessler, A., and Šimkovic, F. (2018). $0\nu\beta\beta$-decay nuclear matrix element for light and heavy neutrino mass mechanisms from deformed quasiparticle random-phase approximation calculations for ^{76}Ge,^{82} Se,^{130} Te,^{136} Xe, and ^{150}Nd with isospin restoration. *Phys. Rev. C* 97:045503. doi: 10.1103/PhysRevC.97.045503

Furry, W. H. (1939). On transition probabilities in double beta-disintegration. *Phys. Rev.* 56:1184. doi: 10.1103/PhysRev.56.1184

Gando, A., Gando, Y., Hachiya, T., Hayashi, A., Hayashida, S., Ikeda, H., et al. (2016). Search for majorana neutrinos near the inverted mass hierarchy region with KamLAND-Zen. *Phys. Rev. Lett.* 117:082503. doi: 10.1103/PhysRevLett.117.082503

Graf, L., Deppisch, F. F., Iachello, F., and Kotila, J. (2018). Short-range neutrinoless double beta decay mechanisms. *Phys. Rev. D* 98:095023. doi: 10.1103/PhysRevD.98.095023

Haxton, W. C., and Stephenson, G. J. (1984). Double beta decay Jr. *Prog. Part Nuclear Phys.* 12:409. doi: 10.1016/0146-6410(84)90006-1

Hergert, H., Bogner, S. K., Morris, T. D., Schwenk, A., and Tsukiyama, K. (2016). The in-medium similarity renormalization group: a novel *ab initio* method for nuclei. *Phys. Rep.* 621:165. doi: 10.1016/j.physrep.2015.12.007

Horoi, M., and Brown, B. A. (2013). Shell-model analysis of the ^{136}Xe double beta decay nuclear matrix elements. *Phys. Rev. Lett.* 110:222502. doi: 10.1103/PhysRevLett.110.222502

Hyvärinen, J., and Suhonen, J. (2015). Nuclear matrix elements for $0\beta\beta$ decays with light or heavy Majorana-neutrino exchange. *Phys. Rev. C* 91: 024613. doi: 10.1103/PhysRevC.91.024613

Kotila, J., and Barea, J. (2016). Occupation probabilities of single particle levels using the microscopic interacting boson model: application to some nuclei of interest in neutrinoless double-β decay. *Phys. Rev. C* 94:034320. doi: 10.1103/PhysRevC.94.034320

Kotila, J., Barea, J., and Iachello, F. (2014). Neutrinoless double-electron capture. *Phys. Rev. C* 89:064319. doi: 10.1103/PhysRevC.89.064319

Kotila, J., Barea, J., and Iachello, F. (2015). Phase-space factors and half-life predictions for Majoron-emitting $\beta^-\beta^-$ decay. *Phys. Rev. C* 91:064310. doi: 10.1103/PhysRevC.91.064310

Kotila, J., and Iachello, F. (2012). Phase-space factors for double-β decay. *Phys. Rev. C* 85:034316. doi: 10.1103/PhysRevC.85.034316

Kotila, J., and Iachello, F. (2013). Phase space factors for $\beta^+\beta^+$ decay and competing modes of double-β decay. *Phys. Rev. C* 87:024313. doi: 10.1103/PhysRevC.87.024313

Lisi, E. (2011). On the discrimination of different mechanisms for $0\nu2\beta$ decay. *AIP Conf. Proc.* 1417:74. doi: 10.1063/1.3671040

Marshalek, E. G. (1980). How microscopic boson models work. *Nuclear Phys. A*. 347:253. doi: 10.1016/0375-9474(80)90528-X

Menéndez, J., Poves, A., Caurier, E., and Nowacki, F. (2009a). Disassembling the nuclear matrix elements of the neutrinoless $\beta\beta$ beta decay. *Nuclear Phys. A* 818, 139–151. doi: 10.1016/j.nuclphysa.2008.12.005

Menéndez, J., Poves, A., Caurier, E., and Nowacki, F. (2009b). Occupancies of individual orbits, and the nuclear matrix element of the ^{76}Ge neutrinoless $\beta\beta$ decay. *Phys. Rev. C* 80:048501. doi: 10.1103/PhysRevC.80.048501

Miller, G. A., and Spencer, J. E. (1976). A survey of pion charge-exchange reactions with nuclei. *Annu. Phys.* (1976) 100:562. doi: 10.1016/0003-4916(76)90073-7

Mirea, M., Pahomi, T., and Stoica, S. (2015). Values of the phase space factors involved in double beta decay. *Roman Rep. Phys.* 67, 872–889. doi: 10.1063/1.4934913

Molina, A., and Pascual, P. (1977). Double beta decay. *Il Nuovo Cimento A* 41:756. doi: 10.1007/BF02730270

Mustonen, M. T., and Engel, J. (2013). Large-scale calculations of the double-β decay of ^{76}Ge, ^{128}Te, ^{136}Xe, and ^{150}Nd in the deformed self-consistent skyrme quasiparticle random phase approximation. *Phys. Rev. C* 87:064302. doi: 10.1103/PhysRevC.87.064302

Muto, K. (1994). Neutrinoless double beta decay beyond closure approximation. *Nuclear Phys. A* 577, 415c–420c. doi: 10.1016/0375-9474(94)90890-7

Neacsu, A., and Horoi, M. (2015). Shell model studies of the ^{130}Te neutrinoless double-β decay. *Phys. Rev. C* 91:024309. doi: 10.1103/PhysRevC.91.024309

Neacsu, A., and Stoica, S. (2014). Shell model calculations for neutrinoless double beta decay through the exchange of heavy neutrinos. *Roman Rep. Phys.* 66, 376–381.

Otsuka, T., Arima, A., Iachello, F. (1978). Nuclear shell model and interacting bosons. *Nuclear Phys. A* 309, 1–33. doi: 10.1016/0375-9474(78)90532-8

Pantis, G., and Vergados, J. D. (1990). Neutrinoless double beta decay matrix elements beyond closure approximation. *Phys. Lett. B* 242:1. doi: 10.1016/0370-2693(90)91584-X

Pastore, S., Carlson, J., Cirigliano, V., Dekens, W., Mereghetti, E., and Wiringa, R. B. (2018). Neutrinoless double-β decay matrix elements in light nuclei. *Phys. Rev. C* 97:014606. doi: 10.1103/PhysRevC.97.014606

Primakoff, H., and Rosen, S. P. (1959). Double beta decay. *Rep. Prog. Phys.* 22:121. doi: 10.1088/0034-4885/22/1/305

Rath, P. K., Chandra, R., Chaturvedi, K., Raina, P. K. (2019). Nuclear transition matrix elements for double-β decay within PHFB model. *Front. Phys.* 7:64. doi: 10.3389/fphy.2019.00064

Rath, P. K., Chandra, R., Chaturvedi, K., Raina, P. K., and Hirsch, J. G. (2010). Uncertainties in nuclear transition matrix elements for neutrinoless $\beta\beta$ decay within the projected-Hartree-Fock-Bogoliubov model. *Phys. Rev. C* 82:064310. doi: 10.1103/PhysRevC.82.064310

Rodin, V., and Faessler, A. (2011). Origin of a sensitive dependence of calculated $\beta\beta$ -decay amplitudes on the particle-particle residual interaction. *Phys. Rev. C* 84:014322. doi: 10.1103/PhysRevC.84.014322

Rodríguez, T. R., and Martínez-Pinedo, G. (2010). Energy density functional study of nuclear matrix elements for neutrinoless $\beta\beta$ decay. *Phys. Rev. Lett.* 105:252503. doi: 10.1103/PhysRevLett.105.252503

Schindler, M. R., and Scherer, S. (2007). Nucleon form factors of the isovector axial-vector current. *Eur. Phys. J. A* 32:429. doi: 10.1140/epja/i2006-10403-3

Šimkovic, F., Faessler, A., Müther, H., Rodin, V., and Stauf, M. (2009). $0\nu\beta\beta$-decay nuclear matrix elements with self-consistent short-range correlations. *Phys. Rev. C* 79:055501. doi: 10.1103/PhysRevC.79.055501

Šimkovic, F., Faessler, A., Rodin, V., Vogel, P., and Engel, J. (2008). Anatomy of nuclear matrix elements for neutrinoless double-beta decay. *Phys. Rev. C* 77:045503. doi: 10.1103/PhysRevC.77.045503

Šimkovic, F., Pantis, G., Vergados, J. D., and Faessler, A. (1999). Additional nucleon current contributions to neutrinoless double β decay. *Phys. Rev. C* 60:055502. doi: 10.1103/PhysRevC.60.055502

Šimkovic, F., Rodin, V., Faessler, A., Vogel, P. (2013). $0\nu\beta\beta$ and $2\nu\beta\beta$ nuclear matrix elements, quasiparticle random-phase approximation, and isospin symmetry restoration. *Phys. Rev. C* 87:045501. doi: 10.1103/PhysRevC.87.045501

Song, L. S., Yao, J. M., Ring, P., and Meng, J. (2014). Relativistic description of nuclear matrix elements in neutrinoless double-β decay. *Phys. Rev. C* 90:054309. doi: 10.1103/PhysRevC.90.054309

Song, L. S., Yao, J. M., Ring, P., and Meng, J. (2017). Nuclear matrix element of neutrinoless double-β decay: relativity and short-range correlations. *Phys. Rev. C* 95:024305. doi: 10.1103/PhysRevC.95.024305

Stoica, S., and Mirea, M. (2013). New calculations for phase space factors involved in double-β decay. *Phys. Rev. C* 88:037303. doi: 10.1103/PhysRevC.88.037303

Suhonen, J., and Civitarese, O. (1998). Weak-interaction and nuclear-structure aspects of double beta decay. *Phys. Rep.* 300, 123–214. doi: 10.1016/S0370-1573(97)00087-2

Suhonen, J., and Civitarese, O. (2008). Nuclear matrix elements for double beta decay in the QRPA approach: a critical review. *Phys. Lett. B* 668:277. doi: 10.1088/1742-6596/173/1/012012

Suhonen, J., and Civitarese, O. (2010). Effects of orbital occupancies and spin-orbit partners on $0\nu\beta\beta$-decay rates. *Nuclear Phys A* 847, 207–232. doi: 10.1016/j.nuclphysa.2010.08.003

Suhonen, J., and Civitarese, O. (2012). Double-beta-decay nuclear matrix elements in the QRPA framework. *J. Phys. G Nuclear Phys.* 39:085105. doi: 10.1088/0954-3899/39/8/085105

Tomoda, T. (1991). Double beta decay. *Rep. Prog. Phys.* 54:53. doi: 10.1088/0034-4885/54/1/002

Wang, X., Hayes, A., Carlson, J., Dong, G., Mereghetti, E., Pastore, S., and Wiringa, R. B. (2019). Comparison between variational Monte Carlo and shell model calculations of neutrinoless double beta decay matrix elements in light nuclei. *Phys. Lett. B* 798:134974. doi: 10.1016/j.physletb.2019.134974

Yao, J. M., Song, L. S., Hagino, K., Ring, P., and Meng, J. (2015). Systematic study of nuclear matrix elements in neutrinoless double-β decay with a beyond-mean-field covariant density functional theory. *Phys. Rev. C* 91:024316. doi: 10.1103/PhysRevC.91.024316

Yao, W-M., Amsler, C., Asner, D., Barnett, R. M., Beringer, J., Burchat, P. R., et al. (2006). Review of particle physics. *J. Phys. G Nuclear Phys.* (2006) 33:1. doi: 10.1088/0954-3899/33/1/001

Yoshida, N., and Iachello, F. (2013). Two-neutrino double-β decay in the interacting boson-Fermion model. *Prog. Theor. Exp. Phys.* 2013:043D01. doi: 10.1093/ptep/ptt007

Conflict of Interest: The author declares that the research was conducted in the absence of any commercial or financial relationships that could be construed as a potential conflict of interest.

frontiers in Astronomy and Space Sciences

MINI REVIEW
published: 28 May 2021
doi: 10.3389/fspas.2021.666383

Ordinary Muon Capture for Double Beta Decay and Anti-Neutrino Nuclear Responses

Izyan Hazwani Hashim[1,2,3]* *and Hiroyasu Ejiri*[3]

[1]Department of Physics, Faculty of Science, Universiti Teknologi Malaysia, Johor Bahru, Malaysia, [2]National Centre for Particle Physics, Universiti Malaya, Kuala Lumpur, Malaysia, [3]Research Center for Nuclear Physics, Osaka University, Osaka, Japan

This is a brief review on ordinary muon capture (OMC) experiments at Research Center for Nuclear Physics (RCNP) Osaka University relevant for the study of double beta decays (DBDs) and astro anti-neutrinos (neutrino) nuclear responses. OMC usually leaves the nucleus in highly excited unbound state. OMC is a charge exchange reaction via the charged weak boson as given by (μ,ν_μ) reactions with μ and ν_μ being the muon and muon neutrino. Subjects discussed include 1) unique features of OMC for studying DBDs and astro anti-neutrino (neutrino) nuclear responses, 2) experiments of OMCs on ^{100}Mo and ^{nat}Mo to study neutrino nuclear responses for DBDs and astro anti-neutrinos, 3) impact of the OMC results on neutrino nuclear responses for DBDs and astro anti-neutrinos. Remarks and perspectives on OMC experiments for neutrino nuclear responses are briefly described.

Keywords: ordinary muon capture, muon charge exchange reaction, neutrino nuclear response, double beta decay, supernova neutrino, nuclear matrix element, neutrino mass

OPEN ACCESS

Edited by:
Theocharis S. Kosmas, University of Ioannina, Greece

Reviewed by:
Dieter Frekers, University Muenster, Germany
Frank Franz Deppisch, University College London, United Kingdom

***Correspondence:**
Izyan Hazwani Hashim
izyan@utm.my

Specialty section:
This article was submitted to High-Energy and Astroparticle Physics, a section of the journal Frontiers in Astronomy and Space Sciences

Received: *10 February 2021*
Accepted: *05 May 2021*
Published: *28 May 2021*

Citation:
Hashim IH and Ejiri H (2021) Ordinary Muon Capture for Double Beta Decay and Anti-Neutrino Nuclear Responses. Front. Astron. Space Sci. 8:666383. doi: 10.3389/fspas.2021.666383

1 INTRODUCTION

Double beta decays (DBDs) and astro (solar and supernova) neutrinos and anti-neutrinos are of current interest. Neutrino-less DBDs are used to explore the fundamental neutrino properties such as the Majorana nature, the absolute mass scale, the mass hierarchy and the CP phases beyond the standard electroweak model. The zero-neutrino (0ν) DBD rate is given by $R^{0\nu} = G^{0\nu} \times \left|M^{0\nu}\right|^2 \times \left|m^{eff}\right|^2$, where $G^{0\nu}$ is the phase space volume, m^{eff} is the effective neutrino mass and $M^{0\nu}$ is the zero-neutrino DBD nuclear matrix element, whose squared value is the nuclear response, i.e: $B^{0\nu} = \left|M^{0\nu}\right|^2$. Here we consider the ground state (0^+) to ground state (0^+) transition ${}^A_Z\mathrm{X} \rightarrow {}^A_{Z+2}\mathrm{X}$. The DBD nuclear matrix element (NME) $M^{0\nu}$ is given by the coherent sum of the individual matrix elements $M_i^{0\nu}$ which connect the initial and final ground states *via* the *i*th intermediate nucleus ${}^A_{Z+1}\mathrm{X}_i$, where these extend up to about 100 MeV.

The supernova nucleo-synthesis rates induced by neutrinos and anti-neutrinos are proportional to the respective nuclear responses

$$B^{\nu,\overline{\nu}} = \frac{1}{2J_A + 1}\left|M^{\nu,\overline{\nu}}\right|^2 \tag{1}$$

where $M^{\nu,\overline{\nu}}$ are the NMEs, and $(2J_A + 1)$ is the spin factor for the initial nucleus. Note that the NMEs $M^{\nu,\overline{\nu}}$ are the coherent sums of individual NMEs $M_i^{\nu,\overline{\nu}}$

$$M^{\nu,\overline{\nu}} = \sum_i M_i^{\nu,\overline{\nu}} \tag{2}$$

for each intermediate state (i) and in the respective isospin directions τ^- for ν or τ^+ for $\overline{\nu}$. Note that the ν and $\overline{\nu}$ NMEs for the ith intermediate state are given by the τ^- and τ^+ NMEs of M_i^- and M_i^+, respectively. Accordingly one needs the $B^{0\nu}$ response to derive the effective neutrino mass m^{eff} from the neutrino-less DBD rate and the astro neutrino (anti-neutrino) response B^V ($B^{\overline{\nu}}$) to derive the synthesis rate from the neutrino (anti-neutrino) flux. The neutrino nuclear responses are evaluated theoretically. However, the theoretical calculations for the neutrino nuclear responses for DBD and astro neutrino (anti-neutrino) depend much on the nuclear models and the nuclear parameters used. The neutrino nuclear responses and DBDs are extensively discussed in review articles and references therein (Ejiri, 2000; Vergados et al., 2012).

Experimental studies for the neutrino nuclear responses are interesting to provide the nuclear parameters to be used for theoretical calculations. Charge exchange reactions (CERs) using light ions have been used to study the neutrino nuclear responses. In particular, high energy-resolution (^{3}He, t) CERs have been used to study the neutrino nuclear responses for nuclei of DBD and astro neutrino interests in the broad energy and momentum regions. The responses studied by these light-ion CERs are the τ^--side ones, and the NMEs M_i^- are derived from CERs. On the other hand, the τ^+-side responses and the NMEs M_i^+ are not well studied since the (t,^{3}He) CERs to be used for studying the τ^+-side responses require the radioactive t beam, and thus high precision measurements are difficult. Medium energy-resolution measurements are made by using (d,^{2}He) reactions. Neutrino nuclear responses studied by these light-ion CERs are discussed in the recent review articles and references therein (Ejiri, 2000; Vergados et al., 2012; Frekers and Alanssari, 2018; Ejiri et al., 2019; Ejiri, 2020).

Recently ordinary muon capture reactions (OMC), where a negative muon in an atomic orbit is captured into the nucleus has been shown useful for studying the τ^+-side responses, and the M_i^+ NMEs at Research Center for Nuclear Physics (RCNP) Osaka University (Hashim, 2015; Hashim et al., 2018; Hashim and Ejiri, 2019). The present report is a brief mini-review on the OMC studies for the DBD and astro anti-neutrinos responses and related subjects on nuclear isotope productions at RCNP.

2 UNIQUE FEATURES OF OMCS FOR NEUTRINO NUCLEAR RESPONSES

In OMC some of the unique feature are as follows:

(1) OMC can be used to study the τ^+-responses of proton (p) $\rightarrow$ neutron(n) in the nucleus, and the NME M_i^+ for DBD and astro anti-neutrino.
(2) OMC transfers energy between 0–50 MeV and a momentum up to 100 MeV/c to the nucleus that are similar to those involved in neutrino-less DBD and supernova anti-neutrino.
(3) A negative muon is finally captured into the nucleus *via* the weak interaction. The capture probability in the medium and heavy nuclei is around 95% after a mean lifetime of about 100 ns in the atomic orbit. Low momentum (a few 10 MeV/c) beam muons at intensities of 10^3–10^4 muons/s are used for OMC studies.
(4) The OMC on ^A_ZX, where A and Z are the mass and the atomic numbers, excites the nucleus $^A_{Z-1}$X up to around 50 MeV, which decays by emitting a number (x) of mostly neutrons and gamma rays to the ground state of the residual nucleus $^{A-x}_{Z-1}$X. The number of neutrons reflects the excitation energy. Accordingly, the relative strength as a function of the excitation energy is evaluated by measuring the number (x) of the neutrons, i.e. the mass distribution $A-x$ of the residual nuclei.
(5) Absolute OMC rate is obtained from the measured lifetime of the trapped muons, and thus the neutrino nuclear responses are derived from the OMC rate.

3 NEUTRINO NUCLEAR RESPONSES FOR MO ISOTOPES BY OMC

The intense 400 MeV proton beam with an intensity around 1 μA from the RCNP cyclotron is used to produce pions. The momentum ($p \approx$ 30–50 MeV/c) negative muons produced by the π-decays are guided by the MuSIC beamline to the target port. They are stopped in the target and are trapped in the inner orbit of the atom. Then, after around 100 ns, the muon is mainly (around 95%) captured into the nucleus via the OMC. The μ-beam spot and the muon beam intensity at the target port are around 6 cm × 6 cm and 5×10^3 per second (Hino et al., 2014). The μ capture rate is derived by measuring the electrons' time signal from the weak decay of the μ trapped in the atomic orbit by plastic scintillation detectors. The residual isotopes are identified by measuring characteristic prompt γ-rays of the residual nucleus by HPGe detectors online and delayed γ-rays from β-decays of residual isotopes by HPGe detectors offline.

Recently OMCs were studied on ^{nat}Mo and ^{100}Mo, which are interesting for DBD and astro neutrino studies (Ejiri et al., 2019). The OMC on $^A_{42}$Mo isotopes with the mass-number A = 92–100 produces $^A_{41}$Nb with the excitation energy $E \approx$ 0–50 MeV. The excited Nb isotope decays mostly by emitting a number 10(x) of neutrons until the final state gets particle-bound. Then it decays by emitting prompt γ rays to the ground state of $^{A-x}$Nb, which is followed by beta decay with comparatively long half-lives.

The OMC strength distribution as a function of the excitation energy E is derived from the mass-number ($A-x$) distribution (x distribution) through the particle cascade model (Hashim et al., 2018; Hashim & Ejiri, 2019; Hashim et al., 2020). The excited states in Nb isotopes decay by emitting mostly neutrons since the Coulomb barrier much suppresses proton emission. Thus, the neutron cascade emission model (NEM) (Hashim et al., 2017; Hashim et al., 2018) was developed to deduce the excitation energy in the initial isotope of ^{A}Nb from the number 10(x) of the emitted neutrons, i.e., the mass-number $A-x$ of the residual isotope $^{A-x}$Nb after the x neutron emission. The neutron energy spectrum for the first neutron consists of the pre-equilibrium (PEQ) and equilibrium (EQ) stages (Ejiri and de Voight, 1989). It is given as

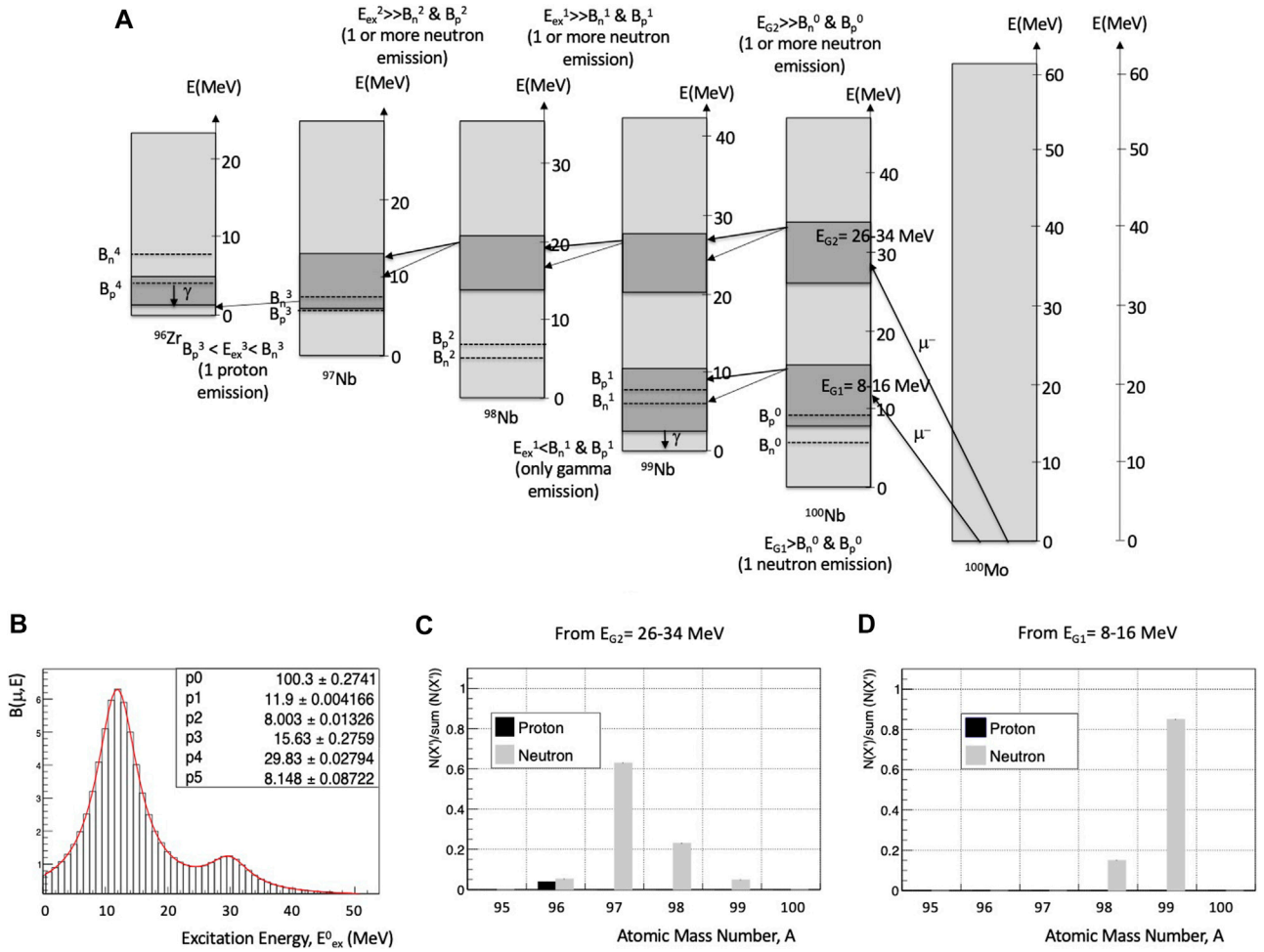

FIGURE 1 | Proton neutron emission model (PNEM) (Hashim et al., 2020). **(A)** When OMC on ^{100}Mo occurs, ^{100}Nb is excited to some energy up to around 50 MeV, with $B_n(B_p)$ = 5.68 MeV (9.46 MeV), 6.87 MeV (8.34 MeV), 5.99 MeV (7.87 MeV) and 8.07 MeV (7.46 MeV) for Nb^A with A = 100, 99, 98, and 97, respectively. **(B)** The excitation energy region of 8–16 MeV, which is strongly excited, decays by emitting mainly 1 neutron, and partly by 2 neutrons, depending on the neutron energy. **(C)** The excitation region of 26–34 MeV day by emitting 3–4 neutrons and also partly by emitting 3 neutrons and 1 proton. **(D)** The muon strength distribution, $B(\mu,E)$ for OMC on ^{100}Mo from the excitation energy distribution in the daughter nucleus of Nb and Zr isotopes following the muon capture process. To reproduce the ^{100}Mo experimental RI mass distribution, the E_{G1} and E_{G2} are observed at 12 MeV, and 30 MeV with an intensity ratio of E_{G1}/E_{G2} = 1/6 (Hashim et al., 2018).

$$S(E_{n1}) = k\left[E_{n1}exp\left(-\frac{E_{n1}}{T_{EQ}(E)}\right) + pE_{n1}exp\left(-\frac{E_{n1}}{T_{PEQ}(E)}\right)\right] \quad (3)$$

where $T_{\mathrm{EQ}}(E)$ and $T_{\mathrm{PEQ}}(E)$ are the EQ and PEQ nuclear temperatures, respectively. $T_{\mathrm{EQ}}(E)$ is given as a function of excitation energy E (Ejiri and de Voight, 1989). The ratio of $T_{\mathrm{PEQ}}(E)/T_{\mathrm{EQ}}(E) = 3$ for the medium excitation $10 < E < 40$ MeV. After one neutron emission, the emission takes place only via the EQ stage. The OMC strength distribution for ^{100}Nb is derived from the observed mass-number $(A–x)$ distribution for the OMC on ^{100}Mo.

The NEM analysis on the observed mass-number distribution of $^{100-x}$Nb shows preferential excitation (muon giant resonance, μ-GR) at 10–14 MeV region and a broad bump at the higher excitation region of 25–40 MeV. The NEM analyses on other medium-heavy nuclei by (Ibrahim, 2018) using experimental data from (Measday et al., 2007b; Measday et al., 2007a) show similar features of the preferential excitation of the 10–15 MeV. This preferential excitation reflects the large branch of the one neutron (x = 1) emission. The NME analyses on the mass-number distributions for OMCs on light nuclei show a preferential excitation around 4–8 MeV region by (Muslim, 2018) using experimental data from (Evans, 1973; Measday et al., 2007c). This observation is consistent with the calculation in (Kortelainen and Suhonen, 2004).

The strength distribution is fitted by the sum of the μ-GR strengths of $B_1(\mu,E_1)$ and $B_2(\mu,E_2)$ given by

$$B(\mu,E) = \sum_{i=1,2} B_i(\mu,E_i), B_i(\mu,E_i) = \frac{B_i(\mu)}{(E - E_{\mathrm{Gi}})^2 + (\Gamma_i/2)^2} \quad (4)$$

where E_{Gi} and Γ_i with i = 1,2 are the resonance energy and the width for the ith GR, and the constant $B_i(\mu)$ is given by $\sigma_i\Gamma_i/(2\pi)$ with σ_i being the total strength integrated over the excitation

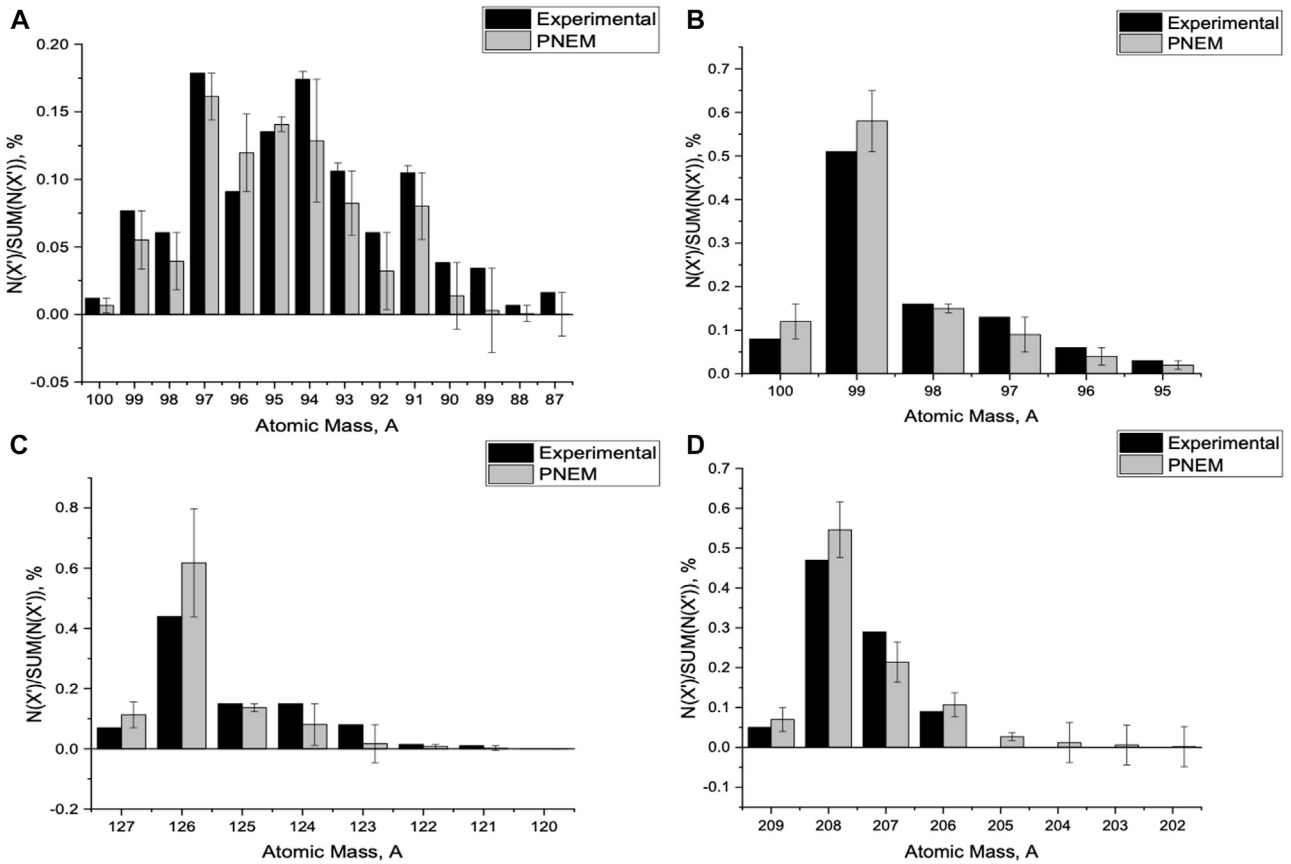

FIGURE 2 | Radioactive isotope (RIs) mass-number distribution from the ratio of number of isotopes N (X′) where X being the atomic mass number of the daughter nucleus in experimental observations over the total isotopes $\Sigma N(X')$ observed for the experiment, and calculations for neutron and proton emission events after muon capture reactions (Hashim et al., 2020). The black bar represents the experimental observation while the gray bar represents calculated value by Proton neutron emission model (PNEM). Errors obtain for the experiment and calculation are included based on statistical and systematical study for each parameters assumption. The value of model error are are assumed to be small since the assumption made are suitable for particle evaporation from medium-heavy nuclei **(A)** ^{nat}Mo (isotopic enrichment of 9.7% of ^{100}Mo, 24.3% of ^{98}Mo, 9.6% of ^{97}Mo, 16.7% of ^{96}Mo, 15.9% of ^{96}Mo), 9.2% of ^{95}Mo and 14.6% of ^{94}Mo) (Ejiri et al., 2013), **(B)** ^{100}Mo (isotopic enrichment of 96% of ^{100}Mo, 2.5% of ^{98}Mo, 0.5% of ^{97}Mo and 1% of ^{96}Mo) (Hashim et al., 2018), **(C)** ^{127}I (isotopic enrichment of 100% of ^{127}I) (Measday et al., 2007) and **(D)** ^{209}Bi (isotopic enrichment of 100% of ^{219}Bi) (Measday et al., 2007).

energy. The obtained GR energies are 12 MeV for the first GR and 32.5 MeV for the second GR, and the widths for both GRs are 8 MeV, as shown in **Figure 1B**. Here we note the GR2 is not entirely clear beyond the statistical error and maybe a broad bump. The μ-GR energy peaks at around 12 MeV, which is lower than the giant dipole resonance (GDR) energy of 14 MeV deduced from a photon-induced reaction (Ejiri et al., 2011). It also features a broader width of about 8 MeV compared to the 5 MeV width of the latter. This is, of course due to the additional multipole components of higher spin states excited by τ^+, i. e.,: (n, p)-type, muon capture.

Recently a proton-neutron emission model (PNEM) has been developed by considering the probability of proton emission as well (Hashim et al., 2020). The proton energy spectrum is given by $S(E_p) = m \times exp(-n \times Ep)$, where m and n are the density parameter constant with the value of 0.832 MeV and 0.163 MeV^{-1}. Here, the proton is assumed to be emitted in the case of $B_p \leq E \leq B_n$ with B_P, E and B_n being the proton binding energy, the excitation energy and the neutron binding energy, because the neutron decays are forbidden and gamma decays are much smaller than the proton emission even below the Coulomb barrier. The PNEM is shown schematically in **Figure 1A**. The analysis of the mass-number distribution of $^{100-x}$Nb shows the same GR1 and GR2 as in case of the NEM analysis. The missing Zr isotopes produced by a proton emission in experimental data are predicted by PNEM for both ^{nat}Mo (Ejiri et al., 2013) and ^{100}Mo (Hashim et al., 2018). The OMC strength distribution shown in **Figure 1A** reproduces the observed radioactive isotope (RI) mass distribution.

Since then, various calculations have been made for understanding the formation of the GR populated by muon capture reactions in 98, $< A <$ 209 (Hashim et al., 2020). These calculations have been compared with previous experimental works by OMC on the nuclei reported in references (Measday, 2001; Measday et al., 2007b; Measday et al., 2007a). The parameters of E_{G1} and E_{G2} as a function of A are given as $E_{G1} = 30A^{-1/5}$ and $E_{G2} = 75A^{-1/5}$ for OMC on ^{nat}Mo, ^{100}Mo, ^{107}Pd, ^{108}Pd, ^{127}I and ^{209}Bi. They

are obtained from a comparison of PNEM calculations with experimental data. The observed mass distributions agree with the predictions as shown in **Figure 2**.

4 IMPLICATIONS FOR DOUBLE BETA DECAYS

The experimental OMC rate for ^{100}Mo as a function of the excitation energy is compared with the theoretical calculation by using proton-neutron quasi-particle random-phase approximation (pn-QRPA) (Jokiniemi et al., 2019). The pn-QRPA well reproduces the GR at around 10–14 MeV with mainly low multipoles of $J^{\pi} = 0^{\pm}$,$1^{\pm}$ and $2^{\pm}$. The observed OMC rate is the same order of magnitude as the empirical value suggested by Primakoff (Suzuki et al., 1987) but is lower by a factor 5 than the pn-QRPA (Jokiniemi et al., 2019; Jokiniemi and Suhonen, 2019). This suggests a quenching coefficient for the axial-vector weak coupling of $g_A^{eff}/g_A \approx 0.5$ (Jokiniemi et al., 2019; Jokiniemi and Suhonen, 2019) for μ-NMEs, being consistent with the quenching factors for Gamow-Teller (GT) and spin dipole (SD) NMEs (Ejiri and Suhonen, 2015; Ejiri et al., 2019). Here the quenching is common in the wide momentum region (Ejiri, 2019a; Ejiri, 2019b). The quenching effects are also discussed theoretically (Menéndez et al., 2011; Suhonen, 2017; Ejiri et al., 2019).

It is interesting to note that the OMC results together with the (^{3}He,t) CERs and $\beta^{\pm}$ data suggest severe quenching of experimental axial-vector NMEs of M_i^- and M_i^+ for multipoles of $J^{\pi} = 1^+, 2^-, 3^+$ (Jokiniemi et al., 2019; Jokiniemi and Suhonen, 2019). The common quenching coefficients of $k_{NM} = g_A^{\text{eff}}/g_A$ for them are around 0.4–0.6 with respect to the pn-QRPA. In this case, the axial-vector DBD NMEs are quenched by the coefficient k_{NM}^2 and the axial-vector anti-neutrino NMEs by k_{NM}. On the other hand, the recent pn-QRPA calculations for OMC rates show no quenching (Šimkovic et al., 2020) or only weak quenching (Ciccarelli et al., 2020). The different quenching coefficients are partly due to the different model space and the different muon-wave functions used in their QRPA calculations (Jokiniemi et al., 2019; Jokiniemi and Suhonen, 2019; Ciccarelli et al., 2020; Šimkovic et al., 2020). Further studies are needed to see how pn-QRPA calculations reproduce both the relative and absolute OMC rates.

5 REMARKS AND PERSPECTIVES

The relative strength distribution of OMC on Mo isotopes show the μ-GR around $E \approx 12$ MeV consistent with the pn-QRPA calculation (Jokiniemi et al., 2019). However, the absolute strength derived from the lifetime is much smaller than the model value, suggesting a similar quenching of the M_i^+ NMEs as the M_i^- NMEs derived from light-ion CERs. Another pn-QRPA (Šimkovic et al., 2020) shows no severe quenching. The quenching for μ NMEs remains to be studied.

The extensive experimental programs on OMC for other nuclei of DBD and supernova anti-neutrino interests are under progress at RCNP and Paul Scherrer Institute (PSI), Switzerland, by the join group of Joint Institute for Nuclear Research (JINR), Dubna, RCNP, Osaka and Universiti Teknologi Malaysia (UTM) (Hashim and Ejiri, 2019). The pn-QRPA theoretical calculation is also in progress at Jyvaskyla (Jokiniemi et al., 2019).

Finally, it is remarked that muon capture isotope production (MuCIP) is used for producing efficiently nuclear isotopes with the atomic number $Z-1$, less by one than the atomic number Z of the target isotope. By using ${}^{A}_{Z}\text{X}$ target isotopes, isotopes of ${}^{A-1}_{Z-1}\text{X}$ are preferentially produced, and several isotopes with A,$A-2$,$A-3$,$A-4$ are also produced (Ejiri et al., 2013; Zinatulina et al., 2019). There is potential for using them for basic and applied science. One RI used for medical checks is the ^{99}Mo, which is well produced by OMC on ^{100}Mo, as studied at RCNP (Ejiri et al., 2013). MuCIP is complementary to photon capture reactions where isotopes of ${}^{A}_{Z}{}^{-1}\text{X}$ are well produced (Ejiri et al., 2011; Szpunar et al., 2013). Note that ppb-level nuclei (impurities) are identified by measuring gamma rays from OMC, which are characteristic of the nuclei, as explained in (Ejiri et al., 2013).

AUTHOR CONTRIBUTIONS

IH and HE are equally accounted for the content of the work.

FUNDING

This work was financially supported by the Universiti Teknologi Malaysia research grants (Q.J130000.3026.01M14 and R.J130000.7854.5F227) and the Ministry of Higher Education Malaysia Fundamental Research Grant Scheme (FRGS/1/2019/STG02/UTM/02/6).

ACKNOWLEDGMENTS

We are grateful to RCNP, UTM, and JINR colleagues for the collaboration and valuable discussions.

REFERENCES

Ciccarelli, M., Minato, F., and Naito, T. (2020). Theoretical Study of Nb Isotope Productions by Muon Capture Reaction on Mo100. *Phys. Rev. C* 102, 034306. doi:10.1103/PhysRevC.102.034306

Ejiri, H., and de Voight, M. J. A. (1989). *Gamma Ray and Electron Spectroscopy in Nuclear Physics*, Oxford: Oxford University Press.

Ejiri, H., and Suhonen, J. (2015). "GT Neutrino-Nuclear Responses for Double Beta Decays and Astro Neutrinos. *J. Phys. G: Nucl. Part. Phys.*, 42, 055201. doi:10.1088/0954-3899/42/5/055201

Ejiri, H., Shima, T., Miyamoto, S., Horikawa, K., Kitagawa, Y., Asano, Y., et al. (2011). Resonant Photonuclear Reactions for Isotope Transmutation. *J. Phys. Soc. Jpn.* 80, 094202. doi:10.1143/JPSJ.80.094202

Ejiri, H., H. Hashim, I., Hino, Y., Kuno, Y., Matsumoto, Y., Ninomiya, K., et al. (2013). Nuclear γ Rays from Stopped Muon Capture Reactions for Nuclear Isotope Detection. *J. Phys. Soc. Jpn.* 82, 044202. doi:10.7566/JPSJ.82.044202

Ejiri, H., Suhonen, J., and Zuber, K. (2019). Neutrino-nuclear Responses for Astro-Neutrinos, Single Beta Decays and Double Beta Decays. *Phys. Rep.* 797, 1–102. doi:10.1016/j.physrep.2018.12.001

Ejiri, H. (2000). Nuclear Spin Isospin Responses for Low-Energy Neutrinos. *Phys. Rep.* 338, 265–351. doi:10.1016/S0370-1573(00)00044-2

Ejiri, H. (2019a). Axial-vector Weak Coupling at Medium Momentum for Astro Neutrinos and Double Beta Decays. *J. Phys. G: Nucl. Part. Phys.* 46, 125202. doi:10.1088/1361-6471/ab4dcb

Ejiri, H. (2019b). Nuclear Matrix Elements for β and ββ Decays and Quenching of the Weak Coupling g_A in QRPA. *Front. Phys.* 7, 30. doi:10.3389/fphy.2019.00030

Ejiri, H. (2020). Neutrino-mass Sensitivity and Nuclear Matrix Element for Neutrinoless Double Beta Decay. *Universe* 6, 225. doi:10.3390/universe6120225

Evans, H. J. (1973). Gamma-rays Following Muon Capture. *Nucl. Phys. A* 207, 379–400. doi:10.1016/0375-9474(73)90354-0

Frekers, D., and Alanssari, M. (2018). Charge-exchange Reactions and the Quest for Resolution. *Eur. Phys. J. A.* 54, 177. doi:10.1140/epja/i2018-12612-5

Hashim, I. H., and Ejiri, H. (2019). New Research Project with Muon Beams for Neutrino Nuclear Responses and Nuclear Isotopes Production. *AAPPS Bull.* 29, 21–26. doi:10.22661/AAPPSBL.2019.29.3.21

Hashim, I. H., Ejiri, H., Othman, F., Saroni, S. S., Amelia, W. N., Hamzah, S. A., et al. (2017). Statistical Neutron Emission Model for Neutrino Nuclear Response. *EPJ Web Conf.* 156, 00005. doi:10.1051/epjconf/201715600005

Hashim, I. H., Ejiri, H., Shima, T., Takahisa, K., Sato, A., Kuno, Y., et al. (2018). Muon Capture Reaction on Mo100 to Study the Nuclear Response for Double-β Decay and Neutrinos of Astrophysics Origin. *Phys. Rev. C* 97, 014617. doi:10.1103/PhysRevC.97.014617

Hashim, I. H., Ejiri, H., Othman, F., Ibrahim, F., Soberi, F., Ghani, N., et al. (2020). Nuclear Isotope Production by Ordinary Muon Capture Reaction. *Nucl. Instr. Methods Phys. Res. Section A: Acc. Spectrometers, Detectors Associated Equipment* 963, 163749. doi:10.1016/j.nima.2020.163749

Hashim, I. H. (2015). *A Study of Weak Nuclear Response by Nuclear Muon capture*. PhD Thesis. Osaka: Osaka University.

Hino, Y., Kuno, Y., Sato, A., Sakamoto, H., Matsumoto, Y., Tran, N. H., et al. (2014). "A Highly Intense Dc Muon Source, Music and Muon Clfv Search. *Nucl. Phys. B - Proc. Supplements* 253–255, 206–207. doi:10.1016/j.nuclphysbps.2014.09.051

Ibrahim, F. (2018). Excitation Energies of Compound Nucleus Following Ordinary Muon Capture on Medium Heavy Nuclei within Neutron Statistical Model. Thesis. Johor: Universiti Teknologi Malaysia

Jokiniemi, L., and Suhonen, J. (2019). Muon-capture Strength Functions in Intermediate Nuclei of 0νββ Decays. *Phys. Rev. C* 100, 014619. doi:10.1103/PhysRevC.100.014619

Jokiniemi, L., Suhonen, J., Ejiri, H., and Hashim, I. H. (2019). Pinning Down the Strength Function for Ordinary Muon Capture on 100Mo. *Phys. Lett. B* 794, 143–147. doi:10.1016/j.physletb.2019.05.037

Kortelainen, M., and Suhonen, J. (2004). Nuclear Muon Capture as a Powerful Probe of Double-Beta Decays in Light Nuclei. *J. Phys. G: Nucl. Part. Phys.* 30, 2003–2018. doi:10.1088/0954-3899/30/12/017

Measday, D. F., Stocki, T. J., Alarcon, R., Cole, P. L., Djalali, C., and Umeres, F. (2007a). Comparison of Muon Capture in Light and in Heavy Nuclei. *AIP Conf. Proc.* 947, 253–257. doi:10.1063/1.2813812

Measday, D. F., Stocki, T. J., and Tam, H. (2007b). Γrays from Muon Capture in I, Au, and Bi. *Phys. Rev. C* 75, 045501. doi:10.1103/PhysRevC.75.045501

Measday, D. F., Stocki, T. J., Moftah, B. A., and Tam, H. (2007c). γ Rays from Muon Capture inAl27and Natural Si. *Phys. Rev. C* 76, 035504. doi:10.1103/PhysRevC.76.035504

Measday, D. F. (2001). The Nuclear Physics of Muon Capture. *Phys. Rep.* 354, 243–409. doi:10.1016/S0370-1573(01)00012-6

Menéndez, J., Gazit, D., and Schwenk, A. (2011). Chiral Two-Body Currents in Nuclei: Gamow-Teller Transitions and Neutrinoless Double-Beta Decay. *Phys. Rev. Lett.* 107, 062501. doi:10.1103/PhysRevLett.107.062501

Muslim, N. F. H. (2018). *Neutron Statistical Model for Muon Capture on Light Nuclei*. Thesis. Johor: Universiti Teknologi Malaysia.

Šimkovic, F., Dvornický, R., and Vogel, P. (2020). Muon Capture Rates: Evaluation within the Quasiparticle Random Phase Approximation. *Phys. Rev. C* 102, 034301. doi:10.1103/PhysRevC.102.034301

Suhonen, J. (2017). Impact of the Quenching of gA on the Sensitivity of 0νββ Experiments. *Phys. Rev. C* 96, 055501. doi:10.1103/PhysRevC.96.055501

Suzuki, T., Measday, D. F., and Roalsvig, J. P. (1987). Total Nuclear Capture Rates for Negative Muons. *Phys. Rev. C* 35, 2212–2224. doi:10.1103/PhysRevC.35.2212

Szpunar, B., Rangacharyulu, C., Daté, S., and Ejiri, H. (2013). Estimate of Production of Medical Isotopes by Photo-Neutron Reaction at the Canadian Light Source. *Nucl. Instr. Methods Phys. Res. Section A: Acc. Spectrometers, Detectors Associated Equipment* 729, 41–50. doi:10.1016/j.nima.2013.06.106

Vergados, J. D., Ejiri, H., and Šimkovic, F. (2012). Theory of Neutrinoless Double-Beta Decay. *Rep. Prog. Phys.* 75, 106301. doi:10.1088/0034-4885/75/10/106301

Zinatulina, D., Brudanin, V., Egorov, V., Petitjean, C., Shirchenko, M., Suhonen, J., et al. (2019). Ordinary Muon Capture Studies for the Matrix Elements in ββ Decay. *Phys. Rev. C* 99, 024327. doi:10.1103/PhysRevC.99.024327

Conflict of Interest: The authors declare that the research was conducted in the absence of any commercial or financial relationships that could be construed as a potential conflict of interest.

frontiers in Astronomy and Space Sciences

ORIGINAL RESEARCH
published: 14 July 2021
doi: 10.3389/fspas.2021.667058

Quenching of Isovector and Isoscalar Spin-M1 Excitation Strengths in $N = Z$ Nuclei

Hiroaki Matsubara[1,2]* *and Atsushi Tamii*[1]

[1]Research Center for Nuclear Physics (RCNP), Osaka University, Ibaraki, Japan, [2]Department of Radiology, Kyoto Prefectural University of Medicine, Kyoto, Japan

Spin-$M1$ excitations of nuclei are important for describing neutrino reactions in supernovae or in neutrino detectors since they are allowed transitions mediated by neutral current neutrino interactions. The spin-$M1$ excitation strength distributions in self-conjugate $N = Z$ nuclei were studied by proton inelastic scattering at forward angles for each of isovector and isoscalar excitations as reported in H. Matsubara et al., Phys. Rev. Lett. **115**, 102501 (2015). The experiment was carried out at the Research Center for Nuclear Physics, Osaka University, employing a proton beam at 295 MeV and the high-resolution spectrometer Grand Raiden. The measured cross-section of each excited state was converted to the squared nuclear matrix elements of spin-$M1$ transitions by applying a unit cross-section method. Comparison with predictions by a shell-model has revealed that isoscalar spin-$M1$ strengths are not quenched from the prediction although isovector spin-$M1$ strengths are quenched similarly with Gamow-Teller strengths in charged-current reactions. This finding hints at an important origin of the quenching of the strength relevant to neutrino scattering, that is, the proton-neutron spin-spin correlation in the ground state of the target nucleus. In this manuscript we present the details of the unit cross-section method used in the data analysis and discuss the consistency between the quenching of the isoscalar magnetic moments and that of the isoscalar spin-M1 strengths.

Keywords: Sd-shell nuclei, shell-model calculation, proton inelastic scattering, spin-M1 transition, GT-transition

OPEN ACCESS

Edited by:
Francesco Cappuzzello, University of Catania, Italy

Reviewed by:
Marco Martini, Institut Polytechnique des Sciences Avancées, France
Zhenbin Wu, University of Illinois at Chicago, United States

***Correspondence:**
Hiroaki Matsubara
mats.hiroaki@gmail.com

Specialty section:
This article was submitted to High-Energy and Astroparticle Physics, a section of the journal Frontiers in Astronomy and Space Sciences

Received: *11 February 2021*
Accepted: *14 June 2021*
Published: *14 July 2021*

Citation:
Matsubara H and Tamii A (2021) Quenching of Isovector and Isoscalar Spin-M1 Excitation Strengths in N = Z Nuclei. Front. Astron. Space Sci. 8:667058. doi: 10.3389/fspas.2021.667058

1 INTRODUCTION

Response of nuclei to incoming neutrinos is categorized into two types of reactions: charged-current (CC) and neutral-current (NC). Gamow-Teller (GT) transition of nuclei belongs to the CC neutrino reaction, while the isovector (IV) spin magnetic-dipole ($M1$) transition to NC. The GT ($\Delta J^{\pi} = 1^{+}$, $\Delta T = 1$ and $\Delta T_z = \pm 1$) transitions are analogous to the IV spin-$M1$ ($\Delta J^{\pi} = 1^{+}$, $\Delta T = 1$ and $\Delta T_z = 0$) transitions under isospin symmetry. Relevant transition rates are predicted by theoretical models such as the shell-model. The experimentally observed transition rates are, however, quenched compared to the model predictions by employing bare transition operators. Quenching is a basic property of nuclear structure and influences the neutrino reaction rates in astrophysical processes and terrestrial neutrino detectors. The nuclear spin responses and their quenching have strong effects on the mean free path of neutrinos in dense nuclear matter, the size of the neutrino sphere formed in the center of a core-collapsing star, and the cooling process of proton-neutron stars.

The quenching has been extensively studied for the GT transitions. The GT transition strength contained in the GT giant resonances studied by (p, n) reactions was found to be ~60% of the prediction by the Ikeda-Fujii-Fujita sum-rule (Ikeda et al., 1963) consistently for a large variety of nuclei. Two mechanisms were presented to explain GT quenching in the context of the mixing of higher-order configurations with the fundamental one-particle-one-hole nature of the GT excitation. One is the Δ-hole mixing originating from the quark degree of freedom. The other is the two-particle-two-hole as well as the higher-order particle-hole excitations within the nucleonic degree of freedom. Detailed study of the GT strength distribution embedded in the continuum located above the GT giant resonance revealed that the major part of quenching is caused by mixing in the nucleonic degree of freedom (Ichimura et al., 2006). The observed GT transition strengths studied by beta-decay are also quenched from shell-model predictions using the bare g-factor. Recent ab initio calculations using the chiral effective field theory (Gysbers et al., 2019) indicated that quenching was resolved by introducing two-body currents and nuclear many-body correlations. Quenching in the analogous spin-$M1$ transitions was studied by proton inelastic scattering (Anantaraman et al., 1984; Crawley et al., 1989). The result was unclear due to the poor quality of the experimental data and to the ambiguity of the transition matrix element relying on the reaction calculation. This problem has been overcome by the achievement of a high-precision measurement (Matsubara et al., 2015) using high-resolution proton scattering at forward scattering angles including zero degrees that reported the quenching of the nuclear matrix elements for the IV spin-$M1$ transitions, similar to the analogous GT transitions, but no-quenching for the isoscalar (IS) spin-$M1$. Exhaustion of the sum-rule of the spin-$M1$ strengths is relevant to the spin susceptibility of asymmetric nuclear matter, its response to the strong magnetic field in magnetars, and possible phase-transition of nuclear medium in a neutron star to the ferromagnetic state.

The experimental work gave new insight, by the use of the non-energy-weighted sum-rule, that the underlying quenching mechanism is embedded in the ground state property as spin-spin correlation of neutron(n)-proton(p) pairs. The expectation value of the correlation in the ground state is equivalent to the difference of the quenching of nuclear matrix elements between the IS and IV spin-$M1$ transitions. Thus, the quenching of the IS and IV spin-$M1$ transitions needs to be described simultaneously and mutually-consistently. The details are described in **Section 5.4**.

The n-p correlation in the nuclear ground state is one of the recent topics in nuclear physics. The short range correlation as well as the tensor correlation are considered to be the origin of the neutron-proton correlation and are relevant to the IS spin-triplet n-p pairing. The high-momentum nature of the correlation has been studied by the knockout reaction by electron scattering (Subedi et al., 2008; Hen et al., 2014; Hen et al., 2017) or by high-momentum transfer reaction by using (p, d) scattering (Ong et al., 2013; Terashima et al., 2018). In both cases, dominant contribution of the n-p pairs is reported rather than the identical pairs, n-n or p-p, to the high-momentum component in the ground state.

In a different approach, the spin-aligned IS n-p coupling of the valence particles around the Fermi surface was studied from a level structure determined by gamma spectroscopy (Cederwall et al., 2011). It is interesting to observe how those n-p paring components and the IS spin-triplet n-p pairing are related to the n-p spin-spin correlation in the ground state.

In the work of Matsubara et al. (2015), IS and IV spin-$M1$ excitation strength distributions were individually determined by a high-resolution proton inelastic scattering experiment at zero degrees and forward angles for self-conjugate even-even nuclei from ^{12}C to ^{36}Ar. The squared nuclear matrix element of each transition was extracted from the observed differential cross-section by using the unit cross-section method. The summed strength up to the excitation energy of 16 MeV was compared with the prediction by a shell-model for the discussion of quenching of the IS and IV transitions. In this article we describe in greater detail the unit cross-section method in the data analysis. Also, the observed no-quenching of the IS spin-M1 transitions is compared with the historical knowledge of the quenching of the IS magnetic moment. The difference of IS and IV quenching is discussed in terms of the n-p spin-spin correlation in the ground state.

In **Section 2**, formalism is presented for discussion of the nuclear matrix elements of the IS and IV spin-$M1$ transitions, the IS and IV magnetic moments of the nuclear ground state, sum-rules, and the n-p spin-spin correlation function. The experimental methods and the data analysis are described in **Section 3**. The nuclear matrix elements are determined from the experimental data by using the unit cross-section method as described in **Section 4**. The quenching of the IS and IV spin-$M1$ nuclear matrix elements, IS magnetic moment, and the n-p spin-spin correlation are discussed in **Section 5**. Summary and prospects are given in **Section 6**.

2 FORMALISM

2.1 Nuclear Magnetic Moment

The $M1$ operator $\widehat{O}(M1)$ for magnetic dipole moments and $M1$ transitions consists of an orbital part ($\overrightarrow{l}$) and a spin part ($\overrightarrow{s}$).

$$\widehat{O}(M1) = \left[\sum_{k=1}^{Z}\left(g_l^{\pi}\overrightarrow{l}_k + g_s^{\pi}\overrightarrow{s}_k\right) + \sum_{k=Z+1}^{A}\left(g_l^{\nu}\overrightarrow{l}_k + g_s^{\nu}\overrightarrow{s}_k\right)\right]\mu_N \quad (1)$$

$$= \left[\sum_{k=1}^{A}\left\{\left(g_l^{\mathrm{IS}}\overrightarrow{l}_k + g_s^{\mathrm{IS}}\frac{\overrightarrow{\sigma}_k}{2}\right) + \left(g_l^{\mathrm{IV}}\overrightarrow{l}_k + g_s^{\mathrm{IV}}\frac{\overrightarrow{\sigma}_k}{2}\right)\overrightarrow{\tau}_{z,k}\right\}\right]\mu_N, \quad (2)$$

where μ_N is the nuclear magneton, $\overrightarrow{\sigma}$ is the Pauli spin matrix, the operator $\overrightarrow{\tau}_{z,k}$ is the third component of the isospin operator $\overrightarrow{\tau}$ acting on the k-th nucleon and its eigen value is +1 for neutrons (ν) and −1 for protons (π). The gyromagnetic factors (g-factors) of g_l^{IS}, g_s^{IS}, g_l^{IV}, and g_s^{IV} are taken as $g_l^{\mathrm{IS}} = \frac{1}{2}(g_l^{\pi} + g_l^{\nu}) = 0.5$, $g_s^{\mathrm{IS}} = \frac{1}{2}(g_s^{\pi} + g_s^{\nu}) = 0.880$, $g_l^{\mathrm{IV}} = -\frac{1}{2}(g_l^{\pi} - g_l^{\nu}) = -0.5$, and $g_s^{\mathrm{IV}} = -\frac{1}{2}(g_s^{\pi} - g_s^{\nu}) = -4.706$, where the g-factors in the free space, $g_l^{\pi} = 1$, $g_l^{\nu} = 0$, $g_s^{\pi} = 5.586$, and $g_s^{\nu} = -3.826$, are employed. The

suffixes of IS and IV denote isoscalar and isovector, respectively. Thus, a magnetic moment is expressed as

$$\mu = \langle i|\widehat{O}(M1)|i\rangle_{M=J}, \tag{3}$$

where $|i\rangle$ denotes an initial state. Here, magnetic moments can be divided into IS and IV parts by corresponding analogous magnetic moments in mirror nuclei ($T_z = \pm T$) as

$$\mu_{\rm IS} = \frac{1}{2}(\mu_+ + \mu_-) \tag{4}$$

$$\mu_{\rm IV} = \frac{1}{2}(\mu_+ - \mu_-), \tag{5}$$

respectively, where $\mu_{+(-)}$ is a magnetic moment in the case of $T_z = +T(-T)$. Because total spin has a relation $J = l + s$, the following can be obtained

$$J = \langle i|L_z|i\rangle_{M=J} + \langle i|S_z|i\rangle_{M=J}, \tag{6}$$

where $L = \sum_k^A \vec{l}_k$ and $S = \sum_k^A \vec{s}_k$ (Brown and Wildenthal, 1983). Applying the above relation to IS magnetic moment ($\mu_{\rm IS} = \langle i|g_l^{\rm IS}L + g_s^{\rm IS}S|i\rangle_{M=J}$), one gets

$$\langle S\rangle \equiv \langle i|S_z|i\rangle_{M=J} = \frac{\mu_{\rm IS} - g_l^{\rm IS}\times J}{g_s^{\rm IS} - g_l^{\rm IS}}, \tag{7}$$

where we denote the function as $\langle S\rangle$ according to Brown and Wildenthal (1983), and it will be discussed in **Section 5.3**.

2.2 M1 Transition Strength

The reduced transition probability (transition strength) for $M1$ excitation is written as

$$\begin{aligned} B(M1) &= \frac{3}{4\pi}\left|\langle f\|\widehat{O}(M1)\|i\rangle\right|^2 \\ &= \frac{3}{4\pi}\left|g_l^{\rm IS}M_{\rm f}\left(\vec{l}\right) + \frac{g_s^{\rm IS}}{2}M_{\rm f}\left(\vec{\sigma}\right) + g_l^{\rm IV}M_{\rm f}\left(\vec{l}\,\tau_z\right)\right. \\ &\quad \left. + \frac{g_s^{\rm IV}}{2}M_{\rm f}\left(\vec{\sigma}\,\tau_z\right)\right|^2\mu_N^2, \end{aligned} \tag{8}$$

where $|f\rangle$ denotes a final state in a transition. Following the convention of Edmonds (Edmonds, 1960; Brown and Wildenthal, 1987), the reduced nuclear matrix element in spin from an initial state to a final state is defined as

$$M_{\rm f}\left(\widehat{O}\right) = \frac{1}{\sqrt{2J_i+1}}\left\langle f\left\|\sum_{k=1}^A \widehat{O}_k\right\|i\right\rangle, \tag{9}$$

where $\widehat{O}_{(k)}$ denotes $\vec{l}_{(k)}$, $\vec{\sigma}_{(k)}$, $\vec{l}_{(k)}\tau_{z(,k)}$, and $\vec{\sigma}_{(k)}\tau_{z(,k)}$. Expressing corresponding analogous $M1$ transitions in mirror nuclei ($T_z = \pm T$) as $B(M1)_\pm$, IS and IV parts of a transition strength $B(M1)$ can be written using $B(M1)_\pm$ (Fujita et al., 2000; Fujita et al., 2011) or using the reduced matrix elements as

$$\begin{aligned} B(M1)_{\rm IS} &= \frac{1}{4}\left[\sqrt{B(M1)_+} - \sqrt{B(M1)_-}\right]^2 \\ &= \frac{3}{4\pi}\left|g_l^{\rm IS}M_{\rm f}\left(\vec{l}\right) + \frac{g_s^{\rm IS}}{2}M_{\rm f}\left(\vec{\sigma}\right)\right|^2\mu_N^2 \end{aligned} \tag{10}$$

$$\begin{aligned} B(M1)_{\rm IV} &= \frac{1}{4}\left[\sqrt{B(M1)_+} + \sqrt{B(M1)_-}\right]^2 \\ &= \frac{3}{4\pi}\left|g_l^{\rm IV}M_{\rm f}\left(\vec{l}\,\tau_z\right) + \frac{g_s^{\rm IV}}{2}M_{\rm f}\left(\vec{\sigma}\,\tau_z\right)\right|^2\mu_N^2, \end{aligned} \tag{11}$$

respectively. If only spin parts are extracted as IS and IV spin-$M1$ transition strengths, they are expressed as

$$B(M1)_\sigma = \frac{3}{4\pi}\left|\frac{g_s^{\rm IS}}{2}M_{\rm f}\left(\vec{\sigma}\right)\right|^2\mu_N^2 \tag{12}$$

$$B(M1)_{\sigma\tau} = \frac{3}{4\pi}\left|\frac{g_s^{\rm IV}}{2}M_{\rm f}\left(\vec{\sigma}\,\tau_z\right)\right|^2\mu_N^2 \tag{13}$$

respectively.

Here, we focus on an IS part, $B(M1)_{\rm IS}$. Because total angular momentum operator ($\vec{j} = \vec{l} + \vec{\sigma}/2$) gives a good quantum number, taking a ground state as $|{\rm g.s.}\rangle$, $\vec{j}\,|{\rm g.s}\rangle$ is proportional to $|{\rm g.s}\rangle$ but is orthogonal to any other eigenstates. Thus, the following restriction (Bernabéu et al., 1992; Kawabata et al., 2004) can be obtained

$$\left\langle {\rm f}\left\|\sum_{k=1}^A\left(\vec{l}_k + \frac{1}{2}\vec{\sigma}_k\right)\right\|{\rm g.s.}\right\rangle = 0 \tag{14}$$

Since the above restriction leads to $M_{\rm f}(\vec{l}) = -\frac{1}{2}M_{\rm f}(\vec{\sigma})$, the right-hand side of **Eq. 10** is rewritten as

$$B(M1)_{\rm IS} = \frac{3}{4\pi}\left|\frac{g_s^{\rm IS} - g_l^{\rm IS}}{2}M_{\rm f}\left(\vec{\sigma}\right)\right|^2\mu_N^2 = \left(\frac{g_s^{\rm IS} - g_l^{\rm IS}}{g_s^{\rm IS}}\right)^2 B(M1)_\sigma \tag{15}$$

2.3 Squared Nuclear Matrix Element

Nuclear excitation $\Delta J^\pi = 1^+$ with $\Delta T_z = 0$ is an $M1$ transition. When nuclear excitation at low momentum transfer is considered, spin-parts of the $M1$ transition are probed due to the local nature of the nucleon-nucleon (NN) interaction (Petrovich and Love, 1981). Thus, the 1^+ excitation by (p, p') reaction at forward angles is spin-$M1$ transition. Since spin-$M1$ transition is not probed by electromagnetic interaction but by nuclear interaction, its transition strength does not relate to g-factors. Therefore, transition strengths of IS and IV spin-M1 transitions from the ground state $|{\rm g.s.}\rangle$ to an excited state $|f\rangle$ are expressed by squared nuclear matrix element (SNME) as

$$\left|M_{\rm f}(\vec{\sigma})\right|^2 = \left|\frac{1}{\sqrt{2J_i+1}}\left\langle {\rm f}\left\|\sum_{k=1}^A \vec{\sigma}_k\right\|{\rm g.s.}\right\rangle\right|^2 \tag{16}$$

$$\left|M_{\rm f}(\vec{\sigma}\,\tau_z)\right|^2 = \left|\frac{1}{\sqrt{2J_i+1}}\left\langle {\rm f}\left\|\sum_{k=1}^{\rm A}\vec{\sigma}_k\tau_{z,k}\right\|{\rm g.s.}\right\rangle\right|^2 \tag{17}$$

respectively. The factor $1/\sqrt{2J_i+1}$ is unity for a 0^+ ground state.

2.4 Relation to Gamow-Teller Excitation

Next, reduced nuclear matrix element and transition strength in GT excitation are defined as

$$M_{\rm f}\left(\overrightarrow{\sigma}\tau_{\pm}\right) = \frac{1}{\sqrt{2J_i+1}}\left\langle {\rm f}\left\|\frac{1}{\sqrt{2}}\sum_{k=1}^{A}\overrightarrow{\sigma}_k\tau_{\pm,k}\right\|{\rm g.s.}\right\rangle \tag{18}$$

$$B(GT^{\pm}) = \left|M_{\rm f}\left(\overrightarrow{\sigma}\tau_{\pm}\right)\right|^2, \tag{19}$$

respectively, where $\tau_{\pm} = \frac{1}{2}(\tau_x \pm i\tau_y)$. Applying the Wigner-Eckart theorem in the isospin space, transition strengths of GT and IV spin-$M1$ excitations are obtained as

$$B(GT^{\pm}) = \left|\frac{1}{\sqrt{2J_i+1}}\frac{\langle T_i, T_{iz}, 1, \pm 1|T_f, T_{fz}>}{\sqrt{2T_f+1}}\frac{1}{\sqrt{2}}M'(GT^{\pm})\right|^2, \tag{20}$$

$$B(M1)_{\sigma\tau} = \frac{3}{4\pi}\left|\frac{g_s^{\rm IV}}{2}\frac{1}{\sqrt{2J_i+1}}\frac{\langle T_i, T_{iz}, 1, 0|T_f, T_{fz}\rangle}{\sqrt{2T_f+1}}M'(M1_{\sigma\tau})\right|^2\mu_N^2, \tag{21}$$

respectively, where $M'(GT^{\pm})$ and $M'(M1_{\sigma\tau})$ are reduced nuclear matrix elements in spin and isospin expressed as

$$M'(GT^{\pm}) = \left\langle {\rm f}\left\|\sum_{k=1}^{A}\overrightarrow{\sigma}_k\tau_{\pm,k}\right\|{\rm g.s.}\right\rangle \tag{22}$$

$$M'(M1_{\sigma\tau}) = \left\langle {\rm f}\left\|\sum_{k=1}^{A}\overrightarrow{\sigma}_k\tau_{z,k}\right\|{\rm g.s.}\right\rangle \tag{23}$$

respectively. Because $|M'(GT^{\pm})|^2 = |M'(M1_{\sigma\tau})|^2$ is realized under the assumption of isospin symmetry, the following relationship between $B(GT^{\pm})$ and $B(M1)_{\sigma\tau}$ can be obtained as

$$\frac{B({\rm GT}^{\pm})}{B(M1)_{\sigma\tau}/\mu_N^2} = \frac{8\pi}{3}\frac{1}{(g_s^{IV})^2}\frac{\langle T_i, T_{iz}, 1, \pm 1|T_f, T_{fz}\rangle^2}{\langle T_i, T_{iz}, 1, 0|T_f, T_{fz}\rangle^2} \tag{24}$$

Here, it should be noted that the isospin symmetry is reasonably assumed within the accuracy of the data in the present study although the meson exchange current contribution can be different between an IV $M1$ transition measured by electron scattering and the analogous GT transition by charge-exchange reaction (Richter et al., 1990; Lüttge et al., 1996).

2.5 Total Spin Correlation in Ground State

For the discussion of total spin correlation in a ground state (Matsubara et al., 2015), the difference between the sums of the IS and IV spin-$M1$ SNMEs integrated up to the excitation energy of E_x, $\Delta_{\rm spin}(E_x)$, is defined as

$$\Delta_{\rm spin}(E_{\rm x}) = \frac{1}{16}\left\{\sum_{E_{\rm f}<E_{\rm x}}\left|M_{\rm f}(\overrightarrow{\sigma})\right|^2 - \sum_{E_{\rm f}<E_{\rm x}}\left|M_{\rm f}(\overrightarrow{\sigma}\tau_{\rm z})\right|^2\right\}$$

With the proton (neutron) total spin operator $\overrightarrow{S}_{p(n)}$ defined as

$$\overrightarrow{S}_{p(n)} = \frac{1}{2}\sum_{k=1}^{Z(N)}\overrightarrow{\sigma}_k, \tag{26}$$

the sum is taken for all the protons (neutron).When a ground state is $J^{\pi} = 0^+$, the IS and IV spin-$M1$ nuclear matrix elements are represented by

$$M_{\rm f}\left(\overrightarrow{\sigma}\right) = 2\left\langle {\rm f}\left|\overrightarrow{S}_n + \overrightarrow{S}_n\right|0\right\rangle \tag{27}$$

$$M_{\rm f}\left(\overrightarrow{\sigma}\tau_{\rm z}\right) = 2\left\langle {\rm f}\left|\overrightarrow{S}_n - \overrightarrow{S}_p\right|0\right\rangle \tag{28}$$

respectively, where $|0\rangle$ denotes the ground state. In the limit of $E_{\rm x}\rightarrow\infty$, the completeness of the final state, $|{\rm f}\rangle$, yields

$$\left\langle\left(\overrightarrow{S}_n + \overrightarrow{S}_p\right)^2\right\rangle = \sum_{\rm f}\langle {\rm g.s.}\left|\overrightarrow{S}_{\rm n} + \overrightarrow{S}_{\rm p}\right|{\rm f}\rangle\langle {\rm f}\left|\overrightarrow{S}_{\rm n} + \overrightarrow{S}_{\rm p}\right|{\rm g.s.}\rangle = \lim_{E_{\rm x}\rightarrow\infty}\frac{1}{4}\sum_{E_{\rm f}<E_{\rm x}}\left|M_{\rm f}\left(\overrightarrow{\sigma}\right)\right|^2 \tag{29}$$

$$\left\langle\left(\overrightarrow{S}_n - \overrightarrow{S}_p\right)^2\right\rangle = \lim_{E_{\rm x}\rightarrow\infty}\frac{1}{4}\sum_{E_{\rm f}<E_{\rm x}}\left|M_{\rm f}\left(\overrightarrow{\sigma}\tau_{\rm z}\right)\right|^2 \tag{30}$$

Here the expectation values of the left side of the equations are taken for the 0^+ ground state. We then derive

$$\Delta_{\rm spin} \equiv \lim_{E_{\rm x}\rightarrow\infty}\Delta_{\rm spin}(E_{\rm x}) = \frac{1}{4}\left\{\left\langle\left(\overrightarrow{S}_n + \overrightarrow{S}_p\right)^2 - \left(\overrightarrow{S}_n - \overrightarrow{S}_p\right)^2\right\rangle\right\} = \langle\overrightarrow{S}_p\cdot\overrightarrow{S}_n\rangle \tag{31}$$

which represents the expectation value of the proton-neutron spin-spin correlation in the ground state.

3 EXPERIMENT

In this section we briefly describe the experimental method and the assignment of the spin-M1 excitations. Details can be found in former publications (Tamii et al., 2009; Matsubara et al., 2015; von Neumann-Cosel and Tamii, 2019).

3.1 Measurement of the (*p,p'*) Reactions

The experiment was performed at the cyclotron facility of the Research Center for Nuclear Physics (RCNP), Osaka University. A proton beam was accelerated by a cascade of two cyclotrons to $E_{\rm p}$ = 295 MeV. The beam was transported to the West-South (WS) beam line (Wakasa et al., 2002), where a high-dispersion on target was created. An excitation-energy resolution of 18 keV (FWHM) was achieved by applying dispersion matching (Fujita et al., 1997; Fujita H. et al., 2002; Fujita et al., 2011) between the WS beam line and the Grand Raiden (GR) spectrometer (Fujiwara et al., 1999). The scattered protons by the target were momentum-analyzed and were detected by two sets of multi-wire drift-chambers and two plastic scintillation counters at the focal plane by GR spectrometer. A scattering angle range of 0–14° was covered by placing the GR spectrometer at 0, 2.5, 4.5, 6, 8, 10, 12, and 14°. The details of the experimental technique are described in Ref. (Tamii et al., 2009; von Neumann-Cosel and Tamii, 2019).

Self-conjugate even-even nuclei, ^{12}C, ^{24}Mg, ^{28}Si, ^{32}S and ^{36}Ar, were used as the target. Areal densities of 1.0–2.5 mg/cm^2 were prepared for ^{12}C, ^{24}Mg, and ^{28}Si. Magnesium and argon targets were isotopically enriched to 100%, while the others were in

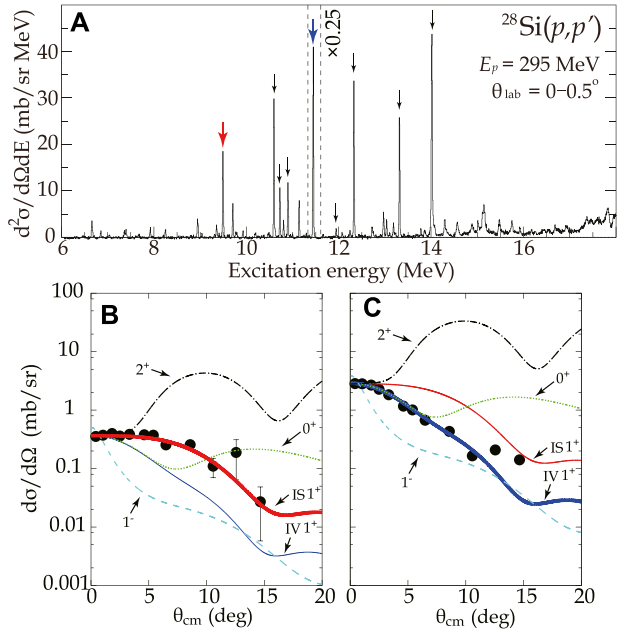

FIGURE 1 | (A) Excitation energy spectrum of the ^{28}Si(p,p') reaction at E_p = 295 MeV and θ_{lab} = 0° – 0.5°. The arrows in the figure indicate conditions that are definitely determined as 1^+. Angular distributions of **(B)** IS and **(C)** IV spin-M1 excitations marked by red and blue arrows in **(A)**, respectively, in comparison with theoretical angular distributions for several multipolarities. The figures were taken from Matsubara et al. (2015).

natural abundance. The ^{32}S target was kept at the liquid nitrogen temperature for preventing sublimation due to heat by charged particle irradiation (Matsubara et al., 2009) with an areal density of 15 mg/cm^2. The ^{36}Ar target was kept at 1.0 atm in a gas cell at room temperature (Matsubara et al., 2012) sealed by aramid foils with a thickness of 6 μm on one side.

3.2 Assignment of Spin-M1 Excitations

Figure 1A shows an excitation energy spectrum of the ^{28}Si(p,p') reaction at a scattering angle of 0.0–0.5°. The excited states below E_x = 16 MeV are well isolated from the others. Excited state with a spin-parity of 1^+ state was identified by comparing the shape of the measured angular distribution of the differential cross-section with Distorted-Wave Impulse Approximation (DWIA) calculations by using the code DWBA07 (Raynal, 2007). One-body transition densities were obtained by shell-model calculations with the code Nushell@MSU (Brown and Rae, 2014) and the USD interactions (Brown and Wildenthal, 1983). No sizable difference in the angular distribution was observed depending on the choice of the effective interaction from USD, USDA, or USDB (Brown and Richter, 2006; Richter et al., 2008). The effective *NN* interaction parametrized at 325 MeV was used after conversion to a beam energy of 295 MeV as indicated in (Love and Franey, 1981; Franey and Love, 1985). Optical potential parameters were determined by fitting the angular distribution of the differential cross-section of the elastic scattering measured in the same experiment (Matsubara, 2010). Harmonic oscillator parameters were taken from a global analysis (Kirson, 2007).

The measured angular distributions of the differential cross-section for the excited states at E_x = 9.495 (1^+: T = 0) and 11.447 MeV (1^+: T = 1) in ^{28}Si are shown in **Figures 1B,C**, respectively, by the solid circles. They are compared with the predictions of the DWIA calculation shown by the curves for J^π = 0^+, 1^-, and 2^+, and for each of the IS and IV 1^+ transitions. The predicted cross-sections are normalized to the experimental data at the smallest measured angle. The angular distribution of the IS 1^+ excitation is predicted to be flatter than the IV 1^+ excitation at the forward angles smaller than 5° due to the relatively stronger contribution of the exchange tensor component compared to the central component in the effective *NN* interaction (Franey and Love, 1985; Tamii et al., 1999). Thus, the measured angular distribution allowed determination of the transferred isospin, ΔT = 0 (IS) or 1 (IV), for the 1^+ transitions.

The IS and IV 1^+ excited states were assigned from the observed discrete excited states by the following method. First the angular distribution of the differential cross-sections for each of the observed discrete excited states was deduced from the data analysis. The excited states were selected according to the angular distribution below 5° for those having an almost flat distribution as a signature of an IS 1^+ state or a quickly dropping distribution of an IV 1^+ state as shown in **Figures 1B,C**, respectively. Second, the most appropriate assignment was chosen from IS 1^+, IV 1^+, 0^+, 1^-, and 2^+ distributions by comparing the angular distribution up to 14° with the theoretical predictions. Third, the assignment for the IS or IV 1^+ states with a reduced χ^2 value close to unity was taken as confident and that for the rests as less confident. The confident assignments of the IS and IV 1^+ states were in good agreement for the conditions studied by electron scattering (Bendel et al., 1971; Richter et al., 1990; Foltz et al., 1994; Lüttge et al., 1996; Hofmann et al., 2002). The high energy-resolution measurement allowed us to observe several new states including the less-confident assignments as shown in **Section 5.1**.

4 UNIT CROSS-SECTION METHOD

4.1 Definition

4.1.1 Unit Cross-Section

The differential cross-section of the 1^+ excitations by proton inelastic scattering at 0° is considered to be approximately proportional to SNME in the intermediate energy region of 100–400 MeV. Unit cross-sections (UCSs), $\hat{\sigma}_{IS}$ and $\hat{\sigma}_{IV}$, are introduced in analogy to the study of Gamow-Teller excitations by (p,n) reactions (Taddeucci et al., 1987; Sasano et al., 2009). The differential cross-section at 0° is written as

$$\frac{d\sigma}{d\Omega}(0^\circ) = \hat{\sigma}_T F_T(q, E_x)\left|M_f(\mathcal{O}_T)\right|^2 \quad (32)$$

where T stands for IS or IV. $\mathcal{O}_T$ is the operator, $\vec{\sigma}$ or $\vec{\sigma}\tau_z$, for IS or IV transitions, respectively. $F_T(q, E_x)$ is the kinematic factor that accounts for dependence on the momentum transfer (q) and the excitation energy (E_x), and was determined by the DWIA

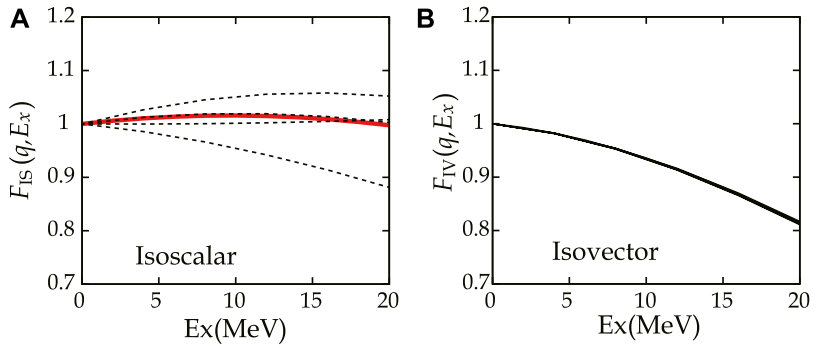

FIGURE 2 | Kinematic correction factors $F_{\mathrm{IS}}(q,E_x)$ and $F_{\mathrm{IV}}(q,E_x)$ in the case of ^{28}Si obtained from DWIA calculation using USD interaction. **(A)** The strongest excitation and others are drawn in red bold and black dashed curves, respectively. **(B)** Distributions of several IV OBTDs are overlapped.

TABLE 1 | Data used for obtaining IV UCSs.

Nuclide	E_x (MeV)	$\frac{d\sigma}{d\Omega}(0.4^\circ)$ (mb/sr)	$F_{\mathrm{IV}}(q,E_x)$	$B(\mathrm{GT}^{\pm})$	$\hat{\sigma}_{\mathrm{IV}}$ (mb/sr)
^{12}C	15.113	3.429 ± 0.62	0.897	0.924 ± 0.04	2.11 ± 0.13
^{26}Mg	13.302	0.703 ± 0.30	0.904	0.408 ± 0.018	1.92 ± 0.12
^{58}Ni	10.655	0.981 ± 0.12	0.916	0.191 ± 0.022	0.94 ± 0.11

calculation as explained in **Section 4.1.2**. The target mass (A) dependence of UCSs is parameterized as (Taddeucci et al., 1987)

$$\hat{\sigma}_T(A) = N_T \exp\left(-x_T A^{1/3}\right) \tag{33}$$

where N_T and x_T are the normalization and mass-dependence parameters. The mass-dependence parameter x_T essentially originates from the distortion effect of the reaction that is common between the IS and IV transitions. Thus we assume $x_{IS} = x_{IV}$, which is held within an accuracy of 5% in DWIA calculations. Details will be discussed in **Section 4.4.2**.

4.1.2 Kinematic Factor

The kinematic factors $F_{\mathrm{IS}}(q,E_x)$ and $F_{\mathrm{IV}}(q,E_x)$ were determined by DWIA calculation using the USD interaction as shown in **Figure 2** as a case of ^{28}Si, where only OBTDs above the experimental detection limit were employed. The distributions were obtained from a ratio of differential cross-section at 0° at $E_x \neq 0$ to that at $E_x = 0$. As seen in **Figure 2B**, IV distributions of the kinematic factor overlap. Since the result suggests that $F_{\mathrm{IV}}(q,E_x)$ does not depend on wavefunction, $F_{\mathrm{IV}}(q,E_x)$ was expressed as a smooth function of E_x and A by fitting. As shown in **Figure 2A**, however, IS distributions of the kinematic factor depend on wavefunction as they do not overlap. Because the result suggests that $F_{\mathrm{IS}}(q,E_x)$ cannot be expressed as a function of E_x owing to dependence of wavefunction, $F_{\mathrm{IS}}(q,E_x) = 1.00 \pm 0.10$ was simply assumed in order to cover the variation of wavefunctions below $E_x = 15$ MeV.

4.2 Derivation From Experiment

4.2.1 Cases of 12-Carbon, 26-Magnesium, 58-Nickel

Isovector UCSs of ^{12}C, ^{26}Mg, and ^{58}Ni were obtained using the data summarized in **Table 1** by assuming isospin symmetry. The differential cross-section of (p,p') reaction at E_p = 295 MeV at scattering angles 0.4° was taken from Tamii et al. (2009), where 0.4° is the most forward angle by selecting scattering angles between 0.0 and 0.5°. The cross-section was extrapolated to E_x = 0 MeV using $F_{\mathrm{IV}}(q,E_X)$.

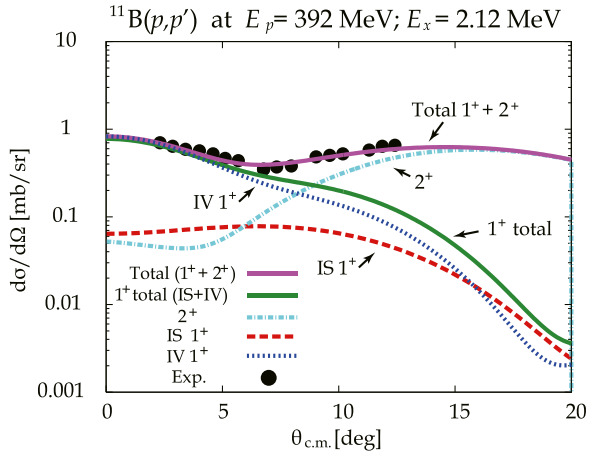

FIGURE 3 | Decomposition of differential cross-section of ^{11}B(p,p') reaction at E_p = 392 MeV compared to the state at E_x = 2.12 MeV. The experimental data were taken from Kawabata et al. (2004).

Log ft-value of β-decay and (^{3}He, t) data (Alburger and Nathan, 1978; Fujita Y. et al., 2002; Zegers et al., 2006; Fujita et al., 2007; Fujita et al., 2011) were used to obtain GT strength ($B(\mathrm{GT}^{\pm})$) from ground state to an excited state corresponding to the (p,p') cross-section under the isospin symmetry. After $B(\mathrm{GT}^{\pm})$ was converted to IV spin-$M1$ SNME following **Eqs. 13**, **24**, $\hat{\sigma}_{\mathrm{IV}}$ was obtained. Here, the (p,n) data (Sasano et al., 2009) were also employed for the calibration of $B(\mathrm{GT}^{-})$ in ^{58}Ni.

4.2.2 Case of 11-Boron

The γ-decay widths of the mirror states in ^{11}B and ^{11}C from the first excited states (Firestone, 1996), corresponding to $B(M1)_{11\mathrm{B}}$ and $B(M1)_{11\mathrm{C}}$, respectively, were employed to obtain $B(M1)_{\mathrm{IS}}$ and $B(M1)_{\mathrm{IV}}$ following **Eqs. 10**, **11**. Then, $B(M1)_{\sigma}$ and $B(M1)_{\sigma\tau}$

TABLE 2 | Data used for obtaining UCSs of ^{11}B. The upper table is expressed in unit of μ_N^2.

$B(M1)_{11_B}$	$B(M1)_{11_C}$	$B(M1)_{IS}$	$B(M1)_{IV}$	$B(M1)_{\sigma}$	$B(M1)_{\sigma\tau}$
0.544 ± 0.043	0.347 ± 0.024	0.0055 ± 0.0013	0.440 ± 0.012	0.030 ± 0.007	0.57 ± 0.04
$\frac{d\sigma}{d\Omega}$ (0°)	392 MeV Kawabata et al. (2004)			295 MeV Tamii et al. (1999), Tamii et al. (2009)	
	Total ($1^+ + 2^+$)	IS 1^+	IV 1^+	IS 1^+	IV 1^+
(mb/sr)	0.820	0.0633	0.818	0.0621 ± 0.0052	0.780 ± 0.042
Nuclide	E_x (MeV)	$F_{IS}(q=0,E_x)$	$\widehat{\sigma}_{IS}$ (mb/sr)	$F_{IV}(q=0,E_x)$	$\widehat{\sigma}_{IV}$ (mb/sr)
^{11}B	2.12	1.00 ± 0.10	0.0971 ± 0.025	0.9926	1.81 ± 0.16

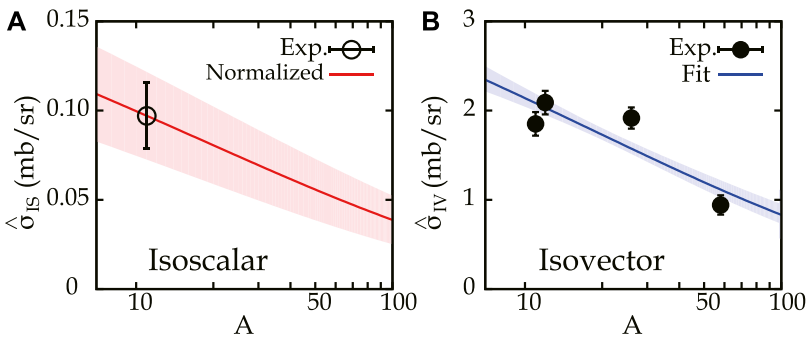

FIGURE 4 | Empirically determined IS **(left)** and IV **(right)** UCSs. The mass dependence of the data were fit with the functional form of **Eq. 33** as shown by the solid lines in the IV panel. The band shows the uncertainty of one sigma. The IS slope parameter x_{IS} is taken to be the same as x_{IV}. The figures were adapted from Matsubara et al. (2015).

were obtained from $B(M1)_{IS}$ and $B(GT^-) = 0.402 \pm 0.031$ (Taddeucci et al., 1990; Kawabata et al., 2004) using **Eqs. 15**, **24**, respectively. Finally, IS and IV spin-$M1$ SNMEs in the case of ^{11}B were obtained using **Eqs. 12**, **13**, respectively.

The differential cross-section data of the ^{11}B(p,p') reaction at E_p = 392 MeV and at E_x = 2.12 MeV was taken from Kawabata et al. (2004). The angular distribution of the differential cross-section was decomposed into IS 1^+, IV 1^+, and 2^+ transitions using the DWIA calculation, where an incoherent (a coherent) sum was assumed between 1^+ and 2^+ (IS 1^+ and IV 1^+) excitations. The OBTDs based on CKPOT interaction (Cohen and Kurath, 1965), the effective *NN* interaction derived at 325 MeV (Love and Franey, 1981; Franey and Love, 1985), and the global optical potential parameters (Cooper et al., 2009) were employed in this calculation. The OBTDs were normalized to reproduce the experimental values of IS and IV SNMEs, and $B(E2)$ (Firestone, 1996) in IS 1^+, IV 1^+, and 2^+ excitations, respectively. Because the normalized OBTDs did not reproduce the experimental angular distribution of the differential cross-section, additional normalization factors of 1.1 and 1.3 were applied to the 1^+ and 2^+ excitations, respectively, as shown in **Figure 3**. The differential cross-section data of total, IS 1^+, and IV 1^+ at E_p = 392 MeV and at 0° were decomposed as summarized in **Table 2**, where the experimental uncertainty was assumed to be negligible because the error bars were invisible in Kawabata et al. (2004). Here, choice of an interaction with OBTDs did not change the final result because differences among CKPOT, SFO (Suzuki et al., 2003), and MK3w (Warburton and Millener, 1989) interactions in the model spaces of *p*, *psd*, and *spsdpf*, respectively, were within 0.5%. Next, the cross-section data at E_p = 392 MeV were converted to those at E_p = 295 MeV by making use of a ratio of the ^{12}C(p,p') reaction at 0° to the states E_x = 12.71 and 15.11 MeV known as IS 1^+ and IV 1^+ excitations, respectively, where the experimental data were taken from Tamii et al. (1999), Tamii et al. (2009). Thus, the data of ^{11}B(p,p') excitation to E_x = 2.12 MeV at E_p = 295 MeV and at 0° were obtained.

Combining the SNMEs with the differential cross-section after correction of $F_T(q,E_x)$, IS and IV UCSs in the case of ^{11}B were obtained as summarized in **Table 2**. Here, $\widehat{\sigma}_{IS}$ does not include uncertainty owing to $F_{IS}(q,E_x)$.

TABLE 3 | Empirically determined UCS parameters from the fit shown in **Figure 4**.

N_{IS} (mb/sr)	N_{IV} (mb/sr)	$x_{IV} = x_{IS}$
0.226 ± 0.043	4.85 ± 0.82	0.38 ± 0.06

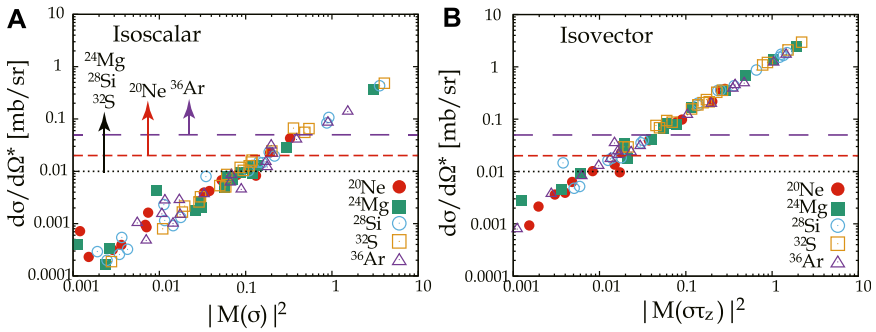

FIGURE 5 | Proportionality of UCS. Horizontal lines indicate experimental detection limit for ^{24}Mg, ^{28}Si and ^{32}S (dotted), ^{20}Ne (short-dashed) and ^{36}Ar (long-dashed). Cross-section is corrected in terms of mass dependence as in **Eq. 34**.

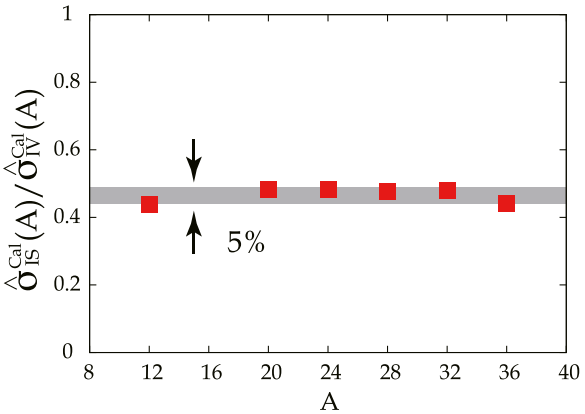

FIGURE 6 | Mass dependence of ratio of IS to IV UCSs studied by calculation.

4.3 Results of Unit Cross-Section

The experimentally obtained IS and IV UCSs were plotted as a function of the mass number in **Figures 4A,B**, respectively. The mass dependence of the IV UCS data was fitted with the functional form of **Eq. 33** having free parameters of N_{IV} and x_{IV}. The result is shown by the solid line in **Figure 4B** with the one-sigma uncertainty band. The IS normalization parameter, N_{IS}, was determined from the data at A = 11. The IS slope parameter, x_{IS}, was taken to be the same as x_{IV} as discussed in **Section 4.4.2**. The IS uncertainty band includes contribution of 10% from the $F_{IS}(q, E_x)$ (**Section 4.1.2**). The obtained parameters are summarized in **Table 3**.

4.4 Model Study

4.4.1 Proportionality of Squared Nuclear Matrix Elements to the Differential Cross-Section

Validity of the application of the UCS method has been theoretically examined by the use of shell-model target wave functions as USD interaction and DWIA calculation. Since $B(M1)_\sigma$ and $B(M1)_{\sigma\tau}$ were calculated using the code Nushell@MSU (Brown and Rae, 2014), SNMEs were obtained from the relations in **Eqs. 12**, **13**. Each differential cross-section at $q = 0$ and at $E_x = 0$ MeV was calculated using corresponding OBTD of the USD interaction. Here the following correction for mass dependence to be normalized to A = 28 was applied as

$$\frac{d\sigma^*}{d\Omega} = \frac{d\sigma}{d\Omega} \times e^{-0.38\times\left(28^{1/3}-A^{1/3}\right)} \tag{34}$$

where $\frac{d\sigma}{d\Omega}^*$ is the corrected cross-section and 0.38 comes from x_T determined in **Table 3**. As shown in **Figure 5**, good linearity was seen especially above the experimental detection limit shown by the lines for each target nucleus.

4.4.2 Distortion Effect

The mass-dependence term in **Eq. 32**, x_T, essentially originates from the distortion effect that is common between the IS and IV transitions. A slope for each nucleus in **Figure 5** corresponds to UCSs theoretically obtained, where the weighting sum within the experimental detection limit was taken. Those ratios of IS to IV UCSs for each nucleus are plotted as a function of mass number in **Figure 6**, where the suffix of "cal" indicates that the value of UCS is obtained from the calculation. The result for ^{12}C is added in **Figure 6**. The SFO interaction (Suzuki et al., 2003), which is applicable to the p-shell nuclei, is used instead of the USD interaction. The results suggest that the assumption is supported, as the ratios are constant within 5%.

5 RESULTS AND DISCUSSION

5.1 Strength Distribution

The SNMEs of the transitions to the excited states assigned as T = 0 (IS) or T = 1 (IV) 1^+ states were determined by using **Eq. 32** from the measured differential cross-section at 0°. The results are plotted in **Figure 7** , where the figure was taken from Matsubara et al. (2015) with addition of the ^{12}C data. The strengths of ^{12}C were observed to be centered to single state, which was consistent with previous work (von Neumann-Cosel et al., 2000). For ^{24}Mg, ^{28}Si, ^{32}S, and ^{36}Ar, we

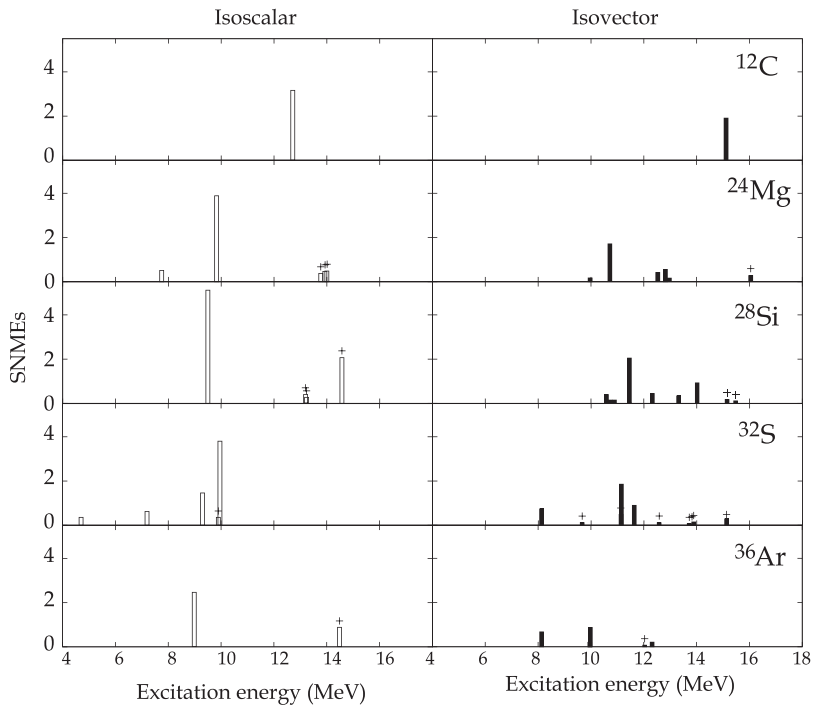

FIGURE 7 | Observed distributions of spin-*M*1 SNMEs. The bars labeled + indicate states with a less confident spin assignment. The figures were taken from Matsubara et al. (2015) with ^{12}C data added.

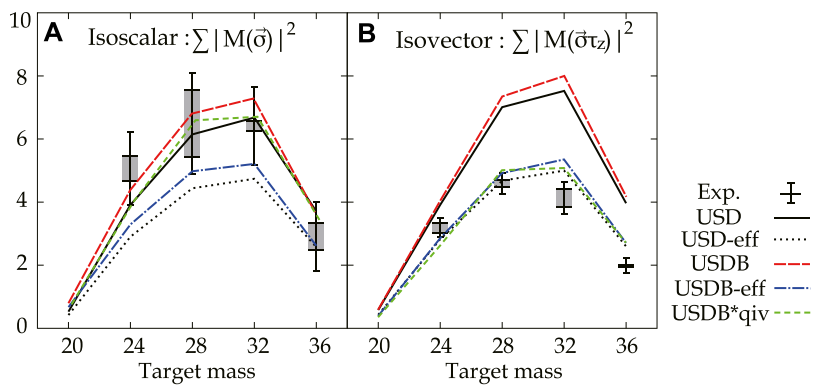

FIGURE 8 | Integrated values of spin-*M*1 SNMEs for IS **(A)** and IV **(B)** transitions up to E_x = 16 MeV as a function of the target mass. Error bars indicate the total experimental uncertainties, and gray bands show partial uncertainties from indefinite spin assignments. Solid and long-dashed lines indicate the prediction of a shell-model calculation using bare USD and bare USDB interactions, respectively. Dotted and dashed-dotted lines applied empirical quenching factors (see text for more details) to USD and USDB interactions, respectively. The short-dashed lines (green) are calculated using the USDB interaction modification in the IS spin-triplet interaction and in the IV quenching factor from Sagawa and Suzuki (2018). The figures were taken from Matsubara et al. (2015) with some updates using the modified interactions (Sagawa and Suzuki, 2018).

identified 1–4 (4–8) states in each target nucleus corresponding to the IS (IV) spin-*M*1 transitions.

Additionally, 1–3 (1–7) states were assigned as IS (IV) spin-*M*1 transitions with less confidence, and they are marked with "+." We reassigned 1–6 states as 0^+, which were claimed as 1^+ in previous studies (Anantaraman et al., 1984; Crawley et al., 1989).

5.2 Quenching of Squared Nuclear Matrix Elements of Isoscalar and Isovector Spin-M1 Transitions

The integrated values of the SNMEs up to E_x = 16 MeV were plotted as a function of the target mass in **Figure 8** for each of the IS (left panel) and IV (right panel) transitions. Error bars show

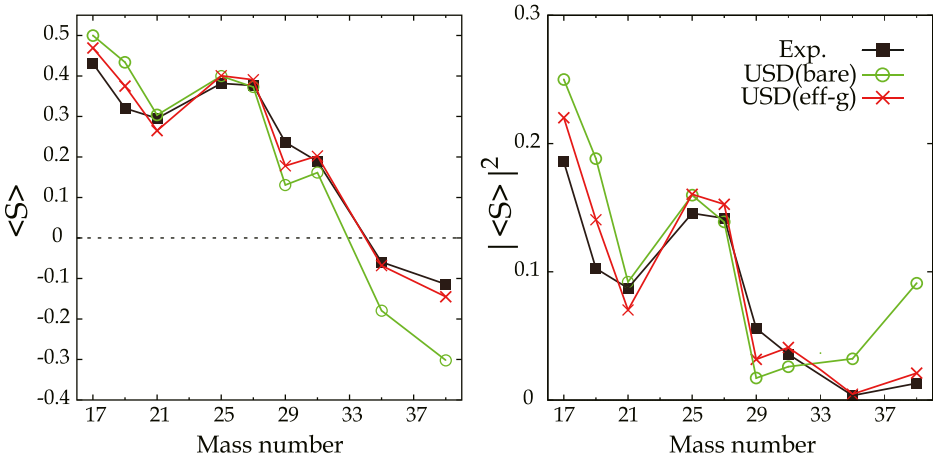

FIGURE 9 | The diagonal spin matrix element $\langle S \rangle$ obtained from the IS magnetic moments of mirror nuclei in the sd-shell region. The data were taken and calculated from Brown and Wildenthal (1983), Brown and Wildenthal (1987). The lines are for guiding the viewer's eyes.

the full experimental uncertainties, while gray bands show the partial uncertainties originating from the less-confident spin-parity assignment of the transitions (see **Section 5.1**). Predicted SNMEs by shell-model calculation employing USD interaction (Brown and Wildenthal, 1987) integrated up to 16 MeV is shown by solid lines. Altering the effective interaction to USDA or USDB (Brown and Richter, 2006; Richter et al., 2008) gave only a small change in the prediction (<10%), as shown in **Figure 8** for USDB (dashed line). It has been found that the measured values are significantly smaller than the model prediction for the integrated IV SNMEs, while the values are consistent with the model prediction of the integrated IS SNMEs within the experimental uncertainties. We defined the quenching factor as the ratio of the experimentally observed SNMEs integrated up to the experimental limit of 16 MeV to the theoretical predictions integrated to the same excitation energy. The numbers are 1.01(9) and 0.61(6), compared with predictions by the shell model using the USD interaction for the IS and IV spin-$M1$ transitions, respectively, when the averages of the measured nuclei are used.

The observed quenching factor of the IV spin-$M1$ transitions is similar to the study of the quenching of the Gamow Teller transitions that is analogous to the IV spin-$M1$ transitions in terms of isospin symmetry (Anderson et al., 1987). Quenching of the reduced transition probability $B(M1)$ is, in a conventional prescription, implemented by modification of the g-factors (Brown and Wildenthal, 1987) that is multiplied to the SNMEs to obtain $B(M1)$. Here, we applied the same empirical quenching factor as used in the modification of g-factors to the SNMEs calculated by the shell model. The results are shown by the dotted lines (USDB$^{\text{eff}}$) in **Figure 8**. The empirical quenching factors are similar between IS and IV transitions. SNMEs of the IV spin-$M1$ transitions with the empirical quenching factor turned out to be compatible with the data.

In contrast, description of the IS transitions became worse by introducing the empirical quenching factor. The present result shows that the widely-used effective g-factors lead to an over-quenching of the IS spin component of the $M1$transition in the sd-shell. It should be noted that the observed $B(M1)$ strength of the 1^+ excited state at 10.23 MeV in ^{48}Ca by (p,p') scattering is more consistent with electron scattering data when no quenching is assumed for the IS part of the transition strength (Birkhan et al., 2016; Mathy et al., 2017). A recent theoretical work (Sagawa et al., 2016; Sagawa and Suzuki, 2018) reported that both the IS and IV SNMEs can be reproduced (short dashed line) by enhancing the IS spin-triplet pairing matrices by a factor of 1.1 in addition to applying the empirical quenching factor to the IV spin-$M1$ operator but not the IS spin-$M1$ operator (USDB*qiv). Note that in (Sagawa and Suzuki, 2018) the USDB*qiv result for the IS spin-$M1$ excitations is not shown, but it is the same as USDB*. The theoretical work implies that the present description of the shell model using USD interactions and the empirical quenching factors may have room to be improved in the IS spin-triplet interaction channel and in the IS quenching factor.

5.3 Isoscalar Magnetic Moments

In this section, we discuss how the new finding of quenching of the IS and IV spin-$M1$ SNMEs is understood in relation to the IS and IV magnetic moment studied in the past. The magnetic moment is described by the diagonal component of the nuclear matrix element with the relevant $M1$ operator while the $M1$ transitions correspond to the off-diagonal components as described in **Section 2**.

The experimental $\langle S \rangle$ data are plotted in the left panel of **Figure 9**, and the squared values in the right panel. The $\langle S \rangle$ values calculated by the shell model with the effective IS g-factors (Brown and Wildenthal, 1983; Brown and Wildenthal, 1987) using the USD interaction are indicated by open circles and crosses for the bare and effective g factors, respectively. The results show clear discrepancies between the experimental data and the prediction with the bare g-factor, corresponding to the quenching, in the edge regions of the sd-shell (A = 17–19 and 35–39) close to the magic numbers of A = 16 and 40. The difference is, however, not obvious in the mid-shell region

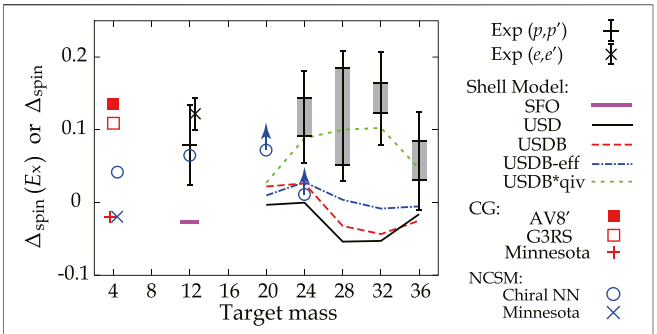

FIGURE 10 | Experimental data of Δ_{spin} (E_x) summed up to E_x = 16 MeV are plotted for proton (electron) scattering by the horizontal bars (cross mark) with the error bars. The definitions of error bars and gray bands are the same as in **Figure 8**. Theoretical predictions of $\Delta_{spin}=\langle \vec{S}_p \cdot \vec{S}_n \rangle$ are plotted for the shell models, Correlated Gaussian (CG) method (Suzuki et al., 2008), and No-Core Shell-Model (NCSM) (Roth et al., 2010). The figure was taken from Matsubara et al. (2015) with updated predictions from Sagawa and Suzuki (2018).

(A = 21–31). The discrepancies in the edge regions are reduced by introduction of the effective IS *g*-factors. The IS magnetic moments in the mid-shell region are reasonably reproduced without introducing the effective IS *g*-factors, which is consistent with our finding of no quenching of the IS spin-*M*1 SNMEs.

5.4 Proton-Neutron Spin-Spin Correlation in the Ground State

Figure 10 shows the Δ_{spin} (E_x) data summed up to E_x=16 MeV by the solid bars. Electron scattering data (von Neumann-Cosel et al., 2000) is plotted at A = 12 by the black cross mark with the error bar, which is consistent with the proton scattering data within experimental uncertainty. It is interesting to note that all the experimental data show positive numbers. The Δ_{spin} values at A = 4 predicted by Correlated Gaussian (CG) method (Suzuki et al., 2008), an ab initio approach, are plotted for each of the *NN* interactions of AV8' (red solid square), G3RS (red open square) and Minnesota (red plus). The predictions by the No-Core Shell-Model (NCSM) (Roth et al., 2010) are plotted for chiral *NN* (Entem and Machleidt, 2003) (blue open circle) and Minnesota (blue cross) interactions. Both predictions using the Minnesota interaction are consistent with each other and are slightly negative. The Minnesota interaction does not contain tensor interactions. It is illuminating to see that the predictions are positive when more realistic *NN* interactions are used: AV8' (Pudliner et al., 1997) and G3RS (Tamagaki, 1968) interactions for the CG method and chiral *NN* interaction (Entem and Machleidt, 2003) for NCSM. The shell model predictions of Δ_{spin} at A = 12 with SFO interaction (solid horizontal line) and A = 20–36 with USD interaction are slightly negative or close to zero, which is significantly smaller than the experimental data of Δ_{spin}. The trend of the USDB interaction (dashed line) is similar. The predicted values increase a little but are still much smaller than the experimental results when the IS and IV effective quenching factors determined in the study of the *g*-factors (Brown and Wildenthal, 1987) are applied to the SNME predicted by the shell model (dot-dashed line). The situation is similar for the other studies of effective *g*-factors (Towner and Khanna, 1983; Arima et al., 1987; Towner, 1987). The experimental data are reproduced when IS spin-triple pairing matrices are enhanced by a factor of 1.1, and only the IV part of SNME is quenched by effective quenching factors (dotted line) (Sagawa and Suzuki, 2018).

NCSM with the chiral *NN* interaction predicts Δ_{spin} values for ^{20}Ne (N_{MAX} = 4) and ^{24}Mg (N_{MAX} = 2), as indicated by the open blue circles in **Figure 10**. Here, N_{MAX} defines the maximal allowed harmonic-oscillator excitation energy above the unperturbed ground state (Roth et al., 2010), hence representing a measure of the model space. Variation of the values depending on N_{MAX} shows a clear trend toward positive when N_{MAX} increases: −0.007, 0.028, and 0.072 for N_{MAX} = 0, 2 and 4 for ^{20}Ne and −0.018 and 0.011 for N_{MAX}=0 and 2 for ^{24}Mg, respectively. Although the values are not converged yet, they are taken as a lower limit in the plot (expressed by arrows). The increase of Δ_{spin} with increasing N_{MAX} implies that mixing of higher-lying orbits is important for reproducing the $\Delta_{spin} > 0$ values.

The observed positive Δ_{spin} value implies that deuteron-like correlated *np* pairs are formed in the ground state of the target nuclei. Note that Δ_{spin} takes a value of 1/4 for the IS *np* pair like a deuteron, −3/4 for the IV *np* pair, and zero for uncorrelated *np* pairs. Thus the IS *np* pairs are favored over the IV *np* pairs. It would be interesting to see how Δ_{spin} values are predicated by ab initio calculations (Gysbers et al., 2019) that reproduce the GT transition strengths studied by beta-decay without a quenching factor by introducing the contribution from the two-body current and many-body correlations. The finding would have relevance to the observed *np* pair dominance in the correlated *NN* pairs with high relative momentum in nuclei observed by electron scattering (Subedi et al., 2008; Hen et al., 2014; Hen et al., 2017) or by ^{16}O(p, d) reactions (Ong et al., 2013; Terashima et al., 2018). The electron scattering data probe all the components of the correlated *NN* pairs due to the high incident energy of the electrons without limitation placed on the excitation energy of the residual nucleus after knockout of a correlated *NN* pair. In contrast, the ^{16}O(p, d) data would be relevant to the *NN* pairs at around the Fermi surface of the target nucleus since the excitation energy of the residual nucleus is limited in the region of several MeV. The present experimental data of Δ_{spin} (E_x) are also limited to 16 MeV and thus are considered to be sensitive to the spin-spin correlation in the *np* pairs at around the Fermi surface. The spin-aligned IS *np* coupling of the valence particles in ^{92}Pd was studied from the level structure determined by gamma spectroscopy (Cederwall et al., 2011), which also indicates the effect of IS *np* pairs at around the Fermi surface. It would be interesting to extend the study of Δ_{spin} (E_x) to higher-excitation energies to observe how the *np* spin-spin correlation changes in deeper single particle orbits.

6 SUMMARY

In summary, spin-$M1$ excitation in nuclei is important for the study of NC neutrino reactions in astrophysical phenomena and in neutrino detectors. Quenching of the IS and IV spin-$M1$ SNMEs for $N = Z$ sd-shell nuclei has been studied by high energy-resolution measurement of proton inelastic scattering up to the excitation energy of 16 MeV. No quenching of the IS spin-$M1$ SNMEs has been observed in the measured nuclei, while the IV spin-$M1$ SNMEs are quenched by an amount comparable with the analogous GT transitions. Consistency with the study of the IS and IV magnetic moment in the same mass region has been discussed. It has been shown by applying the sum rule values that the difference of the IS and IV spin-$M1$ SNMEs is relevant to the np spin-spin correlation in the ground state. Thus, quenching of the IS and IV spin-$M1$ SNMEs needs to be described in a mutually consistent manner by theoretical models. The np spin-spin correlation would have a relevance to the correlated np pair with high relative momentum studied by electron scattering and (p, d) reactions as well as to the spin-aligned IS np coupling. It would be of interest to extend the present study to higher excitation energies and to mass and isotope dependencies. For example, decomposition of the spin-M1 strength in the continuum might be applicable by the multipole decomposition analysis of the angular distribution in combination with an isoscalar probe like deuteron scattering or with a pure isovector probe like (p, n). It is worth considering the measurement of $(^{12}\mathrm{C},^{12}\mathrm{C}^{*})$ reactions for studying each of the IS and IV spin-flip excitations of the target nucleus by tagging the IS and IV 1^{+} states of the ejectile with the coincidence detection of the α or γ emission. Also a measurement in inverse kinematics with an active target based on a time projection chamber would be able to extend the study to larger masses than 40 by employing radioactive secondary beams.

We note that a theoretical work (Isacker and Macchiavelli, 2021) appeared during the review process of this article. That study reported that the positive Δ_{spin} values, referred as $\langle \vec{S}_n \cdot \vec{S}_p \rangle$ in their paper, were not reproduced by Hamiltonian for all the possible parameter values describing neutrons and protons interacting in a single-l shell through a surface delta interaction. Theoretical interpretation of the positive values is still an open question.

DATA AVAILABILITY STATEMENT

The raw data supporting the conclusions of this article will be made available by the authors, without undue reservation.

AUTHOR CONTRIBUTIONS

All authors listed have made a substantial, direct, and intellectual contribution to the work and approved it for publication.

FUNDING

This work was supported by the JSPS International Training Program (ITP) and was partially supported by JSPS (No. 14740154, and 25105509).

ACKNOWLEDGMENTS

The authors gratefully acknowledge the collaborators of the E249 and E299 experiments at the RCNP. They are indebted to the RCNP cyclotron staff for providing us with the excellent beam. We are grateful to Sagawa, Nakada, and Ichimura for valuable discussions.

REFERENCES

Alburger, D. E., and Nathan, A. M. (1978). Beta-Ray Branching and Half-Lives of ^{12}B and ^{12}N. *Phys. Rev. C* 17, 280–286. doi:10.1103/PhysRevC.17.280

Anantaraman, N., Brown, B. A., Crawley, G. M., Galonsky, A., Djalali, C., Marty, N., et al. (1984). Observation of Quenching in Isoscalar and Isovector 0+ → 1+ Transitions in Si28(p,p′). *Phys. Rev. Lett.* 52, 1409–1412. doi:10.1103/PhysRevLett.52.1409

Anderson, B. D., Chittrakarn, T., Baldwin, A. R., Lebo, C., Madey, R., Tandy, P. C., et al. (1987). Gamow-Teller and M1 Strength in the 32S(p,n)32Cl Reaction at 135 Mev. *Phys. Rev. C. Nucl. Phys.* 36, 2195–2205. doi:10.1103/physrevc.36.2195

Arima, A., Shimizu, K., Bentz, W., and Hyuga, H. (1987). Nuclear Magnetic Properties and Gamow-Teller Transitions. *Adv. Nucl. Phys.* 18, 1–106.

Bendel, W. L., Fagg, L. W., Numrich, S. K., Jones, E. C., and Kaiser, H. F. (1971). Excitation of by 180 Electron Scattering. *Phys. Rev. C* 3, 1821–1827. doi:10.1103/PhysRevC.3.1821

Bernabéu, J., Ericson, T., Hernández, E., and Ros, J. (1992). Effects of the Axial Isoscalar Neutral-Current for Solar Neutrino Detection. *Nucl. Phys. B* 378, 131–149. doi:10.1016/0550-3213(92)90006-W

Birkhan, J., Matsubara, H., von Neumann-Cosel, P., Pietralla, N., Ponomarev, V. Y., Richter, A., et al. (2016). Electromagnetic M 1 Transition Strengths from Inelastic Proton Scattering: The Cases of ca 48 and pb 208. *Phys. Rev. C* 93, 041302. doi:10.1103/PhysRevC.93.041302

Brown, B., and Rae, W. (2014). The Shell-Model Code Nushellx@msu. *Nucl. Data Sheets* 120, 115–118. doi:10.1016/j.nds.2014.07.022

Brown, B., and Wildenthal, B. (1987). Empirically Optimum m1 Operator for sd-Shell Nuclei. *Nucl. Phys. A* 474, 290–306. doi:10.1016/0375-9474(87)90619-1

Brown, B. A., and Richter, W. A. (2006). New "usd" Hamiltonians for the *sd* Shell. *Phys. Rev. C* 74, 034315. doi:10.1103/PhysRevC.74.034315

Brown, B. A., and Wildenthal, B. H. (1983). Corrections to the Free-Nucleon Values of the Single-Particle Matrix Elements of the $m1$ and Gamow-Teller Operators, From a Comparison of Shell-Model Predictions With -Shell Data. *Phys. Rev. C* 28, 2397–2413. doi:10.1103/PhysRevC.28.2397

Cederwall, B., Moradi, F. G., Bäck, T., Johnson, A., Blomqvist, J., Clément, E., et al. (2011). Evidence for a Spin-Aligned Neutron–Proton Paired Phase From the Level Structure of 92 pd. *Nature* 469, 68–71. doi:10.1038/nature09644

Cohen, S., and Kurath, D. (1965). Effective Interactions for the 1p Shell. *Nucl. Phys.* 73, 1–24. doi:10.1016/0029-5582(65)90148-3

Cooper, E. D., Hama, S., and Clark, B. C. (2009). Global Dirac Optical Potential from Helium to lead. *Phys. Rev. C* 80, 034605. doi:10.1103/PhysRevC.80.034605

Crawley, G. M., Djalali, C., Marty, N., Morlet, M., Willis, A., Anantaraman, N., et al. (1989). Isovector and Isoscalar Spin-Flip Excitations in Even-Even s-d Shell Nuclei Excited by Inelastic Proton Scattering. *Phys. Rev. C* 39, 311–323. doi:10.1103/PhysRevC.39.311

Edmonds, A. (1960). *Angular Momentum in Quantum Mechanics*. Princeton, NJ: Princeton University Press.

Entem, D. R., and Machleidt, R. (2003). Accurate Charge-Dependent Nucleon-Nucleon Potential at Fourth Order of Chiral Perturbation Theory. *Phys. Rev. C* 68, 041001. doi:10.1103/PhysRevC.68.041001

Firestone, R. (1996). *Table of Isotopes*. 8th Edn. New York: John Wiley & Sons.

Foltz, C. W., Sober, D. I., Fagg, L. W., Gräf, H. D., Richter, A., Spamer, E., et al. (1994). Electroexcitation of Low-Multipolarity Magnetic Transitions in ^{36}Ar and ^{38}Ar. *Phys. Rev. C* 49, 1359–1371. doi:10.1103/PhysRevC.49.1359

Franey, M. A., and Love, W. G. (1985). Nucleon-Nucleon t-Matrix Interaction for Scattering at Intermediate Energies. *Phys. Rev. C* 31, 488–498. doi:10.1103/PhysRevC.31.488

Fujita, H., Fujita, Y., Adachi, T., Bacher, A. D., Berg, G. P. A., Black, T., et al. (2007). Isospin Structure of States in ^{58}Ni and ^{58}Cu Studied by ^{58}Ni(p, p') and ^{58}Ni(^{3}He,t)^{58}Cu Measurements. *Phys. Rev. C* 75, 034310. doi:10.1103/PhysRevC.75.034310

Fujita, H., Fujita, Y., Berg, G., Bacher, A., Foster, C., Hara, K., et al. (2002). Realization of Matching Conditions for High-Resolution Spectrometers. *Nucl. Instr. Methods Phys. Res. A: Acc. Spectr. Detect. Assoc. Equip.* 484, 17–26. doi:10.1016/S0168-9002(01)01970-2

Fujita, Y., Brown, B. A., Ejiri, H., Katori, K., Mizutori, S., and Ueno, H. (2000). Separation of Isoscalar, Isovector, Orbital, and Spin Contributions in Transitions in Mirror Nuclei. *Phys. Rev. C* 62, 044314. doi:10.1103/PhysRevC.62.044314

Fujita, Y., Fujita, H., Adachi, T., Berg, G. P. A., Caurier, E., Fujimura, H., et al. (2002). Gamow-Teller Transitions From ^{58}Ni to Discrete States of ^{58}Cu - The Study of Isospin Symmetry in Atomic Nuclei. *Eur. Phys. J. A.* 13, 411–418. doi:10.1140/epja/iepja1344

Fujita, Y., Hatanaka, K., Berg, G., Hosono, K., Matsuoka, N., Morinobu, S., et al. (1997). Matching of a Beam Line and a Spectrometer New Beam Line Project at rcnp. *Nucl. Instr. Methods Phys. Res. B: Beam Inter. Mater. Atoms* 126, 274–278. doi:10.1016/S0168-583X(96)01008-7

Fujita, Y., Rubio, B., and Gelletly, W. (2011). Spin-Isospin Excitations Probed by Strong, Weak and Electro-Magnetic Interactions. *Prog. Part. Nucl. Phys.* 66, 549–606. doi:10.1016/j.ppnp.2011.01.056

Fujiwara, M., Akimune, H., Daito, I., Fujimura, H., Fujita, Y., Hatanaka, K., et al. (1999). Magnetic Spectrometer Grand Raiden. *Nucl. Instr. Methods Phys. Res. A* 422, 484–488. doi:10.1016/S0168-9002(98)01009-2

Gysbers, P., Hagen, G., Holt, J., Jansen, G. R., Morris, T. D., Navrátil, P., et al. (2019). Discrepancy Between Experimental and Theoretical β-Decay Rates Resolved From First Principles. *Nat. Phys.* 15, 428–431. doi:10.1038/s41567-019-0450-7

Hen, O., Miller, G. A., Piasetzky, E., and Weinstein, L. B. (2017). Nucleon-Nucleon Correlations, Short-Lived Excitations, and the Quarks Within. *Rev. Mod. Phys.* 89, 045002. doi:10.1103/RevModPhys.89.045002

Hen, O., Sargsian, M., Weinstein, L. B., Piasetzky, E., Hakobyan, H., Higinbotham, D. W., et al. (2014). Momentum Sharing in Imbalanced Fermi Systems. *Science* 346, 614–617. doi:10.1126/science.1256785

Hofmann, F., von Neumann-Cosel, P., Neumeyer, F., Rangacharyulu, C., Reitz, B., Richter, A., et al. (2002). Magnetic Dipole Transitions in ^{32}S From Electron Scattering at 180. *Phys. Rev. C* 65, 024311. doi:10.1103/PhysRevC.65.024311

Ichimura, M., Sakai, H., and Wakasa, T. (2006). Spin-Isospin Responses via (p,n) and (n,p) Reactions. *Prog. Part. Nucl. Phys.* 56, 446–531. doi:10.1016/j.ppnp.2005.09.001

Ikeda, K., Fujii, S., and Fujita, J. (1963). The (p,n) Reactions and Beta Decays. *Phys. Lett.* 3, 271–272. doi:10.1016/0031-9163(63)90255-5

Isacker, P. V., and Macchiavelli, A. (2021). Neutron-proton Spin-Spin Correlations in the Ground States of Nuclei. *Eur. Phys. J.* 57, 178. doi:10.1140/epja/s10050-021-00489-6

Kawabata, T., Akimune, H., Fujimura, H., Fujita, H., Fujita, Y., Fujiwara, M., et al. (2004). Isovector and Isoscalar Spin-Flip Strengths in ^{11}B. *Phys. Rev. C* 70, 034318. doi:10.1103/PhysRevC.70.034318

Kirson, M. W. (2007). Oscillator Parameters in Nuclei. *Nucl. Phys. A* 781, 350–362. doi:10.1016/j.nuclphysa.2006.10.077

Love, W. G., and Franey, M. A. (1981). Effective Nucleon-Nucleon Interaction for Scattering at Intermediate Energies. *Phys. Rev. C* 24, 1073–1094. doi:10.1103/PhysRevC.24.1073

Lüttge, C., Neumann-Cosel, Pv., Neumeyer, F., Rangacharyulu, C., Richter, A., Schrieder, G., et al. (1996). Isovector m1 Transitions in and the Role of Meson Exchange Currents. *Phys. Rev. C* 53, 127–130. doi:10.1103/PhysRevC.53.127

Mathy, M., Birkhan, J., Matsubara, H., von Neumann-Cosel, P., Pietralla, N., Ponomarev, V. Y., et al. (2017). Search for Weak m 1 Transitions in ca 48 With Inelastic Proton Scattering. *Phys. Rev. C* 95, 054316. doi:10.1103/PhysRevC.95.054316

Matsubara, H. (2010). Isoscalar and isovector spin-M1 transitions from the even-even, N = Z nuclei across the sd-shell region. PhD thesis. Toyonaka: Osaka University.

Matsubara, H., Sakaguchi, H., Kishi, T., and Tamii, A. (2009). Self-supporting Elemental Sulfur Target for Charged Particle Irradiation. *Nucl. Instr. Methods Phys. Res. B* 267, 3682–3687. doi:10.1016/j.nimb.2009.09.002

Matsubara, H., Tamii, A., Nakada, H., Adachi, T., Carter, J., Dozono, M., et al. (2015). Nonquenched Isoscalar Spin- Excitations in -Shell Nuclei. *Phys. Rev. Lett.* 115, 102501. doi:10.1103/PhysRevLett.115.102501

Matsubara, H., Tamii, A., Shimizu, Y., Suda, K., Tameshige, Y., and Zenihiro, J. (2012). Wide-Window Gas Target System for High Resolution experiment with Magnetic Spectrometer. *Nucl. Instr. Methods Phys. Res. A* 678, 122–129. doi:10.1016/j.nima.2012.03.005

Ong, H., Tanihata, I., Tamii, A., Myo, T., Ogata, K., Fukuda, M., et al. (2013). Probing Effect of Tensor Interactions in 16o via (p,d) Reaction. *Phys. Lett. B* 725, 277–281. doi:10.1016/j.physletb.2013.07.038

Petrovich, F., and Love, W. (1981). The Scattering of Elementary Probes From Nuclei at Medium Energy: A New Look at the Nucleus. *Nucl. Phys. A* 354, 499–534. doi:10.1016/0375-9474(81)90613-8

Pudliner, B. S., Pandharipande, V. R., Carlson, J., Pieper, S. C., and Wiringa, R. B. (1997). Quantum Monte Carlo Calculations of Nuclei With A <= 7. *Phys. Rev. C* 56, 1720–1750. doi:10.1103/PhysRevC.56.1720

Raynal, J. (2007). Computer Code dwba07. Report No. NEA-1209/008.

Richter, A., Weiss, A., Haüsser, O., and Brown, B. A. (1990). New Evidence for Meson-Exchange-Current Enhancement of Isovector M1 Strength. *Phys. Rev. Lett.* 65, 2519–2522. doi:10.1103/PhysRevLett.65.2519

Richter, W. A., Mkhize, S., and Brown, B. A. (2008). *sd*-Shell Observables for the usda and usdb Hamiltonians. *Phys. Rev. C* 78–064302. doi:10.1103/PhysRevC.78.064302

Roth, R., Neff, T., and Feldmeier, H. (2010). Nuclear Structure in the Framework of the Unitary Correlation Operator Method. *Prog. Part. Nucl. Phys.* 65, 50–93. doi:10.1016/j.ppnp.2010.02.003

Sagawa, H., and Suzuki, T. (2018). Isoscalar and Isovector Spin Response in -Shell Nuclei. *Phys. Rev. C* 97, 054333. doi:10.1103/PhysRevC.97.054333

Sagawa, H., Suzuki, T., and Sasano, M. (2016). Effect of Isoscalar Spin-Triplet Pairings on Spin-Isospin Responses in s d-Shell Nuclei. *Phys. Rev. C* 94, 041303. doi:10.1103/PhysRevC.94.041303

Sasano, M., Sakai, H., Yako, K., Wakasa, T., Asaji, S., Fujita, K., et al. (2009). Gamow-teller Unit Cross Sections of the Reaction at 198 and 297 mev on Medium-Heavy Nuclei. *Phys. Rev. C* 79, 024602. doi:10.1103/PhysRevC.79.024602

Subedi, R., Shneor, R., Monaghan, P., Anderson, B., Aniol, K., Annand, J., et al. (2008). Probing Cold Dense Nuclear Matter. *Science* 320, 1476–1478. doi:10.1126/science.1156675

Suzuki, T., Fujimoto, R., and Otsuka, T. (2003). Gamow-Teller Transitions and Magnetic Properties of Nuclei and Shell Evolution. *Phys. Rev. C* 67, 044302. doi:10.1103/PhysRevC.67.044302

Suzuki, Y., Horiuchi, W., Orabi, M., and Arai, K. (2008). Global-vector Representation of the Angular Motion of Few-Particle Systems ii. *Few-Body Syst.* 42. doi:10.1007/s00601-008-0200-3

Taddeucci, T., Goulding, C., Carey, T., Byrd, R., Goodman, C., Gaarde, C., et al. (1987). The (p,n) Reaction as a Probe of Beta Decay Strength. *Nucl. Phys. A* 469, 125–172. doi:10.1016/0375-9474(87)90089-3

Taddeucci, T. N., Byrd, R. C., Carey, T. A., Ciskowski, D. E., Foster, C. C., Gaarde, C., et al. (1990). Gamow-teller Transition Strengths from the ^{11}B(p,nc) Reaction in the Energy Range 160–795 mev. *Phys. Rev. C* 42, 935–946. doi:10.1103/PhysRevC.42.935

Tamagaki, R. (1968). Potential Models of Nuclear Forces at Small Distances. *Prog. Theor. Phys.* 39, 91–107. doi:10.1143/PTP.39.91

Tamii, A., Akimune, H., Daito, I., Fujita, Y., Fujiwara, M., Hatanaka, K., et al. (1999). Polarization Transfer Observables for Proton Inelastic Scattering from 12c at 0. *Phys. Lett. B* 459, 61–66. doi:10.1016/S0370-2693(99)00654-1

Tamii, A., Fujita, Y., Matsubara, H., Adachi, T., Carter, J., Dozono, M., et al. (2009). Measurement of High Energy Resolution Inelastic Proton Scattering at and Close to Zero Degrees. *Nucl. Instrum.Methods Phys. Res. Sect. A.* 605, 326–338. doi:10.1016/j.nima.2009.03.248

Terashima, S., Yu, L., Ong, H. J., Tanihata, I., Adachi, S., Aoi, N., et al. (2018). Dominance of Tensor Correlations in High-Momentum Nucleon Pairs Studied by Reaction. *Phys. Rev. Lett.* 121, 242501. doi:10.1103/PhysRevLett.121.242501

Towner, I., and Khanna, F. (1983). Corrections to the Single-Particle m1 and Gamow-Teller Matrix Elements. *Nucl. Phys. A* 399, 334–364. doi:10.1016/0375-9474(83)90252-X

Towner, I. (1987). Quenching of Spin Matrix Elements in Nuclei. *Phys. Rep.* 155, 263–377. doi:10.1016/0370-1573(87)90138-4

von Neumann-Cosel, P., and Tamii, A. (2019). Electric and Magnetic Dipole Modes in High-Resolution Inelastic Proton Scattering at 0. *Eur. Phys. J. A* 55. doi:10.1140/epja/i2019-12781-7

von Neumann-Cosel, P., Gräf, H. D., Krämer, U., Richter, A., and Spamer, E. (2000). Electroexcitation of Isoscalar and Isovector Magnetic Dipole Transitions in 12c and Isospin Mixing. *Nucl. Phys. A* 669 3–13. doi:10.1016/S0375-9474(99)00564-3

Wakasa, T., Hatanaka, K., Fujita, Y., Berg, G., Fujimura, H., Fujita, H., et al. (2002). High Resolution Beam Line for the Grand Raiden Spectrometer. *Nucl. Instr. Methods Phys. Res. A* 482, 79–93. doi:10.1016/S0168-9002(01)01686-2

Warburton, E. K., and Millener, D. J. (1989). Structure of ^{17}C and ^{17}N. *Phys. Rev. C* 39, 1120–1129. doi:10.1103/PhysRevC.39.1120

Zegers, R. G. T., Akimune, H., Austin, S. M., Bazin, D., van der Berg, A. M., Berg, G. P. A., et al. (2006). The (t,^{3}He) and (^{3}He,t) Reactions as Probes of Gamow-Teller Strength. *Phys. Rev. C* 74, 024309. doi:10.1103/PhysRevC.74.024309

Conflict of Interest: The authors declare that the research was conducted in the absence of any commercial or financial relationships that could be construed as a potential conflict of interest.

The handling editor declared a past co-authorship with one of the authors AT.

frontiers in Astronomy and Space Sciences

ORIGINAL RESEARCH
published: 19 November 2021
doi: 10.3389/fspas.2021.727880

Interacting Shell Model Calculations for Neutrinoless Double Beta Decay of ^{82}Se With Left-Right Weak Boson Exchange

Yoritaka Iwata[1]* *and Shahariar Sarkar*[2]

[1]Faculty of Chemistry, Materials and Bioengineering, Kansai University, Osaka, Japan, [2]Indian Institute of Technology Ropar, Rupnagar, India

In the present work, the λ mechanism (left-right weak boson exchange) and the light neutrino-exchange mechanism of neutrinoless double beta decay is studied. In particular, much attention is paid to the calculation of nuclear matrix elements for one of the neutrinoless double beta decaying isotopes ^{82}Se. The interacting shell model framework is used to calculate the nuclear matrix element. The widely used closure approximation is adopted. The higher-order effect of the pseudoscalar term of nucleon current is also included in some of the nuclear matrix elements that result in larger Gamow-Teller matrix elements for the λ mechanism. Bounds on Majorana neutrino mass and lepton number violating parameters are also derived using the calculated nuclear matrix elements.

Keywords: neutrinoless double beta decay, λ mechanism, nuclear shell model, nuclear matrix element, right-handed weak boson

OPEN ACCESS

Edited by:
Hiroyasu Ejiri,
Research Center for Nuclear Physics, Osaka University, Japan

Reviewed by:
Bhupal Dev,
Washington University in St. Louis, United States
J.D. Vergados,
University of Ioannina, Greece
Javier Menendez,
University of Barcelona, Spain

****Correspondence:***
Yoritaka Iwata
iwata_phys@08.alumni.u-tokyo.ac.jp

Specialty section:
This article was submitted to High-Energy and Astroparticle Physics, a section of the journal Frontiers in Astronomy and Space Sciences

Received: *20 June 2021*
Accepted: *30 August 2021*
Published: *19 November 2021*

Citation:
Iwata Y and Sarkar S (2021) Interacting Shell Model Calculations for Neutrinoless Double Beta Decay of ^{82}Se With Left-Right Weak Boson Exchange. Front. Astron. Space Sci. 8:727880. doi: 10.3389/fspas.2021.727880

1 INTRODUCTION

Neutrinoless double beta decay ($0\nu\beta\beta$) is a rare second-order weak nuclear process. In this process, neutrino comes as a virtual intermediate particle when two neutron pairs decay into two proton pairs inside some even-even nuclei. Thus, it violates the lepton number by two units. The $0\nu\beta\beta$ experiment is one of the possible ways to determine the effective neutrino mass (Schechter and Valle, 1982; Tomoda, 1991; Avignone et al., 2008; Rodejohann, 2011; Deppisch et al., 2012) and can help to solve many mysteries of neutrinos, such as whether neutrinos are their own anti-particle (Majorana neutrino) or not (Dirac neutrino) (Schechter and Valle, 1982; Rodejohann, 2011; Deppisch et al., 2012).

As lepton number conservation is not exact in most of the beyond the standard model (BSM) physics theories, many particle mechanisms of $0\nu\beta\beta$ have been proposed in different BSM theories such as light neutrino-exchange mechanism (Šimkovic et al., 1999; Rodin et al., 2006), heavy neutrino-exchange mechanism (Vergados et al., 2012), left-right symmetric mechanism (Mohapatra and Senjanović, 1980; Mohapatra and Vergados, 1981), and the supersymmetric particles exchange mechanism (Mohapatra, 1986; Vergados, 1987).

The decay rate for any particle mechanism of $0\nu\beta\beta$ is connected by nuclear matrix elements (NMEs) and absolute neutrino mass. These NMEs are calculated using theoretical nuclear many-body models (Engel and Menéndez, 2017). Popular nuclear models are quasiparticle random phase approximation (QRPA) (Vergados et al., 2012), the interacting shell-model (ISM) (Caurier et al., 2008; Horoi and Stoica, 2010; Sen'kov and Horoi, 2013; Brown et al., 2014; Iwata et al., 2016),

the interacting boson model (IBM) (Barea and Iachello, 2009; Barea et al., 2012), the generator coordinate method (GCM) (Rodríguez and Martínez-Pinedo, 2010), the energy density functional (EDF) theory (Rodríguez and Martínez-Pinedo, 2010; Song et al., 2014), and the projected Hartree-Fock Bogolibov model (PHFB) (Rath et al., 2010). Other techniques includes, *ab initio* calculations for lower mass nuclei (A = 6–12) using variational Monte Carlo (VMC) method (Pastore et al., 2018; Cirigliano et al., 2019; Wang et al., 2019).

In the present work, we focus on the left-right weak boson (W_L-W_R) exchange λ mechanism along with the standard light neutrino-exchange mechanism ($W_L - W_L$ exchange) of the $0\nu\beta\beta$ mediated by light neutrinos (Bhupal Dev et al., 2015; Horoi and Neacsu, 2016; Šimkovic et al., 2017). The λ mechanism has origin in the left-right symmetric mechanism with right-handed gauge boson at the TeV scale (Šimkovic et al., 2017). Thus, it will be interesting to study how the λ mechanism can compete with the standard light neutrino-exchange mechanism when both the mechanisms co-exist. Hence, in the present work, we are eager to study the λ and light neutrino-exchange mechanisms together.

In left-right symmetric model, there is another mass independent mechanism called η mechanism which occurs through $W_L - W_R$ mixing. It will be interesting to study η mechanism along with λ mechanism of $0\nu\beta\beta$. But, η mechanism is suppressed due to $W_L - W_R$ mixing as compared to λ mechanism (Barry and Rodejohann, 2013). Hence, in the present work, we are interested to study the mass independent λ mechanism along with the mass dependent standard light neutrino-exchange mechanism. In future studies, we will extensively explore the η mechanism of $0\nu\beta\beta$ along with other mass independent and dependent mechanisms in left-right symmetric model.

One of the motivations of the present work is to include effects of some of the revisited formalism of Ref. (Štefánik et al., 2015) on light neutrino-exchange and λ mechanism of $0\nu\beta\beta$. The revised formalism was exploited to include the effects of the pseudoscalar term of nucleon currents. Using the revised formalism of Ref. (Štefánik et al., 2015), the NMEs for λ, and light neutrino-exchange mechanisms of $0\nu\beta\beta$ are calculated using the QRPA model for several $0\nu\beta\beta$ decaying isotopes using closure approximation in Ref. (Šimkovic et al., 2017). Most of the NMEs relevant for λ and light neutrino-exchange mechanisms are also calculated using ISM in Ref. (Horoi and Neacsu, 2018) using the closure approximation for different $0\nu\beta\beta$ decaying isotopes (including ^{82}Se). In this case, some of the NMEs are calculated without including the higher-order terms (for example, pseudoscalar and weak magnetism terms) of the nucleon currents. Recently, using the revised formalism of Ref. (Štefánik et al., 2015), we have also calculated the NMEs for ^{48}Ca in Ref. (Sarkar et al., 2020a) using the non-closure approximation and found a significant change in some of the NMEs for including the pseudoscalar term. Thus, we have tried here to include the revised higher-order effect of the pseudoscalar term of nucleon current for the λ mechanism of $0\nu\beta\beta$ of ^{82}Se using ISM. The $0\nu\beta\beta$ of ^{82}Se is one of the experimental interests of CUPID (Dolinski et al., 2019; Pagnanini et al., 2019) and NEMO-3 (Arnold et al., 2020) experiments. Hence, it is important to study the nuclear structure aspects of $0\nu\beta\beta$ of ^{82}Se theoretically. In recent years, one of the most important studies on light neutrino-exchange $0\nu\beta\beta$ of ^{82}Se was performed in the ISM framework in Ref. (Sen'kov et al., 2014) using the non-closure approximation. Here we focus on the λ mechanism of $0\nu\beta\beta$ of ^{82}Se in the closure approximation using the revised nucleon current term.

This paper is organized as follows. In **Section 2**, the expression for decay rate and the theoretical formalism to calculate NMEs for the λ and light neutrino-exchange mechanisms of $0\nu\beta\beta$ are presented. The results and discussion are presented in **Section 3**. A summary of the work is given in **Section 4**.

2 THEORETICAL FRAMEWORK

2.1 Decay Rate for λ Mechanism of $0\nu\beta\beta$

If both light neutrino-exchange ($W_L - W_L$ exchange) and λ mechanisms ($W_L - W_R$ exchange) of $0\nu\beta\beta$ co-exist, one can write the decay rate for $0\nu\beta\beta$ as (Štefánik et al., 2015; Šimkovic et al., 2017)

$$[T^{0\nu}_{1/2}]^{-1} = \eta_\nu^2 C_{mm} + \eta_\lambda^2 C_{\lambda\lambda} + \eta_\nu \eta_\lambda \cos\psi C_{m\lambda}, \tag{1}$$

where the coupling constant λ is defined as (Šimkovic et al., 2017)

$$\lambda = \left(M_{W_L}/M_{W_R}\right)^2. \tag{2}$$

The M_{W_L} and M_{W_R} are masses of the Standard Model left-handed W_L and right-handed W_R gauge bosons, respectively. The η_ν of **Eq. 1** is an effective lepton number violating parameters for $W_L - W_L$ exchange, η_λ is an effective lepton number violating parameters for $W_L - W_R$ exchange, and ψ denotes the CP violating phase. These parameters are given in Ref. (Šimkovic et al., 2017) as

$$\eta_\nu = \frac{m_{\beta\beta}}{m_e}, \quad \eta_\lambda = \lambda \left| \sum_{j=1}^{3} m_j U_{ej} T^*_{ej} \right|, \tag{3}$$

$$\psi = \arg\left[\left(\sum_{j=1}^{3} m_j U^2_{ej} \right) \left(\sum_{j=1}^{3} U_{ej} T^*_{ej} \right) \right]. \tag{4}$$

Here, $m_{\beta\beta}$ is the effective Majorana neutrino mass defined by the neutrino mass eigenvalues m_j and the neutrino mixing matrix elements U_{ej} (Horoi and Stoica, 2010):

$$\langle m_{\beta\beta} \rangle = \left| \sum_j m_j U^2_{ej} \right|. \tag{5}$$

The U, and T are the 3×3 block matrices in flavor space, which constitute a generalization of the Pontecorvo-Maki-Nakagawa-Sakata matrix, namely the 6×6 unitary neutrino mixing matrix (Štefánik et al., 2015; Šimkovic et al., 2017).

The amplitude of λ mechanism is given by (Bhupal Dev et al., 2015)

$$\mathcal{A}_\lambda = G_F^2 \lambda \sum_i U_{ej} T^*_{ej} \frac{1}{q}, \tag{6}$$

where λ is defined earlier, G_F is the Fermi constant for weak interaction, and q is the virtual Majorana neutrino momentum.

The coefficients C_I ($I = mm$, $m\lambda$ and $\lambda\lambda$) of **Eq. 1** are linear combinations of products of nuclear matrix elements and phase-space factors (Šimkovic et al., 2017).

$$C_{mm} = g_A^4 M_\nu^2 G_{01}, \tag{7}$$

$$C_{m\lambda} = -g_A^4 M_\nu (M_{2-} G_{03} - M_{1+} G_{04}), \tag{8}$$

$$C_{\lambda\lambda} = g_A^4 \left(M_{2-}^2 G_{02} + \frac{1}{9} M_{1+}^2 G_{011} - \frac{2}{9} M_{1+} M_{2-} G_{010} \right). \tag{9}$$

Calculated values of phase-space factors G_{0i} (i = 1, 2, 3, 4, 10 and 11) for different $0\nu\beta\beta$ decaying nuclei are given in Ref. (Štefánik et al., 2015).

2.2 Nuclear Matrix Elements for λ Mechanism of $0\nu\beta\beta$

Matrix elements required in the expression of C_I are (Šimkovic et al., 2017).

$$M_\nu = M_{GT} - \frac{M_F}{g_A^2} + M_T, \tag{10}$$

$$M_{\nu\omega} = M_{\omega GT} - \frac{M_{\omega F}}{g_A^2} + M_{\omega T}, \tag{11}$$

$$M_{1+} = M_{qGT} + 3\frac{M_{qF}}{g_A^2} - 6M_{qT}, \tag{12}$$

$$M_{2-} = M_{\nu\omega} - \frac{1}{9} M_{1+}. \tag{13}$$

The $(M_{GT,\omega GT,qGT})$ $(M_{F,\omega F,qF})$, and $(M_{T,\omega T,qT})$ matrix elements of the scalar two-body transition operator $\mathcal{O}_{12}^\alpha$ of $0\nu\beta\beta$ can be expressed as (Brown et al., 2014)

$$M_\alpha = \langle f | \mathcal{O}_{12}^\alpha | i \rangle \tag{14}$$

where, $|i\rangle$, and $|f\rangle$ are the initial and the final 0^+ ground state (g.s) for $0\nu\beta\beta$ decay, respectively, and $\alpha = (GT, F, T, \nu, \omega GT, \omega F, \omega T, \nu\omega, qGT, qF, qT, 1+, 2-)$, τ_- is the isospin annihilation operator. The scalar two-particle transition operators $\mathcal{O}_{12}^\alpha$ of $0\nu\beta\beta$ containing spin and radial neutrino potential operators can be written as

$$\begin{aligned} \mathcal{O}_{12}^{GT,\omega GT,qGT} &= \tau_{1-}\tau_{2-} (\sigma_1.\sigma_2) H_{GT,\omega GT,qGT}(r, E_k), \\ \mathcal{O}_{12}^{F,\omega F,qF} &= \tau_{1-}\tau_{2-} H_{F,\omega F,qF}(r, E_k), \\ \mathcal{O}_{12}^{T,\omega T,qT} &= \tau_{1-}\tau_{2-} S_{12} H_{T,\omega T,qT}(r, E_k), \end{aligned} \tag{15}$$

where, $S_{12} = 3(\sigma_1.\hat{\mathbf{r}})(\sigma_2.\hat{\mathbf{r}}) - (\sigma_1.\sigma_2)$, $\mathbf{r} = \mathbf{r_1} - \mathbf{r_2}$, and $r = |\mathbf{r}|$ is inter nucleon distance of the decaying nucleons. The E_k is the energy of the virtual intermediate state ($|k\rangle$) of $0\nu\beta\beta$. The intermediate state $|k\rangle$ is achieved when one neutron from the initial state $|i\rangle$ is converted into one proton. Subsequently, from the $|k\rangle$ state, another neutron is converted into another proton to achieve the final state $|f\rangle$ of the $0\nu\beta\beta$. For the present manuscript, $|i\rangle$ is the 0^+ g.s. of ^{82}Se, $|f\rangle$ is the 0^+ g.s. of ^{82}Kr, and $|k\rangle$ are all the allowed spin-parity states of intermediate nucleus ^{82}Br.

There are two approximations for calculating the NME, one is non-closure approximation and another is the widely used closure approximation. In non-closure approximation, the radial neutrino potential $H_\alpha(r, E_k)$ has explicit dependence on energy of the intermediate state $|k\rangle$. In non-closure approximation, the radial neutrino potential for λ mechanism of $0\nu\beta\beta$ are is given as integral over Majorana neutrino momentum q (Sen'kov and Horoi, 2013):

$$H_\alpha(r, E_k) = \frac{2R}{\pi} \int_0^\infty \frac{f_\alpha(q, r) q dq}{q + E_k - (E_i + E_f)/2)} \tag{16}$$

where R is the radius of the parent nucleus, and the $f_\alpha(q, r)$ factor (**Appendix B**) contains the form factors that incorporates the effects of finite nucleon size (FNS), and higher-order currents (HOC) of nucleons (Šimkovic et al., 1999), which is given in **Appendix B** of the manuscript. The E_i and E_f are the g.s. energy of the initial and final nucleus of the $0\nu\beta\beta$ decay, respectively. The non-closure approximation is computationally very challenging, because in this approximation, the NME has explicit dependence on the energy of large numbers of virtual intermediate state $|k\rangle$ and calculating these states requires enormous computational power. Particularly, for higher mass region isotopes, some of the calculations are still beyond the reach of current generation's high-performance computers. Fortunately, the most of the contributions on NME of $0\nu\beta\beta$ come from low lying energy states up to 10–12 MeV of the intermediate nucleus (Sen'kov and Horoi, 2013; Sarkar et al., 2020a). Thus, one can replace the effects of E_k with a suitable constant energy called closure energy $\langle E \rangle$ without affecting the value of NME too much, and this approximation is known as closure approximation. In this approximation, one assumes (Sen'kov and Horoi, 2013)

$$(E_k - (E_i + E_f)/2) \to \langle E \rangle, \tag{17}$$

and the radial neutrino potential operator of **Eq. 16** becomes

$$H_\alpha(r) = \frac{2R}{\pi} \int_0^\infty \frac{f_\alpha(q, r) q dq}{q + \langle E \rangle}, \tag{18}$$

In closure approximation, the $0\nu\beta\beta$ decay operators defined in **Eq. 15** become

$$\begin{aligned} O_{12}^{GT,\omega GT,qGT} &= \tau_{1-}\tau_{2-} (\sigma_1.\sigma_2) H_{GT,\omega GT,qGT}(r), \\ O_{12}^{F,\omega F,qF} &= \tau_{1-}\tau_{2-} H_{F,\omega F,qF}(r), \\ O_{12}^{T,\omega T,qT} &= \tau_{1-}\tau_{2-} S_{12} H_{T,\omega T,qT}(r). \end{aligned} \tag{19}$$

The closure approximation is widely used in literature as it eliminates the complexity of calculating a large number of virtual intermediate states (Horoi and Stoica, 2010; Sen'kov and Horoi, 2013; Sarkar et al., 2020a). One can find suitable values of $\langle E \rangle$ using the method described in Ref. (Sarkar et al., 2020a), such that using closure approximation, one can get NME near to the non-closure approximation.

TABLE 1 | Parameters for the short-range correlation (SRC) parametrization of **Eq. 21**. Values are taken from Ref. (Horoi and Stoica, 2010).

SRC type	a	b	c
Miller-Spencer	1.10	0.68	1.00
CD-Bonn	1.52	1.88	0.46
AV18	1.59	1.45	0.92

In the calculation of the NME of $0\nu\beta\beta$, it is also necessary to take into account the effects of short-range correlations (SRC). A standard method to include SRC is via a phenomenological Jastrow-like function (Vogel, 2012; Menéndez et al., 2009; Šimkovic et al., 2009). Including SRC effect in the Jastrow approach, one can write the NME of $0\nu\beta\beta$ defined in **Eq. 14** as (Vogel, 2012)

$$M_\alpha = \langle f | f_{Jastrow}(r) O^\alpha_{12} f_{Jastrow}(r) | i \rangle, \tag{20}$$

where Jastrow-type SRC function is defined as

$$f_{Jastrow}(r) = 1 - ce^{-ar^2}(1 - br^2). \tag{21}$$

In literature, three different SRC prametrizationparameterization are used: Miller-Spencer, Charge-Dependent Bonn (CD-Bonn), and Argonne V18 (AV18) to parametrize a, b, and c (Horoi and Stoica, 2010). These parameters are chosen in such a way that the two-body wave function of two-body matrix elements (TBME) for $0\nu\beta\beta$ are still normalized. The parameters a, b, and c in different SRC parametrizations are given in **Table 1**.

This approach of using a Jastrow-like function to include the effects of SRC is extensively used in Refs. (Menéndez et al., 2009; Horoi and Stoica, 2010; Neacsu et al., 2012).

2.3 The Closure Method of Nuclear Matrix Elements Calculation for $0\nu\beta\beta$ in ISM

The $(M_{GT,\omega GT,qGT})$ $(M_{F,\omega F,qF})$, and $(M_{T,\omega T,qT})$ matrix elements of the scalar two-body transition operator O^α_{12} of $0\nu\beta\beta$ can be expressed as the sum over the product of the two-body transition density (TBTD) and anti-symmetric two-body matrix elements $(\langle k_1', k_2', JT | O^\alpha_{12} | k_1, k_2, JT \rangle_A)$ (Brown et al., 2014):

$$\begin{aligned} M^{0\nu}_\alpha &= \langle f | O^\alpha_{12} | i \rangle \\ &= \sum_{J, k_1' \le k_2, k_1 \le k_2} \mathrm{TBTD}(f, i, J) \times \langle k_1', k_2', JT | O^\alpha_{12} | k_1, k_2, JT \rangle_A, \end{aligned} \tag{22}$$

where, $\alpha = (F, GT, T, \omega F, \omega GT, \omega T, qF, qGT, qT)$, J is the coupled spin of two decaying neutrons or two final created protons, τ_- is the isospin annihilation operator, A denotes that the two-body matrix elements (TBME) (**Appendix A**) are obtained using anti-symmetric two-nucleon wavefunctions, and k_1 stands for the set of spherical quantum numbers $(n_1; l_1; j_1)$ (similar definition for k_2, k_1', k_2'). The $|i\rangle$ is 0^+ ground state (g.s.) of the parent nucleus, and $|f\rangle$ is the 0^+ g.s of the granddaughter nucleus.

The TBTD can be expressed as (Brown et al., 2014)

$$\mathbf{TBTD}(f, i, J) = \langle f \| [A^+(k_1', k_2', J) \otimes \tilde{A}(k_1, k_2, J)]^{(0)} \| i \rangle, \tag{23}$$

where,

$$A^+(k_1', k_2', J) = \frac{[a^+(k_1') \otimes a^+(k_2')]^J_M}{\sqrt{1 + \delta_{k_1' k_2'}}}, \tag{24}$$

and

$$\tilde{A}(k_1, k_2, J) = (-1)^{J-M} A^+(k_1, k_2, J, -M) \tag{25}$$

are the two particle creation and annihilation operator of rank J, respectively. Most of the available public shell model code does not provide the option to calculate TBTD directly. One of the ways is to calculate TBTD in terms of a large number of two nucleon transfer amplitudes (TNA), assuming $0\nu\beta\beta$ decay occurs through $(n - 2)$ channel (Brown et al., 2014). In $(n - 2)$ channel of $0\nu\beta\beta$, the TNA are calculated with a large set of intermediate states $|m\rangle$ of the $(n - 2)$ nucleons system, where n is the number of nucleons for the parent nucleus. In this approach, the TBTD in terms of TNA is expressed as (Brown et al., 2014)

$$\mathrm{TBTD}(f, i, J) = \sum_m \mathrm{TNA}(f, m, k_1', k_2', J_m) \mathrm{TNA}(i, m, k_1, k_2, J_m), \tag{26}$$

where, TNA are given by

$$\mathrm{TNA}(f, m, k_1', k_2', J_m) = \frac{\langle f \| A^+(k_1', k_2', J) \| m \rangle}{\sqrt{2J_0 + 1}}. \tag{27}$$

Here, J_m is the spin of the allowed states $|m\rangle$ of intermediate nuclei. J_0 is spin of $|i\rangle$ and $|f\rangle$. $J_m = J$ when $J_0 = 0$ (Brown et al., 2014).

3 RESULTS AND DISCUSSION

We have used *JUN*45 effective shell model Hamiltonian (Honma et al., 2009) of *fpg* model space to calculate the relevant initial, intermediate, and final nuclear states for $0\nu\beta\beta$ of ^{82}Se. In the *fpg* model space, valence nucleons can occupy the orbitals $0f_{5/2}$, $1p_{3/2}$, $1p_{1/2}$, and $0g_{9/2}$. For the $0\nu\beta\beta$ decay of ^{82}Se through $(n - 2)$ channel, the states of allowed spin-parity of ^{80}Se acts as intermediate states for TNA calculations. The nuclear shell model code KSHELL (Shimizu et al., 2019) was used in the calculation. For comparing some of the TNA values, NushellX@MSU (Brown and Rae, 2014) code was also used. In the present calculation, we have included the first 100 states of different allowed spin-parity of ^{80}Se in calculating the TNA. Earlier, it was found that considering around the first 50 states is enough to get the saturated value of NME, as the most dominating contributions come from the first few initial states (Brown et al., 2014; Sarkar et al., 2020b).

We have adopted the widely used closure approximation with the closure energy $\langle E \rangle = 0.5$ MeV. Earlier studies of Refs. (Sarkar et al., 2020a; Sarkar et al., 2020b) suggested that $\langle E \rangle = 0.5$ MeV is a suitable value that is close to optimal closure energy and, thus, gives NME near to the NME in the non-closure approximation.

TABLE 2 | NMEs for $0\nu\beta\beta$ (light neutrino-exchange and λ mechanism) of ^{82}Se.

NME Type	SRC Type			
	None	Miller-Spencer	CD-Bonn	AV18
M_F	−0.633	−0.442	−0.674	−0.621
M_{GT}	3.681	2.536	3.247	3.068
M_T	−0.020	−0.020	−0.020	−0.020
M_ν	3.529	2.790	3.645	3.433
$M_{\omega F}$	−0.630	−0.441	−0.671	−0.618
$M_{\omega GT}$	3.075	2.453	3.165	2.986
$M_{\omega T}$	−0.020	−0.020	−0.020	−0.020
$M_{\nu\omega}$	3.485	2.751	3.599	3.388
M_{qF}	−0.330	−0.274	−0.384	−0.372
M_{qGT}	11.667	10.167	12.538	12.184
M_{qT}	−0.097	−0.097	-0.097	−0.097
M_{1+}	11.636	10.241	12.409	12.076
M_{2-}	2.192	1.613	2.220	2.046

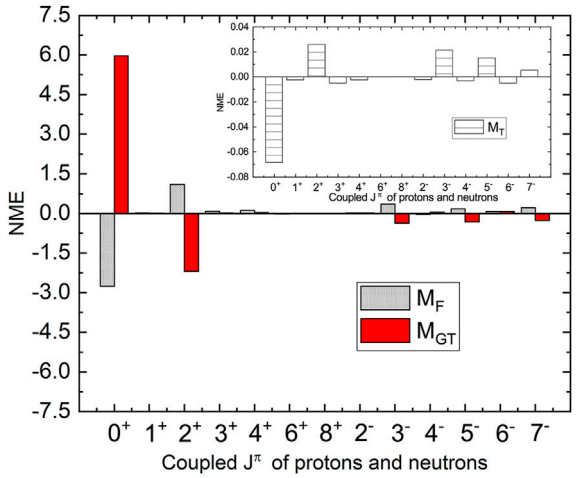

FIGURE 1 | (Color online) Variation of M_F, M_{GT}, and M_T type NMEs with J^π of two initial neutron-neutron and final proton-proton pairs.

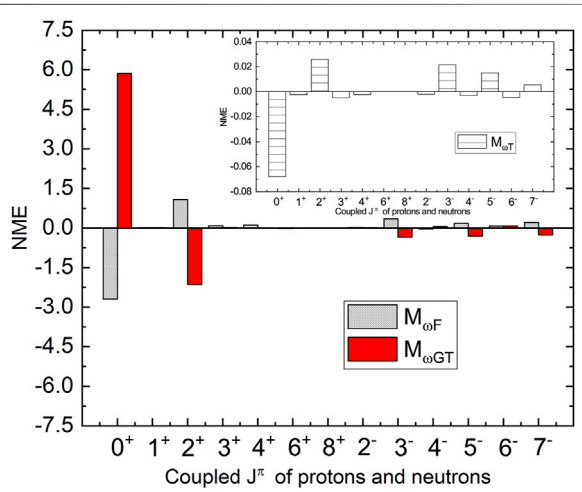

FIGURE 2 | (Color online) Variation of $M_{\omega F}$, $M_{\omega GT}$, and $M_{\omega T}$ type NMEs with J^π of two initial neutron-neutron and final proton-proton pairs.

The non-closure method can give the exact value of NME, but the present study is beyond the scope of studying it. But, according to earlier results (Sarkar et al., 2020a; Sarkar et al., 2020b), with $\langle E \rangle$ = 0.5 MeV, one can get NME in the closure approximation close to the NME in non-closure approximation (within 1% difference).

Different types of NMEs for light neutrino-exchange and λ mechanism of $0\nu\beta\beta$ for ^{82}Se is shown in **Table 2**. Here, NMEs are calculated in different SRC parameterization schemes. All standard effects of FNS + HOC are taken care of in all calculations. It is found that the Gamow-Teller matrix elements dominate over Fermi and tensor type matrix elements. Also, it is found that the M_{qGT} type matrix element associated with the λ mechanism is relatively large as compared to standard light neutrino-exchange Gamow-Teller matrix element M_{GT}. This leads to the large value of total NME M_{1+} for λ mechanism as compared to total NME M_ν for light neutrino-exchange mechanism.

This increment of M_{qGT} type of NME, which is obtained through the new revised expression of the nucleon currents of Ref. (Šimkovic et al., 2017), is surprisingly high. It is coming through the new revised expression of the nucleon currents of Ref. (Šimkovic et al., 2017) which includes the higher-order term (pseudoscalar) of the nucleon currents. In our calculation, **Eq. 39** is used to calculate M_{qGT} type NME using the revised formalism of nucleon currents of Refs. (Štefánik et al., 2015; Šimkovic et al., 2017).

An old equivalent expression of **Eq. 39** is also found in Ref. (Horoi and Neacsu, 2018), which one can write using Eq. (A2c) and Eq. (A4b) of Ref. (Horoi and Neacsu, 2018) as

$$f_{qGT}(q,r) = \frac{1}{\left(1+\frac{q^2}{\Lambda_A^2}\right)^4} qr\, j_1(qr). \tag{28}$$

Using this old value of $f_{qGT}(q, r)$, the M_{qGT} type NME will be significantly smaller, as reported earlier.

Here we include the higher-order current effect of pseudoscalar term in **Eq. 39** as suggested in Ref. (Šimkovic et al., 2017) which is enhancing the M_{qGT} type NME as compared to standard M_{GT} type NME. A similar type of enhancement in M_{qGT} type NME was also found in our earlier study for ^{48}Ca (Sarkar et al., 2020a).

We have also decomposed the NME in terms of coupled spin-parity (J^π) of two decaying neutrons and two created protons in the decay. Decomposed NME gives us a picture of the role of individual spin-parity on NME. The contribution of NMEs through different J^π is shown in **Figures 1–3** for different types of NME. **Figure 1** examines the decomposition for $M_{F,GT,T}$ type matrix elements associated with light neutrino-exchange mechanism, where **Figures 2**, **3** examine the NME as function of J^π for $M_{\omega F,\omega GT,\omega T}$ and $M_{qF,qGT,qT}$ type NMEs, respectively, for λ and interference mechanism. All results are presented for AV18 SRC parameterization.

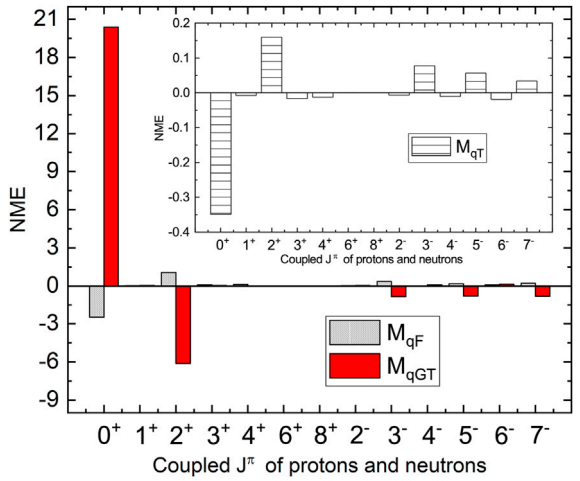

FIGURE 3 | (Color online) Variation of M_{qF}, M_{qGT}, and M_{qT} type NMEs with J^{π} of two initial neutron-neutron and final proton-proton pairs.

For all types of NMEs, the most dominating contribution comes from 0^+ states and 2^+ states. The pairing effect is in play for dominating even-J^{π} contributions (Brown et al., 2014). The NME from 0^+ and 2^+ states has opposite signs and, thus, cancel the effects of each other. Other non-negligible contributions come through 4^+, 3^-, 5^-, and 7^- states.

Now we will discuss how the calculated NMEs will help to determine the bounds on Majorana neutrino mass and various lepton number violating parameters, using the lower limit on the experimental half-life of the decay. The inverse of half-life for $0\nu\beta\beta$ is given in **Eq. 1**. It is found that the half-life is influenced by the term C_I ($I = mm, m\lambda, \lambda\lambda$), lepton number violating term η_ν and η_λ, which are unknown, and CP-violating phase ψ. The C_I are defined in **Eq 7** and **(8)**, **(9)**, which contains mainly phase space factors and relevant NMEs. To calculate C_I, we have used the improved values of phase space factors calculated in Ref. (Štefánik et al., 2015), and for the NMEs, we have used the results of **Table 2** using ISM.

The results for C_I of light neutrino-exchange and λ mechanisms of $0\nu\beta\beta$ decay of ^{82}Se and ^{48}Ca are presented in **Table 3**. Here, the results for ^{48}Ca are taken from our earlier work using the closure approximation on the λ mechanism (Sarkar et al., 2020a). It is found that values of C_{mm} (light neutrino-exchange) and $C_{\lambda\lambda}$ (λ mechanism) are similar in values, which shows the dominance of each of these mechanisms on $0\nu\beta\beta$ half-life. The interference term ($C_{m\lambda}$) of both the mechanisms are relatively smaller, which shows the less importance of the interference mechanism.

We have also calculated the upper bound on unknown Majorana neutrino mass ($m_{\beta\beta}$) and lepton number violating parameter: the right-handed current coupling strength η_λ, using the experimental constraint on $T_{1/2}^{0\nu-exp}$ of Ref. (Arnold et al., 2005) for ^{82}Se and of Ref. (Arnold et al., 2016) for ^{48}Ca. The upper limits on $m_{\beta\beta}$ and η_λ are also presented in **Table 3** for ^{82}Se and ^{48}Ca when both light neutrino-exchange and λ mechanisms co-exist. With the experimental lower limit on $T_{1/2}^{0\nu-exp}$, the upper limits on Majorana neutrino mass ($m_{\beta\beta}$) are found to be 1.83 and 17.92 eV, respectively, for ^{82}Se and ^{48}Ca. This difference of $m_{\beta\beta}$ value for ^{82}Se and ^{48}Ca is quite large and also found in earlier work (Šimkovic et al., 2017). With the recent progress and future prospects of new generation experiments, lower limits on $T_{1/2}^{0\nu-exp}$ will be gradually improved and thus, will improve the upper limit on $m_{\beta\beta}$ and also reduce the differences for different isotopes.

4 SUMMARY

In summary, we have studied how the left-right weak boson exchange (λ) mechanism of $0\nu\beta\beta$ decay is competing with the standard light neutrino-exchange mechanism. Our interest of isotope was one of the prominent $0\nu\beta\beta$ decaying isotope ^{82}Se. Particularly, we have calculated the NMEs for $0\nu\beta\beta$ of ^{82}Se when both standard light neutrino-exchange and λ mechanisms co-exist. The revised formalism for nucleon currents to include the pseudoscalar term was taken care of. The nuclear shell model framework was used in the calculation, and the widely used closure approximation was adopted with suitable closure energy. Nuclear states of initial, final, and intermediate states are calculated for *fpg* model space with *JUN*45 effective shell model Hamiltonian using shell model code KSHELL. These nuclear states are used to calculate TNA, which comes in the expression of NME of $0\nu\beta\beta$ through $(n-2)$ decay channel. Using the calculated NMEs, we have also calculated the upper bounds on Majorana neutrino mass and lepton number violating parameters.

TABLE 3 | Results for half-life and bounds on neutrino mass and lepton number violating parameters. The $T_{1/2}^{0\nu-exp}$ is taken from the experimental lower limit on half-life from Ref. (Arnold et al., 2005) for ^{82}Se and from Ref. (Arnold et al., 2016) for ^{48}Ca. All results are for AV18 type SRC parameterizaionparameterization. We have assumed CP conservation (ψ =0). The results are compared with QRPA calculations for λ mechanism of Ref. (Šimkovic et al., 2017).

Quantity	^{82}Se	^{82}Se Ref. Šimkovic et al. (2017)	^{48}Ca	^{48}Ca Ref. Šimkovic et al. (2017)
$T_{1/2}^{0\nu-exp}$ [Years]	2.5×10^{23}	2.5×10^{23}	2.0×10^{22}	2.0×10^{22}
C_{mm} [Years]$^{-1}$	31.21×10^{-14}	51.3×10^{-14}	4.06×10^{-14}	2.33×10^{-14}
$C_{m\lambda}$ [Years]$^{-1}$	10.46×10^{-14}	-27.0×10^{-14}	3.37×10^{-14}	-1.04×10^{-14}
$C_{\lambda\lambda}$ [Years]$^{-1}$	36.19×10^{-14}	150.0×10^{-14}	5.39×10^{-14}	10.1×10^{-14}
$m_{\beta\beta}$ [eV]	1.83	1.43	17.92	23.7
η_λ	3.32×10^{-6}	1.63×10^{-6}	30.44×10^{-6}	22.30×10^{-6}

The results show that particularly M_{qGT} type matrix element of λ mechanism is significantly enhanced as compared to standard M_{GT} type NME for the inclusion of the higher-order effect of the pseudoscalar term in the nucleon current. A similar type of enhancement in M_{qGT} type NME was also found in our earlier study for ^{48}Ca (Sarkar et al., 2020a). The dominance of 0^+ and 2^+ states of neutron-neutron (proton-proton) pairs were also observed, just like earlier studies.

With the experimental lower limits on the half-life, we have used our calculated NMEs to set the upper bounds on Majorana neutrino mass ($m_{\beta\beta}$). The upper limits of values of $m_{\beta\beta}$ are found to be 1.83 and 17.92 eV, respectively, for ^{82}Se and ^{48}Ca. With the new generation of experiments, the lower limit on half-life will be further improved, and thus we can expect a much more refined upper bound on $m_{\beta\beta}$, which may be below 1 eV. Also, the difference for the value of $m_{\beta\beta}$ will be reduced.

The term C_I ($I = mm, m\lambda, \lambda\lambda$), which contains the phase space factors and NMEs, was also evaluated. The C_{mm} for light neutrino exchange and $C_{\lambda\lambda}$ for λ mechanism were found to be similar in values, that were larger than the term $C_{m\lambda}$ for the interference of both the mechanisms. This shows the dominance of light neutrino exchange and the λ mechanisms over the interference mechanism. The overall dominant effect of light neutrino-exchange mechanism is observed over λ mechanism and interference of both the mechanisms for very small values of lepton number violating η_λ parameter.

In the future, it will be interesting to see the competing effect of the λ mechanism on the light neutrino-exchange mechanism and also how their contribution on $0\nu\beta\beta$ half-life will be evaluated in the current and future generation experiments.

DATA AVAILABILITY STATEMENT

The raw data supporting the conclusion of this article will be made available by the authors, without undue reservation.

AUTHOR CONTRIBUTIONS

The idea of the article was originated by YI. He has also contributed to calculating the nuclear states, interpretation of results, and manuscript writing. SS is responsible for the calculation of the TNA and TBME part of the NME. He has also actively participated in preparing the manuscript. Overall, both the authors have contributed enough in to various stages of preparing the final manuscript.

FUNDING

YI is grateful for the funding support from JSPS KAKENHI Grant No.17K05440.

ACKNOWLEDGMENTS

Numerical computation in this work was carried out at the Yukawa Institute Computer Facility. YI acknowledges the Tokyo Institute of Technology for allowing to use of the high-performance computing facility to perform nuclear states calculation using KSHELL. YI is also grateful to Prof. Noritaka Shimizu, CNS, the University of Tokyo, for providing the 2020 version of shell model code KSHELL.

REFERENCES

Arnold, R., Augier, C., Baker, J., Barabash, A., Broudin, G., Brudanin, V., et al. (2005). First Results of the Search for Neutrinoless Double-Beta Decay with the NEMO 3 Detector. *Phys. Rev. Lett.* 95, 182302. doi:10.1103/PhysRevLett.95.182302

Arnold, R., Augier, C., Bakalyarov, A. M., and Baker, J. D. (2016). Measurement of the Double-Beta Decay Half-Life and Search for the Neutrinoless Double-Beta Decay of ^{48}Ca with the NEMO-3 Detector. *Phys. Rev. D* 93, 112008. doi:10.1103/PhysRevD.93.112008

Arnold, R., Augier, C., Barabash, A. S., Basharina-Freshville, A., Blondel, S., Blot, S., et al. (2020). Search for the Double-Beta Decay of 82se to the Excited States of 82kr with Nemo-3. *Nucl. Phys. A* 996, 121701. doi:10.1016/j.nuclphysa.2020.121701

Avignone, F. T., Elliott, S. R., and Engel, J. (2008). Double Beta Decay, Majorana Neutrinos, and Neutrino Mass. *Rev. Mod. Phys.* 80, 481–516. doi:10.1103/RevModPhys.80.481

Barea, J., and Iachello, F. (2009). Neutrinoless Double-Bdecay in the Microscopic Interacting Boson Model. *Phys. Rev. C* 79, 044301. doi:10.1103/PhysRevC.79.044301

Barea, J., Kotila, J., and Iachello, F. (2012). Limits on Neutrino Masses from Neutrinoless Double-β Decay. *Phys. Rev. Lett.* 109, 042501. doi:10.1103/PhysRevLett.109.042501

Barry, J., and Rodejohann, W. (2013). Lepton Number and Flavour Violation in Tev-Scale Left-Right Symmetric Theories with Large Left-Right Mixing. *J. High Energ. Phys.* 2013, 1–45. doi:10.1007/jhep09(2013)153

Bhupal Dev, P. S., Goswami, S., and Mitra, M. (2015). Tev-scale Left-Right Symmetry and Large Mixing Effects in Neutrinoless Double Beta Decay. *Phys. Rev. D* 91, 113004. doi:10.1103/PhysRevD.91.113004

Brown, B. A., Horoi, M., and Sen'kov, R. A. (2014). Nuclear Structure Aspects of Neutrinoless Double-β Decay. *Phys. Rev. Lett.* 113, 262501. doi:10.1103/PhysRevLett.113.262501

Brown, B. A., and Rae, W. D. M. (2014). The Shell-Model Code NuShellX@MSU. *Nucl. Data Sheets* 120, 115–118. doi:10.1016/j.nds.2014.07.022

Caurier, E., Menéndez, J., Nowacki, F., and Poves, A. (2008). Influence of Pairing on the Nuclear Matrix Elements of the Neutrinoless Betabeta Decays. *Phys. Rev. Lett.* 100, 052503. doi:10.1103/PhysRevLett.100.052503

Cirigliano, V., Dekens, W., de Vries, J., Graesser, M. L., Mereghetti, E., Pastore, S., et al. (2019). Renormalized Approach to Neutrinoless Double-β Decay. *Phys. Rev. C* 100, 055504. doi:10.1103/physrevc.100.055504

Deppisch, F. F., Hirsch, M., and Päs, H. (2012). Neutrinoless Double-Beta Decay and Physics beyond the Standard Model. *J. Phys. G: Nucl. Part. Phys.* 39, 124007. doi:10.1088/0954-3899/39/12/124007

Dolinski, M. J., Poon, A. W. P., and Rodejohann, W. (2019). Neutrinoless Double-Beta Decay: Status and Prospects. *Annu. Rev. Nucl. Part. Sci.* 69, 219–251. doi:10.1146/annurev-nucl-101918-023407

Engel, J., and Menéndez, J. (2017). Status and Future of Nuclear Matrix Elements for Neutrinoless Double-Beta Decay: a Review. *Rep. Prog. Phys.* 80, 046301. doi:10.1088/1361-6633/aa5bc5

Honma, M., Otsuka, T., Mizusaki, T., and Hjorth-Jensen, M. (2009). New Effective Interaction Forf5pg9-Shell Nuclei. *Phys. Rev. C* 80. doi:10.1103/physrevc.80.064323

Horoi, M., and Neacsu, A. (2016). Analysis of Mechanisms that Could Contribute to Neutrinoless Double-Beta Decay. *Phys. Rev. D* 93, 113014. doi:10.1103/PhysRevD.93.113014

Horoi, M., and Neacsu, A. (2018). Shell Model Study of Using an Effective Field Theory for Disentangling Several Contributions to Neutrinoless Double-β Decay. *Phys. Rev. C* 98, 035502. doi:10.1103/PhysRevC.98.035502

Horoi, M., and Stoica, S. (2010). Shell Model Analysis of the Neutrinoless Double-β Decay of ^{48}Ca. *Phys. Rev. C* 81, 024321. doi:10.1103/PhysRevC.81.024321

Iwata, Y., Shimizu, N., Otsuka, T., Utsuno, Y., Menéndez, J., Honma, M., et al. (2016). Large-Scale Shell-Model Analysis of the Neutrinoless $\beta\beta$ Decay of ^{48}Ca. *Phys. Rev. Lett.* 116, 112502. doi:10.1103/PhysRevLett.116.112502

Menéndez, J., Poves, A., Caurier, E., and Nowacki, F. (2009). Disassembling the Nuclear Matrix Elements of the Neutrinoless ββ Decay. *Nucl. Phys. A* 818, 139–151. doi:10.1016/j.nuclphysa.2008.12.005

Mohapatra, R. N. (1986). New Contributions to Neutrinoless Double-Beta Decay in Supersymmetric Theories. *Phys. Rev. D* 34, 3457–3461. doi:10.1103/PhysRevD.34.3457

Mohapatra, R. N., and Senjanović, G. (1980). Neutrino Mass and Spontaneous Parity Nonconservation. *Phys. Rev. Lett.* 44, 912–915. doi:10.1103/PhysRevLett.44.912

Mohapatra, R. N., and Vergados, J. D. (1981). New Contribution to Neutrinoless Double Beta Decay in Gauge Models. *Phys. Rev. Lett.* 47, 1713–1716. doi:10.1103/PhysRevLett.47.1713

Neacsu, A., Stoica, S., and Horoi, M. (2012). Fast, Efficient Calculations of the Two-Body Matrix Elements of the Transition Operators for Neutrinoless Double-β Decay. *Phys. Rev. C* 86, 067304. doi:10.1103/physrevc.86.067304

Pagnanini, L., Azzolini, O., Beeman, J., Bellini, F., Beretta, M., Biassoni, M., et al. (2019). "Results on Double Beta Decay of ^{82}se with CUPID-0 Phase I," in AIP Conference Proceedings (AIP Publishing LLC), 020019. doi:10.1063/1.5130980

Pastore, S., Carlson, J., Cirigliano, V., Dekens, W., Mereghetti, E., and Wiringa, R. B. (2018). Neutrinoless Double-β Decay Matrix Elements in Light Nuclei. *Phys. Rev. C* 97, 014606. doi:10.1103/PhysRevC.97.014606

Rath, P. K., Chandra, R., Chaturvedi, K., Raina, P. K., and Hirsch, J. G. (2010). Uncertainties in Nuclear Transition Matrix Elements for Neutrinoless $\beta\beta$ Decay within the Projected-Hartree-Fock-Bogoliubov Model. *Phys. Rev. C* 82, 064310. doi:10.1103/PhysRevC.82.064310

Rodejohann, W. (2011). Neutrino-less Double Beta Decay and Particle Physics. *Int. J. Mod. Phys. E* 20, 1833–1930. doi:10.1142/s0218301311020186

Rodin, V. A., Faessler, A., Šimkovic, F., and Vogel, P. (2006). Assessment of Uncertainties in QRPA 0ν $\beta\beta$-decay Nuclear Matrix Elements. *Nucl. Phys. A* 766, 107–131. doi:10.1016/j.nuclphysa.2005.12.004

Rodríguez, T. R., and Martínez-Pinedo, G. (2010). Energy Density Functional Study of Nuclear Matrix Elements for Neutrinoless $\beta\beta$ Decay. *Phys. Rev. Lett.* 105, 252503. doi:10.1103/physrevlett.105.252503

Sarkar, S., Iwata, Y., and Raina, P. K. (2020). Nuclear Matrix Elements for the λ Mechanism of 0ν $\beta\beta$ Decay of ^{48}Ca in the Nuclear Shell-Model: Closure versus Nonclosure Approach. *Phys. Rev. C* 102, 034317. doi:10.1103/PhysRevC.102.034317

Sarkar, S., Kumar, P., Jha, K., and Raina, P. K. (2020). Sensitivity of Nuclear Matrix Elements of *0νββ* of ^{48}Ca to Different Components of the Two-Nucleon Interaction. *Phys. Rev. C* 101, 014307. doi:10.1103/PhysRevC.101.014307

Schechter, J., and Valle, J. W. F. (1982). Neutrinoless Double-Bdecay in SU(2)× U(1) Theories. *Phys. Rev. D* 25, 2951–2954. doi:10.1103/physrevd.25.2951

Sen'kov, R. A., and Horoi, M. (2013). Neutrinoless Double-β Decay of ^{48}Ca in the Shell Model: Closure versus Nonclosure Approximation. *Phys. Rev. C* 88, 064312. doi:10.1103/PhysRevC.88.064312

Sen'kov, R. A., Horoi, M., and Brown, B. A. (2014). Neutrinoless Double-β Decay of ^{82}Se in the Shell Model: Beyond the Closure Approximation. *Phys. Rev. C* 89, 054304. doi:10.1103/PhysRevC.89.054304

Shimizu, N., Mizusaki, T., Utsuno, Y., and Tsunoda, Y. (2019). Thick-restart Block Lanczos Method for Large-Scale Shell-Model Calculations. *Comp. Phys. Commun.* 244, 372–384. doi:10.1016/j.cpc.2019.06.011

Šimkovic, F., Faessler, A., Müther, H., Rodin, V., and Stauf, M. (2009). 0*νββ*-decay Nuclear Matrix Elements with Self-Consistent Short-Range Correlation. *Phys. Rev. C* 79, 055501. doi:10.1103/PhysRevC.79.055501

Šimkovic, F., Pantis, G., Vergados, J. D., and Faessler, A. (1999). Additional Nucleon Current Contributions to Neutrinoless Double β Decay. *Phys. Rev. C* 60, 055502. doi:10.1103/PhysRevC.60.055502

Šimkovic, F., Štefánik, D., and DvornickŸ, R. (2017). The λ Mechanism of the 0*νββ*-Decay. *Front. Phys.* 5, 57. doi:10.3389/fphy.2017.00057

Song, L. S., Yao, J. M., Ring, P., and Meng, J. (2014). Relativistic Description of Nuclear Matrix Elements in Neutrinoless Double-β Decay. *Phys. Rev. C* 90, 054309. doi:10.1103/PhysRevC.90.054309

Štefánik, D., DvornickŸ, R., Šimkovic, F., and Vogel, P. (2015). Reexamining the Light Neutrino Exchange Mechanism of the 0*νββ* Decay with Left-And Right-Handed Leptonic and Hadronic Currents. *Phys. Rev. C* 92, 055502. doi:10.1103/PhysRevC.92.055502

Tomoda, T. (1991). Double Beta Decay. *Rep. Prog. Phys.* 54, 53–126. doi:10.1088/0034-4885/54/1/002

Vergados, J. D., Ejiri, H., and Šimkovic, F. (2012). Theory of Neutrinoless Double-Beta Decay. *Rep. Prog. Phys.* 75, 106301. doi:10.1088/0034-4885/75/10/106301

Vergados, J. D. (1987). Neutrinoless Double β-decay without Majorana Neutrinos in Supersymmetric Theories. *Phys. Lett. B* 184, 55–62. doi:10.1016/0370-2693(87)90487-4

Vogel, P. (2012). Nuclear Structure and Double Beta Decay. *J. Phys. G: Nucl. Part. Phys.* 39, 124002. doi:10.1088/0954-3899/39/12/124002

Wang, X. B., Hayes, A. C., Carlson, J., Dong, G. X., Mereghetti, E., Pastore, S., et al. (2019). Comparison between Variational Monte Carlo and Shell Model Calculations of Neutrinoless Double Beta Decay Matrix Elements in Light Nuclei. *Phys. Lett. B* 798, 134974. doi:10.1016/j.physletb.2019.134974

Conflict of Interest: The authors declare that the research was conducted in the absence of any commercial or financial relationships that could be construed as a potential conflict of interest.

Publisher's Note: All claims expressed in this article are solely those of the authors and do not necessarily represent those of their affiliated organizations, or those of the publisher, the editors, and the reviewers. Any product that may be evaluated in this article, or claim that may be made by its manufacturer, is not guaranteed or endorsed by the publisher.

APPENDIX A

One can write anti-symmetric two-body matrix elements for transition operator O^{α}_{12} of $0\nu\beta\beta$ defined in **Eq. 22** as

$$\begin{aligned}&\langle n_1'l_1'j_1', n_2'l_2'j_2'\colon JT|\tau_{-1}\tau_{-2}O^{\alpha}_{12}|n_1l_1j_1, n_2l_2j_2\colon JT\rangle_A\\&=\frac{1}{\sqrt{(1+\delta_{j_1'j_2'})(1+\delta_{j_1j_2})}}\\&(\langle n_1'l_1'j_1', n_2'l_2'j_2'\colon JT|\tau_{-1}\tau_{-2}O^{\alpha}_{12}|n_1l_1j_1, n_2l_2j_2\colon JT\rangle\\&-(-1)^{j_1+j_2+J}\\&\times\langle n_1'l_1'j_1', n_2'l_2'j_2'\colon JT|\tau_{-1}\tau_{-2}O^{\alpha}_{12}|n_2l_2j_2, n_1l_1j_1\colon JT\rangle),\end{aligned}\tag{29}$$

where,

$$\begin{aligned}&\langle n_1'l_1'j_1', n_2'l_2'j_2'\colon J|O^{\alpha}_{12}|n_1l_1j_1, n_2l_2j_2\colon J\rangle\\&=\sum_{S',S}\sum_{\lambda',\lambda}\begin{bmatrix}l_1' & \frac{1}{2} & j_1'\\ l_2' & \frac{1}{2} & j_2'\\ \lambda' & S' & J\end{bmatrix}\begin{bmatrix}l_1 & \frac{1}{2} & j_1\\ l_2 & \frac{1}{2} & j_2\\ \lambda & S & J\end{bmatrix}\\&\times\sum_{n',l',N',L'}\sum_{n,l,N,L}\sum_{\mathcal{J}}\frac{1}{\sqrt{2S+1}}\frac{1}{\sqrt{2\mathcal{J}+1}}U(L',l',J,S'\colon\lambda'\mathcal{J})\\&\times U(L,l,J,S\colon\lambda\mathcal{J})\langle n',l',N',L'|n_1',l_1',n_2',l_2'\rangle_{\lambda'}\\&\times\langle n,l,N,L|n_1,l_1,n_2,l_2\rangle_{\lambda}\langle l',S'\colon\mathcal{J}\|S^{\alpha}_{12}\|l,S\colon\mathcal{J}\rangle\\&\times\langle n',l'|H_{\alpha}(r)|n,l\rangle.\end{aligned}\tag{30}$$

One can write in terms of 9j symbol

$$\begin{bmatrix}l_1' & \frac{1}{2} & j_1'\\ l_2' & \frac{1}{2} & j_2'\\ \lambda' & S' & J\end{bmatrix}=\sqrt{(2j_1'+1)(2j_2'+1)(2\lambda'+1)(2S'+1)}\times\begin{Bmatrix}l_1' & \frac{1}{2} & j_1'\\ l_2' & \frac{1}{2} & j_2'\\ \lambda' & S' & J\end{Bmatrix}.\tag{31}$$

In terms of 6j symbol one can write

$$U(L',l',J,S'\colon\lambda'\mathcal{J})=(-1)^{L'+l'+S'+J}\sqrt{2\lambda'+1}\sqrt{2\mathcal{J}+1}\begin{Bmatrix}L' & l' & \lambda'\\ S' & J & \mathcal{J}\end{Bmatrix}.\tag{32}$$

$\langle n', l', N', L'|n_1', l_1', n_2', l_2'\rangle_{\lambda'}$ is the harmonic oscillator bracket used to convert the radial integral of neutrino potential from individual coordinate system of nucleons to relative and center of mass coordinate system of the nucleons.

APPENDIX B

The $f_{\alpha}(q, r)$ factor of **Eq. 16** can be written in terms of radial dependence, spherical Bessel function j_p (qr) (p = 0, 1, 2 and 3), and FNS + HOC coupling form factors in closure approximation as (Šimkovic et al., 2017).

$$\begin{aligned}f_{GT}(q,r) &= \frac{j_0(qr)}{g_A^2}\left(g_A^2(q^2)-\frac{g_A(q^2)g_P(q^2)}{m_N}\frac{q^2}{3}\right.\\&\left.+\frac{g_P^2(q^2)}{4m_N^2}\frac{q^4}{3}+\left(2\frac{g_M^2(q^2)}{4m_N^2}\frac{q^2}{3}\right)\right),\end{aligned}\tag{33}$$

$$f_F(q,r) = g_V^2(q^2)j_0(qr),\tag{34}$$

$$\begin{aligned}f_T(q,r) &= \frac{j_2(qr)}{g_A^2}\left(\frac{g_A(q^2)g_P(q^2)}{m_N}\frac{q^2}{3}-\frac{g_P^2(q^2)}{4m_N^2}\frac{q^4}{3}\right.\\&\left.+\frac{g_M^2(q^2)}{4m_N^2}\frac{q^2}{3}\right),\end{aligned}\tag{35}$$

$$f_{\omega GT}(q,r) = \frac{q}{(q+\langle E\rangle)}f_{GT}(q,r),\tag{36}$$

$$f_{\omega F}(q,r) = \frac{q}{(q+\langle E\rangle)}f_{F}(q,r),\tag{37}$$

$$f_{\omega T}(q,r) = \frac{q}{(q+\langle E\rangle)}f_{T}(q,r),\tag{38}$$

$$\begin{aligned}f_{qGT}(q,r) &= \left(\frac{g_A^2(q^2)}{g_A^2}q+3\frac{g_P^2(q^2)}{g_A^2}\frac{q^5}{4m_N^2}\right.\\&\left.+\frac{g_A(q^2)g_P(q^2)}{g_A^2}\frac{q^3}{m_N}\right)rj_1(q,r),\end{aligned}\tag{39}$$

$$f_{qF}(q,r) = rg_V^2(q^2)j_1(qr)q,\tag{40}$$

$$\begin{aligned}f_{qT}(q,r) &= \frac{r}{3}\left(\left(\frac{g_A^2(q^2)}{g_A^2}q-\frac{g_P(q^2)g_A(q^2)}{2g_A^2}\frac{q^3}{m_N}\right)j_1(qr)\right.\\&\left.-\left(9\frac{g_P^2(q^2)}{2g_A^2}\frac{q^5}{20m_N^2}[2j_1(qr)/3-j_3(qr)]\right)\right),\end{aligned}\tag{41}$$

where one can write in dipole approximation (Šimkovic et al., 1999).

$$g_V(q^2) = \frac{g_V}{\left(1+\frac{q^2}{M_V^2}\right)^2},\tag{42}$$

$$g_A(q^2) = \frac{g_A}{\left(1+\frac{q^2}{M_A^2}\right)^2},\tag{43}$$

$$g_M(q^2) = (\mu_p-\mu_n)g_V(q^2),\tag{44}$$

$$g_P(q^2) = \frac{2m_p g_A(q^2)}{(q^2+m_\pi^2)}\left(1-\frac{m_\pi^2}{M_A^2}\right). \quad (45)$$

$\mu_p - \mu_n = 4.7$, $M_V = 850$ MeV, $M_A = 1{,}086$ MeV m_p and m_π are the mass of protons and pions (Sen'kov and Horoi, 2013). In the present calculation, vector constant $g_V = 1.0$ and bare axial-vector constant $g_A = 1.27$ (Sarkar et al., 2020b) are used. Both the pseudo scalar and weak magnetism terms of the nucleon currents are included in $f_{GT,T,\omega GT,\omega T}$ $(q,\ r)$ factors whereas pseudo scalar term is included in $f_{qGT,qT}$ (q, r) factors (Šimkovic et al., 2017).

frontiers in Astronomy and Space Sciences

REVIEW
published: 23 February 2022
doi: 10.3389/fspas.2021.763276

Evolution of Hot and Dense Stellar Interiors: The Role of the Weak Interaction Processes

T. S. Kosmas[1]*, *I. Tsoulos*[2], *O. Kosmas*[2,3] and *P. G. Giannaka*[1]

[1]Department of Physics, University of Ioannina, Ioannina, Greece, [2]Department of Informatics and Telecommunications, University of Ioannina, Arta, Greece, [3]Department of Mechanical, Aerospace and Civil Engineering, University of Manchester, Manchester, United Kingdom

The evolution of the hot and dense interior of massive stars has aroused the intense interest of researchers the last more than three decades. In this article, the role of the semi-leptonic weak interaction processes of leptons (involving neutrinos) with nucleons and nuclei in the late stages of stellar evolution, as well as in the relevant terrestrial neutrino detection experiments, is reviewed. Such processes play crucial role for the massive stars' evolution in the final stages of their life, and specifically in the core-collapse supernova leading to the supernova explosion phenomenon. We start by mainly focusing on the neutrino producing charged-lepton capture, like the electron-capture and the muon-capture on nuclei and, then, we discuss the neutrino absorbing reactions which are essential in the neutrino-driven explosive nucleo-synthesis. These processes are also significant in many ongoing and planned worldwide underground sensitive experiments aiming to detect astrophysical neutrinos which rely on the interactions of neutrinos with the bound nucleons inside atomic nuclei.

Keywords: core collapse supernova, explosive nucleo-synthesis, electron capture, muon capture, neutrino-nucleus reactions, semi-leptonic weak processes, quasi-particle RPA

OPEN ACCESS

Edited by:
Nunzio Itaco,
University of Campania Luigi Vanvitelli, Italy

Reviewed by:
Emanuel Ydrefors,
Institute of Modern Physics (CAS), China
Domenico Logoteta,
University of Pisa, Italy

***Correspondence:**
T. S. Kosmas
hkosmas@uoi.gr

Specialty section:
This article was submitted to Nuclear Physics, a section of the journal Frontiers in Astronomy and Space Sciences

Received: *23 August 2021*
Accepted: *17 November 2021*
Published: *23 February 2022*

Citation:
Kosmas TS, Tsoulos I, Kosmas O and Giannaka PG (2022) Evolution of Hot and Dense Stellar Interiors: The Role of the Weak Interaction Processes. Front. Astron. Space Sci. 8:763276. doi: 10.3389/fspas.2021.763276

1 INTRODUCTION

It is well known that stars are born out of the gravitational collapse of cool and dense molecular clouds when they collapse into smaller regions which finally contract to form stellar cores, the proto-stars (Bethe, 1990; Phillips, 2013; Giannaka, 2015; Woosley, 2019). Due to the contraction of proto-stars, the central temperature increases up to the point where nuclear reactions start by firstly converting hydrogen into helium in the core and this way the star enters the stage of the main sequence (Fuller et al., 1982; Bethe, 1990; Suzuki et al., 2006; Phillips, 2013; Balasi et al., 2015). Subsequently, the interior of evolved high mass stars develop layers (fusion shells) like an onion where the outer shell drops fuel to the lower shell while heavier and heavier nuclear isotopes are being synthesized as we move towards the center of the star (Gastaldo et al., 2017; Woosley, 2019; Cantiello et al., 2021).

During the evolution of the massive stars ($M \geq 8M\_\{solar\}$, with $M\_\{solar\}$ being the Sun's mass), specifically during the late stages of their life (Fuller et al., 1982; Bethe, 1990; Oda et al., 1994), a great number of thermonuclear reactions and among them weak interaction processes on nucleons and nuclei like the charged-lepton capture, the neutrino production and neutrino absorption, the β-decay modes and others, play key role. In addition, other charge-changing semi-leptonic processes (the elementary β-decay reactions, the elementary semi-leptonic ν-nucleon reactions, etc.,) play also

significant role in core-collapse supernova (SN) (Langanke and Martinez-Pinedo, 1998; Langanke and Martínez-Pinedo, 1999). In this review we are going to pay special attention on the main conclusions of the state-of-the-art approaches related to the structure and evolution of the hot and dense stellar interior, focusing on those reactions taking place in the presence of nuclei as well as in the plethora of terrestrial astrophysical neutrino detection experiments.

In general, the semileptonic weak interactions in nuclei are of great interest for many physical reasons. At first, the accurate knowledge of the above mentioned processes determines to a large extent the evolution of massive stars, especially in their pre-supernova, their core-collapse supernova (CCSN) and their explosion phase (Fischer et al., 2020; Nagakura and Hotokezaka, 2021). Thus, the better the cross sections we know for these semi-leptonic processes the better the description of successful stars' explosions is coming out of the various SN scenarios and relevant algorithms (explosion codes) (Langanke et al., 2001; Langanke et al., 2003; Langanke and Martínez-Pinedo, 2003; Titus et al., 2017). Nowadays, this knowledge needs to be extended so as to include as great as possible number of nuclear isotopes and number of different semi-leptonic electro-weak processes (Titus et al., 2017). Furthermore, various theoretical ideas related to the fundamental theory of the weak interactions between the involved nuclei with leptons, may be tested through terrestrial experiments aiming to investigate the nuclear and particle physics of these processes (Langanke et al., 2003; Bollig et al., 2017; Sieverding et al., 2019). In addition, once the fundamental nature of the weak interactions is fully understood, this can be used for testing the theoretical ideas on new nuclear excited states not being accessible by the electromagnetic interactions (O'Connell et al., 1972; Donnelly and Walecka, 1976; Donnelly and Peccei, 1979).

Moreover, from a nuclear theory viewpoint, it is important to note that the semi-leptonic weak processes are studied with the same methods employed for electron-nucleus scattering (for example, using the Donnelly-Walecka multipole decomposition and constructing the nuclear states within the context of the shell models, RPA, QRPA, etc.,) because there is a close analogy between these two classes of processes and because the electromagnetic interaction plays a similar role to that of the weak interactions (Donnelly and Peccei, 1979; Kosmas and Oset, 1996; Ejiri et al., 2019). Due to the fact that, the matrix elements of the vector current component of the operators are identical in the electromagnetic electron scattering and the weak interactions (conserved-vector-current, CVC theory), these operators represent half of the overall independent operators needed to describe the weak processes (Chasioti and Kosmas, 2009; Tsakstara and Kosmas, 2011a; Tsakstara and Kosmas, 2011b; Tsakstara and Kosmas, 2012). Furthermore, electron scattering data offer reliable tests for the calculated nuclear wave functions in order to acquire confidence on predictions relevant to the weak processes which in many cases, helps to eliminate nuclear physics uncertainties. In addition, the semi-leptonic weak reactions are, in principle, richer sources of information on nuclear structure because of the axial vector spin dependent operators of the interaction between the leptons and the target nucleus (Ejiri et al., 2019; Papoulias et al., 2019).

Regarding the ν-nucleus reactions, it is worth mentioning the challenges of the neutral current (NC) neutrino–nucleus scattering of which the measurements rely on a different signal to that of the charged current (CC) ν-nucleus reactions (Donnelly and Peccei, 1979; Kosmas and Oset, 1996). From these two different neutrino–nucleus reaction channels, the charged-current reaction in which the parent nucleus changes charge and the daughter one appears, in general, in an excited (final) state, has been firstly measured long ago. The neutral current channel has only recently been measured for the first time (forty three years after its first theoretical prediction), in the COHERENT experiment at ORNL, United States (Akimov et al., 2017). Today, the operating or planned worldwide neutral current "coherent elastic neutrino-nucleus scattering (CEvNS) experiments" are based on precise measurements of the nuclear-recoil and among their highest priorities are the investigation of the neutrino properties, the fundamental ν-matter weak interactions, etc., (Papoulias and Kosmas, 2018; Papoulias et al., 2020). The planned advances in the precision of these experiments require a commensurate effort in the understanding and modeling of the nuclear physics aspects of these interactions, which are incorporated as a particle model in neutrino physics and play important role in interpreting the respective experimental results (Akimov et al., 2017; Papoulias and Kosmas, 2018; Papoulias et al., 2020).

In core-collapse supernova simulations, precise description of neutrino processes deep into the hot and dense matter is required. In this review, we summarize the main conclusions extracted from the studies aiming to estimate the rates of charged-current weak processes involving electrons, muons and their anti-particles inside the massive stars' matter (Suzuki et al., 2006; Suzuki et al., 2011; Suzuki and Kajino, 2013; Suzuki et al., 2018). The neutrino processes inside the hot and dense stellar medium are important in many aspects of core-collapse supernovae and, in particular for the explosion mechanism and the explosive neutrino nucleo-synthesis leading to the creation of the heavy elements (heavy nuclear isotopes) (Langanke and Martinez-Pinedo, 1998; Kajino et al., 2014). The multi-dimensional (2-D, 3-D, 4-D) simulations of successful explosions of core-collapse supernovae have shown that the neutrino-driven mechanism and the neutrino transport in hot and dense proto–neutron stars must necessarily be accurately described which means that the cross sections and event rates of the relevant reactions are appreciably important (Giannaka and Kosmas, 2013; Suzuki and Kajino, 2013; Giannaka and Kosmas, 2015b; Suzuki et al., 2018).

As is well known, in general, the gravitational collapse plays a vital role in the structural formation of the Universe, and in the death of massive stars through the gravitational collapse and the subsequent supernova explosions that are spectacular and very complex astrophysical events. Further, under the extreme conditions of the hot and dense interior of massive stars, all four known forces of nature are involved. Thus, the

presence of the strong gravitational field determines the dynamics of the astrophysical plasma while the weak interactions govern the energy and lepton number loss of the system through the transport of neutrinos from high-opacity regions to the free-streaming ones (Langanke and Wiescher, 2001; Woosley et al., 2002). Electromagnetic and strong interactions determine the thermodynamic properties, while nuclear and weak interactions modify the stellar gas composition. Focusing on the stellar weak interaction processes we are interested in the present article, in recent years there has been much progress in describing these processes towards many directions involving their intimate connection with the stellar evolution phenomena. In a single article, however, one can hardly cover all interesting aspects of the massive star's evolution and their death through the gravitational collapse followed by the supernova explosion related to the semi-leptonic weak interaction processes (Langanke and Wiescher, 2001).

For the above reason, in the present review we will focus on some selected topics (chosen according to our preference) mostly related to the role of the stellar weak interaction processes taken place in the presence of nuclei (Tsakstara and Kosmas, 2011a; Tsakstara and Kosmas, 2011b; Tsakstara and Kosmas, 2012; Giannaka and Kosmas, 2015a; Giannaka and Kosmas, 2015b). For the benefit of the reader, however, we mention some relevant topics like for example: 1) The neutrino absorption on nucleons, which is crucial for the supernova explosion mechanism and the explosive nucleosynthesis. 2) The elementary pair-production processes which are important for neutron star cooling. 3) The production mechanisms of muon and tau neutrinos in the late stages of collapse (because of their current interest, we will discuss in **Section 7** their detection by Earth bound detectors through the production of muons or tau particles). 4) The neutrino–lepton scattering (as neutrino–muon scattering) (Bollig et al., 2017). On the other hand, we consider as purely astrophysical aspects the following: 1) the current progress occurred in astrophysical models and the treatment of the related uncertainties in each of these models in connection to the relevant experimental data, 2) phenomena related to the supernova dynamics, 3) the shock acceleration phases and the neutrino-spectra formation, etc., which are, of course, important and crucial for massive stars' evolution, but they fall out of the scope of the special Volume and the Research Topic of the Journal for which the present review has been written.

The article is organized as follows. At first (**Section 2**), we review the general evolution of the massive stars as well as that of their main burning stages (H, He, C, Ne, O, . . .). Next (in **Section 3**), we recapitulate the relevant formalism used for the semi-leptonic processes. Then, the muon capture (in **Section 4**), the electron capture (in **Section 5**) and the neutrino-nucleus reactions (in **Section 6**) under laboratory and stellar conditions are discussed. While the results presented for the muon capture rates (in **Section 4**) are based on a mean value of the muon-nucleus overlap integrals, we discuss here the accurate muon wave functions calculated by our group recently. Next (**Section 7**), we review the role of the aforementioned semi-leptonic processes in Earth neutrino detectors and, finally (**Section 8**), we summarize the main research addressed in this article and we discuss next generation investigations.

2 STELLAR EVOLUTION AND THE ROLE OF THE WEAK INTERACTION PROCESSES

In this section, we summarize briefly the main conclusions of the state-of-the-art approaches related to the structure and evolution of the hot and dense stellar interior focusing on the relevance of the weak interaction processes with the stellar dynamics and stellar evolution. The latter includes the way that stars change with time, although on human time-scale most stars (those being in the main sequence stage) do not show at all changes and this holds for millions of years. In general, the evolution of a star, is strongly determined by its mass (M) during the long lasting main sequence phase of its life and is expected to lead in a wide variety of outcomes (Fuller et al., 1982; Bethe, 1990; Phillips, 2013; Woosley, 2019). Thus, the gravitational contraction of stars is, in general, balanced from the nuclear fusion reactions taking place in their interior and lead to the development of a sequence of burning shells which from outer to inner are the H-burning, the He-, the C-, the Ne-, the O- and finally the Si-burning shell (the cycle of contraction, heating, ignition of another nuclear fuel is repeated several times from the outer to the inner layer).

As mentioned above, massive stars go through six burning stages [see e.g., (Langanke and Wiescher, 2001)]: H, He, C, Ne, O, and Si burning with the lifetimes of these stages to be: H- and He-burning stages last for roughly 10^{6-7} y and 10^{5-6} y, respectively, while the lifetime for the other phases is much shorter (due to neutrino losses dominating energy losses over radiation from C burning onward). Therefore C-, Ne-, O-, and Si-burning phases last about 10^{2-3} y, 1 y, 1 y, and 10^{-2} y, respectively. During these stages, the mass density ρ and temperature T of the star's core increase gradually and, at the end of Si-burning core, reach values up to $\rho = 10^9 gcm^{-3}$ and up to $T = 10^9$ K, respectively. Under the latter conditions, the bidirectional nuclear reactions reach the equilibrium, a situation known as nuclear statistical equilibrium (NSE). Then, the nuclear composition is described through the three variables: T, ρ and proton-to-nucleon ratio Y_e (Langanke and Wiescher, 2001; Woosley et al., 2002).

During the NSE phase, the nuclear fusion reactions cannot release energy anymore, which implies that the important thermonuclear pressure that balances the gravitational contraction is canceled. In more detail, at this stage the star's core (known as Fe-core) is mainly made of Fe-group nuclei, produced by the Si-burning shell, namely nuclei in the Fe-Ni nuclear mass region which are favored under the core values of ρ and T mentioned above, while Y_e is a bit smaller than $Y_e = 0.5$. But, since Fe cannot be burned to heavier elements (this reaction requires energy to proceed and does not generate energy), the star finally runs out of fuel and collapses under its own gravity. The neutrinos generated at this phase interact with matter mainly via neutral-current coherent scattering on nucleons and nuclei (the rate is large so that their diffusion time-scale is longer than the collapse time-scale).

Moreover, the electrons of the core inside such an environment form a degenerate relativistic gas that can balance the gravitational contraction only if the stellar mass is below the known Chandrasekhar mass limit $M_{Ch} = 1.44(Y_e)^2 M_{\{solar\}}$. If this limit is exceeded (due to the e-capture and the Si-burning that modify the Y_e), the electron gas cannot stabilize the core any more and the star collapses.

Furthermore, during the early phase of the collapse, the neutrinos produced by the e^--capture process can leave the star unhindered carrying away energy that constitutes an effective cooling mechanism which keeps the entropy and core-temperature at low levels (for low entropy heavy nuclei exist during the entire collapse phase) (Langanke and Wiescher, 2001; Woosley et al., 2002). The situation changes when the collapse reaches densities of the order of $\rho = 10^{12} gcm^{-3}$. Then, due to the neutral current coherent neutrino-nucleus scattering mentioned above (the diffusion time-scale is longer than the collapse time of the core), neutrinos are effectively trapped in the core. At neutrino trapping ($\rho = 10^{12} gcm^{-3}$), the values of Y_e are significantly lower, while at higher densities the total lepton fraction Y_{lep} becomes constant (the trapped neutrinos increase the total lepton fraction in the core) but the Y_e still decreases. We note that during neutrino trapping, the continuous e^--capture reduces the electron abundance. Due to this crucial role of the electron capture in determining the dynamics of the core collapse of massive stars for core densities in the range $10^9 gcm^{-3} \leq \rho \leq 10^{12} gcm^{-3}$, in this article we discuss in detail this process (see **Section 5**). We mention however that, despite the progress achieved in recent years in the determination of stellar e^--capture rates, further improvements are certainly required at least in specific regions of the periodic table (Langanke et al., 2021).

As mentioned before, the star's life depends primarily on the star's mass M at birth. Thus, stars with $M \lessapprox 8 M\_\{solar\}$ proceed mainly through H- and He-burning. As they lose significant mass by stellar winds, at the end of He burning their masses are not sufficient to ignite further burning stages. Their life ends as White Dwarfs, that are compact objects with a mass limit $M \leq 1.44 M\_\{solar\}$, i.e., Chandrasekhar mass, stabilized by electron degeneracy pressure (Hirschi et al., 2004; Jones et al., 2016; Langanke et al., 2021). The so called intermediate-mass stars ($8 \lessapprox M \lessapprox 11 M\_\{solar\}$) follow in-between fate and collapse into a neutron star or are ending in a thermonuclear runaway which disrupts most of the core (Langanke and Wiescher, 2001; Woosley et al., 2002). Simulations of such stars are quite sensitive to astrophysical uncertainties like convective mixing or mass loss rates (Hirschi et al., 2004; Jones et al., 2016; Langanke et al., 2021). Most of the mass loss of stars takes place during H- and He-burning phases (mainly for red giant stars). On the other hand, the major nuclear uncertainty, related to electron capture on ^{20}Ne, has recently been removed as this rate is now known experimentally at the relevant astrophysical conditions (Langanke et al., 2021). Finally, stars with $M \gtrapprox 11 M\_\{solar\}$ develop a core at the end of each burning phase which exceeds the Chandrasekhar mass, so that they can ignite the full cycle of hydrostatic burning and end their lives as core-collapse supernovae, leaving either neutron stars or black holes as remnants (Langanke and Wiescher, 2001; Woosley et al., 2002).

3 FORMALISM FOR MODEL CALCULATIONS ON SEMI-LEPTONIC WEAK PROCESSES

Usually, the event rates (total cross sections) calculations of the semi-leptonic processes (electron capture, muon-capture, neutrino induced reactions, beta decay modes, etc.,) start from the corresponding differential cross sections which, within the context of the Donnelly-Walecka multipole decomposition method, are obtained by the expression (O'Connell et al., 1972; Donnelly and Walecka, 1976; Donnelly and Peccei, 1979).

$$\begin{aligned}\frac{d\sigma_{ec}}{d\Omega} = \frac{G_F^2 \cos^2\theta_c}{2\pi} \frac{F(Z,E_e)}{(2J_i+1)} \Big\{ &\sum_{J\geq 1} \mathcal{W}(E_e,E_\nu) \Big\{ [(1 - (\hat{\nu}\cdot\hat{\mathbf{q}})(\hat{\boldsymbol{\beta}}\cdot\hat{\mathbf{q}}))] \\ &\left[|\langle J_f \| \hat{\mathcal{T}}^{mag}_J \| J_i \rangle|^2 + \left| \langle J_f \| \hat{\mathcal{T}}^{el}_J \| J_i \rangle \right|^2 \right] \\ &-2\hat{\mathbf{q}}\cdot(\hat{\nu}-\hat{\boldsymbol{\beta}}) Re\langle J_f \| \hat{\mathcal{T}}^{mag}_J \| J_i \rangle \langle J_f \| \hat{\mathcal{T}}^{el}_J \| J_i \rangle * \Big\} \\ &+ \sum_{J\geq 0} \mathcal{W}(E_e,E_\nu) \Big\{ (1+\hat{\nu}\cdot\hat{\boldsymbol{\beta}}) |\langle J_f \| \hat{\mathcal{M}}_J \| J_i \rangle|^2 \\ &+ \Big(1 - \hat{\nu}\cdot\hat{\boldsymbol{\beta}} + 2(\hat{\boldsymbol{\beta}}\cdot\hat{\mathbf{q}}) |\langle J_f \| \hat{\mathcal{L}}_J \| J_i \rangle|^2 \\ &-2\hat{\mathbf{q}}\cdot(\hat{\nu}+\hat{\boldsymbol{\beta}}) Re\langle J_f \| \hat{\mathcal{L}}_J \| J_i \rangle \langle J_f \| \hat{\mathcal{M}}_J \| J_i \rangle * \Big\} \Big\} \end{aligned} \quad (1)$$

(G_F and θ_c stand for Fermi constant and the known Cabibbo angle of the weak interactions) where $\mathcal{W}(E_e,E_\nu) = E_\nu^2/(1+E_\nu/M_T)$, takes into consideration the nuclear recoil (M_T is the mass of the target nucleus) (Niu et al., 2011), while $F(Z, E_e)$ denotes the well known Fermi function (Langanke et al., 2003; Langanke and Martínez-Pinedo, 2003). We note that, this kind of calculations do not take into account possible modifications due to the final state interaction of the outgoing lepton like those applied in electron scattering where the effective momentum approximation may significantly improve this effect (Aste and Jourdan, 2004).

The nuclear matrix elements between the initial state $|J_i\rangle$ and a final state $|J_f\rangle$ refer to the Coulomb $\hat{\mathcal{M}}_{JM}$, longitudinal $\hat{\mathcal{L}}_{JM}$, transverse electric $\hat{\mathcal{T}}^{el}_{JM}$ and transverse magnetic $\hat{\mathcal{T}}^{mag}_{JM}$ multipole operators [see Ref. (Giannaka and Kosmas, 2015a)]. Also, $\hat{q}$, $\hat{\nu}$ are the unit vectors of the momentum transfer $\mathbf{q}$, the outgoing-particle momentum and $\hat{\boldsymbol{\beta}} = \mathbf{k}/E_e$ with $\mathbf{k}$ being the corresponding 3-momentum of the incoming particle (Donnelly and Peccei, 1979). For the evaluation of the wave functions $|J_i\rangle$ and $|J_f\rangle$ required for the reaction rates of semi-leptonic nuclear processes, up to now various microscopic models have been used which are briefly summarized as follows. The independent particle model (Fuller et al., 1982), the shell model for light s-d shell nuclei (Oda et al., 1994; Suzuki et al., 2006; Suzuki et al., 2018), the large scale shell model (Langanke and Martı´nez-Pinedo, 2000), the ordinary random phase approximation (RPA) (Nabi et al., 2007a; Nabi et al., 2007b; Nabi, 2011; Nabi and Riaz, 2019), the continuum RPA (CRPA) (Kolbe et al., 1997), the relativistic RPA (Paar et al., 2009; Niu et al., 2011; Fantina et al., 2012), the quasi-particle RPA (QRPA) (Chasioti and Kosmas, 2009; Tsakstara and Kosmas, 2011a; Tsakstara and Kosmas, 2011b; Tsakstara and Kosmas, 2012; Giannaka and Kosmas, 2015a; Giannaka and Kosmas, 2015b), the deformed QRPA (Sarriguren et al., 2001), the thermal QRPA (Dzhioev et al., 2020), and others (Hix et al., 2003). Each of these methods has advantages and disadvantages. We mention that, several of the above

calculations are comprehensive. What is, however, worth noting at this point is the fact that the available results cover still a small portion of the input required in Supernova evolution codes (mostly those referred to the e-capture and ν-nucleus process designed to predict the SN explosions and multi-messenger signatures of many important astrophysical phenomena) (Titus et al., 2017). Furthermore, in the majority of the above studies, a number of simplifying assumptions (zero momentum transfer to the target nucleus, forward scattering angles of the outgoing particles, employment of schematic nucleon-nucleon interaction, etc.,) have been made (Ejiri et al., 2019). Under these assumptions, several authors found that the Gammow-Teller operators, $GT^{\pm} = \sum_j \tau_j^{\pm}\sigma(j)$ with $\Delta T = 1$, $\Delta L = 0$, $\Delta J^{\pi} = 1^{+}$, dominate the cross sections of several semi-leptonic processes. Even though these methods are still reliable and the results obtained interesting, some important details are missing and also some computations need to be further improved (Chasioti and Kosmas, 2009; Tsakstara and Kosmas, 2011a; Tsakstara and Kosmas, 2011b).

In the following sections, we will summarize briefly some muon-capture, e^{-}-capture and neutrino-nucleus reactions cross sections obtained within the framework of a refined version of the proton-neutron QRPA (p-n QRPA) (Giannaka and Kosmas, 2013; Giannaka and Kosmas, 2015b; Giannaka and Kosmas, 2015a), but, for the sake of completeness we will also discuss the comparison of these QRPA results with some of those computed within the context of other methods as mentioned above. The p-n QRPA method offers a reliable construction of the ground state $|i\rangle$ and all the accessible final states $|f\rangle$ of the daughter nuclei entering the calculations of **Eq. 1** for single charge-exchange nuclear reactions (Kosmas et al., 1994; Kosmas and Oset, 1996; Kosmas et al., 1997a). The method is tested through the reproducibility of: 1) nuclear ground state properties, 2) various electron scattering data, 3) experimental muon capture rates (Giannaka and Kosmas, 2015a), 4) beta-decay rates, etc. The corresponding QRPA predictions, may come out of state-by-state calculations of exclusive, partial and total rate transition matrix elements (Donnelly and Peccei, 1979; Kosmas et al., 1997b; Eramzhyan et al., 1998; Kolbe et al., 2000; Kosmas et al., 2001; Zinner et al., 2006). The use of the p-n QRPA with rich model space and adopting as realistic nucleon-nucleon interaction the Bonn C-D potential leads to reliable agreement with experimental data. This high confidence level encouraged its use to find muon-capture rates, electron capture cross sections in various nuclear isotopes (Giannaka and Kosmas, 2015a) and also neutrino nucleus neutral current reaction (Chasioti and Kosmas, 2009; Tsakstara and Kosmas, 2011a; Tsakstara and Kosmas, 2011b; Tsakstara and Kosmas, 2012; Papoulias and Kosmas, 2018).

4 THE MUON CAPTURE ON NUCLEI

In the stellar interior, but also in current experimental research, several well known processes involving muons and muonic neutrinos take place on nuclei as: 1) The conventional bound muon capture by the nucleus (A,Z), with A denoting the mass- and Z the atomic-number of the parent nucleus. Most important channels are: a) the ordinary muon-capture, represented by the reactions

$$\mu_b^- + (A,Z) \rightarrow \nu_\mu + (A,Z-1)^*, \tag{2}$$

(the asterisk * stands for "excited state" of the daughter nucleus), b) the muon-decay-in-orbit (MDIO): $\mu_b^- \rightarrow \nu_\mu + e^- + \tilde{\nu}_e$, and c) the radiative muon capture: $\mu_b^- + (A,Z) \rightarrow \nu_\mu + (A,Z-1)^* + \gamma$. 2) The exotic neutrinoless capture of a bound muon (μ_b^-), known as muon-electron conversion: $\mu_b^- + (A,Z) \rightarrow e^- + (A,Z)^*$, as well as the known as muon-positron conversion: $\mu_b^- + (A,Z) \rightarrow e^+ + (A,Z-2)^*$. 3) Reactions producing muons through muonic neutrino absorption by nuclei inside the stellar environment or at the terrestrial nuclear detectors (see **Section 6** and **Section 7**). Below we will discuss briefly some recent results obtained for the process of **Eq. 2** in connection with terrestrial relevant experiments.

An exclusive capture rate, $\Lambda_{i\rightarrow f}$, of the process (2), for a transition from the initial $|i\rangle$ to a final $|f\rangle$ state of the muonic atom (in laboratory conditions), takes the form (Giannaka and Kosmas, 2015a).

$$\Lambda_{i\rightarrow f} = \frac{2G^2E_f^2}{2J_i+1} W_f \Big[\langle J_f \| \Phi_\mu \Big(\hat{\mathcal{M}}_J - \hat{\mathcal{L}}_J \Big) \| J_i \rangle^2 + | \langle J_f \| \Phi_\mu \Big(\hat{\mathcal{T}}_J^{el} - \hat{\mathcal{T}}_J^{magn} \Big) \| J_i \rangle |^2 \Big], \tag{3}$$

where $\Phi_\mu(\mathbf{r})$ represents the exact bound muon wave function (for the ground state of the muon-nucleus system, the muonic atom). From the latter expression exact muon-capture rates, by using a realistic bound-muon wave function through solving numerically the Schroedinger (Kosmas and Lagaris, 2002) or Dirac (Tsoulos et al., 2019) equations, may be obtained (Jokiniemi et al., 2021). Multipole muon-capture transition rates, referred to a given multipolarity Λ_{J^π}, but also total muon capture rates, have been recently obtained by various research groups (Giannaka and Kosmas, 2015a). The evaluation of partial and total rates of such muonic processes was mostly realized by employing approximate wave functions for the bound muons in nuclei (Kosmas and Oset, 1996; Giannaka and Kosmas, 2015a; Giannaka and Kosmas, 2015b).

In **Figures 1**, **2** we show some multipole transition rates for the ^{48}Ti, ^{56}Fe, ^{66}Zn and ^{90}Zr isotopes obtained within the context of the *pn* QRPA. Such calculations indicate the dominance of $J^\pi = 1^-$ and 1^+ multipolarities in the studied nuclear isotopes. Moreover, individual contribution of Polar-vector, Axial-vector and the overlap part into the total muon-capture rate have also been obtained (Giannaka and Kosmas, 2015a). Furthermore, in **Table 1**, the total muon capture rates obtained by using the pn-QRPA for the light nuclei ^{28}Si and ^{32}S (with the free nucleon coupling constant $g_A = 1.262$), and for the medium weight nuclei ^{48}Ti, ^{56}Fe, ^{66}Zn and ^{90}Zr (with $g_A = 1.135$), are compared with the available experimental data as well as with the theoretical rates of Ref. (Zinner et al., 2006). For additional results the reader is referred to Ref. (Giannaka and Kosmas, 2015a; Giannaka and Kosmas, 2015b).

The nuclear method used offers the possibility of estimating separately the individual contributions to the total and partial rates of the polar-vector and axial-vector components of the weak-interaction Hamiltonian for each accessible final state of the

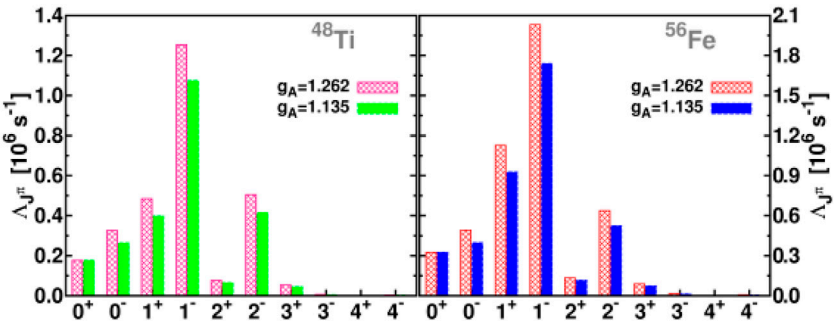

FIGURE 1 | Contribution of multipole transition rates Λ_{J^π} (up to $J^\pi = 4^\pm$) into the total muon capture rate for the ^{48}Ti and ^{56}Fe isotopes with inclusion (filled histograms) and without inclusion (double dashed histogramms) of the g_A quenching effect. The dominance of $J^\pi = 1^-$ and 1^+ multipolarities is obvious for all nuclei.

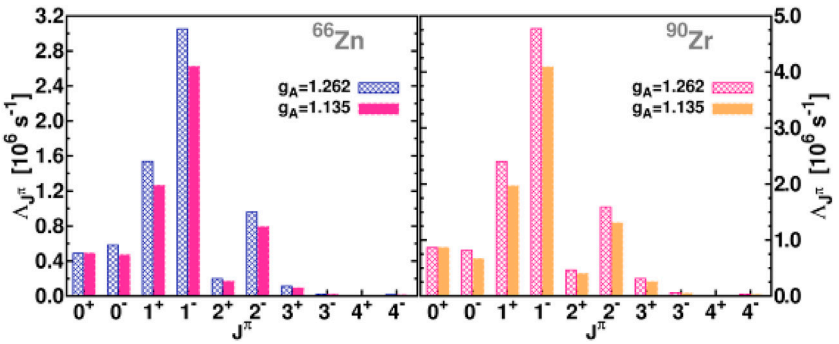

FIGURE 2 | Same as in **Figure 1** but here the muon capture rate refers to the ^{66}Zn and ^{90}Zr isotopes.

TABLE 1 | Individual contribution of Polar-vector, Axial-vector and Overlap part into the total muon-capture rate. Also, the total muon capture rates obtained by using the pn-QRPA with 1) the quenched value of $g_A = 1.135$, for the medium-weight nuclei ^{48}Ti,^{56}Fe,^{66}Zn and ^{90}Zr and 2) the free nucleon coupling constant $g_A = 1.262$, for the light nuclei ^{28}Si and ^{32}S, are compared with the available experimental data and with the theoretical total rates of Ref. (Zinner et al., 2006).

Total muon-capture rates $\Lambda_{tot}(\times 10^6)s^{-1}$

Nucleus	pn-QRPA calculations				Experiment	RPA
	Λ^{V}_{tot}	Λ^{A}_{tot}	Λ^{VA}_{tot}	Λ_{tot}	Λ^{exp}_{tot}	Λ^{theor}_{tot} (Zinner et al., 2006)
^{28}Si	0.150	0.751	-0.009	0.892	0.871	0.823
^{32}S	0.204	1.078	-0.017	1.265	1.352	1.269
^{48}Ti	0.628	1.902	-0.081	2.447	2.590	2.214
^{56}Fe	1.075	3.179	-0.129	4.125	4.411	4.457
^{66}Zn	1.651	4.487	-0.204	5.934	5.809	4.976
^{90}Zr	2.679	7.310	-0.357	9.631	9.350	8.974

daughter nucleus. One of our main goals is to provide a reliable description of the charge-changing transitions matrix elements entering the description of other similar semileptonic nuclear processes like the charged-current (muonic) neutrino-nucleus reactions, the electron capture on nuclei, the single $\beta^\pm$-decay modes, etc., which play important role in currently interesting laboratory and astrophysical applications like the neutrino detection through lepton-nucleus interaction probes and neutrino nucleo-synthesis (Kolbe et al., 2003). Such results can also be useful in various ongoing muon capture experiments at Paul Scherrer Institute (PSI), at Fermilab, at Japan Proton Accelerator Research Complex (JPARC), and at the Research Center for Nuclear Physics (RCNP), Osaka University (Hashim et al., 2018; Ejiri, 2019; Hashim and Ejiri, 2021).

Recently, various sensitive experiments take advantage of the powerful muon beams produced in the above well-known muon factories for standard and nonstandard muon physics probes (Marketin et al., 2009; Cook et al., 2017; Hashim et al., 2018; Jokiniemi et al., 2019; Hashim and Ejiri, 2021). Among the standard-model probes, those involving muon capture on nuclei, specifically those emitting X-rays and/or several particles (p, n, α, etc.) after μ-capture (which are important for understanding the rates and spectra of these particles) are intensively investigated (Hashim et al., 2018; Hashim and Ejiri, 2021). For example, at PSI researchers are interested in experiments based on the emission of charged particles from the nuclei muonic atoms of Al, Si, and Ti or neutron emission following muon capture from Fe, Ca, Si, and Al (Hashim et al., 2018; Hashim and Ejiri, 2021). Also very recently, in the highly intense facilities of Muon Science Innovation Commission (MuSIC) at RCNP, nuclear muon capture reactions on Mo,

Pb, etc., are planned to study nuclear weak responses for neutrino reactions, etc., (Hashim et al., 2018; Jokiniemi et al., 2019; Hashim and Ejiri, 2021; Jokiniemi et al., 2021). For such experiments, it is important to know the ordinary muon capture rates to the final (excited) states of the daughter nucleus, before proceeding to event rates of emitted X-rays or particles through de-excitation processes (Cook et al., 2017; Hashim and Ejiri, 2021).

4.1 Accurate Calculation of Muon-Nucleus Overlap Integrals Entering Muonic Reactions

The evaluation of reliable predictions in μ^--capture and e^--capture required for various physical observables (Giannaka and Kosmas, 2015b; Giannaka et al., 2021), must be based on accurate muon and electron wave functions [coming out of solutions of the Schroedinger (Kosmas and Lagaris, 2002) and Dirac (Giannaka et al., 2021) equations] obtained through the application of advanced algorithms (Kosmas and Vlachos, 2010; Kosmas and Leyendecker, 2015; Kosmas and Vlachos, 2016; Kosmas and Leyendecker, 2018). Recently, for the solution of the Dirac equations a fast algorithm has been derived by our group within the neural networks and stochastic optimization techniques (Giannaka et al., 2021).

Three intelligent independent algorithms, namely the Genetic algorithms, the Particle Swarm Optimization and the Simulated Annealing method (Kosmas and Vlachos, 2012) each of them with individual advantages, have been incorporated in the same numerical method (Giannaka et al., 2021). Its use is favored from intuitive, theoretical and practical arguments, since appropriate multi-parametric expressions representing the radial Dirac wave functions i.e., its small (bottom) and large (top) components for a bound muon orbiting around complex nuclear system, are optimized. These parameters reflect those of the assumed feed-forward artificial neural network (Kosmas and Lagaris, 2002), applied to obtain the ground state wave function describing a muon-nucleus system (muonic atom). From a computational point of view, the training in this method is performed by using the DiracSolver software package that proved to be both convenient and efficient (Tsoulos et al., 2019) and offers the possibility to be effectively applied in other atomic, nuclear and molecular systems. Among the interesting applications of the DiracSolver algorithm are the calculations of the up (large) and bottom (small) components of the radial wave functions for bound leptons in the Coulomb field of nuclei (atoms) as, electron (e^-), muon (μ^-) and tau (τ^-), in the field of complex nuclei (Tsoulos et al., 2019; Jokiniemi et al., 2021).

In the Dirac Hamiltonian, the potential energy $V(\mathbf{r})$ describing the extended nuclear Coulomb field, created by the nuclear charge density distribution $\rho(\mathbf{r})$, is calculated as (Kosmas and Lagaris, 2002; Tsoulos et al., 2019).

$$V(\mathbf{r}) = -e^2 \int \frac{\rho(\mathbf{r}')}{|\mathbf{r}-\mathbf{r}'|} d^3\mathbf{r}', \tag{4}$$

where the (finite size) nuclear charge density $\rho(\mathbf{r})$ is taken from electron scattering experimental data (De Vries et al., 1987). For the chosen nuclear systems (assuming spherically symmetric charge distributions) the radial charge density entering **Eq. 4** is described by two-parameter Fermi distributions extracted from model-independent analysis of electron scattering data (De Vries et al., 1987). It should be also noted that, for the Dirac solutions, in addition, to the above potential $V(r)$, the rather significant vacuum polarization correction, described by an effective potential V_{vp} [see e.g., Ref. (Kosmas and Lagaris, 2002)] is also considered.

Detailed calculations of the known muon-nucleus overlap integrals, entering the partial and total rates of the ordinary muon capture discussed above, could be obtained through the accurate muon wave functions $\Phi_\mu(\mathbf{r})$ inserted in **Eq. 3** (Jokiniemi et al., 2021). In ref. Giannaka et al. (2021) specifically, we concentrate on the prominent nuclear systems ^{28}Si and ^{64}Zn isotopes. By using such wave functions, one may perform accurate muon capture rate calculations for currently interesting nuclear isotopes (e.g., ^{28}Si, ^{32}S, ^{48}Ti, ^{56}Fe, ^{66}Zn and ^{90}Zr studied previously by using a mean value of the ground state muon wave functions) (Giannaka and Kosmas, 2015a). The reader is also referred to the recent works by Jokiniemi et al. (2021) for recent similar accurate calculations.

Before closing this Section, we should stress that current Earth bound detectors of high energy supernova neutrinos (e.g., muonic neutrinos, see **Section 7.1**) are based on signals created through charged-current reactions taking place with the detector materials (involving the ν_μ-nucleus reaction). The latter processes are particle conjugate reactions of the lepton-nucleus capture including the μ^--capture on nuclei which is, for this reason extensively discussed in the present article and is studied by many authors, see, e.g., Ref. (Kolbe et al., 2000; Kosmas et al., 2001; Zinner et al., 2006; Giannaka and Kosmas, 2015a; Jokiniemi et al., 2021) and references therein. The production of the aforementioned high energy supernova neutrinos (which are mostly the heavy flavor neutrinos ν_μ, ν_τ and their anti-particles) are closely related to processes taking place in the late stages of core-collapse SN and also the muonization process (see below) (Bollig et al., 2017; Fischer et al., 2020).

4.2 Muons Inside Core-Collapse Supernovae Environment

In the stellar interior, free muons (μ^-) may be produced through the particle conjugate processes of **Eq. 2** taking place when the temperature is high enough or the matter-density in the stellar interior is high enough so that the chemical potential difference of nucleons, $\lambda_n - \lambda_p$, or the interaction potential difference, $U_n - U_p$, reach the muon rest mass (m_μ = 105.6 MeV). In such cases, the muonization occurs in the stellar interior mainly through the semi-leptonic processes (Bollig et al., 2017; Fischer et al., 2020).

$$\nu_\mu + n \rightarrow \mu^- + p$$
$$\nu_\mu + (A, Z) \rightarrow \mu^- + (A, Z+1)$$

The latter semi-leptonic nuclear processes always dominate at high neutrino energies E_ν due to larger nuclear matrix elements. The charged current reactions of nucleons and nuclei with the

high energy leptons (muon anti-neutrinos, $\tilde{\nu}_\mu$, and muon neutrinos, ν_μ, as well as the negative muon μ^-, and the positive muon μ^+) are crucial. Reaction rates of all the relevant weak processes which involve μ^- or ν_μ are required as input in the numerical simulations for the description of muonization mechanism inside the hot and dense stellar interior (Bollig et al., 2017; Fischer et al., 2020).

Recent calculations (Fischer et al., 2020) for the semileptonic reactions involving the μ^- with large energy-momenta transfer concluded that the pseudoscalar coupling term in the hadronic weak current (normally this is neglected for ν_e reactions), is as important as the weak magnetism. On the other hand, the effects of nucleon form factors become significant as the energy-momenta transfer increases and they must be considered rather equally important as the weak magnetism and the pseudoscalar corrections.

5 THE ELECTRON CAPTURE ON NUCLEI

The process of bound-electron capture by a nucleus (analogous to the ordinary muon capture), called also orbital (ordinary) electron capture, is represented by the reaction (Giannaka and Kosmas, 2015b).

$$e_b^- + (A, Z) \rightarrow (A, Z-1)* + \nu_e, \tag{5}$$

(e_b^- denotes a bound electron). In the latter process, the daughter nucleus appears at a definite energy level while, in general, the outgoing neutrino may carry off a portion of the available energy in process (5). Because process 5) is a charge-changing one (charge transfer occurs from the parent to the daughter nucleus), it is possible that, part of the available energy may escape as a γ-ray photon, so that only the remaining energy is carried away by the neutrino. This means that transitions to intermediate states, giving a continuous energy spectrum, are allowed. As a result, the maximum possible energy of the emitted γ-ray photon corresponds to the case in which the neutrino carries a very small (approximately zero) energy equal to the energy of its production. Consequently, the maximum endpoint energy of the above γ-ray which is measured experimentally, is equal to the energy available in the orbital electron capture process. This, for example, in the case of ^{59}Ni is $E_\gamma = 1.065$ MeV, in ^{65}Zn it is $E_\gamma = 1.114$ MeV, and in ^{60}Co it is $E_\gamma = 1.320$ MeV. Thus, the maximum neutrino energy E_ν is rather low (lower than $E_e \leq 3\, m_e \approx 1.5$ MeV).

The ordinary electron capture differs from the stellar electron capture which takes place under the conditions of the stellar environment, i.e., core densities between $10^9\, g\, cm^{-3} \leq \rho \leq 10^{12}\, g\, cm^{-3}$ and temperatures $10^9 \leq T \leq 10^{12}\, K$ (Nabi et al., 2007a; Nabi et al., 2007b; Nabi, 2011; Giannaka and Kosmas, 2015b; Nabi and Riaz, 2019). This process is crucial for the dynamics of the core collapse of massive stars and it is more interesting in nuclear astrophysics. In the hot and dense stellar environment, electrons (e^-) have total energy $E_e \lessapprox 30, -, 50$ MeV, so the relevant nuclear calculations of the cross sections of process 5) in order to be translated to stellar cross sections through the folding procedure must have E_e up to this energy region (see below) (Giannaka and Kosmas, 2015b).

Within the J-projected multipole decomposition formalism of Donnelly-Walecka, the differential cross section of electron capture on nuclei under laboratory conditions takes the form

$$\frac{d\sigma_{ec}}{d\Omega} = \frac{G_F^2 cos^2\theta_c}{2\pi}\frac{F(Z,E_e)}{(2J_i+1)}\cdot\Big\{\sum_{J\geq 1}\mathcal{W}(E_e,E_\nu)\{[1-\alpha cos\Phi + bsin^2\Phi]\Big[|\langle J_f\|\hat{\mathcal{T}}_J^{mag}\|J_i\rangle|^2 + \Big|\langle J_f\|\hat{\mathcal{T}}_J^{el}\|J_i\rangle|^2\Big] - \Big[\frac{(\varepsilon_i+\varepsilon_f)}{q}(1-\alpha cos\Phi) - d\Big]2Re\langle J_f\|\hat{\mathcal{T}}_J^{mag}\|J_i\rangle\langle J_f\|\hat{\mathcal{T}}_J^{el}\|J_i\rangle^*\} + \sum_{J\geq 0}\mathcal{W}(E_e,E_\nu)\Big\{(1+\alpha cos\Phi)|\langle J_f\|\hat{\mathcal{M}}_J\|J_i\rangle|^2 + (1+\alpha cos\Phi - 2bsin^2\Phi)|\langle J_f\|\hat{\mathcal{L}}_J\|J_i\rangle|^2 - \Big[\frac{\omega}{q}(1+\alpha cos\Phi)+d\Big]2Re\langle J_f\|\hat{\mathcal{L}}_J\|J_i\rangle\langle J_f\|\hat{\mathcal{M}}_J\|J_i\rangle^*\Big\}\Big\} \tag{6}$$

The latter expression is consistent with **Eq. 1**. The kinematical parameters α, b, d are given e.g., in Chasioti and Kosmas (2009). In the above equation, Φ represents the scattering angle (for forward scattering, used by many authors, $\Phi = 0$) while $\omega_{if} = E_f - E_i$ denotes the excitation energy of the daughter nucleus. The energy E_ν of the outgoing neutrino in the reaction (5), due to energy conservation, is written as

$$E_\nu = E_e - Q - \omega_{if}, \tag{7}$$

where Q is the known Q-value determined from the experimental masses of the parent (M_i) and the daughter (M_f) nuclei as $Q = M_f - M_i$ (Dean et al., 1998).

Based on **Eq. 6** one may perform state-by-state calculations on the electron capture differential cross sections with respect to the excitation energy $d\sigma/d\omega$ defined by

$$\Big[\frac{d\sigma}{d\omega}\Big]_{J_f^\pi} \equiv \int\frac{d\sigma_{ec}}{d\Omega}d\Omega = \frac{G_F^2 cos^2\theta_c}{2\pi}\frac{F(Z,E_e)}{(2J_i+1)}\cdot\Big\{\int d\Omega\mathcal{W}(E_e,E_\nu)\Big\{[1-\alpha cos\Phi + bsin^2\Phi]\Big[|\langle J_f\|\hat{\mathcal{T}}_J^{mag}\|J_i\rangle|^2 + \Big|\langle J_f\|\hat{\mathcal{T}}_J^{el}\|J_i\rangle|^2\Big] - \Big[\frac{(\varepsilon_i+\varepsilon_f)}{q}(1-\alpha cos\Phi) - d\Big]2Re\langle J_f\|\hat{\mathcal{T}}_J^{mag}\|J_i\rangle\langle J_f\|\hat{\mathcal{T}}_J^{el}\|J_i\rangle^* + (1+\alpha cos\Phi)|\langle J_f\|\hat{\mathcal{M}}_J\|J_i\rangle|^2 + (1+\alpha cos\Phi - 2bsin^2\Phi)|\langle J_f\|\hat{\mathcal{L}}_J\|J_i\rangle|^2 - \Big[\frac{\omega}{q}(1+\alpha cos\Phi)+d\Big]2Re\langle J_f\|\hat{\mathcal{L}}_J\|J_i\rangle\langle J_f\|\hat{\mathcal{M}}_J\|J_i\rangle^*\Big\}\Big\} \tag{8}$$

($J \equiv J^\pi$). By evaluating the exclusive e^--capture cross sections of **Eq. 8** for all multipolarities (usually it's enough for $J^\pi \leq 5^\pm$), for the interior of core-collapse supernova we consider incident electron energies $E_e \leq 50.0$ MeV, other authors consider E_e energies up to $E_e = 30\ MeV$ (Fantina et al., 2012; Dzhioev et al., 2020). In **Eq. 8** the transition matrix elements are considered to be between the ground state $|J_i\rangle = |i\rangle \equiv |0^+_{g.s.}\rangle$ for a spherical target nucleus and an excited state $|J_f^\pi\rangle \equiv |f\rangle$ of the resulting odd-odd nucleus. The cross sections as functions of the incident electron energy E_e are evaluated after integrating numerically **Eq. 6** over angles for each specific final state $|J_f^\pi\rangle$.

TABLE 2 | Total e^--capture cross sections (in $10^{-42}\ MeV^{-1}\ cm^2$) for $E_e = 25MeV$ in $^{66}Z_n$. The percentage of each multipolarity into the total e^--capture cross section, evaluated with our pn-QRPA code, are also tabulated here.

Positive parity			Negative parity		
J^π	$\sigma_e\ (\times 10^{-42}\frac{cm^2}{MeV})$	Portions (%)	J^π	$\sigma_e\ (\times 10^{-42}\frac{cm^2}{MeV})$	Portions (%)
0^+	31.164	25.96	0^-	5.288	4.41
1^+	52.779	43.98	1^-	13.409	11.14
2^+	6.921	5.77	2^-	3.262	2.72
3^+	5.499	4.58	3^-	0.905	0.75
4^+	0.244	0.20	4^-	0.299	0.25
5^+	0.208	0.17	5^-	0.042	0.04

In the pn-QRPA code employed in Giannaka and Kosmas (2015b), Giannaka (2015), the excitations of the daughter nucleus appear as sets of multipole states and provide the possibility to calculate the contribution to the total cross sections of each multipole set of states separately. The dependence of the differential cross sections on the excitation energy ω through the entire pn-QRPA spectrum of the daughter nucleus may be illustrated (by using a special code which rearranges all possible excitations with the corresponding cross sections) in ascending order of the respective excitation energy ω_{if} [see Ref. (Tsakstara and Kosmas, 2011b; Tsakstara and Kosmas, 2011a)]. In **Table 2**, we list some representative results for the total e^--capture cross sections in $^{66}Z_n$ (corresponding to electron energy $E_e = 25MeV$). The percentages of each low-spin multipolarity into the total e^--capture cross section evaluated with the p-n QRPA code, are also tabulated in this table. It is worth mentioning that, in calculating the original total electron capture cross sections, the use of a quenched value of the static axial-vector coupling constant g_A is necessary, for the renormalization of the transition matrix elements (Wildenthal, 1984; Zinner et al., 2006; Marketin et al., 2009). The coupling constant g_A enters the axial-vector form factors, $F_A(q^2)$, and in the QRPA calculations the free nucleon value of $g_A = 1.262$ is multiplied by a factor of about 0.8 (Wildenthal, 1984; Häusser et al., 1991; Zinner et al., 2006; Marketin et al., 2009).

5.1 e-Capture Cross Sections in Stellar Environment

In astrophysical environment, where the finite temperature T and the matter density ϱ effects can't be ignored (the initial nucleus is at finite temperature), the initial nuclear state must be a weighted sum over an appropriate energy distribution. Assuming that this distribution is of a Maxwell-Boltzmann type for the initial state $|i\rangle$ (Dean et al., 1998; Langanke and Martı´nez-Pinedo, 2000), the total e^--capture cross section is given by the expression (Paar et al., 2009).

$$\sigma(E_e,T) = \frac{G_F^2\cos^2\theta_c}{2\pi}\sum_i F(Z,E_e)\frac{(2J_i+1)e^{-E_i/(kT)}}{G(Z,A,T)} \times \sum_{f,J}\left(E_e - Q + E_i - E_f\right)^2\frac{|\langle i|\hat{O}_J|f\rangle|^2}{(2J_i+1)} \tag{9}$$

with $G(Z, A, T)$ the corresponding partition function (Paar et al., 2009) and O_J denoting any of the multipole tensor operators [see Appendix of Ref. (Giannaka and Kosmas, 2015b)]. In other words, the sum over initial states in **Eq. 9** denotes a thermal average of the initial energy levels. We should stress that, the first summation in **Eq. 9** includes as initial states, in addition to the ground state $|i\rangle$ of the parent nucleus, also some low-lying excited states. This is because in the interior of stars the parent nucleus appears in excited states that follow Boltzmann distributions. Such studies have been taking into consideration in Paar et al. (2009), Fantina et al. (2012) and references therein. For example, ^{48}T, ^{56}Fe and ^{66}Zn have 2^+ states below one MeV and their contributions can be large at high densities and temperatures.

Then, one may calculate the partial rate contributions of some specific individual multipolarities J^π by summing over the exclusive contributions of the multipole J^π states as

$$\left[\frac{d\sigma}{d\omega}\right]_{J^\pi}^{stel}(E_e,T,\omega) = \sum_f\left[\frac{d\sigma}{d\omega}\right]_{J_f^\pi}^{stel}(E_e,T,\omega) = \frac{G_F^2\cos^2\theta_c}{2\pi}\sum_i F(Z,E_e)\frac{(2J_i+1)e^{-E_i/(kT)}}{G(Z,A,T)} \times \sum_f\left(E_e - Q + E_i - E_f\right)^2\frac{|\langle i|\hat{O}_J|J_f^\pi\rangle|^2}{(2J_i+1)} \tag{10}$$

As an example, in **Figure 3** we illustrate the electron capture cross sections for the ^{66}Zn parent nucleus, being inside stellar environment with temperature T = 0.5 MeV (high temperature). They have been obtained by assuming that the incident electrons follow the Fermi-Dirac energy distribution.

We, furthermore, mention that in the central core of the stellar environment, the e^- (or positron e^+) spectrum is well described by the known Fermi-Dirac distribution function parametrized with the stellar temperature T and the chemical potential of the electron μ_e as (Juodagalvis et al., 2005).

$$S_{e,p} = \frac{1}{1 + exp\left[\left(E_e - \mu_{e,p}\right)/(k_BT)\right]}. \tag{11}$$

The positron chemical potential is simply $\mu_p = -\mu_e$, while the Firmi-Dirac distribution for the e^+ spectrum results from **Eq. 11** by replacing μ_e with μ_p. In addition, at core collapse supernova, the neutrinos released through the weak interaction processes that take place in the presence of nuclei (mostly with $45 \le A \le 65$) can escape (there is no-blocking of neutrinos in the phase space), i.e., $S_\nu \approx 0$.

In the above case, the connection of the matter density ϱ with the important quantity Y_e, i.e., the electron to baryon ratio, and the electron (positron) chemical potential μ_e (μ_p) is written as

$$\varrho Y_e = \frac{1}{\pi^2 N_A}\left(\frac{m_e c}{\hbar}\right)^3\int_0^\infty\left(S_e - S_p\right)p^2\,dp \tag{12}$$

S_e (S_p) is the electron's (positron's) distribution function, respectively, and N_A is the well known Avogadro number.

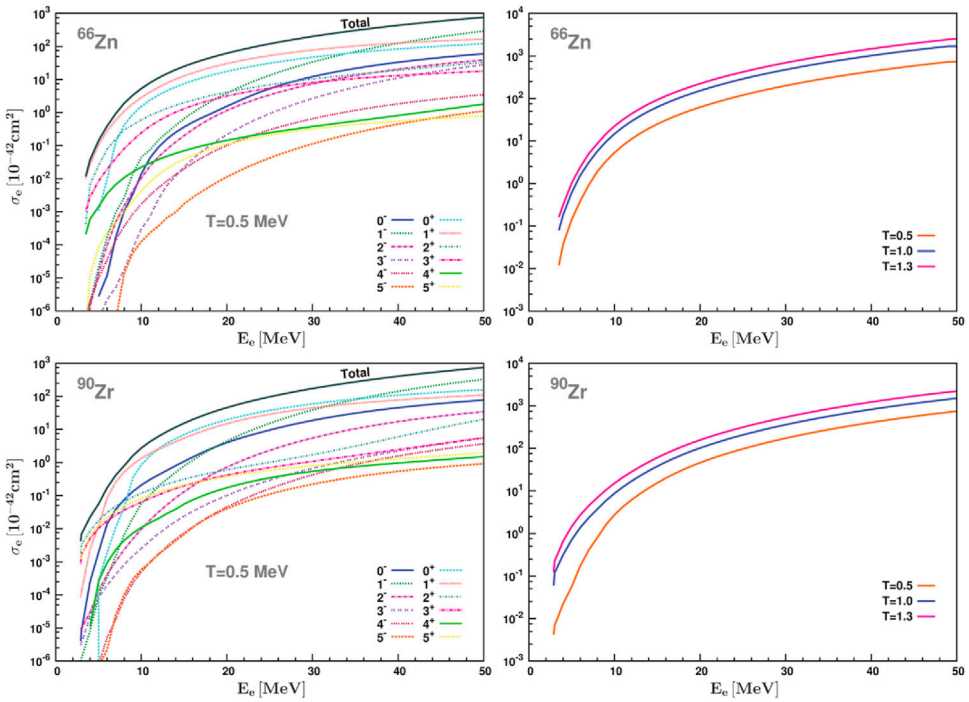

FIGURE 3 | Electron-capture cross sections for the ^{66}Zn and ^{90}Zr parent nuclei at high temperature (T = 0.5 MeV) in stellar environment obtained by assuming Fermi-Dirac distribution for the incident electrons. The total cross sections and the dominant individual multipole channels ($J^{\pi} \leq 5^{\pm}$) are demonstrated as functions of the incident electron energy E_e. Moreover, the right panels show the temperature dependence of the stellar cross sections for these nuclei. As can be seen, the cross sections increase doesn't follow the stellar Temperature increase and a saturation of the cross sections is expected to occur at higher Temperatures (about at T = 1.5–1.8 MeV) (Giannaka, 2015).

Furthermore, $p = \sqrt{w^2 - 1}$ represents the electron (positron) momentum, with w being the corresponding total energy (rest mass plus kinetic energy), both in units of $m_e c^2$. **Eq. 12**, is an important expression and may provide the Y_e for a given matter density ρ at the point in question inside the stars' core.

6 NEUTRINO–NUCLEUS REACTIONS IN STELLAR ENVIRONMENT

The charged-current neutrino absorption by nucleons and nuclei and the neutral current neutrino-nucleus scattering, represented by the reactions.

$$\nu_\ell + (A, Z) \rightarrow \ell^- + (A, Z+1), \tag{13}$$

$$\nu_\ell + (A, Z) \rightarrow \nu_\ell + (A, Z)^* \tag{14}$$

(with $\ell = e, \mu, \tau$), are significant semileptonic processes occurring inside stellar environment. Their cross sections and event rates are crucial and important for the description of the stars' evolution. In general, the calculations of charged-current ν-nucleus reaction cross sections, for processes involving μ^- and μ^+ (or ν_μ and $\tilde{\nu}_\mu$), require full relativistic treatment where the Dirac muon wave functions are employed (Giannaka et al., 2021). On the other hand, as in any semi-leptonic reaction, the hadronic weak current (including weak magnetism and pseudoscalar terms as well as weak form factor effects) must be accurately treated (Kosmas and Oset, 1996; Chasioti and Kosmas, 2009; Tsakstara and Kosmas, 2011a; Tsakstara and Kosmas, 2011b; Tsakstara and Kosmas, 2012). The muonic semi-leptonic processes dominate at $E_\nu \geq 110$ MeV and play essential role in μ^- production as well as in the known muonization process shortly after supernova core bounce. The impact of the various weak processes, and especially of the muonic reactions, was studied with emphasis by considering the specific conditions (with densities $\rho > 10^{13} g\, cm^{-3}$) encountered in proto-neutron star ≈ 0.4 s after the core-bounce (Dzhioev et al., 2020).

Nowadays, neutrinos generated in astrophysical sources (supernova explosion, interior of Sun and Earth, etc.,) are key-role particles in studying the structure and evolution of the star's interior, the thermonuclear reactions taking place inside star's, neutrino-driven mechanisms of core-collapse of massive stars, etc. The relevant observations, in conjunction with theoretical and phenomenological modeling offer further insight in deepening our knowledge on the fundamental interactions and the nuclear weak responses. Original neutrino-nucleus cross sections obtained with realistic nuclear structure calculations, e.g., using the QRPA method (Tsakstara and Kosmas, 2011a; Tsakstara and Kosmas, 2011b), through the application of the convolution procedure by adapting specific spectral distributions

describing supernova neutrino energy spectra, provide simulated signals of the detector responses expected to be recorded by terrestrial ν-detection experiments (Tsakstara and Kosmas, 2011a; Tsakstara and Kosmas, 2011b; Tsakstara and Kosmas, 2012).

Such convoluted cross sections, like the double-differential, $d^2\sigma(\omega)/d\omega$, the single differential, $d\sigma(\omega)/d\omega$, and the total, σ_{tot}, cross sections reflect the neutrino signals generated at the chosen nuclear isotopes in terrestrial detectors due to neutrinos emanating from specific ν-sources. Results like, for example, those of Refs. (Tsakstara and Kosmas, 2011a; Tsakstara and Kosmas, 2011b) demonstrate clearly the weak responses to pronounced low-spin multipoles (1^-, 1^+1, 2^+, 0^+, 2^-, etc.,) generated by supernova neutrino spectra in a specific detector medium. They show rich responses in the energy range 20, − , $30 \leq E_x \leq 100$, − , 120 MeV, which is relevant for low- and intermediate-energy supernova neutrinos, and also for neutral-current neutrino-nucleus scattering processes.

Moreover, reliable descriptions of the responses of various nuclear isotopes (Fe, Zn, Ge, Mo, Te, and others) provide precious information for the understanding of the isospin and spin-isospin nuclear responses for supernova physics, neutrino physics, the fundamental weak interactions, and specifically the SN dynamics and explosive neutrino-nucleosynthesis. Pursuing theoretical neutrino scattering calculations, at low and intermediate energies, is important in unraveling unknown properties of neutrinos and in understanding deeply their role in a plethora of open neutrino physics issues (Kosmas and Oset, 1996; Chasioti and Kosmas, 2009; Tsakstara and Kosmas, 2011a; Tsakstara and Kosmas, 2011b).

6.1 Neutrino Induced Nucleosynthesis

Inside the hot interior of massive stars, the neutrinos created through the various semi-leptonic processes mentioned above, may subsequently induce reactions leading to nucleo-synthesis of various (radioactive) isotopes as well as to the synthesis of new elements (Suzuki et al., 2006; Cheoun et al., 2012). As the interior of an evolved high mass star has layers (fusion shells) heavier and heavier nuclear isotopes are being synthesized as we move towards the center of the star (see **Section 2**) (Kolbe et al., 2003; Sieverding et al., 2018). Moreover, it is known that a set of important nuclides are produced by the neutrinos created during supernova explosions. The latter may create abundant nuclei in the outer stellar shells contributing this way to the synthesis of elements with dominant galactic abundances. Such nuclides produced in significant portion by neutrino nucleosynthesis are the: ^{7}Li, ^{11}B, ^{15}N, ^{19}F, ^{138}La, ^{180}Ta, and the radionuclides ^{22}Na and ^{26}Al (Sieverding et al., 2018).

In general, stellar neutrinos may induce nuclear reactions that contribute to the synthesis of new elements (ν-process). Several important processes of this type have been studied (Sieverding et al., 2019), as the ^{12}C(ν,$\nu'p$)^{11}B and ^{20}Ne(ν,$\nu'p$)^{19}F reactions which produce the quite abundant ^{19}F and ^{20}Ne nucleides. These reactions are mainly induced by the ν_x neutrinos, with $x = \mu, \tau$, which have larger average energies than ν_e and $\tilde{\nu}_e$ neutrinos (Tsakstara and Kosmas, 2011a; Tsakstara and Kosmas, 2011b). Furthermore, from detailed stellar evolution investigation, researchers concluded that the rare odd-odd heavy nuclides ^{138}La and ^{180}Ta are mainly products of the charged-current reactions ^{138}Ba$(\nu_e, e^-)^{138}$ La and ^{180}Hf$(\nu_e, e^-)^{180}$Ta and that the ν-process is rather sensitive to the spectra and luminosity of ν_e and ν_x neutrinos (note that these neutrinos have not been observed in the SN 1987a) (Suzuki et al., 2006; Cheoun et al., 2012).

6.2 Neutrino Spectra in Core Collapse Supernovae

The energy-spectra of neutrinos emanating from core-collapse SN resembles to the two-parameter Fermi-Dirac distribution (or to the two-parameter Power-Law distribution). They are of quasi-thermal shape, on peak pattern, which seems to be reliable for most of the SN phases (Langanke and Wiescher, 2001; Tsakstara and Kosmas, 2011a; Tsakstara and Kosmas, 2011b). As has been pointed out, the neutrino shock acceleration, which may create the non-thermal shape in the neutrino spectrum occurs in the early post-bounce phase (this argument is also supported by recent CCSN simulations). The main conclusions regarding the energy-spectra of such neutrinos may be summarized as follows. The neutrino shock acceleration is strongly ν-flavour dependent, so the heavy neutrinos ν_τ and $\tilde{\nu}_\tau$ may acquire energy up to about 200 MeV, while ν_μ and $\tilde{\nu}_\mu$ have similar spectra but up to about 120 MeV where a sharp cut-off appears. The spectra for ν_e and $\tilde{\nu}_e$ appear to be of quasi-thermal shape.

Recent studies of the neutrino spectra in massive stars core collapse supernovae have shown that the outcome of the neutrino emission (and, in particular, its time-dependence) is a combined result of the neutrino-induced reactions and the effect of the shock wave. The competition of these two effects depends sensitively on the radial position into the star at which the nucleo-synthesis reactions occur (Sieverding et al., 2018). In the latter work, the neutrino emission from the core of a collapsing star is considered as including the three major distinguishable phases. Such a discussion here goes beyond the scope of the present article and the reader is referred to Ref. (Langanke and Wiescher, 2001) for more details.

The detection of the high energy ν_μ and ν_τ neutrinos through charged-current reactions will be a clear evidence that neutrinos undergo flavour conversions which implies that, the neutrino shock acceleration offers the possibility of muon productions in Earth detectors. If muons would be observed in these detectors, this will be a precious information to put constraints on the neutrino oscillation parameters, which will open up the need this issue to be investigated in the future (Dzhioev et al., 2020; Nagakura and Hotokezaka, 2021). We should mention that, although up to now we haven't taken into account the neutral-current reactions of neutrinos with the detectors, in reality, they may play important role for the data analysis (Papoulias and Kosmas, 2018). Since these reactions are sensitive to all ν-flavours, by combining the NC data with those of the CC reactions, we may extract constraints on relevant transition probabilities from each heavy neutrino-

flavour to the other species. We also note that, it is expected the rapid drop off of neutrino distribution at $E_\nu \approx 100 - 120$ MeV to be more pronounced in neutral current reactions than that of the charged current, which would be a rather direct indication for the disappearance of ν_μ and $\tilde{\nu}_\mu$ around the energy of the core-collapse SN ν-source.

From the above discussion, one may conclude that, the survival probabilities of all neutrino-flavours constitute important quantities that may be inserted in various neutrino oscillation models. We must also remark that, in measuring the quite small event rates of the above high energy neutrinos, despite the fact that the neutrino shock acceleration increases them by a few orders of magnitude, the detection statistics on each detector will be rather poor. Hence, it will be crucial to combine the observed data of each neutrino detector in order to obtain reliable analyses of the high energy ν_μ and ν_τ neutrinos. The joint analysis will enable us to look for flavour-dependent features in the core-collapse SN neutrinos and put stringent constraints on the model parameters of neutrino oscillations in the future (Dzhioev et al., 2020; Nagakura and Hotokezaka, 2021).

7 THE ROLE OF SEMI-LEPTONIC PROCESSES IN TERRESTRIAL DETECTORS

A great class of Earth detectors aiming to detect cosmic neutrinos, are based on the charge-changing neutrino-nucleus reactions (13). In the other class of terrestrial detectors, aiming to detect neutrinos through the neutral current ν-nucleus scattering (14), the measured signal is the recoil energy of the nuclear-target isotope (detector medium). We mention that, some cosmic neutrino detectors on Earth are based on the scattering of neutrinos with the electrons or muons of the detector. Before closing this article, we consider of great interest to concentrate on the heavy neutrino detection in terrestrial ν-detectors proposed very recently focusing specifically on the muon production in extremely sensitive terrestrial experiments (Dzhioev et al., 2020; Nagakura and Hotokezaka, 2021).

7.1 Muon Production in Earth Detectors

In the operating and designed to operate at the Earth neutrino detectors, like the Super-Kamiokande (SK), the Hyper-Kamiokande (HK) and others, the muons (μ^- or μ^+) can be created from the supernova ν_μ and $\tilde{\nu}_\mu$ neutrinos if they carry energies larger than the muon's rest mass M_μ, i.e., $E_\nu > M_\mu$ (E_ν should exceed M_μ by at least the detector's threshold energy E_{thresh}). The detector signal may come out of charged current reactions taking place with the detector materials which are particle conjugate reactions of the muon capture on nuclei studied by many authors [see, e.g., Ref. (Giannaka and Kosmas, 2015a) and references therein]. As is well known, core-collapse SN neutrinos provide precious information to study various neutrino phenomena (neutrino properties, neutrino oscillation, etc.). The event rates on each detector, could be estimated on the bases of various scenarios of the neutrino shock acceleration, and the necessary conditions to observe a given number of events, relevant to charged-current reactions with ν_μ and $\tilde{\nu}_\mu$ in the early post-bounce phase (Nagakura and Hotokezaka, 2021). The expected number of events is small (less than 1 for all detectors), indicating that the muon production may not happen in this case. It should be noted, however, that there remains a possibility to detect them, in particular for Hyper-Kamiokande (HK) detector, by taking into account uncertainties of the parameters and the neutrino cross-sections.

Recent estimations have shown that, the possibilities for muons to be produced in terrestrial detectors, like the Super-Kamiokande (SK), HK, DUNE, JUNO etc., through core-collapse SN (CCSN) neutrino, is rather high if these neutrinos are created during the late post-bounce phase for failed CCSN (Nagakura and Hotokezaka, 2021). For example, these authors found that, about 10 muons may be produced in HK (few of them having energy $E_\nu \approx 150$ MeV). The muons created from such high energy neutrinos have large enough kinetic energy to produce observable signal by emitting Cherenkov lights in the HK detector. Furthermore, muon production may also occur in SK, but the detectability depends on other factors (e.g., the distance to the CCSN source is an important factor). We mention that, the charged current reaction $\nu - {}^{16}\mathrm{O}$, with the Oxygen of the water molecule, play dominant role for the muon productions in Water Cherenkov detectors.

As mentioned above, the distance to the CCSN source is an important parameter when discussing the detectability of the heavy flavor neutrinos. For example, the muon productions in DUNE and JUNO detectors seem to be unlikely if the CCSN distance is smaller than 10 kpc. However, the efficiency of neutrino shock acceleration depends on the mass accretion rate in the late post-bounce hence, ν_μ-detectability through muon productions. Furthermore detailed studies should be made with more quantitative arguments and statistical improvements regarding neutrino cross-sections with heavy nuclear detectors (Nagakura and Hotokezaka, 2021). In the early post-bounce phase, the muon production requires that the CCSN is located nearby about 5 kpc (for HK) and about 3 kpc (for SK). For other detectors the supernova should be very nearby, about 1 kpc (for DUNE) and about 0.5 kpc (for JUNO). In the late phase for failed CCSN, on the other hand, the threshold distance is increased by a factor of about 4 than that in the early phase, indicating muon productions likely occur in HK for all Galactic failed CCSN.

8 SUMMARY AND OUTLOOK

In this article, at first we review the role of the semi-leptonic weak interaction processes that involve leptons and nuclei in the late stages of stellar evolution, i.e., inside the hot and dense stellar environment. Then, we review the role of these processes in the relevant neutrino detection experiments that operate or have been planned to operate

in the near future at the Earth (underground, under ice, and under sea water). Such processes are of key role in the massive stars' evolution and specifically in the final stages of their life, i.e., the pre-supernova and the core-collapse supernova leading to the SN explosion phenomenon. We also focus on the neutrino producing charged-lepton capture, like the electron-capture and the muon-capture on nuclei, and, then, we discuss the neutrino absorbing reactions which are essential in the neutrino-driven explosive nucleo-synthesis. These processes are also significant in many ongoing and planned worldwide sensitive experiments aiming to detect astrophysical neutrinos which rely on the interactions of neutrinos with the bound nucleons inside atomic nuclei.

Such astrophysical neutrino signals provide a precious information on deciphering the inner dynamics of CCSN, from which researchers may extract important constraints on the neutrino oscillation parameters. In core-collapse supernova, the key-particle players are the heavy neutrinos, ν_μ with energies above 110 MeV and ν_τ neutrinos with energies up to about ≈ 200 MeV (in water Cherencov detectors). The neutrino energy, as suggested recently, is acquired through the known shock acceleration mechanism. Researches estimated that this effect occurs in the early post-bounce phase (about 50 ms after bounce) for all massive stellar collapse experiencing core bounce and would reoccur in the late phase (about 100 ms after bounce) for failed core-collapse supernovae. Due to the fact that the SN distance is crucial for the detectability of Galactic core-collapse SN, the event rate is not far from the sensitivity of operating detectors like the Hyper-Kamiokande, the Super-Kamiokande, the DUNE, and the JUNO, which offers new possibilities to detect high energy neutrinos by terrestrial detectors.

AUTHOR CONTRIBUTIONS

Software, writing–original draft preparation and visualization (OK), software, project administration and writing–original draft preparation (IT), conceptualization, methodology, supervision, project administration and funding acquisition (TK), writing–original draft preparation and formal analysis (PG).

FUNDING

This research is co-financed by Greece and the European Union (European Social Fund-ESF) through the Operational Programme "Human Resources Development, Education and Lifelong Learning 2014–2020" in the context of the project MIS-5047635. This review article was supported by the Special Account for Research Funds (Research Committee) of the University of Ioannina. OK acknowledges gratefully the support of the Engineering and Physical Sciences Research Council (EPSRC), UK, via grand EP/N026136/1.

REFERENCES

Akimov, D., Albert, J. B., An, P., Awe, C., Barbeau, P. S., Becker, B., et al. (2017). Observation of Coherent Elastic Neutrino-Nucleus Scattering. *Science.* 357, 1123–1126. doi:10.1126/science.aao0990

Aste, A., and Jourdan, J. (2004). Improved Effective Momentum Approximation for Quasielastic (e , e ′) Scattering off Highly Charged Nuclei. *Europhys. Lett.* 67, 753–759. doi:10.1209/epl/i2004-10113-x

Balasi, K. G., Langanke, K., and Martínez-Pinedo, G. (2015). Neutrino-Nucleus Reactions and Their Role for Supernova Dynamics and Nucleosynthesis. *Prog. Part. Nucl. Phys.* 85, 33–81. doi:10.1016/j.ppnp.2015.08.001

Bethe, H. A. (1990). Supernova Mechanisms. *Rev. Mod. Phys.* 62, 801–866. doi:10.1103/RevModPhys.62.801

Bollig, R., Janka, H.-T., Lohs, A., Martínez-Pinedo, G., Horowitz, C. J., and Melson, T. (2017). Muon Creation in Supernova Matter Facilitates Neutrino-Driven Explosions. *Phys. Rev. Lett.* 119, 242702. doi:10.1103/PhysRevLett.119.242702

Cantiello, M., Jermyn, A. S., and Lin, D. N. C. (2021). Stellar Evolution in AGN Disks. *ApJ.* 910, 94. doi:10.3847/1538-4357/abdf4f

Chasioti, V. C., and Kosmas, T. S. (2009). A Unified Formalism for the Basic Nuclear Matrix Elements in Semi-Leptonic Processes. *Nucl. Phys. A.* 829, 234–252. doi:10.1016/j.nuclphysa.2009.08.009

Cheoun, M.-K., Ha, E., Hayakawa, T., Chiba, S., Nakamura, K., Kajino, T., et al. (2012). Neutrino Induced Reactions Forv-Process Nucleosynthesis of92Nb and98Tc. *Phys. Rev. C.* 85, 065807. doi:10.1103/PhysRevC.85.065807

Cook, S., D'Arcy, R., Edmonds, A., Fukuda, M., Hatanaka, K., Hino, Y., et al. (2017). Delivering the World's Most Intense Muon Beam. *Phys. Rev. Accel. Beams.* 20, 030101. doi:10.1103/PhysRevAccelBeams.20.030101

De Vries, H., De Jager, C. W., and De Vries, C. (1987). Nuclear Charge-Density-Distribution Parameters From Elastic Electron Scattering. *At. Data Nucl. Data Tables.* 36, 495–536. doi:10.1016/0092-640x(87)90013-1

Dean, D. J., Langanke, K., Chatterjee, L., Radha, P. B., and Strayer, M. R. (1998). Electron Capture on Iron Group Nuclei. *Phys. Rev. C.* 58, 536–544. doi:10.1103/PhysRevC.58.536

Donnelly, T. W., and Peccei, R. D. (1979). Neutral Current Effects in Nuclei. *Phys. Rep.* 50, 1–85. doi:10.1016/0370-1573(79)90010-3

Donnelly, T. W., and Walecka, J. D. (1976). Semi-Leptonic Weak and Electromagnetic Interactions With Nuclei: Isoelastic Processes. *Nucl. Phys. A.* 274, 368–412. doi:10.1016/0375-9474(76)90209-8

Dzhioev, A. A., Langanke, K., Martínez-Pinedo, G., Vdovin, A. I., and Stoyanov, C. (2020). Unblocking of Stellar Electron Capture for Neutron-Rich N=50 Nuclei at Finite Temperature. *Phys. Rev. C.* 101, 025805. doi:10.1103/PhysRevC.101.025805

Ejiri, H. (2019). Nuclear Matrix Elements for β and ββ Decays and Quenching of the Weak Coupling gA in QRPA. *Front. Phys.* 7, 30. doi:10.3389/fphy.2019.00030

Ejiri, H., Suhonen, J., and Zuber, K. (2019). Neutrino-Nuclear Responses for Astro-Neutrinos, Single Beta Decays and Double Beta Decays. *Phys. Rep.* 797, 1–102. doi:10.1016/j.physrep.2018.12.001

Eramzhyan, R. A., Kuz'min, V. A., and Tetereva, T. V. (1998). Calculations of Ordinary and Radiative Muon Capture on 58,60,62Ni. *Nucl. Phys. A.* 642, 428–448. doi:10.1016/S0375-9474(98)00541-7

Fantina, A. F., Khan, E., Colò, G., Paar, N., and Vretenar, D. (2012). Stellar Electron-Capture Rates on Nuclei Based on a Microscopic Skyrme Functional. *Phys. Rev. C.* 86, 035805. doi:10.1103/PhysRevC.86.035805

Fischer, T., Guo, G., Martínez-Pinedo, G., Liebendörfer, M., and Mezzacappa, A. (2020). Muonization of Supernova Matter. *Phys. Rev. D.* 102, 123001. doi:10.1103/PhysRevD.102.123001

Fuller, G. M., Fowler, W. A., and Newman, M. J. (1982). Stellar Weak Interaction Rates for Intermediate-Mass Nuclei. II - A = 21 to A = 60. *ApJ.* 252, 715–740. doi:10.1086/159597

Gastaldo, L., Blaum, K., Chrysalidis, K., Day Goodacre, T., Domula, A., Door, M., et al. (2017). The Electron Capture in 163Ho Experiment - ECHo. *Eur. Phys. J. Spec. Top.* 226, 1623–1694. doi:10.1140/epjst/e2017-70071-y

Giannaka, P. G., Kosmas, O., Tsoulos, I., and Kosmas, T. S. (2021). Exploiting Dirac Equations Solution for Exact Integral Calculations in Processes of Muonic Atoms. *J. Phys. Conf. Ser.* 1730, 012140. doi:10.1088/1742-6596/1730/1/012140

Giannaka, P. G., and Kosmas, T. S. (2015a). Detailed Description of Exclusive Muon Capture Rates Using Realistic Two-Body Forces. *Phys. Rev. C.* 92, 014606. doi:10.1103/PhysRevC.92.014606

Giannaka, P. G., and Kosmas, T. S. (2015b). Electron Capture Cross Sections for Stellar Nucleosynthesis. *Adv. High Energ. Phys.* 2015, 1–11. doi:10.1155/2015/398796

Giannaka, P. G., and Kosmas, T. S. (2013). Electron-capture and its Role to Explosive Neutrino-Nucleosynthesis. *J. Phys. Conf. Ser.* 410, 012124. doi:10.1088/1742-6596/410/1/012124

Giannaka, P. (2015). *Stellar and Explosive Nucleosynthesis Producing and Induced by Neutrinos*. Ioannina: Ioannina University Press. doi:10.12681/eadd/39690

Hashim, I. H., and Ejiri, H. (2021). Ordinary Muon Capture for Double Beta Decay and Anti-Neutrino Nuclear Responses. *Front. Astron. Space Sci.* 8, 82. doi:10.3389/fspas.2021.666383

Hashim, I. H., Ejiri, H., Shima, T., Takahisa, K., Sato, A., Kuno, Y., et al. (2018). Muon Capture Reaction on Mo100 to Study the Nuclear Response for Double-β Decay and Neutrinos of Astrophysics Origin. *Phys. Rev. C.* 97, 014617. doi:10.1103/PhysRevC.97.014617

Häusser, O., Vetterli, M. C., Fergerson, R. W., Glashausser, C., Jeppesen, R. G., Smith, R. D., et al. (1991). Nuclear Response in theFe54(p→,p→') Reaction at 290 MeV. *Phys. Rev. C.* 43, 230–249. doi:10.1103/physrevc.43.230

Hirschi, R., Meynet, G., and Maeder, A. (2004). Stellar Evolution With Rotation. *A&A.* 425, 649–670. doi:10.1051/0004-6361:20041095

Hix, W. R., Messer, O. E. B., Mezzacappa, A., Liebendörfer, M., Sampaio, J., Langanke, K., et al. (2003). Consequences of Nuclear Electron Capture in Core Collapse Supernovae. *Phys. Rev. Lett.* 91, 201102. doi:10.1103/PhysRevLett.91.201102

Jokiniemi, L., Suhonen, J., Ejiri, H., and Hashim, I. H. (2019). Pinning Down the Strength Function for Ordinary Muon Capture on 100mo. *Phys. Lett. B.* 794, 143–147. doi:10.1016/j.physletb.2019.05.037

Jokiniemi, L., Suhonen, J., and Kotila, J. (2021). Comparative Analysis of Nuclear Matrix Elements of 0ν β+β+ Decay and Muon Capture in 106Cd. *Front. Phys.* 9, 142. doi:10.3389/fphy.2021.652536

Jones, S., Röpke, F. K., Pakmor, R., Seitenzahl, I. R., Ohlmann, S. T., and Edelmann, P. V. F. (2016). Do electron-Capture Supernovae Make Neutron Stars? *A&A.* 593, A72. doi:10.1051/0004-6361/201628321

Juodagalvis, A., Langanke, K., Martínez-Pinedo, G., Hix, W. R., Dean, D. J., and Sampaio, J. M. (2005). Neutral-Current Neutrino-Nucleus Cross Sections for Nuclei. *Nucl. Phys. A.* 747, 87–108. doi:10.1016/j.nuclphysa.2004.09.005

Kajino, T., Mathews, G. J., and Hayakawa, T. (2014). Neutrinos in Core-Collapse Supernovae and Nucleosynthesis. *J. Phys. G: Nucl. Part. Phys.* 41, 044007. doi:10.1088/0954-3899/41/4/044007

Kolbe, E., Langanke, K., Martínez-Pinedo, G., and Vogel, P. (2003). Neutrino-Nucleus Reactions and Nuclear Structure. *J. Phys. G: Nucl. Part. Phys.* 29, 2569–2596. doi:10.1088/0954-3899/29/11/010

Kolbe, E., Langanke, K., and Vogel, P. (1997). Comparison of Continuum Random Phase Approximation and the Elementary Particle Model for the Inclusive Muon Neutrino Reaction on 12C. *Nucl. Phys. A.* 613, 382–396. doi:10.1016/S0375-9474(96)00417-4

Kolbe, E., Langanke, K., and Vogel, P. (2000). Muon Capture on Nuclei WithN>Z,random Phase Approximation, and In-Medium Value of the Axial-Vector Coupling Constant. *Phys. Rev. C.* 62, 055502. doi:10.1103/PhysRevC.62.055502

Kosmas, O., and Leyendecker, S. (2015). Family of Higher Order Exponential Variational Integrators for Split Potential Systems. *J. Phys. Conf. Ser.* 574, 012002. doi:10.1088/1742-6596/574/1/012002

Kosmas, O., and Leyendecker, S. (2018). Variational Integrators for Orbital Problems Using Frequency Estimation. *Adv. Comput. Math.* 45, 1–21. doi:10.1007/s10444-018-9603-y

Kosmas, O. T., and Vlachos, D. S. (2010). Phase-Fitted Discrete Lagrangian Integrators. *Computer Phys. Commun.* 181, 562–568. doi:10.1016/j.cpc.2009.11.005

Kosmas, O. T., and Vlachos, D. S. (2012). Simulated Annealing for Optimal Ship Routing. *Comput. Operations Res.* 39, 576–581. doi:10.1016/j.cor.2011.05.010

Kosmas, O., and Vlachos, D. S. (2016). A Space-Time Geodesic Approach for Phase Fitted Variational Integrators. *J. Phys. Conf. Ser.* 738, 012133. doi:10.1088/1742-6596/738/1/012133

Kosmas, T., Faessler, A., Šimkovic, F., and Vergados, J. (1997a). State-by-State Calculations for All Channels of the Exotic (μ-,e-) Conversion Process. *Phys. Rev. C.* 56, 526–534. doi:10.1103/physrevc.56.526

Kosmas, T. S., Faessler, A., and Vergados, J. D. (1997b). The New Limits of the Neutrinoless , Conversion Branching Ratio. *J. Phys. G: Nucl. Part. Phys.* 23, 693–703. doi:10.1088/0954-3899/23/6/008

Kosmas, T. S., Kovalenko, S., and Schmidt, I. (2001). B-Quark Mediated Neutrinoless μ−-e− Conversion in Presence of R-Parity Violation. *Phys. Lett. B.* 519, 78–82. doi:10.1016/s0370-2693(01)01096-6

Kosmas, T. S., and Lagaris, I. E. (2002). On the Muon Nucleus Integrals Entering the Neutrinoless e Conversion Rates. *J. Phys. G: Nucl. Part. Phys.* 28, 2907–2920. doi:10.1088/0954-3899/28/12/302

Kosmas, T. S., and Oset, E. (1996). Charged Current Neutrino-Nucleus Reaction Cross Sections at Intermediate Energies. *Phys. Rev. C.* 53, 1409–1415. doi:10.1103/PhysRevC.53.1409

Kosmas, T. S., Vergados, J. D., Civitarese, O., and Faessler, A. (1994). Study of the Muon Number Violating (μ−, e− Conversion in a Nucleus by Using Quasi-Particle RPA. *Nucl. Phys. A.* 570, 637–656. doi:10.1016/0375-9474(94)90077-9

Langanke, K., Kolbe, E., and Dean, D. J. (2001). Unblocking of the Gamow-Teller Strength in Stellar Electron Capture on Neutron-Rich Germanium Isotopes. *Phys. Rev. C.* 63, 032801. doi:10.1103/PhysRevC.63.032801

Langanke, K., and Martínez-Pinedo, G. (2003). Nuclear Weak-Interaction Processes in Stars. *Rev. Mod. Phys.* 75, 819–862. doi:10.1103/RevModPhys.75.819

Langanke, K., Martínez-Pinedo, G., Sampaio, J. M., Dean, D. J., Hix, W. R., Messer, O. E. B., et al. (2003). Electron Capture Rates on Nuclei and Implications for Stellar Core Collapse. *Phys. Rev. Lett.* 90, 241102. doi:10.1103/PhysRevLett.90.241102

Langanke, K., and Martinez-Pinedo, G. (1998). Supernova Electron Capture Rates for 55co and 56ni. *Phys. Lett. B.* 436, 19–24. doi:10.1016/S0370-2693(98)00892-2

Langanke, K., and Martínez-Pinedo, G. (1999). Supernova Electron Capture Rates on Odd-Odd Nuclei. *Phys. Lett. B.* 453, 187–193. doi:10.1016/S0370-2693(99)00363-9

Langanke, K., and Martínez-Pinedo, G. (2000). Shell-model Calculations of Stellar Weak Interaction Rates: II. Weak Rates for Nuclei in the Mass Range in Supernovae Environments. *Nucl. Phys. A.* 673, 481–508. doi:10.1016/s0375-9474(00)00131-7

Langanke, K., Martínez-Pinedo, G., and Zegers, R. G. T. (2021). Electron Capture in Stars. *Rep. Prog. Phys.* 84, 066301. doi:10.1088/1361-6633/abf207

Langanke, K., and Wiescher, M. (2001). Nuclear Reactions and Stellar Processes. *Rep. Prog. Phys.* 64, 1657–1701. doi:10.1088/0034-4885/64/12/202

Marketin, T., Paar, N., Nikšić, T., and Vretenar, D. (2009). Relativistic Quasiparticle Random-Phase Approximation Calculation of Total Muon Capture Rates. *Phys. Rev. C.* 79, 054323. doi:10.1103/PhysRevC.79.054323

Nabi, J.-U. (2011). Ground and Excited States Gamow-Teller Strength Distributions of Iron Isotopes and Associated Capture Rates for Core-Collapse Simulations. *Astrophys Space Sci.* 331, 537–554. doi:10.1007/s10509-010-0477-9

Nabi, J.-U., Rahman, M.-U., and Sajjad, M. (2007a). Electron and Positron Capture Rates on 55Co in Stellar Matter. *Braz. J. Phys.* 37, 1238–1245. doi:10.1590/s0103-97332007000800009

Nabi, J.-U., Sajjad, M., and Rahman, G. I. K. (2007b). *Electron Capture Rates on Titanium Isotopes in Stellar*. Acta Physica Polonica B 38, 3203–3223. arXiv: [nucl-th] 1108.053.

Nabi, J.-U., and Riaz, M. (2019). Electron Capture Cross Sections and Nuclear Partition Functions for Fp-Shell Nuclei. *J. Phys. G: Nucl. Part. Phys.* 46, 085201. doi:10.1088/1361-6471/ab2347

Nagakura, H., and Hotokezaka, K. (2021). Non-Thermal Neutrinos Created by Shock Acceleration in Successful and Failed Core-Collapse Supernova. *Monthly Notices R. Astronomical Soc.* 502, 89–107. doi:10.1093/mnras/stab040

Niu, Y. F., Paar, N., Vretenar, D., and Meng, J. (2011). Stellar Electron-Capture Rates Calculated With the Finite-Temperature Relativistic Random-Phase Approximation. *Phys. Rev. C.* 83, 045807. doi:10.1103/PhysRevC.83.045807

O'Connell, J. S., Donnelly, T. W., and Walecka, J. D. (1972). Semileptonic Weak Interactions With C12. *Phys. Rev. C.* 6, 719–733. doi:10.1103/physrevc.6.719

Oda, T., Hino, M., Muto, K., Takahara, M., and Sato, K. (1994). Rate Tables for the Weak Processes of Sd-Shell Nuclei in Stellar Matter. *At. Data Nucl. Data Tables.* 56, 231–403. doi:10.1006/adnd.1994.1007

Paar, N., Colò, G., Khan, E., and Vretenar, D. (2009). Calculation of Stellar Electron-Capture Cross Sections on Nuclei Based on Microscopic Skyrme Functionals. *Phys. Rev. C.* 80, 055801. doi:10.1103/PhysRevC.80.055801

Papoulias, D. K., and Kosmas, T. S. (2018). COHERENT Constraints to Conventional and Exotic Neutrino Physics. *Phys. Rev. D.* 97, 033003. doi:10.1103/PhysRevD.97.033003

Papoulias, D. K., Kosmas, T. S., and Kuno, Y. (2019). Recent Probes of Standard and Non-Standard Neutrino Physics With Nuclei. *Front. Phys.* 7, 191. doi:10.3389/fphy.2019.00191

Papoulias, D. K., Kosmas, T. S., Sahu, R., Kota, V. K. B., and Hota, M. (2020). Constraining Nuclear Physics Parameters With Current and Future COHERENT Data. *Phys. Lett. B.* 800, 135133. doi:10.1016/j.physletb.2019.135133

Phillips, A. C. (2013). *The Physics of Stars*. John Wiley & Sons.

Sarriguren, P., Moya de Guerra, E., and Escuderos, A. (2001). βdecay in Odd-Aand Even-Even Proton-Rich Kr Isotopes. *Phys. Rev. C.* 64, 064306. doi:10.1103/PhysRevC.64.064306

Sieverding, A., Huther, L., Martínez-Pinedo, G., Langanke, K., and Heger, A. (2018). Neutrino Nucleosynthesis in Core-Collapse Supernova Explosions. *J. Phys. Conf. Ser.* 940, 012054. doi:10.1088/1742-6596/940/1/012054

Sieverding, A., Langanke, K., Martínez-Pinedo, G., Bollig, R., Janka, H.-T., and Heger, A. (2019). The ν-Process With Fully Time-Dependent Supernova Neutrino Emission Spectra. *ApJ.* 876, 151. doi:10.3847/1538-4357/ab17e2

Suzuki, T., Chiba, S., Yoshida, T., Kajino, T., and Otsuka, T. (2006). Neutrino-Nucleus Reactions Based on New Shell Model Hamiltonians. *Phys. Rev. C.* 74, 034307. doi:10.1103/PhysRevC.74.034307

Suzuki, T., Chiba, S., Yoshida, T., Takahashi, K., and Umeda, H. (2018). Neutrino-Nucleus Reactions on O16 Based on New Shell-Model Hamiltonians. *Phys. Rev. C.* 98, 034613. doi:10.1103/PhysRevC.98.034613

Suzuki, T., Honma, M., Mao, H., Otsuka, T., and Kajino, T. (2011). Evaluation of Electron Capture Reaction Rates in Ni Isotopes in Stellar Environments. *Phys. Rev. C.* 83, 044619. doi:10.1103/PhysRevC.83.044619

Suzuki, T., and Kajino, T. (2013). Element Synthesis in the Supernova Environment and Neutrino Oscillations. *J. Phys. G: Nucl. Part. Phys.* 40, 083101. doi:10.1088/0954-3899/40/8/083101

Titus, R., Sullivan, C., Zegers, R. G. T., Brown, B. A., and Gao, B. (2017). Impact of Electron-Captures on Nuclei nearN= 50 on Core-Collapse Supernovae. *J. Phys. G: Nucl. Part. Phys.* 45, 014004. doi:10.1088/1361-6471/aa98c1

Tsakstara, V., and Kosmas, T. S. (2011a). Analyzing Astrophysical Neutrino Signals Using Realistic Nuclear Structure Calculations and the Convolution Procedure. *Phys. Rev. C.* 84, 064620. doi:10.1103/PhysRevC.84.064620

Tsakstara, V., and Kosmas, T. S. (2011b). Low-energy Neutral-Current Neutrino Scattering onTe128,130isotopes. *Phys. Rev. C.* 83, 054612. doi:10.1103/PhysRevC.83.054612

Tsakstara, V., and Kosmas, T. S. (2012). Nuclear Responses of64,66Zn Isotopes to Supernova Neutrinos. *Phys. Rev. C.* 86, 044618. doi:10.1103/PhysRevC.86.044618

Tsoulos, I. G., Kosmas, O. T., and Stavrou, V. N. (2019). Diracsolver: A Tool for Solving the Dirac Equation. *Computer Phys. Commun.* 236, 237–243. doi:10.1016/j.cpc.2018.10.010

Wildenthal, B. H. (1984). Empirical Strengths of Spin Operators in Nuclei. *Prog. Part. Nucl. Phys.* 11, 5–51. doi:10.1016/0146-6410(84)90011-5

Woosley, S. E., Heger, A., and Weaver, T. A. (2002). The Evolution and Explosion of Massive Stars. *Rev. Mod. Phys.* 74, 1015–1071. doi:10.1103/RevModPhys.74.1015

Woosley, S. E. (2019). The Evolution of Massive Helium Stars, Including Mass Loss. *ApJ.* 878, 49. doi:10.3847/1538-4357/ab1b41

Zinner, N. T., Langanke, K., and Vogel, P. (2006). Muon Capture on Nuclei: Random Phase Approximation Evaluation Versus Data for6⩽Z⩽94nuclei. *Phys. Rev. C.* 74, 024326. doi:10.1103/PhysRevC.74.024326

Conflict of Interest: The authors declare that the research was conducted in the absence of any commercial or financial relationships that could be construed as a potential conflict of interest.

Publisher's Note: All claims expressed in this article are solely those of the authors and do not necessarily represent those of their affiliated organizations, or those of the publisher, the editors and the reviewers. Any product that may be evaluated in this article, or claim that may be made by its manufacturer, is not guaranteed or endorsed by the publisher.

Frontiers in
Astronomy and Space Sciences

Explores planetary science and extragalactic astronomy in all wavelengths

Advances the understanding of our universe - from planetary science to extragalactic astronomy, to high-energy and astroparticle physics.

Discover the latest Research Topics

See more →

Frontiers

Avenue du Tribunal-Fédéral 34
1005 Lausanne, Switzerland
frontiersin.org

Contact us

+41 (0)21 510 17 00
frontiersin.org/about/contact